# Developing Nanocomposites with Highly Aligned Nanoscale Reinforcement


A thesis submitted to

**the Cardiff University**

for the degree of

**Doctor of Philosophy**

in the

**Cardiff School of Engineering**

2021

**Gkaliou Kyriaki**

**Cardiff School of Engineering**

# Abstract

Developing Nanocomposites with Highly Aligned Nanoscale Reinforcement

Cardiff School of Engineering

Doctor of Philosophy

In this project the deposition of magnetic nanoparticles onto different graphene morphologies was investigated, to facilitate their alignment in nanocomposites. A simple co-precipitation method was used and detailed chemical analysis confirmed that the synthesis of iron oxide nanoparticles produces a mixed phase of magnetite ($Fe_3O_4$)/ maghemite ($\gamma$-$Fe_2O_3$). Better nanoparticle dispersion and a narrower size distribution was achieved on a higher surface area materials. As the size of the nanoparticles decreases, the ratio of magnetite to maghemite decreases, which leads to a lower magnetic saturation (Ms).

The effect of different graphene morphologies on the curing of the epoxy system was investigated by adjusting: (a) the nanofiller loading and mixing methods, (b) the surface functionalisation, (c) the stoichiometric ratio of epoxy resin and (d) the cross-linking density. The nanofillers reduced the density of the epoxy network due to either catalytic interactions with surface functionalization or acting as physical barriers between reacting molecules. This results in a lower stress transfer efficiency in the interphase region and such effects can explain the lower than anticipated reinforcement, especially as filler loading is increased.

A comprehensive study developed optimised experimental conditions for magnetic alignment of magnetic graphene flakes. Both theoretical and experimental studies confirmed the orientation of the magnetic flakes in epoxy nanocomposites under low magnetic fields. The alignment effect on the mechanical properties was evaluated using Raman Spectroscopy and tensile measurements. Compared with the nanocomposites containing randomly oriented magnetic flakes, a higher stress transfer between the aligned nanofillers and the matrix was achieved, as well as higher values of stiffness obtained in nanocomposites with certain dispersion state.

# Contents

# List of Abbreviation

DGEBA Diglycidyl Ether of Bisphenol A

DMA Dynamic Mechanical Spectroscopy

DSC Differential Scanning Calorimetry

FLG Few-layer Graphene

FLG-COOH Plasma-treated FLG

GNP Graphene nanoplatelet

GNPs-COOH Plasma-treated GNPs

GO Graphene oxide

HSM High Speed mixing method

MNPs@graphene Magnetic nanoparticles@graphene

MNPs@GNPs Magnetic nanoparticles@GNPs

MNPs@FLG Magnetic nanoparticles@FLG

MNPs@rGO Magnetic nanoparticles@rGO

PI Polyimide

PMMA Poly (methyl methacrylate)

PVA Polyvinyl alcohol

rGO reduced Graphene oxide

SAXS Small Angle X-ray Scattering

SEM Scanning electron microscopy

TEM Transission electron microscopy

TRM Three roll mill

Tg Glass transition temperature

TGA Thermal gravitational analysis

TRGO Thermally reduced graphene oxide

MWCNTs Multi-wall CNTs

wt. % Percentage by weight

vol % Percentage by volume

VSM Vibrating Sample Magnetometer

XPS X-ray photoelectron spectroscopy

s Aspect ratio

ξ Shape parameter

μm Micrometer

nm Nanometer

# List of Figures

# List of Tables

# Acknowledgement

First, I would like to express my appreciation to Dr Mark Eaton for his enthusiastic supervision and valuable encouragement. He was a great mentor who motivated me to continue even on the difficult days throughout this PhD project. Secondly, my gratitude goes also to Dr Jeremy Hall for his helpful suggestions and to Professor Philip R. Davies for his incredible supervision and support on the chemical data analysis.

I would like to thank Dr Samuel Pattisson who assisted me in so many experiments and has provided excellent ideas throughout my laboratory work. Moreover, I would like to thank Dr Dan Read and his PhD student, Alex Evans for their kind support on the VSM measurements. My thanks also go to Dr Craig James for performing the SAXS data and helping me with their analysis. Furthermore, I would like to thank Dr Duncan Muir of Earth Science, Dr David Morgan and Dr Tom Davies of School of Chemistry and Dr Wayne Nishio Ayre of Dental School for their assistance on the materials' characterization.

I would like also to thank all my colleagues from the Magnetics and the CUSP (Cardiff University Performance and Structure) groups for their inspiring ideas in the joint meetings. To add this, I would like to thank my colleague Perminder Sagha, who is a great colleague but also a faithful friend.

I also express my appreciation to Engineering and Physical Sciences Research Council (EPSRC) for their financial support through these years and to Haydale Ltd. for kindly offering the materials.

I would like to extend a final thank to Professor Costas Galiotis, Dr Tasos Manikas and Dr George Trakakis for their incredible support on my project as well as all to the research group at FORTH/ICE-HT (Patras, Greece) for my fruitful three-month placement.

At last but not least, I would express my gratitude to my family and all the friends for their constant support and encouragement. Finally, I would like to dedicate my PhD work to my little brave niece, Konstantia.

# Chapter 1 Introduction

## 1.1. Background of this project

Polymer nanocomposites reinforced with graphene-related materials (GRMs) or carbon nanotubes (CNTs) have been explored extensively for use as engineering materials in a number of demanding applications as a result of their low density and exceptional mechanical properties (Papageorgiou et al. 2020). Although many studies have explored the mechanical reinforcement of CNTs (Ma et al. 2010) as well as the synergetic effects with graphene nanomaterials into the polymer composites (Bagotia, Choudhary, and Sharma 2019; Yue et al. 2014; Jen and Huang 2019), the addition of CNTs in nanocomposites has been limited for industrial applications due to three factors: the poor dispersion which leads to the need of complex procedures, the dramatic increase in the viscosity of the polymer matrix by increasing the concentration of CNTs, resulting in the degradation of the composite performance (Qian, Greenhalgh et al. 2010) and their prohibitively high cost (Prolongo et al. 2014; Ramanathan et al. 2008).

After the first report of free-standing few-layer and single-layer graphene sheets in 2004 (Novoselov et al. 2004), many research strategies have been developed for the synthesis, structure, properties and applications of graphene-based materials in polymer nanocomposites. This worldwide interest is mainly due its unique properties, such as thermal conductivity in the order of 5000 W/mK (Balandin et al. 2008), high electron mobility in room temperature (250,000 cm2/Vs) (Novoselov et al. 2005), large surface area (2630 $m^2/g$) (Papageorgiou, Kinloch, and Young 2017), high modulus of elasticity (1TPa) (Lee et al. 2008) and good electrical conductivity, making it attractive for a list of potential applications (Potts et al. 2011; Huang et al. 2012), such as composites, electronics devices, energy storage, sensors, EMI shielding and biomedical applications. This has led to a massive investment in academic research and industry for the development of technology that bridges these two sectors and focuses on commercialization of graphene in real applications (Segal 2009) (Kong et al. 2019).

The study of the mechanical properties of graphene-based composites has raised a number of scientific challenges in both academia and industry. One of them is the individual morphological properties of the graphene nanofillers, such as the planar size (Anagnostopoulos et al. 2015) or the thickness (Gong et al. 2012), and also other critical parameters (wrinkling,

stacking, defects) which are strongly related with the mechanical reinforcement of graphene and play an important role in determining the ultimate properties of polymer composites.

Another challenge is the dispersion state in a bulk polymer system, which is essential for graphene flakes to be able effectively to enhance the properties of a matrix. Especially in thermosetting composites, the dispersion of graphene indicates fundamental changes in polymer mobility and thus in polymer dynamics due to the interaction of the polymer chains with the nanofiller surface, a region which is typically termed the 'interphase' (Putz et al. 2008). These interphase regions are of critical importance for nanocomposites because they can significantly affect their bulk properties, such as the glass transition temperature ($T_g$) and modulus (Tang et al. 2013). Many results have been reported in the literature that shows an increase of $T_g$ in graphene-reinforced epoxy systems mainly due to the strong interfacial interactions in the interphase region between the nanofiller and the matrix (Zaman et al. 2012; Naebe et al. 2014; Rafiee et al. 2009). However, there are examples that showed lower $T_g$ values linked to the dispersion state of the nanofiller, which lead to a decreased cross-linked matrix and hence in the diminishment of its mechanical properties (Bao et al. 2011). Little discussion is offered behind the cure effects on the mechanical properties, which will establish a better understanding for the mechanisms of mechanical reinforcement in epoxy systems.

The spatial orientation of the fillers is also a very important parameter in polymer nanocomposites because the reinforcement is significantly higher when the fillers are aligned in the direction of strain (Li et al. 2016). The in-plane orientation of the graphene nanosheets can be achieved due to their two-dimensional nature (Papageorgiou et al. 2020). Many efforts have been made to achieve graphene alignment in polymer matrices, as shown in Figure 1.1. These include out-plane forces, such as filtering/evaporation (Yousefi et al. 2013), shear forces (Boothroyd et al. 2018) or external electric (Martin et al. 2005; Wu et al. 2015; Xia et al. 2018) and magnetic fields (Wu et al. 2016). For magnetic fields, it has reported that a very high field strengths (9–16 T) are required to align graphene oxides, which is prohibitive in industrial applications (Li et al. 2015). For this reason, researchers have developed facile chemical methods to decorate superparamagnetic iron oxide nanoparticles ($Fe_3O_4$ or $Fe_3O_2$) onto the graphene surface. This facilitates alignment in much lower magnetic fields (40-500 mT) during the polymer composite manufacturing, achieving anisotropic thermal (Yan et al. 2014) and mechanical properties (Wu et al. 2016). Aside from fracture toughness no other mechanical properties have been studied or reported for magnetically aligned graphene nanocomposites. Further to this, there is no published work studying the effect of alignment on the curing process

of epoxy resins. Hence, there is still much to understand about the efficacy of reinforcement of thermosetting matrices by aligned iron oxide decorated graphene sheets.

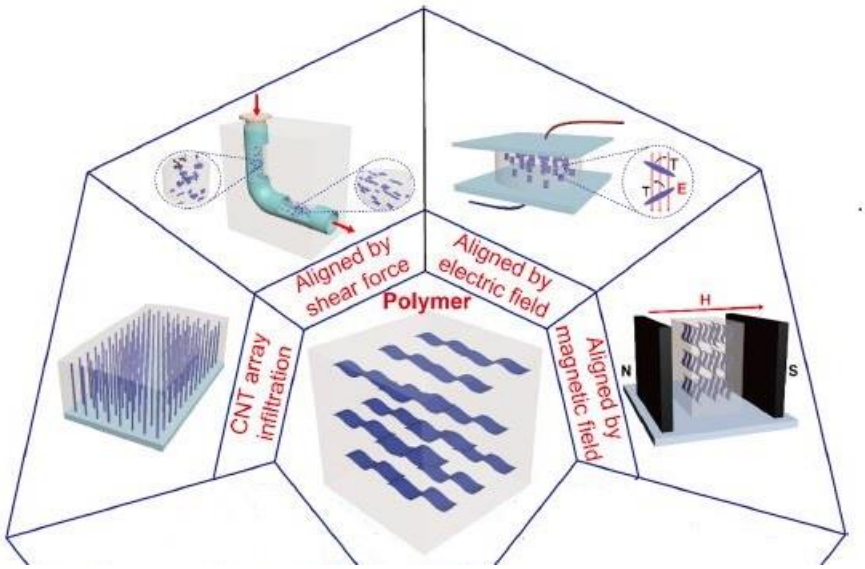


Figure 1. 1.Typical methods to achieve the alignment architecture in polymer matrices (Zhang, Zhao, and He 2020).

## 1.2. Objectives of this PhD work

The thesis aims to investigate the relationship between the structure and the properties of three different graphene morphologies with different functionalization states (more details in Chapter 3) which have been aligned in an epoxy system using low magnetic fields. The mains objectives of this project are following:

- a better understanding between the curing effects and the mechanical properties of the final nanocomposites. For this reason, the morphology of these materials that have been randomly dispersed in an epoxy matrix was determined using different mixing methods and the effect of the final structure was discussed while analysing the rheological and mechanical properties of composites in different filler loadings.
- the magnetic orientation by using low magnetic fields. This was achieved by attaching iron oxide nanoparticles into the graphene surface via a simple co-precipitation method.
- the growth mechanism of the magnetic nanoparticles into the graphene surface was explored and the effect of the particle size on the magnetic properties was investigated.
- the optimization of magnetic graphene alignment into the epoxy matrix was examined theoretically and experimentally by the following parameters: (a) the planar size of the

starting material, (b) the strength field, (c) the dispersion state through the different mixing methods and (d) the filler loading.

- Finally, the last objective is to understand about the efficacy of alignment on the curing process and its effect on the mechanical properties of the epoxy system. Hence, the orientation of three different magnetic graphene sheets on the thermo-mechanical and tensile properties was studied and compared with literature data.

## 1.3. Outline of the thesis

Chapter 2 provides a review of the relevant literature. A background to the structure of graphene, graphene oxide (GO) and reduced graphene oxide (rGO) is given first. Their properties, methods of production and their use as reinforcement in composite material is discussed. In addition, the chemical structure of epoxy resin and its mechanical properties will be discussed. A critical review of the published literature in the field of graphene-reinforced epoxy composites is presented along with methods and approaches used to align graphene in polymer matrices. In particular, it focuses on processing and dispersion methods for improving mechanical performance as well as the dispersion and functionalization effect on rheological properties. The effect of graphene and its functionalization on the epoxy cross-linking density and its influence into the final mechanical properties of graphene/epoxy composites is presented. Finally, the micromechanics of the reinforcement in graphene nanocomposites is reviewed. Gaps in research which need to be addressed are highlighted.

The third chapter describes the materials and the equipment used in this project for the chemical characterization of as received and produced materials, the structural morphology of the composites and the study of their mechanical properties.

The fourth chapter describes the deposition of iron oxide nanoparticles into the surface of three different graphene-based materials: GNPs-COOH, FLG-COOH and rGO. A detailed chemical characterization of the resulting nanomaterials is presented. The effect of different graphene morphologies on a simple co-precipitation method and the relationship between the particle size and the magnetic properties of the nanocomposites are investigated.

The fifth chapter presents the optimisation of the manufacturing parameters and the structural characterisation of epoxy resin filled with five different nanofillers, GNPs, GNPs-COOH, FLG, FLG-COOH and rGO. The effect of plasma treatment and the mixing method on the dispersion state of the nanofiller has been investigated before and after the curing process. The mechanical reinforcement of the epoxy by the addition of these nanofillers is studied via

Dynamic Mechanical Analysis (DMA) and tensile testing. The effect of nanofillers on the crosslinking density of the epoxy system and its relationship with the mechanical properties of the final composites has been studied using a second epoxy system with two different cross-linking density levels (linear and highly cross-linked polymerization). The study of the micromechanics through the 'rules of mixtures' and the analytical model Halpin-Tsai approaches are then applied to add interpretation of the data obtained.

The sixth chapter presents the manufacturing and structural characterisation on epoxy resin filled with magnetic graphene nanofillers: MNPs@GNPs, MNPs@FLG and MNPs@rGO. The effect of the mixing method on the dispersion state has been investigated before and after the curing process. Additionally, the orientation process under the application of low magnetic fields is described using firstly a mathematical model and then experimentally using optical and analytical methods. The effect of this alignment on the thermomechanical properties via DMA and tensile properties is explored. The study of the micromechanics through the 'rules of mixtures' and the analytical model Halpin-Tsai approaches for oriented nanofillers are then applied to the data obtained.

The conclusions of the project and opportunities for further work are discussed in Chapter 7.

# Chapter 2 Literature review

In this chapter, the reader is introduced on the background in graphene/polymer composites. In depth, the physical properties and preparation methods of graphene and graphene oxide (GO) as well as the manufacturing techniques of graphene-thermosetting composites are discussed. Then, the dispersion challenges of graphene into the thermosetting polymers are explained, focused on the dispersion effect on the mechanical and rheological properties of the final composites. The effect of graphene functionalisation on cross-linking density and curing was explored along with the subsequent effect on the mechanical properties of the composites. Also, the micromechanics models are included, highlighting the parameters that affect the mechanical reinforcement of the graphene into the polymers. The last part of this chapter is about the alignment methods of graphene in polymer matrices.

## 2.1. Graphene and its history

Graphene consists of a single atomic layer of $sp^2$ hybridized carbon atoms arranged in a honeycomb structure as shown in Figure 2.1. It has been viewed as the basic building block of all graphitic forms of carbon with different dimensionalities (Geim and Novoselov 2010). It can be wrapped to form the 0-D buckyballs, rolled to form the 1-D nanotubes, and stacked to form the 3-D graphite.

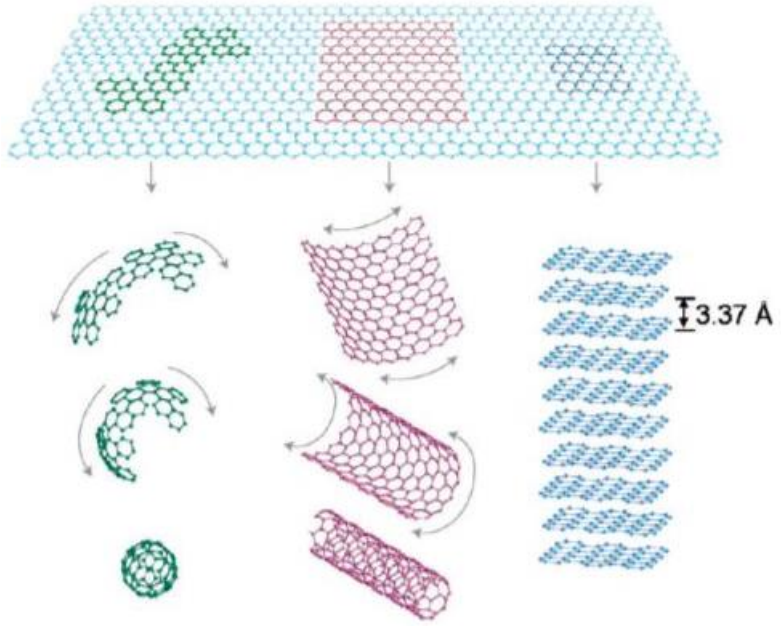


Figure 2. 1. Graphene: mother of all graphitic forms (Geim and Novoselov 2010).

Research about graphene, essentially an isolated single-atom plane of graphite, started back to the 1960s when surprisingly higher basal-plane conductivity of graphite intercalation compounds were discovered compared to that of the original graphite (Bacon 1961, Ubbelohde, Lewis et al. 1961). Then, it has grown slowly in late 20$^{th}$ century with the hope to observe superior electrical properties from thin graphite or graphene layers while obtaining graphene was considered to be a formidable task in both theoretical and experimental aspect (Singh, Joung et al. 2011). It was generally believed that, based on both theoretical calculation and experimental observation, 2D materials did not exist without a 3D base, as a result single layers of graphene to be considered thermodynamically unstable and could not exist under ambient conditions (Mermin 1968, Landau, Lifshitz et al. 1981). Although, many approaches were made to synthesize graphene, these could not reach the production of perfectly monolayer graphene. It was until 2004 that a first report by Andre Geim and Konstantin Novoselov was published which shows the preparation and isolation of single graphene layers by peeling graphite with adhesive tape, named as micromechanical cleavage (Novoselov, Geim et al. 2004). This resulted in an enormous rise of interest in the structure and properties of graphene in both scientific and engineering communities.

## 2.2. Preparation

Up to now, several methods have been explored to prepare high-quality graphene in large quantities for both research purposes and with a view to possible applications for graphene-based materials in polymer composites (Kotov 2006). These methods can be categorized into two major classes, one is known as ‘bottom-up’ methods and the other one is named as ‘top-down’ methods. The former depends on the chemical reaction of molecular building blocks to form covalently linked 2D networks and the latter relies on the exfoliation of graphite (Kim, Abdala et al. 2010).

### 2.2.1. Bottom-up Graphene

In bottom-up processes, graphene is synthesized by a variety of methods such as chemical vapour deposition (CVD) (Dervishi, Li et al. 2009, Wang, You et al. 2009),arc discharge (Wu, Wang et al. 2010), epitaxial growth on SiC (Berger, Song et al. 2006), chemical conversion (Park and Ruoff 2009), reduction of CO (Kim, Min et al. 2009), unzipping carbon nanotubes (Kosynkin, Higginbotham et al. 2009, Cai, Ruffieux et al. 2010) and self-assembly of surfactants (Zhang, Cui et al. 2009). Some of the main advantages are that they can yield high-quality graphene with large size (from sub-μm using CO reduction to cm range with CVD) and controllable thickness, providing a small number of defects. However, the resultant graphene is

mainly a good candidate for fundamental studies and electronic applications, especially the epitaxial and CVD techniques show a high compatibility with the current complementary metal–oxide–semiconductor (CMOS) technology (Zheng, Li et al. 2014). Moreover, these substrate-based techniques suffer from a limited scale and expensive production, and cannot meet the requirements of macroscopic quantities of graphene and are not a suitable source for polymer nanocomposites that require a large amount of graphene sheets preferably with modified surface structure (Kim, Abdala et al. 2010).

### 2.2.2. Top-down Graphene

In top-down processes, graphene or modified graphene sheets are produced by separation/exfoliation of graphite or graphite derivatives (such as graphite oxide (GO) and graphite fluoride (Worsley, Ramesh et al. 2007). Large-scale production of graphene at a low cost has been demonstrated to be possible using top-down techniques, making them suitable for polymer composite applications.

The first recognised method of this category is the micromechanical cleavage of HOPG (Highly Ordered Pyrolytic Graphite), illustrating by the Figure 2.2. The exfoliation mechanics of this method is that the Scotch tape is applied to the HOPG surface and thus exerts a normal force. One a normal force can overcome the van der Waals attractions between adjacent graphene flakes when peeling off two graphite layers apart, resulting in the graphite exfoliation. If one takes great pains to repeat this normal force numerous times, the graphitic layer becomes thinner and thinner and finally it will become single-layer graphene. Graphene prepared by this method is helped to discover many outstanding properties of graphene (Peres 2009, Stadler, Schmid et al. 2011) and it is generally suitable for fundamental studies because of the high quality and large lateral dimension, but not impossible to scale up for industrial production.

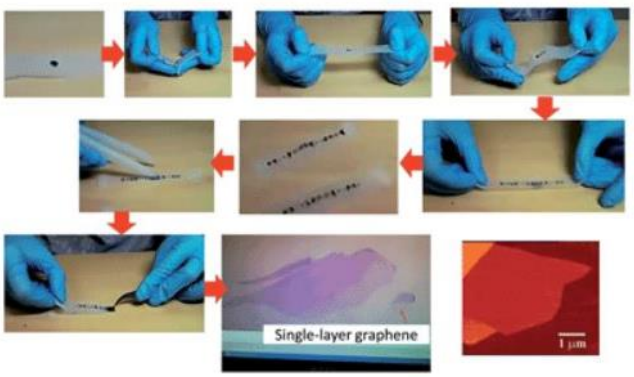


Figure 2. 2. An illustrative procedure of the Scotch-tape based micromechanical cleavage of HOPG (Yi and Shen 2015).

A micromechanical technique inspired by the "Scotch tape" method uses a three-roll mill with a polymer adhesive (Chen, Duan et al. 2012) in order to exfoliate natural graphite to single and few-layer graphene sheets. By this method, the graphite was mixed with polyvinyl chloride (PVC) dissolved in dioctyl phthalate (DOP) and the dispersion and exfoliation happen in the adhesive. The presented scalable process can be effective for the high-yield and low-cost production of graphene sheets or in situ fabrication of polymer/graphene nanocomposites (Li, Zhang et al. 2016).

Sonication based liquid-phase exfoliation of graphite to produce graphene has made the large-scale production of graphene possible. The first attempt was performed with graphite powder that dispersed in specific organic solvents, such as N,N-dimethylformamide (DMF) and N-methylpyrrolidone (NMP), followed by sonication and centrifugation (Hernandez, Nicolosi et al. 2008). This method opens a whole new route for the large-scale and low-cost production of graphene. The main benefit of this method is that the production of graphene is very easy and the energy per unit area required to overcome the van der Waals forces when peeling two sheets apart is very small. When the graphene and solvent surface energies are close, the mixing enthalpy (2.1) will be smaller, and the exfoliation occurs more easily. This energy balance for the graphene and solvent system can be expressed as the enthalpy of mixing per unit volume:

$$\frac{\Delta H_{mix}}{V_{mix}} \simeq \frac{2}{T_{flake}} (\delta_G - \delta_{sol})^2 \varphi \qquad (2.1)$$

in which $T_{flake}$ is the thickness of a graphene flake, $\phi$ is the graphene volume fraction, and $\delta_i$ is the square root of the surface energy of phase i (i denotes graphene or solvent). The drawback of this suggested method is that it gives an extremely low graphene concentration ($\sim$0.01 mg $mL^{-1}$), which is far from practical application. Based on the same idea, many researchers have contributed to achieving high-concentration graphene by prolonging the sonication time, increasing the initial graphite concentration, adding surfactants and polymers (Liu, Xie et al. 2011, Nicolosi, Chhowalla et al. 2013), solvent exchange methods (Yi and Shen 2015), and mixing solvents (Yi, Shen et al. 2012). However, the production of graphene or graphene oxide is very sensitive to sonication time and temperature (Lin, Zheng et al. 2014) to graphene with more defects than expected (Yi, Shen et al. 2013). Interestingly, the efficiency of sonication in the liquid-phase exfoliation of graphene depends on the cavitation field in the liquid (Han, Jang et al. 2014) which is almost static. A moving cavitation field or sonication combined with stirring should be helpful for efficient exfoliation, avoiding the case of graphite flakes to be exfoliated many times in the region of high cavitation intensity while may remain intact in the region of low cavitation intensity. The direct sonication method has potential to be scaled up to produce large quantities of graphene or functionalized

graphene that can be used for composite applications, but many parameters such as sonication frequency, sonication power, sonication source distribution, temperature, etc. should also be considered.

Besides the sonication-based exfoliation method which is a normal-force-dominated way, shear force can also be utilized to laterally exfoliate graphite into graphene flakes. Ball (wet or dry) milling, a common technique in the powder production industry, is a good candidate for generating shear force. By wet ball milling, graphite is dispersed in suitable solvents which have a matched surface energy for overcoming the van der Waals forces of adjacent graphene flakes. In order to achieve a good quality of exfoliation in few layer graphene sheets, a high energy ball milling could be needed with the additional use of sonication. Using the approach of dry ball milling, graphite was dispersed with chemically inert water-soluble inorganic salts to achieve a shifting of the layers in graphite (Posudievsky, Khazieieva et al. 2013). The dispersant-free liquid exfoliation of the mechanochemically delaminated graphite leads to a principal decrease of the thickness of graphene particles in the dispersions. The main drawbacks for both types of ball milling are the long processing times required, the reduction of the graphene lateral size and the introduction of defects, especially basal defects.

Another alternative route reported for the exfoliation of natural graphite to single- or few layers of graphene is through dissolution in chlorosulphonic acid (Behabtu, Lomeda et al. 2010) and the electrochemical functionalization of graphite assisted with ionic liquids (Liu, Luo et al. 2008). The first method can produce high-concentration graphene solutions, both isotropic and liquid crystalline that could be particularly useful for making flexible electronics as well as multifunctional fibres. However, it has potential for a large-scale production, but the hazardous nature of the hydrosulfonic and the cost of its removal may limit this potential. By the electrochemical exfoliation, an applied voltage drives the ionic species in an electrolyte to intercalate into the graphite electrode and increase the inter-layer distance between the graphite platelets (Achee, Sun et al. 2018). For instance, in ammonium sulfate, the sulfate ions and water molecules migrate into the interstitial regions of the graphite and locally form gas bubbles (such as $SO_2$, $O_2$), which open up graphene sheets, causing their expansion and exfoliation of the graphene layers (Parvez, Wu et al. 2014). However, the exfoliation in ionic liquids results in a low yield of graphene with has a small lateral size and often functionalization with ionic liquids, disrupting the electronic properties of graphene (Ilnicka, Skorupska et al. 2019).

## 2.3. Properties of Graphene

Graphene combines unique properties such as thermal conductivity in the order of 5000 W/mK (Balandin, Ghosh et al. 2008), high electron mobility in room temperature (250,000 $cm^{2/}V$ s) (Neto, Guinea et al. 2009), large surface area (2630 $m^2/g$), good electrical conductivity and great optical transmittance (~97.7%) (Zhu, Murali et al. 2010), making it attractive for many structural, thermal and electrical applications.

One of the reasons that make graphene stand out both as an individual material and as a reinforcing nanofiller in composites is the impressive mechanical properties. The reason for the exceptional mechanical properties of graphene lies in the stability of the $sp^2$ bonds that form the hexagonal lattice and oppose a variety of in-plane deformations. Lee et al. (2008) firstly determined the elastic properties and intrinsic breaking strength of free-standing monolayer graphene membranes by nanoindentation in an atomic force microscope (AFM). The authors isolated the monolayers through the use of optical microscopy and identified them with Raman spectroscopy. Then, graphene membranes suspended over holes of 1.0-1.5 μm in a diameter on a silicon substrate, as represented in Figure 2.3. They determined the variation of force with indentation depth (displacement response) from the graphene membranes and derived stress–strain curves by assuming that the graphene behaved mechanically as a 2D membrane of thickness 0.335 nm. By the indentation experiment, a Young's modulus of E = 1.0 ± 0.1 TPa (similar to bulk graphite), third-order elastic stiffness of D = –2.0 TPa and a strength of up to 130 ± 10 GPa for a graphene monolayer were calculated which are well-compared with the theoretical estimations (Kelly and Macmillan 1986, Liu, Ming et al. 2007). These experiments establish graphene as the strongest material ever measured and show that atomically perfect nanoscale materials can be mechanically tested to deformations well beyond the linear regime.

Raman spectroscopy is a powerful technique for the identification and characterisation of different forms of graphene, and it is also a very good way of following the molecular deformation of graphene through observing stress-induced Raman band shifts. Raman spectroscopy to probe the mechanical properties of graphene has been reviewed by Ferralis (2010). An exfoliated graphene deposited on a substrate which is then stretched or flexed in a Raman spectrometer. There was a large shift in the position of the 2D band with strain and the slope of the line is of the order of −60 ± 5 $cm^{-1}$/% strain. This slope corresponds to a Young's modulus for a graphene monolayer of 1200 ± 100 GPa using the universal calibration of −5 $cm^{-1}$/GPa for carbon fibres (Cooper, Young et al. 2001). Moreover, Cheong et al. (2012) estimated the Young's modulus of single and bi-layer graphene by measuring the strain applied

by a pressure difference across graphene membranes using Raman spectroscopy. The Young's modulus values for single- and bilayer graphene, 2.4 ± 0.4 and 2.0 ± 0.5 TPa, respectively which are significantly higher than the previous work, due to the different strain ranges used. Hence, Young Modulus may be larger in small strain ranges.

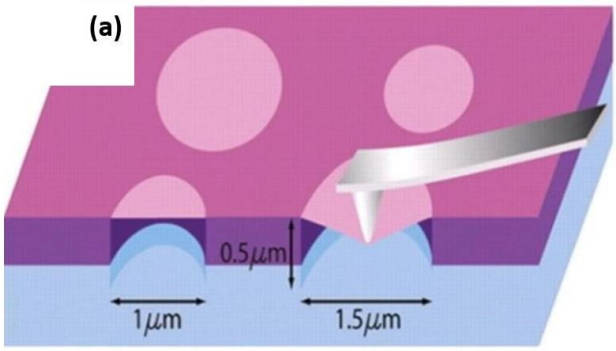


Figure 2. 3. Illustration of the nanoindentation setup in a suspended monolayer graphene membrane.

However, some reports have obtained lowered values of stiffness due to different types of defects, such as crumpling and wrinkling. Under realistic experimental conditions, free-standing (or even substrate-supported) graphene is never flat but is inevitably crumpled in the out-of-plane direction. These surface corrugations are responsible for the deterioration of the mechanical properties of the material and explain the large variation in its in-plane stiffness. For instance, Nicholl et al. (2015) found a decreased stiffness (20–100 N $m^{-1}$, smaller than 340 N $m^{-1}$ for the value expected for flat graphene, at room temperature for both of CVD and exfoliated graphene) by applying an electrostatic force based on interferometric profilometry. Moreover, the number of the graphene layers can affect the measurements of Young modulus. Annamalai et al. (2012) used AFM technique and estimated the Young's modulus of monolayer, bilayer, trilayer and five-layered graphene devices to be 1.12, 3.25, 3.25 and 3.43 TPa, respectively, showing the enormous increasing trend in Young's modulus with the increase in thickness. This is attributed to the clamping boundary condition (contact stiffness) that is different for different graphene thickness. In the case of monolayer graphene, van der Waals force influences the adhesion between graphene and the underlying substrate whereas in a multilayer graphene, this force controls the graphene and substrate adhesion as well as the adhesion between graphene layers (inter layer coupling). Hence, the different contact stiffness yields to a varying Young's modulus for different layers of graphene. Similarly, Poot et al (2008) also reported that the mechanical parameters of few-layer graphene (down to eight-graphene layers) show a strong dependence on thickness. This is well agreed with some simulation studies that showed a linear relation with the increase of the number of layers (from

a monolayer to 8-layers graphene, Young's modulus: 1.09 to 1.13 TPa, respectively) (Zhang and Gu 2013).

## 2.4. Graphene Oxide (GO)

### 2.4.1. Preparation

GO is generally produced by the treatment of graphite using strong mineral acids and oxidizing agents, typically via treatment with $KMnO_4$ and $H_2SO_4$, as in the Hummers method or its modified derivatives, or $KClO_3$ (or $NaClO_3$) and $HNO_3$ as in the Staudenmaier or Brodie methods (Potts, Dreyer et al. 2011). These reactions achieve similar levels of high oxidation (C:O ratios of approximately 2:1) which ultimately disrupts the delocalized electronic structure of graphite and imparts a variety of oxygen-based chemical functionalities to the surface, such as carboxyl (-OOH), hydroxyl (-OH), or epoxy (-O), on their basal planes and edges, as illustrated by Figure 2.4. The polar oxygen functional groups of GO render it hydrophilic; GO can be exfoliated in many solvents and disperses particularly well in water.

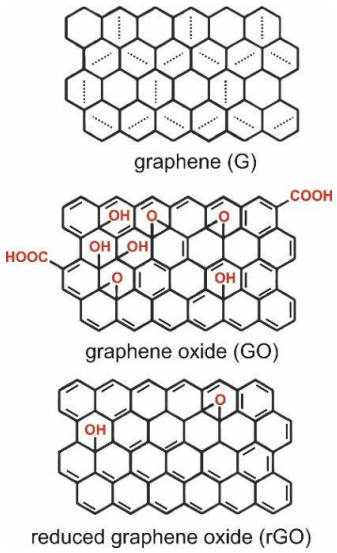


Figure 2. 4. Structures of graphene (G), graphene oxide (GO), and reduced graphene oxide (rGO) (Tadyszak, Wychowaniec et al. 2018).

Chemical (Stankovich, Dikin et al. 2007), thermal (McAllister, Li et al. 2007), microwave (Voiry, Yang et al. 2016), electrochemical (Toh, Loh et al. 2014), or microbial/bacterial treatments (Wang, Qian et al. 2011) can be used on GO to reduce the oxygen content and lead to production of so-called reduced graphene (rGO). The complete reduction of graphene oxide would lead to a perfect graphene layer as a product; however, there almost always remain some oxygen-containing functional groups, since not all $sp^3$ bonds return to a $sp^2$ configuration. Generally, the key design factors in GO reduction include the C/O ratio of the end product,

healing of the surface defects of the GO from oxidation, and choice of green reducing agents (De Silva, Huang et al. 2017), as well as maintaining or improving the desired physical and chemical properties of the GO.

### 2.4.2. Properties of GO

GO produced by graphite has a much lower thermal conductivity by 2-3 orders of magnitude comparing with graphene, due to the oxygen groups on the surface destroying lattice symmetry and creating local strains that lead to a decrease in thermal conductivity (Yang, Cao et al. 2019). A recent study showed that not only the concentration but also the configuration of the oxygen functional groups (e.g., hydroxyl, epoxide, and ether) has significant influence on the thermal conductivity. Through phonon mode analysis, phonon defect scattering as well as phonon localization are mainly responsible for the conspicuous reduced thermal conductivity (Zhang, Fonseca et al. 2014). Reduction of GO is critical for incorporation of rGO into polymers to improve their thermal conductivity. Using different reduction methods, the thermal conductivity of GO can vary 2 to 1000 W/mK (Schwamb, Burg et al. 2009).

Like its thermal conductivity, the electrical conductivity of GO is inhibited after the addition of oxygen groups and the disruption of the $sp^2$ bonding orbitals, making GO electrically resistive ($1.64 \times 104\ \Omega\ m$) (Wang, Nelson et al. 2012). As a result of this high resistivity, researchers have explored reduction techniques of GO to form rGO. Even after reduction, the rGO contains residual $sp^3$ bonded carbon to oxygen, which disturbs the movement of charge carriers through the rest of the $sp^2$ clusters. Electrical transport in rGO occurs primarily by hopping, which differs from that of mechanically exfoliated graphene (Bagri, Mattevi et al. 2010).

The mechanical properties of graphene oxide are inferior to those of graphene due to the disruption of the structure through oxidation and the presence of $sp^3$ rather than $sp^2$ bonding. The observed properties vary depending on the number of surface groups and defects leftover from oxidation or other treatment processes. Dikin et al. (2007)first investigated the mechanical properties of micron thick samples of graphene oxide paper and found it to have a stiffness of up to 40 GPa but a strength of only 120 MPa. Suk et al. (2010) undertook a similar study of the AFM indentation of monolayer graphene oxide with an effective thickness of 0.7 nm and measured a lower Young's modulus of $208 \pm 23$ GPa comparing with the reported valued of pristine graphene. Gao et al. (2011) have recently undertaken a study of the mechanical properties of graphene oxide paper (chemically modified by glutaraldehyde and water

molecules) and also followed its deformation using Raman spectroscopy, enabling its Young's modulus to be estimated. The effective Young's modulus of the graphene oxide was found to be 230 GPa, which is within the range of values determined using AFM indentation by Suk et al. Relating to the stiffness of rGO, using a similar indentation method, Gómez-Navarro et al. (2008) measured the stiffness of chemically reduced GO to be ~250 GPa, approaching that of the pristine monolayer graphene but it is still remarkable lower. Although, the properties of graphene oxide and its derivatives are lower in comparison with the graphene, they are more attractive for industrial applications due to their easier scalable production methods and their compatibility with the polymer matrices, providing a uniform material on the bulk composite.

## 2.5. Plasma functionalization of graphene

As mentioned above, the synthesis of GO relies mainly on the wet-chemistry based oxidation that involves the use of strong oxidizing agents. This method produces acid by-product waste and lacks control over kinetics. These harsh oxidative condition inherent in this method can lead to degradation of functional performance, heavy deterioration of the crystal quality of graphene sheets and mechanical strength of the final product (Liu, Xie et al. 2012).

Compared with other chemical treatments methods of graphene, plasma treatment is an effective and economical process for graphene functionalization. It is the simplest, quickest, and most non-polluting process, with ease of scale-up (Guy and Walker 2016). It provides a wide range of functional groups, dependent upon the chemical nature of the gas used (for instance, $H_2$, $O_2$, $N_2$, and $SF_6$) (Bianco, Losurdo et al.) and the plasma parameters reactions (processing time, power delivery and generation, and chamber pressure). It is used to control hydrophobicity/hydrophilicity of graphene, which is useful for graphene in composites (where graphene needs to bind with polymer chains) (Poosala, Hrimchum et al. 2015) or to prevent aggregation of exfoliated graphene flakes (Bon, Valentini et al. 2009). Plasma doping of graphite or multilayer graphene involves reaction of high-energy radicals or ions which can sometimes lead to unavoidable surface damage create imperfections in the graphene lattice, which can severely degrade the carrier transport properties (Jeong, Lee et al. 2011). Senthilnathan et al. (2014) used a liquid micro-plasma discharge process in order to add nitrogen atoms on to graphene sheets for electrochemical applications and observed by Raman spectroscopy an increase of the D-band indicating an increase in $sp^3$ hybridisation. If plasma functionalization can be controlled to minimize damage to the graphene, it may be no more detrimental to the graphene structure than wet acid based chemical modification procedures. For instance, Haydale Ltd. (2020) has achieved 21% functionalisation through its scalable

plasma process which is comparable of the wet chemical methods of graphene oxide production. Haydale's plasma process can also remove contaminations such as amorphous carbon, effectively increasing the crystallinity of the material, which is important for mechanical and electrical properties (Williams, Seunarine et al. 2013).

## 2.6. Classification framework for different graphene-type materials

Due to the high level of interest on graphene-based research by the scientific and industrial community, the term graphene is used in a generic manner and not in a precise way by scientists to describe many graphene-based materials (GBMs). This has resulted in a misunderstanding on the actual material than can really be named as graphene, which is a single-atom thick, two-dimensional sheet of hexagonally arranged carbon atoms isolated from its three-dimensional parent material, graphite. In order to fill this gap and guide the international scientific community, Bianco (2013) and Wick (2014) published two works describing the family of 'graphene materials', highlighting the importance of every author who undertake research on graphene and graphene-based composites to report all the information of the graphene-based materials, such as thickness or lateral planar size (Sanchez, Jachak et al. 2012).

According to these two publications, they build a nomenclature model which considers the three fundamental attributes of carbon-based two-dimensional materials: the number of layers, the C/O ratio and the lateral dimensions, as presented in Figure 2.5. Based on those three properties, a classification of graphene-based materials can be performed. Initially, monolayer graphene is the one-atom-thick material in which $sp^2$-bonded carbon atoms are hexagonally arranged. When the term 'nanosheet' is used mean that the lateral size is less than 100 nm. Otherwise, graphene microsheet is used when the lateral size is between 100 nm and 100 μm. Few-layer graphene is the material consisting of 2–5 sheets of graphene, while multi-layer graphene consists of 5–10 layers of graphene. Moreover, graphite nanoplatelets also consist of graphene sheets but their lateral dimensions/thickness are higher than those of many-layer graphene (more than 10 layers, less than 100 nm thickness). Finally, exfoliated graphite is a multi-layer material that can be prepared by partial exfoliation of graphite and retains its 3D crystal stacking (Papageorgiou, Kinloch et al. 2017).

Relating to C/O atomic ratio, Graphite oxide is a bulk solid made by strong acid oxidation of graphite through processes that functionalize the basal planes and in-crease the interlayer spacing. Graphite oxide can be exfoliated (i.e., sonication) in solution to form (monolayer) graphene oxide or partially exfoliated to form few-layer graphene oxide (GO). Typically, GO

with chemical compositions corresponding to a C/O ratio of 4:1 to 2:1 are produced (Wick, Louw-Gaume et al. 2014). Graphene can also be transformed into reduced rGO and this will increase the C/O ratio to approximately 12:1 but values as large as 246:1 have been reported (Gao, Alemany et al. 2009). Also, there is an ISO Standard (ISO/TS 80004-13:2017) associated to graphene terminology and classification that follows similar definitions.

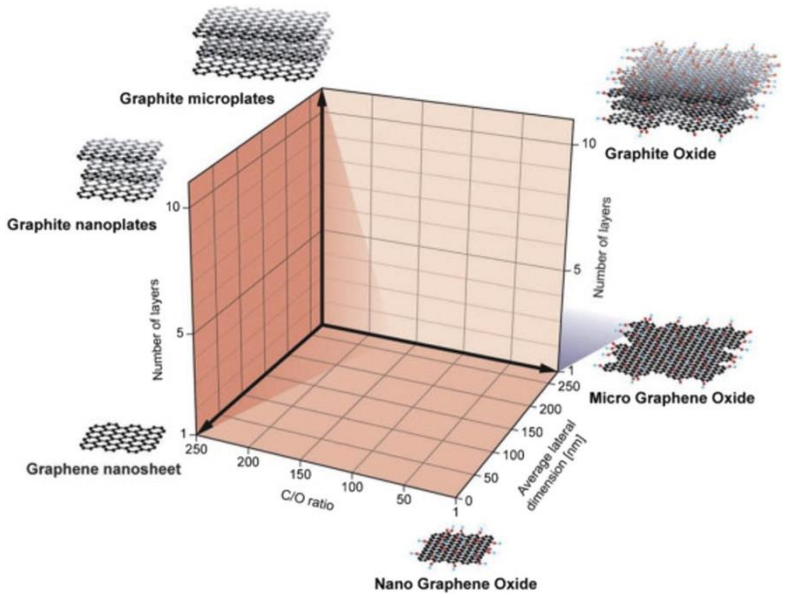


Figure 2. 5. Classification for different graphene-type materials based on the number of layers, the C/O ratio and the lateral dimensions (Wick, Louw-Gaume et al. 2014).

## 2.7. Graphene-based bulk nanocomposites

Since 2004 the number of graphene-related academic publications has substantially increased. The growth of graphene research sector can be evident by the publication record (Mohan, Lau et al. 2018), as shown in Fig. 2.6. There were over 35,000 papers published with the keyword 'graphene' in 2016 (Web of Science 2016). Recently, the number of reports on graphene-based composites has increased which are focused on the production and enhanced properties of graphene-based polymer composites. Researchers have made successful attempts for GO and graphene–polymer composites similar to CNT-based polymer composites (Ma, Siddiqui et al. 2010). The main drawbacks of the CNTs-based polymer composites are the poor dispersion, resulting in the need of complex procedures of dispersion and the high cost of carbon nanotubes which limits their industrial applications (Prolongo, Moriche et al. 2014). 2-D graphene also has better electrical, thermal and mechanical properties, compared with other reinforced materials, such as CNTs or Kevlar fibres, making graphene an interesting filler to manufacture composite materials with improved multifunctional properties.

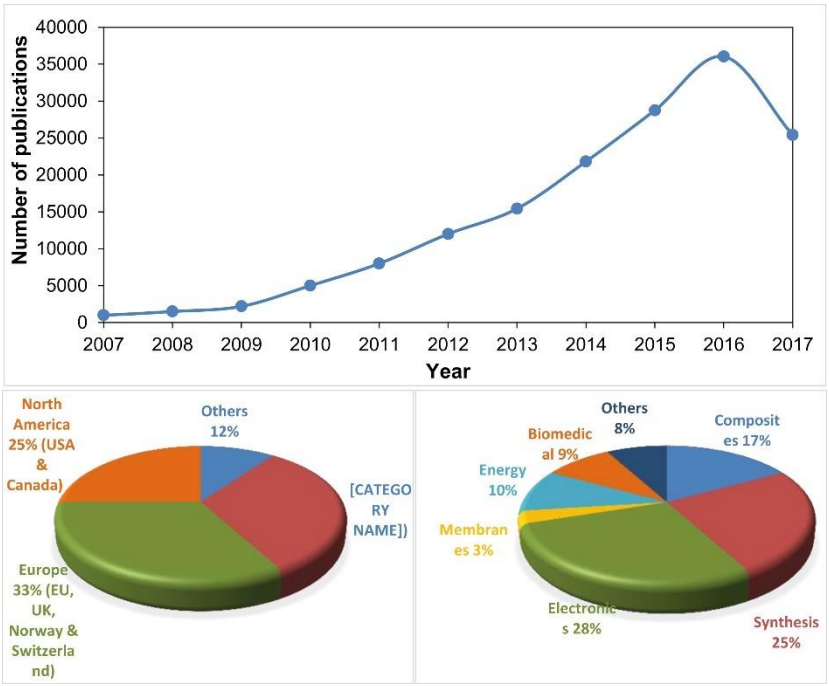


Figure 2. 6. (a) Publications on graphene from 2007 to 2017 and it is expected to reach at least 40000–45000 publication by the end of 2017. [Source- Web of Science], (b) proportion of overall publications by countries and (c) by sectors (Mohan, Lau et al. 2018).

There are several challenges needed to be overcome to manufacture graphene or graphene oxide based polymer composites which are a) functionalization of graphene sheets b) homogeneous dispersion of materials into the polymer matrix with minimal restacking or agglomerations (Li, Slater et al. 2019), c) understanding of the interfacial structure and properties, d) controlling the folding, crumpling, bending of graphene materials or even breaking within the composites (Singh, Joung et al. 2011). These last observations can significantly reduce their effective aspect ratio and subsequently their reinforcement characteristics. In the next section, an introduction to thermosetting polymers is included and the manufacturing methods of graphene based thermoset nanocomposites will be reviewed.

## 2.8. Graphene –thermoset nanocomposites

Thermosetting polymers are obtained by a large number of cross-linking routes of linear prepolymers or by the formation of cross-linked networks due to the reaction between two monomers by the application of heat (Pascault, Sautereau et al. 2002). Typical examples of thermosetting polymers include epoxies, polyurethane, natural rubber, phenol formaldehyde, silicone, vinyl ester, unsaturated polyester resin etc.

Epoxy is a well-established thermoset polymer with a wide variety of applications ranging from electronics to aerospace. Epoxy resins are versatile monomers characterised by the possession of more than one 1, 2-epoxy group per molecule, as shown in Figure 2.7 (a). This group may lie within the body of the molecule but is usually terminal. The epoxy ring is highly strained and is reactive to many substances (named as catalysts or hardeners), particularly by proton donors, so that reactions such as that shown in Figure 2.7. (b) can occur (Brydson 1999):

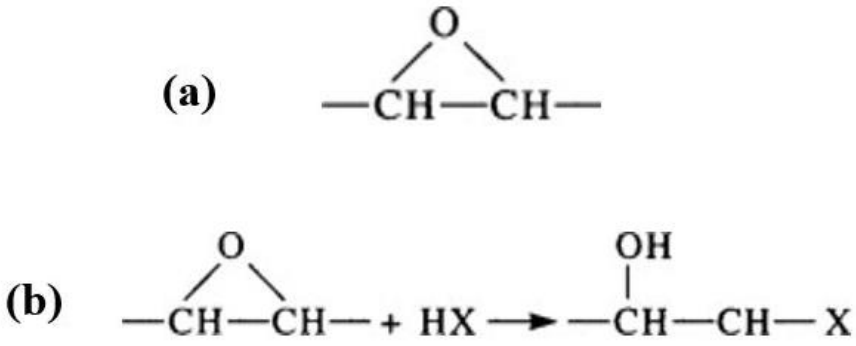


Figure 2. 7. (a) Structure of an epoxide ring, (b) typical reaction between the epoxide ring and a reagent (Brydson 1999).

The most common epoxy is diglycidyl ether of bisphenol A (DGEBA) which is characterized by the presence of two epoxide groups (Figure 2.8). The epoxide group is subjected to a variety of chemical reactions to obtain different epoxy resin structures. The crosslinking agents (hardeners) commonly used for generation of cross-linked structures are aliphatic amines, aromatic amines, polyamines, and anhydrides. These types of compound react directly with the epoxy and other groups of the resin, and so influence the structure of the cured resin. Cure temperatures from below 0°C to > 200°C are used, depending on the reactivity of the hardener (Mullins, Liu et al. 2018). The degree of the cross-linking and the inter-chain bond nature provides desirable mechanical, adhesive, chemical and corrosion resistance properties (Saleem, Edathil et al. 2016).

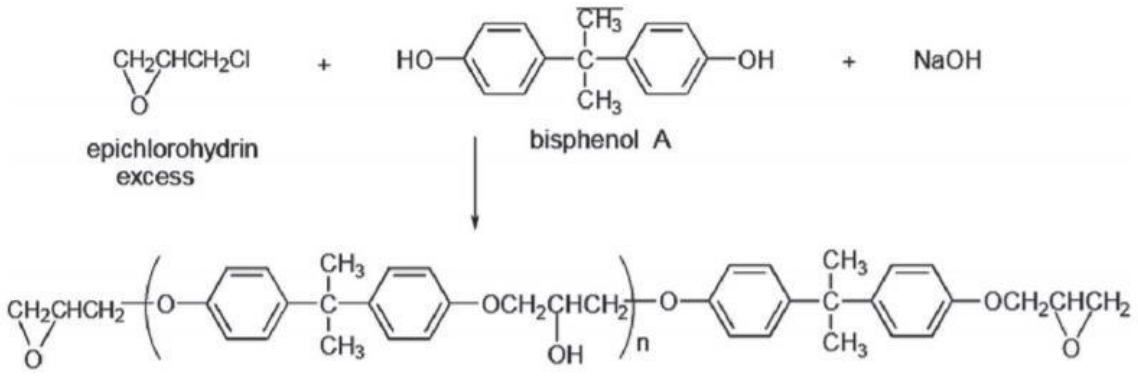


Figure 2. 8. Schematic of synthesis of DGEBA (Saleem, Edathil et al. 2016).

Due to these characteristics, epoxy is extensively used for applications such as structural adhesives, surface coatings, electronics, engineering composites and packaging (Kausar, Rafique et al. 2016). However, its brittleness limits on its applications and it has put forward requirements of higher performance and multifunction of the epoxy materials. One of the main characteristics of thermosets is that wide ranges of properties are achievable depending on the combined choices of monomer, catalyst, cross-linker, chain extender, cure schedule, and additives such as fillers and fibers. For example, the same epoxy monomer can be prepared to exhibit $T_g$ (glass transition temperature) values from < 20°C to > 200°C, from highly cross-linked network to noncross-linked thermoplastics, and from hydrophilic to hydrophobic character. The modulus can range from 2 GPa for neat resin to over 100 GPa with continuous fiber reinforcement (Mullins, Liu et al. 2018). Thus, researchers are still trying to improve their toughness and strength in order to satisfy the increasing demands in high-performance applications, like structural elements of large high-speed aircraft. To address this issue, the incorporation of nano-fillers has been investigated as an effective approach to improve the performance of epoxy resins. Several research groups have already investigated the reinforcement of epoxy resin with graphene nanofillers in order to develop multifunctional polymer composites.

It is well known that the practical performance of polymer composites depends not only on the individual properties of the nanofillers as well as the exceptional properties of the matrix, but also, the synergistic combination of high specific surface area of graphene, their uniform dispersion and strong interfacial interactions with the polymer matrix. Pristine graphene is characterized by its highly cohesive van der Waals energy (5.9 kJ/mol), making it hard to achieve good dispersion in most polymer matrices, including epoxy. Moreover, the weak interfacial interaction between the graphene nanofiller and the matrix due to atomically smooth

surface and chemical inertness of pristine graphene, results in an inefficient load transfer from matrix to graphene (Dai, Wang et al. 2015, Zhao, Chang et al. 2016).

Therefore, chemical functionalization of graphene sheets is normally adopted with aim to facilitate the compatibility and interfacial interaction between the graphene and the epoxy matrix. Graphene has been functionalized with molecules and macromolecules covalently or non-covalently depending on the application. Covalent functionalization approach involves formation of strong chemical bonds between the groups present on the graphene surface and polymer matrix, while non-covalent functionalization is mainly based on weak van der Waals force or π-π interaction of aromatic molecules on the graphene basal plane and non-covalent functional groups. In comparison, the main benefit of non-covalent functionalization is that does not induce defects sites unlike covalent modification, while covalent functionalization ensures a strong and irreversible bond between the polymer matrix and graphene (Layek and Nandi 2013),providing better results on the dispersion state. In the next section, significant methods of covalent and non-covalent modifications of graphene are reported for enhancing their mechanical reinforcement in epoxy composites.

### 2.8.1. Covalent functionalization

Based on the consideration of load transfer efficiency, covalent decoration of pristine graphene sheets is a realistic solution to improve their dispersion in epoxy matrices. One common method is focused on the modification of graphene sheets with functional ends of amine or epoxy groups that are chemically similar to the components of the epoxy resin matrix. Fang et al. (2010) prepared amino-functionalized graphene sheets ($NH_2$-GN) starting by reduced GO (rGO) and epoxy composites as illustrated by Figure 2.9. Then, $NH_2$-GN mixed with the epoxy resin by ultrasonication and casted followed a specific curing process under heat. The resulting composites exhibited significant enhancement in mechanical properties with the addition of only 0.6 wt. % amine-functionalized graphene sheets. Similarly, GO sheets were functionalized chemically with hexachlorocyclotriphosphazene (HCTP) and glycidol (Bao, Guo et al. 2011) and created a rich-epoxy environment around the graphene sheets and leads to strong interfacial interactions between the filler and the epoxy matrix and hence a good dispersion of functionalized graphene in epoxy nanocomposites. The resulting graphene/epoxy composites showed improved mechanical, electrical and thermal properties.

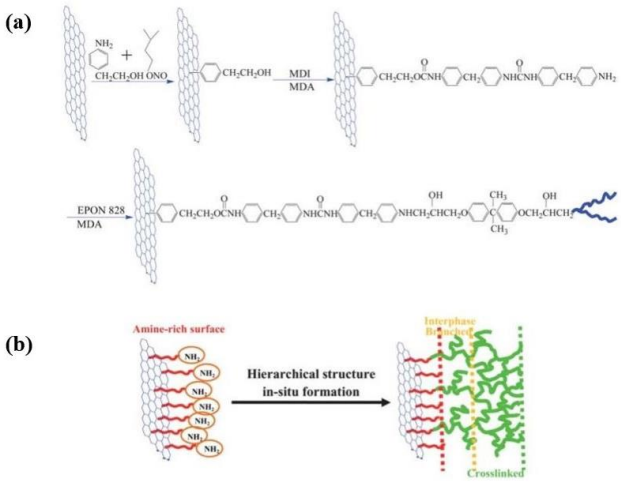


Figure 2. 9. Synthetic route for $NH_2$-GNs and preparation of GN-epoxy nanocomposites; (b) amine-rich graphene surface and hierarchical interphase structure.

Many reports are included in the literature (Kim, Yim et al. 2012, Li, Wang et al. 2013, Liu, Zhao et al. 2014, Naebe, Wang et al. 2014, Zhang, Wang et al. 2014, Bose, Das et al. 2018) that showed a very good interfacial interaction via the covalent bonding between the filler and the matrix. Comparing with the mechanical properties of the untreated-graphene composites, these strong interfacial interactions result on a significant improvement to the mechanical properties of the final composites with a very low treated-graphene filler content (<1% wt.). Interestingly, the first report by Li et al. dispersed 0.2 wt. % epoxy- and amino-functionalized graphene sheets into epoxy composites and showed increases of 20% and 32% in Young's modulus, respectively, compared with the pure epoxy. Both functionalized-graphene epoxy composites showed lower $T_g$ values that has been attributed to the modification of the epoxy stoichiometry via the epoxy- and amino- groups of the graphene sheets which leads to a 'soft' interphase in the region of functionalized GO/epoxy composite. The rest reports, referred to the beginning of this paragraph, include results with $T_g$ values higher than the untreated graphene composites with enhancing thermomechanical, flexural and tensile properties. It is clear that more investigation is needed to understand better the effect of the crosslinking density on the final mechanical properties using different graphene materials. This will be explored later in the literature review chapter (Section 2.11).

The most common strategy for covalent functionalization begins with graphene oxide (GO) as the starting material or reduced GO in order to avoid the excessive disruption of the graphene structure through the acid chemical reaction. As mentioned on the section 2.4.2., GO suffers

from significant loss in its properties comparing with pristine graphene and even after the reduction processes, rGO has still large defects which make the physical properties of the obtained composites to be far below the anticipated potentials.

### 2.8.2. Non-covalent functionalization

To avoid damage to graphene's structure, the non-covalent functionalization can be a good approach to functionalize graphene sheets since this approach is based on Van der Waals force or π–π interaction of aromatic molecules on the graphene basal plane, which can avoid generating defects and disrupting the conjugation on the graphene surface (Teng, Ma et al. 2011). Recently, a novel approach was developed to prepare non-covalently functionalized graphite flakes, which are used to produce nanocomposites with epoxy showing improved mechanical properties and thermal conductivities. Figure 2.10 illustrates all the steps of the preparation of the functionalized graphene/epoxy composites: 2D graphite flakes, dispersed in pyridine, were then functionalized with pyrenebutyric acid (PBA), termed as f-GFs and was then dispersed into epoxy matrix. The storage modulus of the f -GF composites increased by as much as 100% relative to the pure epoxy modulus, and by 57% compared with that of GO composites which is attributed to the interaction between the carboxylic group of PBA functionalized on the surface of the GFs and the epoxy matrix, which enhances interfacial adhesion and restricts the motion of the epoxy segmental chains.

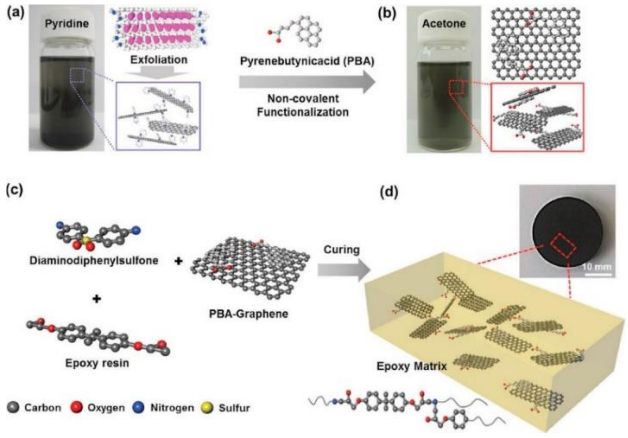


Figure 2. 10. Schematic diagram showing the overall processing required for the f -GFs and f -GFs-nanocomposites: a) GFs using ternary eutectic system of the alkali salts and digital photography image of dispersed f -GFs in pyridine. b) Non-covalent functionalized GFs by PBA and digital photograph image of dispersed f -GFs in acetone. c) Mixing epoxy resin, Curing Agent, and f -GFs through sonication. d) Curing process for the fabrication f -GFs-nanocomposites and digital photograph image of f -GFs–Nanocomposites (Song, Park et al. 2013).

## 2.9. Mechanical dispersion of graphene into the epoxy composites

The incorporation of graphene fillers into the epoxy matrix can lead to large agglomerations of graphene nanoparticles, resulting in difficulties to uniformly disperse these particles. Apart from the chemical functionalization of graphene that ensures the strong interfacial interactions between the nanofillers and the epoxy matrix, researchers have tried to enhance their dispersion through mixing, using mainly: calendering (three roll miller), ultrasonication, and shear mixing. A review of each approach is given below and focuses on the potential to improve mechanical properties of the final composites.

### 2.9.1. Calendering process (three roll mill)

A three-roll mill is a machine which depends on compressive impact as well as shear force produced by three horizontally positioned rolls rotating at different speeds relative to each other and in opposite directions. This high shear force is the driving force to shear and disperse nanoplatelets into polymer system (Figure 2.11. (a)). The three adjacent rolls of a three-roll mill (called the feed roll, centre roll and apron roll) rotate at progressively higher speeds (1:3:9) (Figure 2.11 (b)).

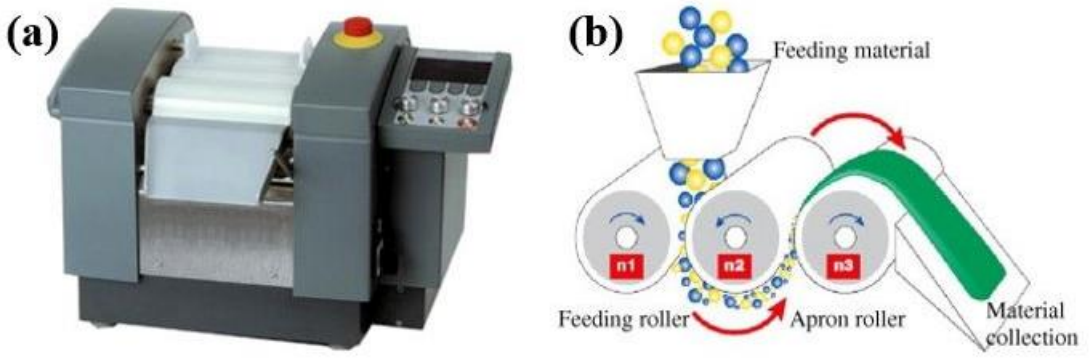


Figure 2. 11. Calendering (or three roll mills) machine (a) and schematic diagram showing the general configuration and its working mechanism (b) (Ma, Siddiqui et al. 2010).

The uncured polymer composite is fed into the hopper, where it is drawn between the feed and center roller. Because of the liquid surface tension, the material flows without dropping under and over the adjacent rollers. Then, the material that remains on the center roller moves through the second nip between the center roller and apron roller, which subjects it to even higher shear forces. A knife blade then scrapes the processed material off the apron roller and into the material collection point. The milling cycle can be repeated multiple times to maximize dispersion. The gap and speed settings on the mill can be controlled. Specifically, in our system

(EXAKT 80E), the narrow gaps can be controlled from 5 to 200 μm between the rollers, combined with the mismatch in angular velocity of the adjacent rollers, result in locally high shear forces with a short residence time. Relating to the speed rollers, the range is from 30-600 rpm. In our experiments, the shear rate reaches the value of $2.6*10^5$ $s^{-1}$, considering that the lowest gap size was 5 μm with speed of 450 μm. The calculations were done following the model by Palmese et al. (2015), as described in Chapter 5. One of the unique advantages of this technique is that the gap width between the rollers can be mechanically or hydraulically adjusted and maintained, thus it is easy to get a controllable and narrow size distribution of particles in viscous materials. In some operations, the width of gaps can be decreased gradually to achieve the desired level of particle dispersion (Ma and Kim 2011). Comparing with other mixing methods (for instance, ultrasonication), large volumes of polymer suspensions can be used and mixed uniformly.

This method has proven very effective in dispersing 1D nanofillers such as carbon nanotubes (Rosca and Hoa 2009) or 2D nanoparticles such as nanoclays (Agubra, Owuor et al. 2013), within epoxy resins. More recently the three-roll mill (TRM) method has been used in order to disperse or exfoliate graphite materials in epoxy matrices (Wang, Drzal et al. 2015). Prolongo et al. (2014) tried to disperse graphite nanoplatelets (GNPs-planar size 25 μm) into a DGBEA-based epoxy resin by sonication firstly and then followed by three roll miller. Although they achieved a good dispersion level (without exfoliation of GNPs), the storage modulus increased at 38% regarding the pure epoxy resin when a quite high loading of 8 wt. % GNPs was used. This was explained by the poor interfacial interaction that occurs between the untreated GNPs and the epoxy resin that prevents the load transfer from matrix to nanofiller. A slight increase of ~24% at tensile modulus at 3 wt. % GNPs was observed, while higher percentages of GNPs induce a slight decrease. Similar behaviour was observed by B. Ahmadi-Moghadam (2014) that investigate multifunctional properties of GNPs (GNPs-planar size 25 μm) dispersed on a commercial epoxy system (Araldite LY1564, Bisphenol-A) by TRM. A moderate increase on stiffness was observed, only 10% with an optimum loading of 2wt. %. In their later publication, the authors used four different surface modifications (namely, unmodified GNPs, graphene oxide GNPs (GO), G-$NH_2$ and G-Si) dispersed using TRM in the same epoxy matrix (Ahmadi-Moghadam, Sharafimasooleh et al. 2015). In general, the functionalized nanocomposites reinforced with functionalized GNPs (i.e., G-Si and G-$NH_2$) provided a higher elastic modulus (~14% at 0.5 wt. %) and strength (~50% at 0.5 wt. %) than that obtained using unmodified

GNPs or GO. This again confirms the importance of the interfacial interactions between the nanofiller and the host matrix.

Throckmorton et al. (2015) presents a novel method of few layer graphite epoxy nanocomposite preparation directly from untreated flake graphite (diameter range: 300-700 μm and thickness: 20-50 μm) using a room temperature ionic liquid as solvent/dispersant. An exfoliation of the few-layer graphite was achieved using a three-roll mill by passing 30 times through a variety of gap spacings, reaching a low thickness (1-3 layers) and an increase ~18% of the mechanical modulus was observed with 3 wt. % loading. One year later, Yan Li et al. (2016) firstly presented an effective and powerful route to produce in situ exfoliated FLG/GNP (thickness:5-17 nm) directly to the epoxy matrix by three roll milling, avoiding any intermediate steps, such as filtering, removal of the dispersing liquid medium, purification, drying of powder, re-dispersion into the final matrix. The authors have been studied three different protocols using a range of gap sizes, number of cycles and rotation speeds. The starting material was graphite flakes with lateral dimensions ~600±150 μm and ~800±200 μm and a thickness of 40 μm. FLG/GNPs particles achieve the highest mechanical reinforcement ever reported (bending elastic modulus increasing by ~160% for 4 wt. % of FLG/GNPs), demonstrating the potential in future applications for in situ exfoliation process and consequently a great homogeneous dispersion of these nanoparticles in epoxy.

### 2.9.2. Ultrasonication

Ultrasonication is the act of applying ultrasound energy to agitate particles in a solution for various purposes (Loos 2014). In the laboratory, it is usually achieved using an ultrasonic bath or an ultrasonic probe. It is the most frequently used method for nanoparticle dispersion. When ultrasound propagates via a series of compression, attenuated waves are induced in the molecules of the medium through which it passes. Ultrasonication generates alternating low-pressure and high-pressure waves in liquids, leading to the formation and violent collapse of small vacuum bubbles (Gou, Zhuge et al. 2012). This phenomenon is called cavitation and thus results in the separation of individualized nanoparticles from the bundles.

Ultrasonication is considered as an effective method to disperse graphene sheets in liquids having a low viscosity, such as water, acetone, and ethanol. Graphene dispersed firstly in other solvents like THF (Zaman, Kuan et al. 2012, Chong, Hinder et al. 2016), and DMF (Papageorgiou, Kinloch et al. 2017) and then added to the resin. However, it should be noted that such dispersions require another step to remove the solvents (>24 hrs) prior to curing. This

can lead to operational complexities and lengthy processing durations. The residual solvent also has detrimental effect on the final properties of the composite material (Tang, Wan et al. 2013). In order to avoid these drawbacks, some researchers are directly disperse graphene with epoxy resin or the hardener without using solvents (Wei, Atif et al. 2015). Muhammad Razlan Zakaria et al. (2017) mixed GNPs (planar size: 15 μm and sheet thickness: 11 to 15 nm) directly with the epoxy matrix (for 30 min) and compared the mechanical properties of these composites with MWCNTs/ epoxy composites that manufactured with the same method. Up to 1 wt.%, slightly lower mechanical properties for the GNPs/epoxy nanocomposites compared with the MWCNT filled epoxy nanocomposites was found which the authors attributed to these reasons: (a) the 2D structure of GNP is more easily aggregated than MWCNT due to its larger surface areas and plane-to-plane contact areas and (b) the poor interfacial interactions between the GNPs and the matrix as their wrinkle structure is easier to detach from the epoxy matrix compared to the MWCNT structure.

### 2.9.3. Shear mixing

While ultrasonication is a versatile method to disperse nanofillers in the laboratory, it always causes certain level of damages to the nanofillers and is not scalable for industrial applications. Alternatively, shear mixing is less intensive and has the potential to be scaled up for industrial productions. Shear mixing is already widely used to disperse nanoparticles in liquids.

For lab research, a high shear laboratory mixer is usually used (Silverson), reaching a shear rate of $10^4$-$10^6$ $s^{-1}$. The mixer provides a maximum rotor speed of 8000 rpm (6000 rpm under load) and a range of capacity from 1 ml to 12 litres. The standard mixing assembly comprises a frame, rotor with four blades sited by the stator, screen and base plane, as shown in Figure 2.12 (a), (b). During the rotation, the shear mixer acts as a pump, pulling both liquids and solids into the mixing head where centrifugal forces drive them towards the edge of the rotor/stator. This is accompanied by intense shear as the materials are driven at high velocity and forced out through the perforations in the stator and circulated into the main body of the mix (Figure 2.12 (c)).

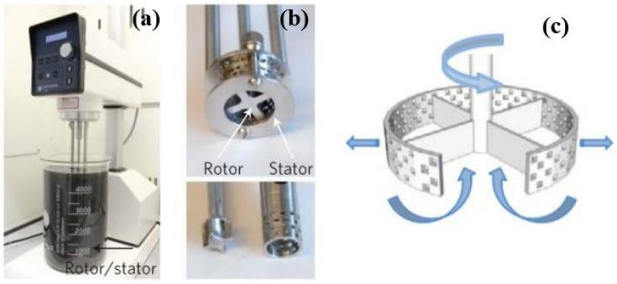


Figure 2. 12. A typical example of a lab high-shear mixer (a), the head of the mixer consists of rotor and stator (b), the top arrow indicates the direction of rotation while the other arrows illustrate the direction of liquid (and associated solids) flow (c) (Paton, Varrla et al. 2014).

One main advantage of this methodology is that laboratory-scale shear mixers typically deliver hundreds of watts into a few litres of liquid resulting in energy densities of ~100 W per litre compared to sonicators that need energy densities of thousands of watts per litre. Recently, shear mixing was used in order to exfoliate untreated graphite crystals in liquids in order to give large quantities of defect-free graphene that is many times more efficient comparing with the ultrasonication which can be scaled-up to an industrial level (Paton, Varrla et al. 2014). According to this research, they found that the graphite exfoliation occurs whenever the local shear rate exceeds a critical value of ~$10^4$ $s^{-1}$. Such shear rates can be achieved in a range of mixers including simple kitchen blenders. Moreover, they performed large scale trials and they managed to reach a production of very large quantities of exfoliated graphene (5.3 g/hr in 300 L batch process). In order to compare the efficiency of the shear mixing with the sonication, the graphite was sonicated in similar volumes and times. The data is shown in Figure 2.13 and clearly shows shear mixing to be far superior in all cases. However, sonication gives better results at small volumes, but this results in limited production rates which is not desirable for industrial applications.

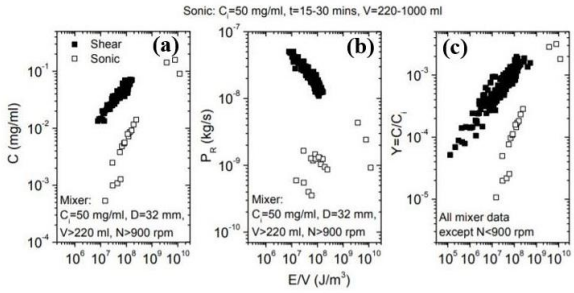


Figure 2. 13. Comparison of a) graphene concentration, b) production rate and c) yield for both shear exfoliated graphene and graphene produced by sonication plotted versus the total inputted energy per volume. (E/V is the total energy input per unit volume)

Research has shown that shear mixing as a technique is an effective and scalable way of dispersing GNP in epoxy (Yasmin and Daniel 2004, King, Klimek et al. 2013, Klimek-McDonald, King et al. 2018). Recently, Edward Pullicino et al.(2017) investigated the effect of shear mixing speed and time on the mechanical properties of GNP/Epoxy Composites. GNPs with dimensions 25 μm and thickness of 6–8 nm are dispersed in epoxy matrix and a correlation among the shear mixing speed and time with the size of agglomerates. It appears that increasing the speed (1000 rpm, 3000 rpm, and 9000 rpm) and time of shear mixing (1 and 2 hrs) has a positive impact on the size of agglomerates. The highest increase of Young's modulus was around ~14% (0.1 wt. % GNPs, 3000 rpm & 2 hrs) with no significant increase in the Young's modulus for higher nanofiller (>5 wt. %). Although, the highest speed used (9000 rpm) decreased significantly the size of agglomeration, no more effect was found on Young's modulus. By FTIR results, it has been showed that there are no defects on the surface of GNPs. Hence, the authors suggested the insignificant improvement on the mechanical properties is relating to the poor interfacial interactions between the GNPs and the epoxy matrix.

### 2.9.4. Summary

In summary, graphene nanofillers can provide great improvement to mechanical properties of epoxy matrices when there is a strong interfacial interaction as well as good dispersion. Comparing the three mechanical dispersion techniques, sonication firstly is more effective for low volumes of graphene dispersion. However, its main drawback is the use of toxic solvents and the lack of scalability, especially for industrial applications. High-shear mixing is a great dispersion technique for industrial scale applications. Comparing with three roll mill that also is widely used in industry, Prolongo et al. (2013) investigated the dispersion level of GNPs (average lateral particle size was 3–7 μm and thickness 20–30 nm) into the epoxy resin and found that TRM is an effective technique for the dispersion/partial exfoliation of graphene nanofiller while high-shear mixing process produces composites with a uniform distribution of non-exfoliated GNPs. Relating to their thermo-mechanical performance, the storage modulus (SM) of the GNPs/epoxy composites mixed by high-shear mixing is found higher (2.41 GPa) than the calendaring process (2.13 GPa), with the SM of pristine resin to be at 2.32 GPa. The difference between the two manufactured composites was explained that the interface with the polymer network is more efficient and stronger with thick initial GNPs than with thinner GNPs (produced by TRM). However, this explanation is insufficient as the results of glass transition temperature ($T_g$) for the TRM-mixed composites were higher than the high-shear mixed-composites using DMTA and DSC analytical method, indicating a higher crosslinking density

and a restricted movement of polymer chains after the exfoliation of GNPs. It is clear that more investigation is needed for understanding the relation between the dispersion level and the mechanical behaviour of graphene/epoxy composites.

## 2.10. Effect of graphene dispersion and functionalization on the rheological properties of graphene/epoxy composites

The properties of filled polymers and nanocomposites are strongly linked to the adequate dispersion of the nanofiller in the pre-polymer during the composite preparation. It is accepted that a fully dispersed and stable state will lead to optimal properties. On the contrary, the presence of particle agglomerates will lead to loss of material performance. Many methods are developed in order to obtain the degree and quality of dispersion within a polymer composite system. Optical methods, such as microscopy and light scattering provides an easy-to-use way for a good image approach, but they do not have sufficient resolution to visualize the dispersion in detail (Wei, Atif et al. 2015, Fan, Yu et al. 2019), providing sometimes a very subjective analysis. For this reason, various quantitative methods based on the analysis of optical microscopy images have been developed (e.g., ImageJ software, MATLAB (Zaccardi, Santonicola et al. 2018), binarization of grayscale images (Yourdkhani and Hubert 2013) in order to perform a more critical point of view. Electron microscopic techniques (SEM or TEM) can be used as supplementary analytical tools. However, it requires long-times on observing locally the sample microstructure with the resulting images to be often representative of a restricted area of the sample. Also, SEM with the combination of energy-dispersive X-ray (EDX) (Mills, Lees et al. 2002) and Raman spectroscopy (Li, Chu et al. 2018) have been used in order to analyse the dispersion degree of the nanofillers by mapping the sample surface, but this is a time-consuming process. For instance, typical acquisition times for Raman maps can be in the order of 1s-10 s per point (or longer), resulting in total measurement times in the order of hours or days (Horiba). Last, Wide angle X-ray diffraction (WAXD) has been used analysing quantitatively the diffraction pattern because the intensity from a particular phase in a mixture of phases depends on the concentration of that phase in the mixture (Kalyon, Dalwadi et al. 2006). Several samples for every graphene reinforced nanocomposite batch are necessary to be analysed in order to represent a good indicator of the dispersion. Also, X-ray diffraction (XRD) has been used for determining the exfoliation of graphene which is a dedicator of its dispersion degree in the nanocomposites (Liang, Huang et al. 2009). Normally, the disappearance of the characteristic diffraction peak for graphene sheets in the graphene/polymer composites can demonstrate that the sheets are fully exfoliated in the matrix (Wan, Gong et al. 2014). It is clear

that a combination of techniques is needed to give a more complete picture of the dispersion degree of the nanofiller into the polymer matrix. Different attempts to analyse the state of dispersion of nanofiller suspensions were reviewed in the Table 1.

Table 1.1. Summary chart of the analysis tools used to study the quality of dispersion and distribution for highly filled systems (Rueda, Auscher et al. 2017).

| **Analysis tool** | | **Remarks** |
|---|---|---|
| Imagining techniques | SEM | Qualitative method<br>Quantitative, if coupled with image-analysis software<br>From micro- to nanoscopic level<br>In BSED mode, faster acquisition than SEM-EDX |
| | TEM | Qualitative method<br>Quantitative, if coupled with image-analysis software<br>From nanoscopic to angstrom level |
| | Tomography | Quantitative method<br>Macroscopic level |
| | Optical microscopy | Qualitative method<br>Quantitative with image-analysis software<br>Microscopic level |
| X-ray diffraction techniques | SEM-EDX | Quantitative method<br>Limited to the acquisition time |
| | WAXD | Quantitative method<br>Not very precise |
| Global analysis | Mixing torque rheology | Qualitative method<br>Complementary but not sufficient |

Rheological or flow-properties have been used as an analytical tool in development and optimization of nanocomposites with a range of matrices and nanofillers. It is a simple and non-expensive tool for control of nanocomposite preparation and can verify the nanocomposite internal structure at an early stage of their preparation (Galindo-Rosales, Moldenaers et al. 2011, Ivanov, Velichkova et al. 2017). In general during a flow experiment, a change in viscosity implies a structural reorganization of particles and polymer chains such as, orientation of components, formation of a filler network, interlocking of particles and so on (Rueda, Auscher et al. 2017). The macroscopic connectivity of the filler network can be produced from

the physical interaction between filler-filler, polymer-filler, polymer-polymer, etc. The long-range connectivity (transport, thermal and electrical properties are related to the long-range connectivity) can be attributed mainly to chemical interactions, such as van de Waals forces, hydrogen bonds and electrostatic interactions are responsible for this long-range connectivity within the composites. Thus, filled materials present significant changes in the rheological behaviour and viscosity beyond a certain value of filler loading. The viscosity is a key parameter that must be optimized to be low enough for the suspension to be processed and high enough to improve the dispersion process. Carrot's research group (2010) and Tadmor and Gogos (2013) concluded that the most influential factor in dispersion is the matrix viscosity; it is a cause effect of the dispersion which becomes high when good dispersion is achieved. The mechanism that occurs when nanoparticles are considered is that breaking up the nanoparticle agglomerates, leads to a sharp increase in the surface area between the nanofiller and matrix, resulting in a higher shear viscosity (Küçük, Gevgilili et al. 2013).

The study of rheological response of carbon-based polymer nanocomposites, such as CNTs/epoxy composites has been studied widely in the past (Kim, Seong et al. 2006) (Rahatekar, Koziol et al. 2006, He, Zhang et al. 2013). However, the rheological properties of graphene polymer composites have focused mainly on thermoplastics (Li, Zhu et al. 2011, Tang, Wan et al. 2013, Vallés, Young et al. 2014). Specifically, Vallès et al. (2014) studied the viscoelastic properties of GO/PMMA and compared with the aqueous dispersion of GO. Using the same filler loading (0.6 vol %), it was found that the relative increase on viscosity of aqueous dispersed GO is higher than those observed in GO/PMMA. This can be attributed to the hydrogen bonding that occurs between the GO and water ($H_2O$). The small increase found in GO/PMMA solution was attributed to possible agglomerations through Van der Waals forces and $\pi$–$\pi$ interactions. The interfacial interactions between the GO and PMMA can be modified by either changing the surface chemistry of GO (Zhang, Zheng et al. 2012) or the nature of polymer matrix (El Achaby, Arrakhiz et al. 2012) and hence the rheological properties can be tuned. They proved that graphene with a higher C/O ratio provided a more homogeneous dispersion in PMMA. They also showed that GO reacts better with polypropylene (PP) and a larger relative in viscosity of GO/PP solution was observed for the same filler loading used in their GO/PMMA composite.

Limited reports refer to the effect of rheological behaviour on graphene dispersions in epoxy matrices (Clausi, Santonicola et al. 2016, Nobile, Raimondo et al. 2016). In these two reports, the shear thinning properties were studied relating to the exfoliation degree of graphite (using

acid intercalation and heat treatment) and the geometrical characteristics of the nanofillers (different planar sizes of graphite nanoplatelets). A shear thinning behaviour occurred when higher is the exfoliation degree of graphite as well as the planar size. A high increase in steady-shear viscosity for GO/epoxy systems was also reported more recently that indicates an increase in the degree of exfoliation (Surnova, Balkaev et al. 2019).

Yi Wei et al. (2018) studied the influence of oxidation level on the rheological performances of epoxy/GO composites. Five different types of GO were used (GO-1 to GO-5) with increasing oxidation levels. When GO-types are dispersed on the curing agent (Figure 2.14 (a)-(e)), GO-1 shows a poor dispersion due to its low content of functional groups and high proportion of graphitic carbon. As the oxidation level increases, the dispersibility of GO exhibits an apparent improvement, up to the level of GO-4. Then, GO-5 tends again to aggregate which was attributed to possible agglomerations through hydrogen bonding and dipolar interactions between the GO-5 sheets. Similar results are obtained for the cured samples. Relating to the rheological study, it is expected the better dispersion to provide a higher viscosity value. Indeed, at 25 ºC when GO-2, GO-3, GO-4 and GO-5 are added, the viscosity values of epoxy/GO blends increase from 0.46 (neat epoxy) to 0.72, 0.81, 0.92 and 0.66 Pa.s, respectively (Figure 2.14.) These results are strongly correlated with the dispersion state.

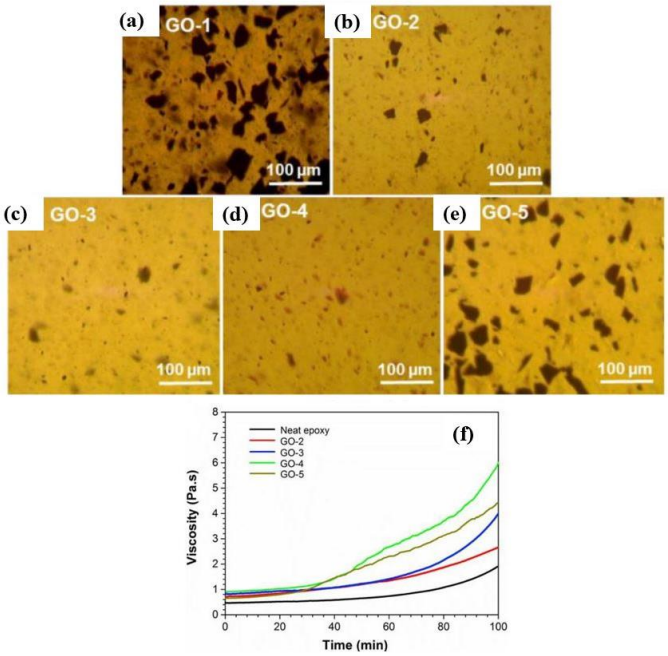


Figure 2. 14. Optical micrographs of five GO/curing blends (a–e). viscosity versus time (b) curves of the neat epoxy resin and epoxy/GO composites. The filler loading is 0.2 wt.%.

## 2.11. Effect of graphene functionalization on the epoxy cross-linking density and its influence into the final mechanical properties of graphene/epoxy composites

It is known that the mechanical properties of the epoxy composites depends on the formation of the cross-linked network in the system and the structure of the interphase region between the continuous phase (resin) and the discontinuous phase (reinforcement) (Galpaya, Fernando et al. 2015). Understanding the influence of nanofillers on the curing reaction of epoxy systems is important, because any negative changes to the curing could lead to a detrimental effect on composite mechanical properties.

Putz et al (2008) investigated the effect on curing kinetics of the inclusion of MWCNTs in an epoxy resin systems (Diglycidyl ether of bisphenol A-DGEBA) with varying cross-link density (different ratio of mono-amine and di-amine used) *via* Differential Scanning Calorimetry (DSC). They found that the inclusion of the nanoparticles interrupts the cross-linking network, resulting in reduced values of glass transition temperature ($T_g$), whereas an increase of $T_g$ was observed at low cross-link density composites, as shown in Figure 2.15. They found that two opposing effects may be occurring: (1) the cross-link network disruption at the nanotube-polymer interface in highly cross-linked systems, resulting in reduced values of $T_g$ and (2) the formation of an interphase in low cross-linked systems, in which chain dynamics were retarded leading to increased values of $T_g$. Such interphase regions can also affect the efficiency of stress transfer from the matrix into the reinforcing filler. However, they did not present any results for mechanical reinforcement.

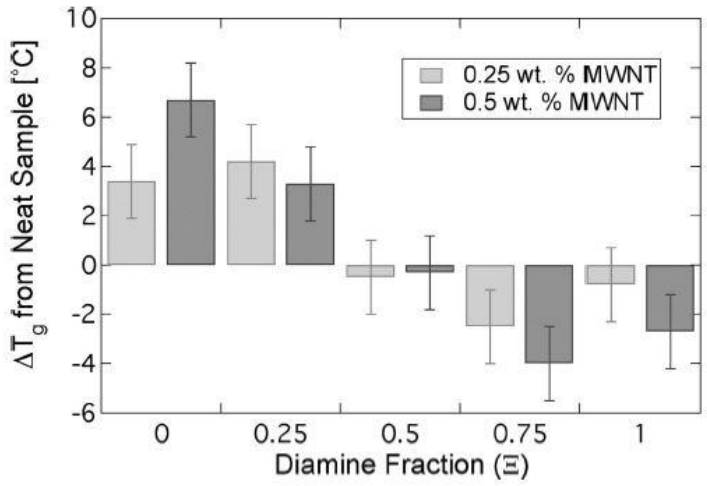


Figure 2. 15. Difference between $T_g$ of the nanocomposites and neat epoxy as a function of diamine fraction (Ξ). Ξ was varied from linear chains (Ξ=0) to a fully cross-linked network cured (Ξ=1) with intermediate steps of 0.25, 0.5 and 0.75 diamine fraction (Putz, Palmeri et al. 2008).

Several studies have focused on the effect of graphene-based materials concentration on the curing behaviour of the epoxy resin systems. It is well established that when the filler loading is too high in nanocomposites, the possibility of agglomeration as well as restacking increases dramatically, resulting in a less efficient mechanical reinforcement (Kernin, Wan et al. 2019). To add this, it has been reported in the past (Li, Young et al. 2013, Vallés, Beckert et al. 2016) that after a certain filler loading, the Young's modulus of the final nanocomposites remains stable. It has been suggested that the formation of possible agglomerations leads to this plateau trend, but the mechanism behind these data has not been explored as it is out of the papers' purpose. Bao et al (2011) reported a ''cross-linking density reduction'' effect by increasing the concentration at 5 wt. % of few layer GO (FGO, planar size: 0.2-1 μm and thickness: 1.5 nm) that led to lower mechanical properties compared with the pure epoxy resin (E-44, Chinese supplier). Despite the fact that FGO enhances the $T_g$ of epoxy nanocomposites at low filler contents, the authors suggested by introducing more FGO sheets, this disrupts the stoichiometry of the matrix at this high filler loading through the interfacial interaction with the epoxy matrix, without allowing the epoxy molecule chains to react with the hardener agent. Similar results were observed for highly-exfoliated GO (planar size:5-20 μm and thickness: up to 3 layers) and epoxy composites (NPEL-128, bisphenol-A based resin) (Surnova, Balkaev et al. 2019) but at much lower filler loadings (0.6 wt. %) due to the higher surface area of GO. Huang et al. (2016) reported lower Tg values of multilayer graphene (MLG, planar size: 5 μm and thickness: 10 nm)/epoxy composites (bisphenol-A-based epoxy), suggesting two possible mechanisms: a catalytic effect of MLG oxygen groups which leads to insufficient ratio between the hardener and the epoxy (Vryonis, Virtanen et al. 2019) or due to the weak adhesion between the filler and the matrix that cannot effectively restrict the segmental motion of the polymer chains. Chong et al. (2016) reported a decrease of 6 $^{o}$C and 2 $^{o}$C in $T_g$ of plasma-treated GNPs-COOH (by Haydale Ltd) and GNPs-$O_2$/epoxy (DGEBA) composites, respectively, with no significant mechanical improvement (fracture toughness and Young's modulus). The poor mechanical reinforcement was attributed mainly to the small planar size of the platelets (0.3 μm). By using some SEM images, the authors showed a good dispersion of these functionalized nanofillers into the epoxy matrix and the lower values of $T_g$ were attributed to the possible interactions of the carboxyl and carbonyl functional groups with the epoxy resin.

More recently, the catalytic activity of GO and reduced GO (rGO)(Galpaya, Fernando et al. 2015, Acocella, Corcione et al. 2016, Monteserín, Blanco et al. 2017) has been reported on the curing kinetics of epoxy amine composites. By using GO, the accelerating effect on the curing

is higher comparing with the rGO (lower oxygen content), which reduces the formation of the 3D network structure in epoxy matrix, especially near the interphase region between epoxy and GO, leading to the increase of more linear polymer chains and hence to a lower $T_g$. However, none of these studies have presented the effect of catalytic activity on the mechanical properties.

Clearly the addition of nanofillers to cross-linked epoxy resins has an influence on the curing of the base polymer. What is not clear is the impact that has on the mechanical properties of the resulting nanocomposites. If the matrix properties are reduced compared with an unfilled material, then the reinforcing effect of the nano-fillers could be somewhat masked. Such effects are not yet fully understood and for this reason, more investigation is needed.

## 2.12. Micromechanics of reinforcement

The mechanics of the reinforcement of polymers by graphene has been reviewed (Young, Kinloch et al. 2012). The 'rule of Mixtures' is a classical analytical approach that has been developed to describe the stiffness of a continuous high modulus-filler in a low modulus polymer composite, where its uniform strain/stress cases are widely accepted as the upper/lower bounds (Young and Lovell 2011). To determine the Young's Modulus of a particulate composite ($E_c$) it is necessary the particles and the matrix are subjected to either uniform strain or stress. Under uniform strain, the Young's modulus $E_c$ of the composites is given as:

$$E_c = E_f V_f + E_m(1 - V_f) \qquad (2.2)$$

Where $E_f$, $E_m$ are the modulus of the filler and the modulus of the matrix and $V_f$ and $V_m$ are the volume fractions of the filler and the matrix, respectively. Despite its simplicity, this equation has been found to predict well the modulus of the composites, especially at low loadings (the possible agglomerations of the filler at high loadings are not considered on this linear equation) but should be always taken as an approximation than single values, since it does not account important factors such as Poisson's ratio. Moreover, this equation was referred only to specific parameters, such as, perfect interfacial bonding with continuous long fibres. Indeed, it does not take account more significant parameters in the case of nanocomposites, such as the discontinuous phases between the filler and the matrix which is related strongly with the possible formation of an interphase along with the orientation or the distribution in the matrix, the structural and geometrical characteristics of the filler (critical length or aspect ratio) and

the filler orientation along the uniaxial load, which are play a major role that need to be reflected in this model. These key parameters are explained in detail in the next section (2.12.1).

A review by Papageorgiou et al. (2017), suggested that in terms of the enhancement in mechanical properties with the addition of graphene, the polymer matrices with the lower modulus (such as elastomers) show higher percentage increases in stiffness and strength than stiffer matrices (thermoplastics-thermosets). Interestingly, the above relationship (2.1) has been applied in a large number of publications of polymers reinforced with GNP-, GO- and rGO-based materials and the results clearly revealed the differences in the stress transfer mechanisms among polymer matrices with different degrees of stiffness. From the $E_f$ versus $E_m$ log-log plot for different graphene-derivatives (Figure 2.16), although there is considerable scatter in the data, it was concluded that the filler modulus (not the actual modulus of the material) is not independent of the matrix, but there is a linear relation between the filler modulus scales with the matrix modulus. It can be seen that stiffer the matrix ($E_m$), the higher the effective modulus of the filler ($E_f$), a fact that also depends on additional parameters such as the orientation, the interphase, the functionalization and others. This indicates that although impressive levels of reinforcement can be obtained through the use of graphene nanomaterials in soft matrices, stress transfer from the matrix to the filler that takes place through the interface is relatively inefficient. This means that the full potential of reinforcement by these nanofillers is difficult to achieve in such soft systems.

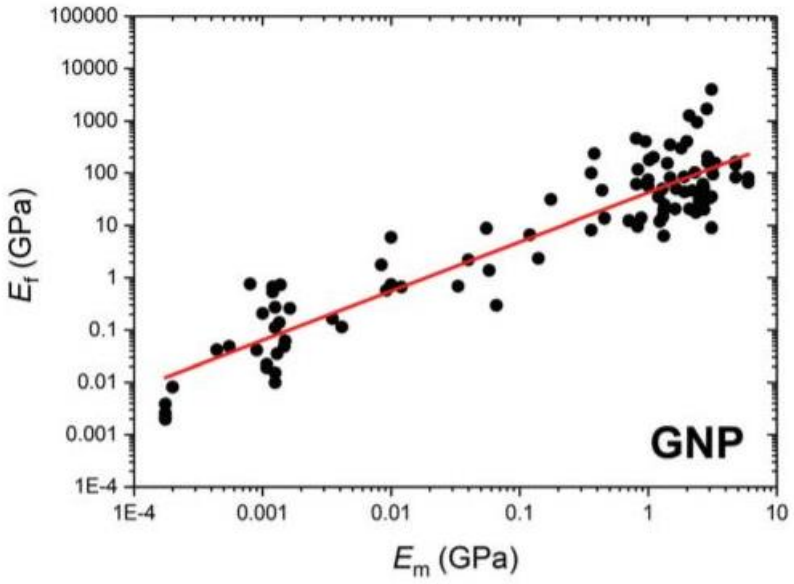


Figure 2. 16. Filler modulus ($E_f$, determined from the rules of mixtures) versus matrix modulus ($E_m$) for a number of different literature reports where polymers of varying degrees of stiffness were reinforced by graphene nanoplatelets (Papageorgiou, Kinloch et al. 2017).

### 2.12.1. Interface (Shear-lag analysis)

The filler-matrix interface plays a significant role in deciding the properties of composites as a strong interface is the premise for the filler to bear load (Hull 1981). As the interfacial adhesion is related closely to the size of filler, when the filler has a finite size, the stress transfer through interfacial adhesion is reduced. G. A. Cooper and A. Kelly (1969) discussed how stress can be transferred from matrix to fibers when a discontinuous length occurs, where the interfacial shear strength of the interface affects primarily the load transfer length of the fiber-matrix system and how the properties of this interface will affect the properties of the composite. Young et al. (2012) investigated the load transfer on a polymer system reinforced by graphene sheets aligned in the direction of stress. Figure 2.17 represents the deformation patterns of a nanocomposite with an aligned filler incorporated. Before deformation (Figure 2.17 (a)), parallel lines perpendicular to the nanoplatelet can be drawn from the matrix through the nanoplatelet. When the system is subjected to axial stress, $\sigma_l$, parallel to the plane of the nanocomposites, the lines become distorted as shown in Figure 2.17 (b), since the Young's modulus of the matrix is much less than that of the nanoplatelet. This induces a shear stress at the nanoplatelet/matrix interface. It can be seen that under axial deformation, the filler deforms the most in the central part while deforms the least at the edges, as shown in Figure 2.17 (c). If the nanoplatelet is long enough, then there is a uniform strain assumption, as the strain in the middle of the nanoplatelet is equal of that matrix. Since the nanoplatelets have a much higher Young's modulus than the matrix carries most of the load in the composite (Young, Liu et al. 2018).

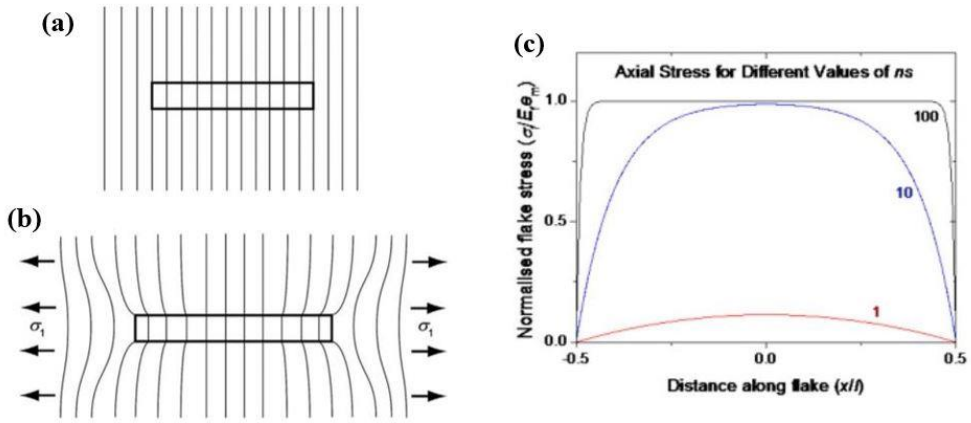


Figure 2. 17. Deformation patterns for a discontinuous aligned nanoplatelet in a polymer matrix without deformation (a) and under stress (b) (Hull 1981). (c) Predicted variation of normalized axial stress with distance along the nanoplatelet for a short aligned nanoplatelet in a matrix. (The term ns is

regarded as a measure of the stress transfer efficiency, depending on the filler morphology and interfacial adhesion.) (Gong, Kinloch et al. 2010, Young, Kinloch et al. 2012)

The stress is transferred from matrix to the filler primarily through interfacial shear stress, and the stress in the filler $\sigma_{filler}$ is given by (Gibson 2016):

$$\sigma_{filler} = \frac{4}{d}\int_0^x \tau \, dx \qquad (2.3)$$

where τ is the interfacial shear stress, d is the thickness for flake filler or diameter for fibre filler, and x is the distance along the filler from one end.

This stress distribution can be modelled using the well-established shear lag theory (Cox model) (Hull 1981, Nairn 1997, Gong, Kinloch et al. 2010) in which it is assumed that the nanoplatelet of length l and thickness t is surrounded by a layer of resin with an overall thickness of T. Both the nanoplatelet and matrix deform elastically with a linear relation (Figure 2.18 (a)).

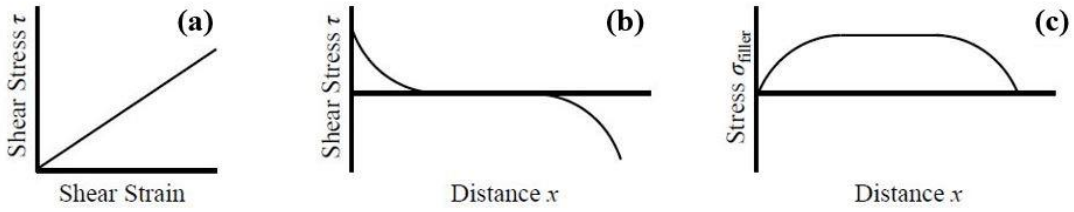


Figure 2. 18. The Cox model: (a) Stress-strain curve of the elastic matrix material. (b) Shear stress and (c) axial stress distribution along the filler.

By using the shear-lag theory, the final equation for the distribution of nanoplatelet stress as a function of distance, x along the nanoplatelet at a given level of matrix strain, $e_m$, was determined (Gong, Kinloch et al. 2010) for 2D fillers, such as graphene, following a non-linear increase of filler at both ends of filler with the interface between the polymer and filler remains intact at a specific stress value (Figure 2.18 (c)):

$$\sigma_f = E_{eff} e_m \left[1 - \frac{cosh\left(\frac{nx}{t}\right)}{cosh\left(\frac{nl}{2t}\right)}\right] \qquad (2.4)$$

where n is the shear-lag fitting parameter and it can be taken as an indication of the stress transfer efficiency between the flake and matrix and depends on the interactions and the morphology of the flake:

$$n = \sqrt{\frac{2G_m}{E_{eff}}\frac{(t)}{(T)}} \qquad (2.5)$$

where:

$E_{eff}$ is the effective Young's modulus of the nanoplatelet and $G_m$ is the shear modulus of the matrix. The effective Young's modulus of few-layer graphene in a nanocomposite can be related to the number of layers $n_l$ though a relationship of the form:

$$E_{eff} = \frac{E_g}{\frac{n_1}{2} - k_i\left(\frac{n_1}{2} - 1\right)}, \qquad (2.6)$$

where Eg is the Young's modulus of monolayer graphene (1050 GPa) and $k_i$ is the efficiency of stress transfer between the layers (~0.6) (Ahmad, Xue et al. 2017).

The shear stress $\tau_i$ along the filler can be derived by differentiating equation 2.3 to give:

$$\tau_i = nE_{eff}e_m\frac{sinh\left(\frac{nx}{t}\right)}{cosh\left(\frac{nl}{2t}\right)} \qquad (2.7)$$

It is obvious that a high interfacial shear stress at the edges of filler occurs, as shown in Figure 2.18 (b). It is convenient to use the concept of the nanoplatelet aspect ratio, s=l/t, so the equation (2.4) can be rewritten:

$$\sigma_f = E_{eff}e_m\left[1 - \frac{cosh\left(ns\frac{x}{l}\right)}{cosh\left(\frac{ns}{2}\right)}\right] \qquad (2.8)$$

By Figure 2.18 (c), it can be seen that the nanoplatelet is most highly stress, so the most efficient reinforcement is obtained, when the product ns is high; therefore, high aspect ratio is always desirable for the reinforcement of the composite. Moreover, chemical modification of the surface may significantly increase the interfacial interactions between the graphene and the polymer, reducing the critical length and increasing the n.

### 2.12.2. Geometrical characterizations (length and thickness)

The evaluation of the ability of a graphene flake to be able to enhance the properties of a matrix can be affected also by the critical length (lateral size of the reinforcement) and the number of the graphene layers. For fibre-reinforced composites, the quality of reinforcement is often described in terms of the 'critical length', lc. This parameter is defined as 2× the distance over which the strain rises from the fibre ends to the plateau level and is smaller for stronger interfaces. Following the shear-lag theory (equation 2.3), Gong (2010) showed that the strain

rises to about 90% of the plateau value over about 1.5 μm from the edge of the flake making the critical length to be of the order of 3 μm for the graphene reinforcement (Figure 2.19 (a)). According to the general assumption that the efficient reinforcement needs flakes or fibres with length to be ~10*Ic, flakes of 25-30 μm are needed for efficient reinforcement in composites. Anagnostopoulos et al. (2015) studied the distribution of stress along a supported monolayer graphene flake in detail by Raman line mapping near the edges of the flake. The authors found out that the preparation method and doping of the flakes PMMA (Poly (methyl methacrylate) substate and a thin layer of an epoxy based photoresist SU-8) can affect the stress transfer mechanism at a distance of 2 μm away from the edges. The transfer length for stress transfer from each side of graphene flake edge consists of a region affected by doping effects for which the stress transfer is poor and another region that is dominated by elastic, shear-lag type, effects. Efficient load transfer can take place at around 4 μm from the edge of the flake (Figure 2.19 (b)). In this experiment, the transfer length for stress transfer is calculated as the sum of the affected area due to the residual stress plus the length required for elastic stress transfer; therefore, they suggested flakes with a critical size length greater than 10 μm is required. This is a very important conclusion for practical applications and may be valued not only for graphene/PMMA composites but also for other polymer matrices for which inclusions of sizes greater than 10 μm are required for efficient reinforcement.

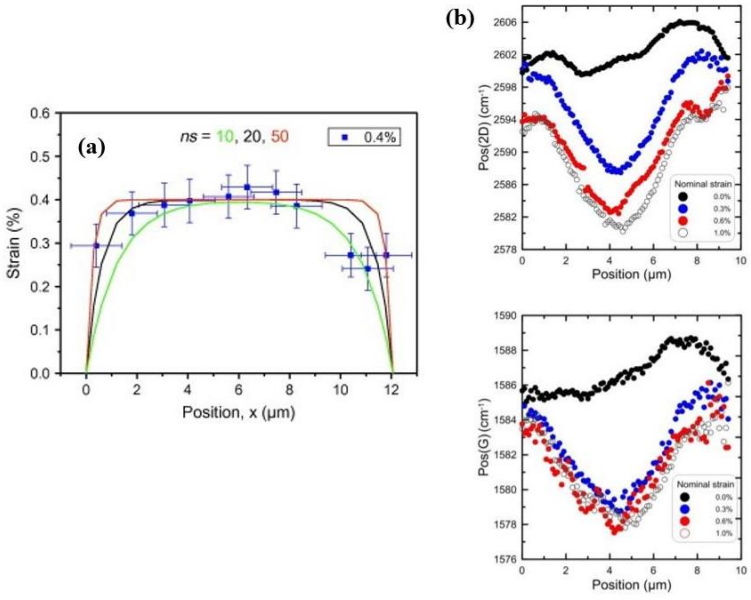


Figure 2. 19. Distribution of strain in the graphene in the direction of the tensile axis across a single monolayer at 0.4% strain (a). Raman position of 2D peak and G peak distributions along the mapping line at various levels of strain (b).

Apart from the lateral size, the number of the layers can affect the reinforcement of the polymer composite. It is well known the relatively weak van der Waals bonding between the individual graphene layers of graphite allows sliding between the layers to take place relatively, explaining the low-friction properties of graphite. Many reports have studied the efficiency of the stress transfer between the graphene layers, so the reinforcement level in composites. Large stress-induced shifts of the G and 2D Raman bands are found when graphene is subjected to deformation and these could be related to the Young's modulus of the material (Yu, Ni et al. 2008, Proctor, Gregoryanz et al. 2009, Frank, Tsoukleri et al. 2011). It has been found that the interfacial stress transfer when graphite flake submitted to PMMA substrate gives poor interfacial stress comparing with the monolayer graphene (Tsoukleri, Parthenios et al. 2009). This was to be expected since the weak van der Waals forces keep the graphite crystal attached to the PMMA substrate may not be sufficient to allow efficient stress transfer through the thickness of the graphitic block. Similarly, Proctor et al.(2009) found that monolayer graphene on a silicon substrate exhibited a higher rate of band shift when compared with few-layer graphene (no materials details included by the authors). The possible explanation was attributed either to the poor adhesion with the substrate or the easy shear between the graphene layers, as mentioned above.

Gong et al. (2012) studied the stress transfer of the monolayer, bilayer, trilayer and many-layer graphene upon the surface of a PMMA beam. They assessed stress transfer for both uncovered flakes and those coated with an epoxy polymer. The efficiency of the reinforcement on polymer composites using the rules of mixtures was compared in order to determine the optimum number of graphene layers for the best reinforcement. Strain-induced Raman band shifts have also been evaluated for separate flakes of graphene with different numbers of layers, and it is found that the band shift rate tends to decrease with an increase in the number of layers, indicating poor stress transfer between the inner graphene layers, as shown in Figure 2.20 (a). However, they suggested more advantage to the use of bilayer or trilayer graphene for mechanical reinforcement, instead of monolayer graphene. Considering the cost and time production of monolayer graphene, it is more advantageous to enhance the stiffness of the composite with higher filler loadings. In high volume fraction nanocomposites, the packaging density of graphene is greater on the polymer chains with a trilayer graphene, as shown in Figure 2.20 (b). The minimum separation of the graphene flakes will depend upon the type of polymer and its interaction with the graphene. This minimum separation is unlikely to be less than 1 nm and probably more like several nm (multilayer) but the separation of the layers in

multilayer graphene is only of the order of 0.34 nm (monolayer). By the rules of mixtures, it was found that the Young modulus of the composite ($E_c$) is higher for the trilayer-graphene based composite (1 nm) than the monolayer-graphene based composite (0.34 nm). Then, the modulus decreases while the number of graphene layer in the flakes and polymer thickness increase. Hence, although the monolayer graphene gives the highest stress transfer, it will not necessarily give the best reinforcement. The optimum graphene layers for the best reinforcement will depend upon the polymer layer thickness and the efficiency of stress transfer between the graphene layers.

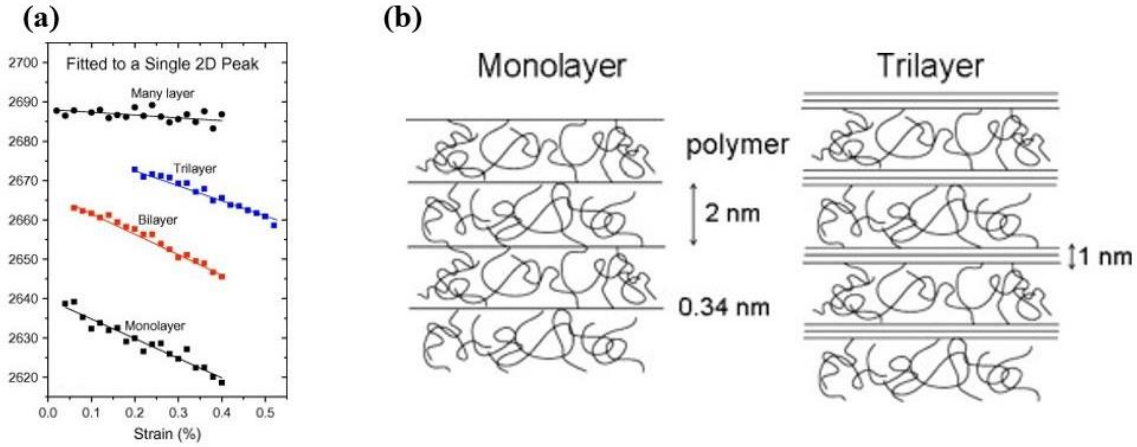


Figure 2. 20. Shifts with strain of the 2D band for adjacent monolayer, bilayer and trilayer regions along with the shift with strain for the 2D band of a multilayer flake on the same specimen (a), Schematic diagram of the microstructure of graphene-based nanocomposites based upon either monolayer or trilayer reinforcements (b).

### 2.12.3. Orientation

The orientation of the filler plays a significant role in the composite reinforcement and the rules of mixtures has been modified for the calculation of Young's modulus of a composite as:

$$E_c = E_{eff} V_f \eta_o \eta_1 + E_m(1 - V_f) \qquad (2.9)$$

Where $E_{eff}$ is the effective modulus of the filler, $\eta_o$ is the Krenchel orientation which depends on the average orientation of the filler with respect to the applied stress, while $\eta_1$ is the length distribution factor and takes values of 0 and 1, depending on both the length of the filler and the interface between the filler and the matrix. The length distribution factor is based on the shear-lag theory (2.12.1) and can be calculated by using the Cox equation:

$$\eta_1 = 1 - \frac{tanh\left(\frac{ns}{2}\right)}{\frac{ns}{2}} \qquad (2.10)$$

Where s is the aspect ratio of the filler and $n = \sqrt{\frac{2G_m}{E_{eff}}\frac{(t)}{(T)}}$. The main assumption behind the use of the length factor is that the matrix and the filler remain elastic during deformation, the interfacial bonding is perfect, while based on the shear-lag theory the shear stress at the ends of the fibre is maximum and falls to zero after half the critical length. For a continuous fibre, the length distribution is equal to 1.

The Krenchel orientation factor was calculated firstly for randomly oriented and oriented in-plane fibres and it was found 3/8 and 1, respectively (Krenchel 1964). Li et al. (2015) applied the method to a number of GO reinforced systems and obtained the Krenchel orientation factor ($\eta_o$) by measuring the spatial orientation factor using Polarized Raman Spectroscopy, and then substituted in the modified rule of mixtures. The local orientation of graphene is defined by its surface normal and can be seen in Figure 2.21 (a) as the z direction in the x, y plane. The Krenchel factor for composites reinforced with theoretically perfectly oriented graphene sheets was found to be $\eta_o$=1 and for randomly oriented graphene sheets to be $\eta_o$= 8/15 (Figure 2.21 (b)). A schematic is provided (Figure 2.21 (c)) with all the Krenchel factors for all the cases of randomly oriented and aligned.

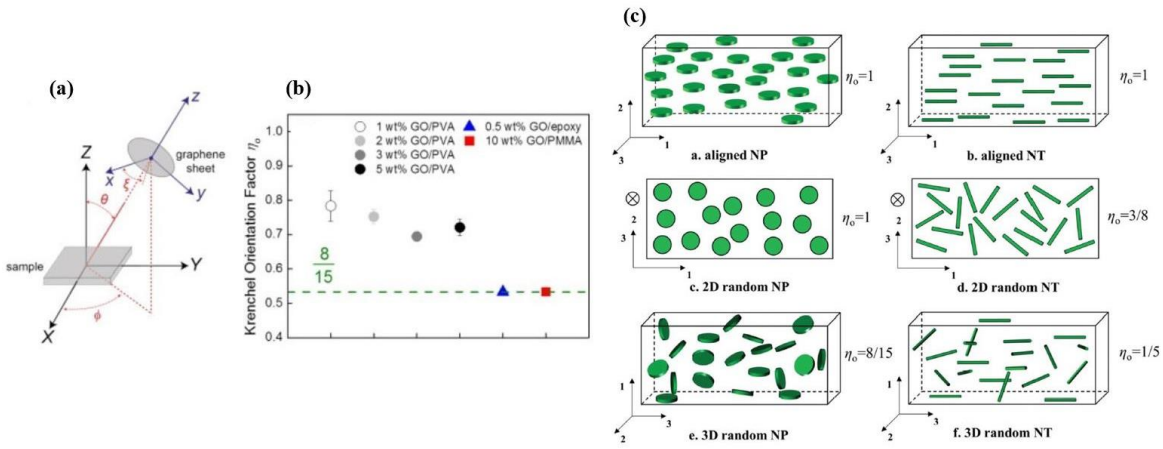


Figure 2. 21. The relationship between the local coordinate system of a graphene flake (x, y, z) and the nanocomposite sample (X, Y, Z), as defined by three Euler angles (a) (Li, Young et al. 2015). Krenchel factors for materials with oriented and disoriented GO nanoplatelets. The dashed line represents the Krenchel orientation factor of 8/15 for the materials with random alignment of their flakes (b) (Li, Young et al. 2016). Schematics of nanoplatelet (NP) and nanotube (NT) nanocomposites with different orientation of the nanofillers: (a and b) aligned, (a, c and d) randomly oriented, in-plane and (e and f ) 3D randomly oriented (Liu and Brinson 2008).

By using the modified rules of mixtures (2.9), random orientation of fillers such as graphene should reduce the Young's modulus of the nanocomposites by just less than a factor of 2 compared with the fully-aligned material. Compared to the reduction in the modulus of a factor of 5 going from aligned to 3D randomly-oriented fibres and nanotubes it means that the reinforcing efficiency of nanoplatelets, is much higher than fibre.

Apart from the Krenchel or Herman's model that used in the work of Polarized Raman (Li, Young et al. 2015), there are also some semi-empirical models, such as Halpin and Tsai (Affdl and Kardos 1976) or Mori-Tanaka (Tandon and Weng 1984) that have been successfully used in a variety of composite systems, taking account the orientation of the 2D fillers as well as the aspect ratio, the geometry and the Poisson ratio for the evaluation of the modulus of the composite materials. In this thesis, the model of Halpin and Tsai has been used. Halpin-Tsai equations can take into account the orientation of the filler in either the longitudinal (L) or the transverse (T) direction and in this project, it was employed to theoretically predict the Young's modulus of the graphene-epoxy systems. The Young's modulus of composites with randomly dispersed ($E_r$) are defined as the following modified Halpin-Tsai equations(Yousefi, Gudarzi et al. 2013):

$$E_r = E_{matrix}\left(\frac{3}{8}\frac{1+\eta_L\xi V_f}{1-\eta_L V_f} + \frac{5}{8}\frac{1+2\eta_T V_f}{1-\eta_T V_f}\right) \qquad (2.11)$$

where,

$$\eta_L = \frac{\frac{E_f}{E_{matrix}}-1}{\frac{E_f}{E_{matrix}}+\xi} \qquad (2.12)$$

$$\eta_T = \frac{\frac{E_f}{E_{matrix}}-1}{\frac{E_f}{E_{matrix}}+2} \qquad (2.13)$$

$\xi = \frac{2}{3s}$ (Yang, Rigdon et al. 2013) (2.14)

$E_f$ and $E_{matrix}$ is the Young's modulus of the nanofillers and the matrix, respectively. The $\xi$ is a shape parameter that takes into consideration the geometry of the nanofiller along with packaging arrangement; therefore, it is related to the aspect ratio s (Papageorgiou, Kinloch et al. 2017). In the case of nanoplatelets, $\xi$ can be found by the equation (2.14), while for the case of fibres $\xi$=2s. Halpin-Tsai has been used successfully in the literature (Huang, Lu et al. 2012, Yousefi, Gudarzi et al. 2013) in order to compare the Young's modulus between the

experimental data and the analytical model and identify directly the possible alignment of the nanofillers into the polymer matrix.

## 2.13. Alignment of graphene into the polymer matrices

As discussed above, aligning graphene in a polymer matrix, can achieve greater improvements in mechanical properties compared with composites with randomly distributed graphene. Many efforts have been made in order to control the 3D orientation of the reinforcing graphene nano-platelets and facilitate the properties of composites that close the gap to the expected theoretical values. The main methods that have been used for this purpose are:

- Self-alignment
- External Electric fields
- External Magnetic fields

### 2.13.1. Self-alignment

Graphene as a 2D nanomaterial has a good potential for self-assembly into ordered structures. Self-assembly into lyotropic nematic liquid crystalline (LC) phases has been reported for GO aqueous dispersions (Aboutalebi, Gudarzi et al. 2011). GO is known for its hydrophilic structure and can be dispersed homogeneously in water and water-soluble polymers, such as poly(vinyl alcohol) (PVA)(Gong, Kinloch et al. 2010), polyurethane (PU) (Yousefi, Gudarzi et al. 2013) or waterborne epoxy polymers (Yousefi, Lin et al. 2013). Self-assembly originates from the ultra-high specific area and moderate viscosity of the mixtures. Steric hindrance forms in low viscosity liquid mixture polymer/graphene and when the graphene sheets overlap, the effect induces a transition from isotropy to a long-range-order liquid crystal structure. This phenomenon can be extended to graphene/polymer systems diluted in proper solvents. Upon evaporation of the solvent and consolidation into a solid material, the graphene colloids can be translated into layered nanostructures (Yousefi, Lin et al. 2013). The main parameter of this method which can control the structure of aligned graphene is the critical concentration of the filler, due to their linear relation (2.14) (Aboutalebi, Gudarzi et al. 2011):

$$\rho D^3 = \frac{CD^2}{\frac{\pi}{4}td} \qquad (2.15)$$

where D, C, d, and t represent graphene parameters: diameter, concentration (in $g/m^3$), mass density (in $g/cm^{-3}$) and thickness, respectively. Other parameters that affect the steric hindrance behaviour and therefore the formation of liquid crystals include: the shape of the graphene, the presence of oxygen groups on the graphene surface and the viscosity of the solvents.

One example of self-aligned monolayer graphene sheets with a range of few to few hundreds $m^2$ using the liquid crystal method is presented in Figure 2.22, illustrating the fracture surface of 0.5 wt. % random dispersed rGO/epoxy composites (Figure 2.22 (a)) and 2 wt. % aligned rGO/epoxy composites (Figure 2.22 (b)). This proves strongly that the critical concentration in order to achieve a highly layered structure graphene-composite is 2 wt. %, where the steric hindrance between the nanosheets is occurred with the excluded volume to prevail. Similar results were taken by GO/epoxy composites.

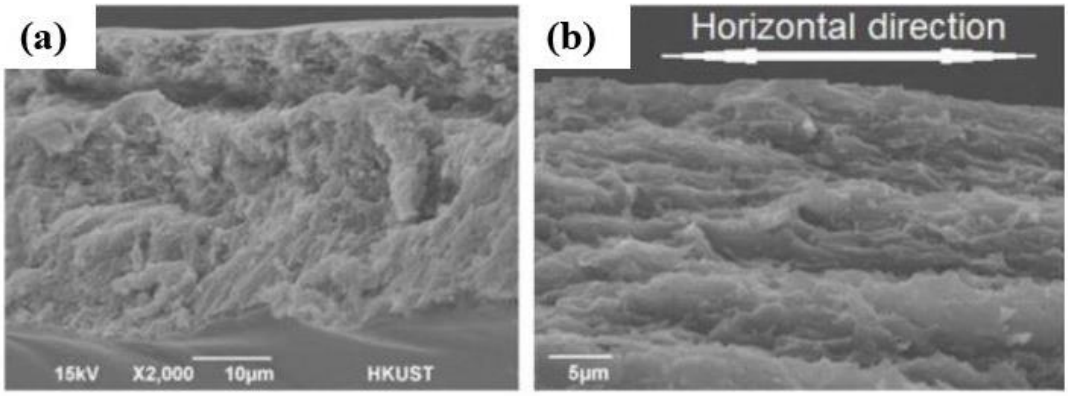


Figure 2. 22. SEM images of 0.5 wt. % rGO/EP (a) and 2 wt. % rGO/EP composites (b) (Yousefi, Lin et al. 2013).

Relating to the above work by Yousefi et al (2013), the introduction of rGO and GO to the waterborne epoxy system increased significantly its Young's modulus and strength. Remarkable results were achieved with rGO which creates strong covalent bonds with epoxy structure, leading to a high load transfer. For the GO/epoxy system, the proposed possible mechanism is the π-π stacking (non-covalent) between the epoxy molecules and GO, resulting to lower mechanical properties comparing with rGO-composites. Despite the simplicity of this method, various limitations still exist. Several parameters, especially the filler concentration, are limited to a narrow range, due to the requirements of critical concentration and viscosity of polymer liquid or the difficulties in getting a fully homogeneous dispersion. Also, it can only be applied to polymers that are easily dispersed in water or solvents, which is not achievable in many polymer matrices.

Similar with the previous system, GO/PVA composites can provide highly aligned structures due to the hydrogen bonding between the –OH functional groups of PVA and oxygen groups of GO or rGO (Bao, Guo et al. 2011). A high degree of orientation was identified with Polarized

Raman Spectroscopy (Li, Young et al. 2015) and provide fundamental studies for mechanical reinforcement of graphene in polymer composites (Li, Young et al. 2016). However, the preparation is quite long, requiring a one-week process under ambient conditions to allow the GO platelets to become aligned by gravity within the film. Also, Bao et al. (2011) showed that rGO /PVA provide better stiffness during DMA analysis, compared with GO/PVA. Although, the total hydrogen bond amount in PVA/GO should be larger than PVA/rGO because of its high amount of oxygen groups, the crystallinity of PVA is increased with rGO due to the molecule movement restriction effect. GO provides better dispersion due to the high hydrogen bonding but it is mechanically poorer comparing with rGO, as a result to give poorer crystallinity to the PVA structure. This shows that although the GO can disperse better in PVA with higher load transfer, this is not enough for the mechanical reinforcement of PVA. It is clear that there is again some parameters that restricts the use of this method for the preparation of aligned graphene structures, such as the amount of oxygen groups attached on the GO, the critical concentration that are need in order to allow the graphene to develop a stack morphology due to the van der Waals forces (Zhao, Zhang et al. 2010).

### 2.13.2. External Electric fields

The application of electric field has been used in order to control the orientation carbon-based materials, such as carbon fibres (Martin, Sandler et al. 2005) or graphene nanofillers and improve structural and functional properties of polymeric composites. Due to the high electron mobility and the large specific area, graphene sheets can orient under the application of an electric field. Both direct current (DC) or alternating-current (AC) can achieve the graphene alignment in liquid; however, graphene is inclined to electrophoretic motion in DC electric field resulting in their aggregation near electrodes (Wang, Wang et al. 2019). Kim et al. developed epoxy nanocomposites with graphite aligned in an AC field and found that these materials had anisotropic tensile modulus and strength (KIM, MOELLER et al. 2004). Recently, Wu et al. (2015) studied theoretically and experimentally the response of GNPs in an epoxy matrix to an AC field (25 V/mm, 10 kHz) . They investigated the effect of orientation on the electrical, thermal and fracture toughness properties of the epoxy composites. The final composites exhibited 7–8 orders of magnitude improvement in the electrical conductivity in comparison with the pure epoxy resin and achieve an increase in the mode I fracture toughness of nearly 900%. The application of an AC electric field led to the GNPs being transversely aligned to the crack growth direction and the flakes exhibited increased interactions with the crack tip. A number of intrinsic and extrinsic mechanisms were identified as being responsible

for this increase; however, the contribution from each individual mechanism is difficult to determine. Figure 2.23. illustrates optical microscope images of random dispersed and aligned chains of GNPs (Figure 2.23. (a), (b), (c), (d)) and also the proposed mechanism ‘end to end’ that made GNPs to connect each other and form clusters under the AC field (Figure 2.24 (e)).

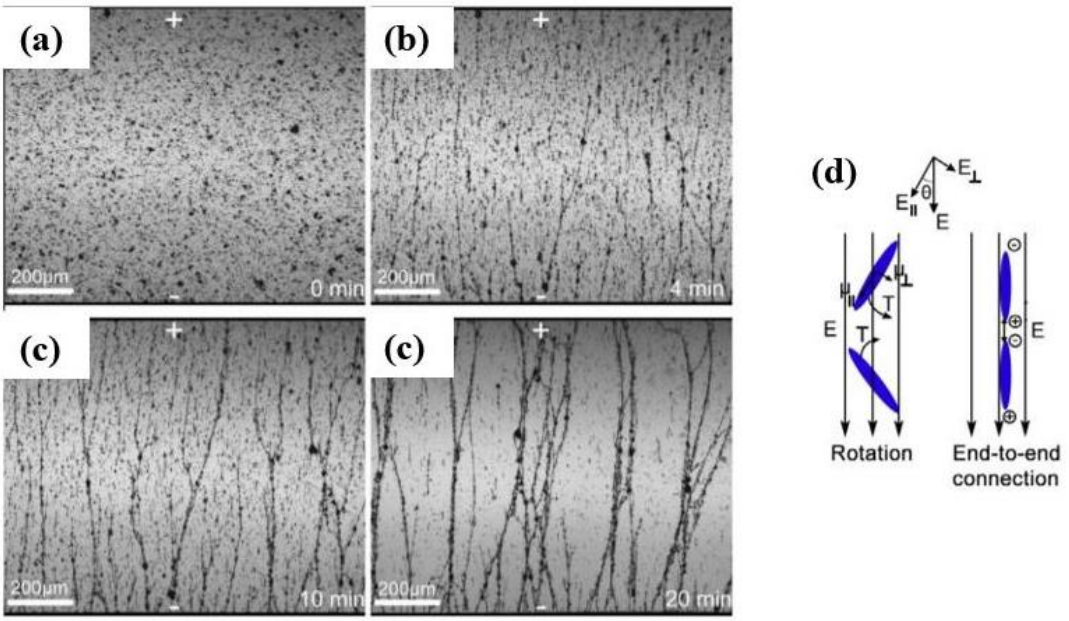


Figure 2. 23 Optical micrographs of GNPs in the liquid epoxy resin (0.054 vol%) during the application of the AC electric field (25 V/mm): Randomly-oriented GNPs before the field was applied (a); after the field was applied for 4 min, 10 min, and 20 min (b), (c), and (d), respectively. (The positive and negative electrodes are indicated by ‘‘ + ’’ and ‘‘-’’.), (d) alignment mechanisms of the GNPs by the AC electric field (Wu, Ladani et al. 2015).

Limited reports have been published for the use of external electric fields in order to create aligned graphene architectures on polymer composites, especially focused on the mechanical reinforcement. One limitation of this technique is the poorer dispersion state through the agglomerated aligned chains than performed than individual aligned graphene sheets (as shown in Figure 2.23), which is not ideal for the mechanical efficiency. Moreover, a high-cost experimental equipment and energy consumption requirements are needed which restrict its largescale development and application.

### 2.13.3. External Magnetic Fields

Magnetic fields have been used to manipulate nonmagnetic particles in suspensions, such as spheres, rods and platelets (Erb, Segmehl et al. 2012) . Graphene is featured as having diamagnetism, a ubiquitous property of materials due to the magnetic response of orbital

electrons. Because of unique electronic band structure and high electron mobility, graphene exhibits higher susceptibility than graphite (Lin, Zhu et al. 2017). Hence, the application of the magnetic field in the orientation of the graphene sheets into the polymer composites started to be quite attractive as a non-destructive and contactless manner without any limitation in size and shape of the samples. However, a high external magnetic field (over than 10 T) is needed in order to align and position anisotropic reinforcing graphene nanoparticles within the composite matrix (Wu, Ohtani et al. 2014, Li, Liu et al. 2015). These extremely high range of magnetic fields requires national facilities and limits the applications for the manufacturing of composites at large scale. For this reason, the decoration of graphene sheets by superparamagnetic nanoparticles has been explored in order to make them more responsive in lower magnetic fields.

Yoonessi et al. (2015) decorated graphene (planar size:10-15 μm of o individual or small stacks of graphene) with supermagnetic, tethered nickel nanoparticles, oriented their fillers by applying high (~100 mT) and low magnetic field (1 mT). It was found that the tensile modulus of all nanocomposites cast in a LMF (low magnetic field) or HMF (high magnetic field) increased initially with incorporation of 0.16 vol. % Ni-graphene to the polyimide, as shown in Figure 2.24 (a). Increasing more the concentration of the aligned graphene (0.3 vol.% and 0.6 vol.%), it also gave an increase at the tensile modulus of the polyimide (PI) nanocomposites in comparison with the pure polymer matrix. However, comparing with the random dispersion nanofillers/PI nanocomposites, there was no significant reinforcement, considering the error bars (Figure 2.24 (b)). Further addition of aligned graphene nanosheets (1.3 vol. %) to the polyimide does not contribute to additional increase on modulus. Not a clear explanation was provided by the authors and for this reason, more investigation is needed to understand the mechanical reinforcement of the graphene orientation into the polymer matrices.

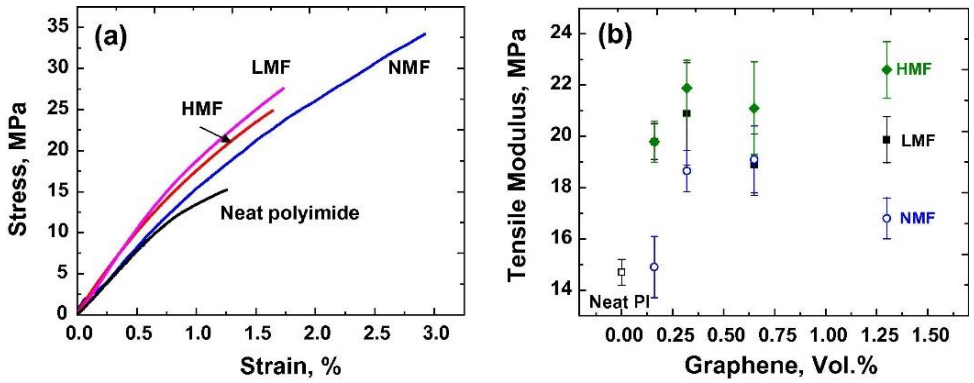


Figure 2. 24. Stress strain curves of the neat polyimide and the 0.16 vol. % nickel graphene polyimide nanocomposites prepared with no magnetic field, low magnetic field, and high magnetic field (a). Tensile moduli of neat polyimide compared with 0.16, 0.32, 0.65, and 1.3 vol.% nickel graphene polyimide nanocomposites in no magnetic field, low magnetic field, and high magnetic field (Yoonessi, Gaier et al. 2015).

Magnetic iron oxide nanoparticles, especially magnetite ($Fe_3O_4$) and maghemite ($\gamma$-$Fe_2O_3$) have received considerable interest as a result of their attractive properties, such as their strong magnetic properties, low toxicity, chemical stability and biocompatibility in physiological environments. Decorating iron oxide nanoparticles onto graphene, can make a composite that is promising for a variety of fields such as biomedicine, magnetic energy storage, magnetic fluids, catalysis and engineering (He and Gao 2010). Up to now, many procedures have been developed to fabricate magnetic graphene, such as hydrothermal (Zhao, Zhang et al. 2013), or solvothermal (Chang, Ren et al. 2012) methods, covalent (He, Fan et al. 2010) and co-precipitation methods (Yang, Zhang et al. 2009, Chandra, Park et al. 2010). Among these fabrication methods, most suffer from complicated and time-consuming procedures, which greatly limit their potential large-scale application. Often, the separate synthesis of functionalized graphene and pre-formed NPs is conducted (Bhuvaneswari, Pratheeksha et al. 2014), which are then connected in a complicated procedure requiring additional experimental synthetic efforts (i.e. suitable surface functionalization of NPs to match the surface chemical groups of graphene (Fullerton, Cole et al. 2014)) and chemical reagents/organic solvents. Despite the significant progress which has been reported, there are some challenges in the field of the graphene/magnetic nanoparticles (MNPs) composites, such as the functionalization of graphene without largely diminishing its properties, dispersibility of the MNPs into the graphene sheets and the control of the crystal size and shape which are important for defining their chemical and magnetic properties.

Many approaches have been fabricated in order to anchor iron oxide nanoparticles (especially $Fe_3O_4$) on graphene sheets (Youn, Kim et al. 2011, Jiao, Shioya et al. 2014, Renteria, Legedza et al. 2015, Ma, Kumar et al. 2018) for their orientation in polymer composites. These studies have focussed mainly on thermal management, electrical or packaging applications. Recently, Wu et al. (2016) investigated the use of a theoretical model, developed by Erb R. (2012) for microscale particles, for predicting the alignment of iron oxide decorated GNPs in epoxy. They showed that very low magnetic fields (20 mT) can be used to induce alignment and confirmed their results by SEM analysis (Figure 2.25 (a), (b)). A 50% enhancement in fracture energy was achieved for nanohybrids (1% wt.) aligned transverse to the crack growth direction (Figure 2.25 (c)).

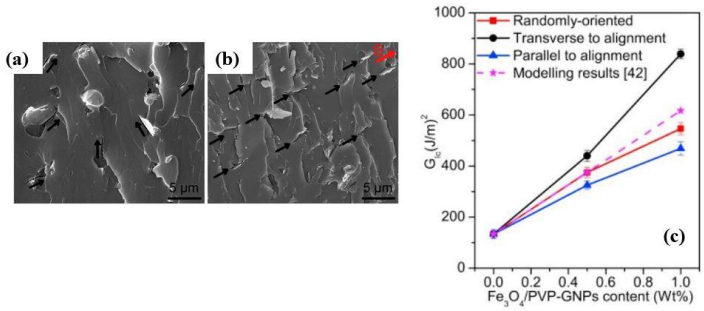


Figure 2. 25. SEM images of epoxy polymer nanocomposites with 1 wt% of randomly-oriented Fe3O4/PVP-GNPs nanohybrids (a) and (b) aligned $Fe_3O_4$/PVP-GNPs nanohybrids (b), mode I fracture energy, $G_{Ic}$, of the epoxy nanocomposites as a function of the $Fe_3O_4$/PVP-GNPs nanohybrid content (c) (Wu, Zhang et al. 2016).

### 2.13.4. Other alignment methods

The formation of multilayer graphene/polymer composites, where graphene is oriented in plane-direction has been explored using the vacuum filtration method which is complementary method of the liquid crystal. It is mainly focused on the vacuum filtration of large surface area graphene papers in a mixture of water/ethanol and then immersed in a mixture of the polymer monomer and cure in order to get the graphene paper/polymer composite. Although, ultrahigh thermal conductivity has been achieved (Li, Guo et al. 2014), it is limited on a lab scale. The freeze-casting technique with traits of versatility, facile accessibility, and capability of producing materials with complex shapes and structures, is extensively used to fabricate 3D graphene architecture (Xu, Zhang et al. 2012). Despite the advantages of this method, such as porous structure, ultra-low density, and the interface connection between graphene sheets which provides high electrical and thermal conductivity, the obvious drawback of the

requirement of ultra-high super-cooling in the progress hinders its large-scale application (Wang, Wang et al. 2019). Last, fluidic flows have been used in order to provide anisotropic graphene structures such as graphene stacked papers and tunable fibres starting from individual 2D graphene oxide sheets into an elastomer by fluidic flows (Xin, Zhu et al. 2019). Although, this manufacturing method has provided significant thermal, electrical and mechanical properties, there are limitations on controlling the flow rate on the surface and the centre of the graphene fibers, which is strongly influenced by the viscosity of the liquid.

## 2.14. Summary

In summary, an extended progress has been reported in the literature in order to evaluate the effect of graphene-based nanomaterials on the mechanical reinforcement of polymer nanocomposites. As mentioned in section 2.11, by increasing the filler loading, the cross-linking network of the epoxy matrices can be dramatically affected, leading to a non-significant or a reduced mechanical reinforcement. The main reasons that have been considered are: (a) the presence of agglomeration that occur due to the van der Waal forces at high filler loadings and (b) the catalytic activity on the curing process *via* the oxygen-containing groups on the graphene surface. Both of two cases lead to a non-stoichiometric ratio between the resin and hardener, resulting in a lower $T_g$ and hence a less cross-linking density. However, there are many reports that showed an increase on $T_g$ (higher cross-linking density) due to the positive chemical interactions between the nanofiller and the epoxy matrix or the physical interactions which restricts the movement of the polymer chains. It is clear that the nanomaterials can affect the curing reaction of the epoxy systems, but there is not really a link how these curing effects can influence the mechanical reinforcement of the polymer composites. In this project, the influence of different key parameters, such as filler loading, dispersion state, stoichiometry and crosslinking density will be explored, relating to the curing process of the epoxy resin and the final mechanical properties of the nanocomposites.

Last, the orientation of the graphene nanosheets into the polymer nanocomposites has showed a significant improvement on the final mechanical properties of the nanocomposites using different alignment methods. Limited is the published work relating to the mechanical efficiency of the aligned graphene into the epoxy systems by the application of an external magnetic field. For this reason, more study is needed to optimize the manufacturing process of aligned graphene/epoxy nanocomposites under the applied magnetic fields and the effect of alignment into the mechanical properties of the epoxy nanocomposites.

# Chapter 3 Experimental Methods

## 3.1. Materials

Four different graphene sheets were supplied by Haydale Ltd. Graphene nanoplatelets (GNPs) and few-layer Graphene (FLG) named as ″pristine″ and also, GNPs and FLG which have been plasma treated in a COOH atmosphere (HDPlas®GNPs). The planar sizes of GNPs and FLG are in the range of 0.3-5 μm with thickness <50 nm and ~8 μm with thickness of 2 nm, respectively. One last material was studied (partially reduced GO-rGO), which supplied by Avanzare, with planar size of 40 μm and thickness of < 3 nm. For the deposition of iron oxide particles, the following materials were used: Iron (II) sulfate heptahydrate ($Fe_3SO_4 \cdot 7H_2O$), anhydrous iron chloride ($FeCI_3$) and ammonium hydroxide ($NH_4OH$, 28.0-30.0 % $NH_3$ basis) were sourced from Sigma – Aldrich, UK. For the magnetic measurements, Iron (II, III) oxide nanopowder (50-100 nm particle size (SEM), 97% trace metals basis) and Iron (III) oxide nanopowder (<50 nm particle size (BET)) were provided from Sigma-Aldrich, UK.

Two different polymer matrices were investigated; IN2 epoxy infusion resin (1,6-bis (2,3-epoxypropoxy)hexane, epichlorohydrin-formaldehyde-phenol polymer and bisphenol-A-(epichlorhydrin) modified epoxy resin, Easy Composites Ltd) and bisphenol A diglycidyl ether (DGBEA, Sigma-Aldrich, UK). The infusion resin was catalysed using a fast hardener by ratio 100:30 (cycloaliphatic and aliphatic amine based mixture, AT30) which has a pot-life of 9-14 min, a gelation time of 2-4 hrs and is de-mouldable in around 6 hrs, provided by Easy Composites Ltd. For the curing process of the second resin system, the cyclohexylamine (CHA, Sigma-Aldrich), and isophorone diamine (IPD, Sigma-Aldrich) were used (Putz, Palmeri et al. 2008). The epoxide to amine stoichiometry was kept constant at 2:1. The cross-link density is defined by the diamine fraction (Ξ), which varies from linear chains cured with CHA (diamine Ξ=0) to a fully cross-linked network cured with IPD (Ξ=1).

## 3.2. Chemical Characterization of graphene and graphene-based composites

### 3.2.1. X-ray Photoelectron Spectroscopy (XPS)

X-ray photoelectron spectroscopy (XPS) is a surface-sensitive analytical technique which provides both elemental and chemical state information from the surface of the material which is studied. XPS is typically accomplished by analysing the kinetic energy spectrum of photoelectrons ejected from the surface of the sample by the irradiating X-ray having a constant

energy, $h_v$, in vacuum (normally better than $10^{-7}$ Pa). The balance between $h_v$ and a kinetic energy of photoelectron, $E_K$, is expressed as:

$$hv = E\kappa + E_B + \varphi \qquad (3.1)$$

Where $E_B$ is a binding energy of electron to nucleus relative to the Fermi level and φ a work function of specimen, in the case of solid. The value of $E_B$ and chemical shift are utilized for identification of an element and estimation of its chemical bonding state in the sample (Inagaki and Kang 2016). X-ray Photoelectron spectroscopy (XPS) was performed in order to investigate the oxidized functional groups on the surface of graphene and the oxidation state of the synthesized iron oxide nanoparticles. Thermo K-alpha XPS instrument was used at a pressure ~ 1 x $10^{-9}$ Torr with the core levels aligned with the C 1s binding energy of 284.8 eV (Shirley backgrounds). Data analysis was performed using the software CasaXPS.

### 3.2.2 X-ray Diffraction (XRD)

X-ray diffraction is an analytical technique which provides information about the structure of the crystalline materials. The principle is based on the elastic scattering of x-ray photons by atoms in a periodic lattice. Due to the crystalline nature, the atoms are arranged periodically. The incident X-ray beam is scattered at different planes of the material. The resulting diffracted X-rays therefore have a different optical path length to travel. The magnitude of this path length only depends on the distance between the crystal planes and the incident angle of the X-ray beam. The geometrical interpretation of the XRD phenomenon is given by Bragg law (Bragg 1929) in equation:

$$\eta\lambda = 2dhkl \sin(\theta) \qquad (3.2)$$

Where: n is the order of diffraction, λ the wavelength of the incident beam in nm, $d_{hkl}$ the lattice spacing in nm and θ the angle of the diffracted beam in degree.

Figure 3.1 gives the details about the geometrical condition for diffraction and the determination of Bragg's law.

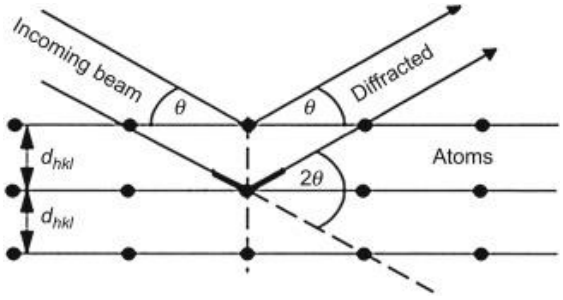


Figure 3. 1. Geometrical condition for diffraction from lattice planes (Epp 2016).

Here, the crystallographic structure of the samples was investigated with X-ray diffraction (XRD) measurements, which were collected using a PANalytical X'pert pro diffractometer with a Cu Kα x-ray source (λ = 1.54 Å). Typical scans were from 2θ of 10 to 80 ° at 40 kV and 40 mA. Resulting peaks were analysed by using X' Pert HighScore Plus software.

#### 3.2.2.1. Small-angle X-ray Scattering (SAXS)

X-ray diffraction has been used in the past in order to identify quantitatively the anisotropy of various materials, such as cellulose (Hermans, Hermans et al. 1946), graphite (Bacon 1956), or polymer fibers (Trottier, Zwanziger et al. 2008), following mostly a Gaussian or Lorentzian distribution function . There are two types of x-ray measurements, the wide-angle scattering (WAXS) and the small-angle scattering (SAXS), in which the distance between the sample to detector is longer. During the Small-angle X-ray scattering experiments, the elastic scattering of X-rays by a sample which has inhomogeneity in the nm-range, is recorded at very low angles (typically 0.1 – 1$^{o}$). This angular range contains information about the shape and size of macromolecules, characteristic distances of partially ordered materials, pore sizes, and other data. SAXS is capable of delivering structural information of macromolecules between 5 and 25 nm, of repeat distances in partially ordered systems of up to 150 nm (Walenta 1985). Information relative to the size distribution of scattering objects or of the space between these nano-objects can be retrieved from the scattering intensity plotted versus the scattering vector:

$$q = \frac{4\pi}{\lambda} \sin\left(\frac{\theta}{2}\right) \qquad (3.3)$$

where q is the scattering vector forming a scattering angle theeta with the beam direction and λ is the beam wavelength (Dumee, Thornton et al. 2012).

Small-angle X-ray measurements were performed recently in order to investigate the orientation distribution of carbon nanotubes (Wang, Bennett et al. 2007, Yang, Yuan et al. 2013), magnetic nanoparticles (Yuan, Zvonkina et al. 2017) and graphene nanofillers (Lu, Feng et al. 2017) into the polymer composites. In this project, Small Angle X-ray measurements were performed in order to study the quantitative anisotropic behaviour of aligned graphene fillers under the application of different magnetic fields into the epoxy matrix. To clarify the scope and limitation of the alignment method that was used for the orientation of graphene nanosheets, the effects of the parameters (magnetic field intensity, graphene concentration and dispersion state) on the orientation order are estimated based on 2D SAXS.

2D SAXS measurements were carried out at Xenocs–Xeuss 2.0 laboratory SAXS beamline with X-ray wavelength of 1.54 Å and a sample-to-detector distance of 2.5 M, providing the structural feature on the order of 0.5-100 nm. A Kapton cell was used as a background before the measurements. For azimuthal angle plots, scattering in 2D SAXS images at q=0.006 -0.01 $Å^{-1}$ was integrated for every 5° in azimuthal angle. The quantitative analysis of the orientation has been proceeded, estimating the orientation order using the software DawnDiamond with q range: 0.0112-0.014 $Å^{-1}$. The Cinader and Burghardt equation was used, where the orientation factor is given by the weighted average of the second moment tensor of u (Boothroyd, Johnson et al. 2018):

$$\sqrt{\langle uu \rangle} = \begin{bmatrix} \langle \cos^2 \beta \rangle & \langle \sin \beta \cos \beta \rangle \\ \langle \sin \beta \ \cos \beta \rangle & \langle \sin^2 \beta \rangle \end{bmatrix} \qquad (3.4)$$

Where:

$$\langle \beta \rangle = \frac{\int_0^{2\pi} I(\beta) d(\beta)}{\int_0^{2\pi} I(\beta) d(\beta)} \qquad (3.5)$$

And u is a unit vector representing a point on the azimuthal scan, β is the azimuthal angle and I(β) is the azimuthal intensity distribution.

### 3.2.3. Microwave plasma atomic emission spectroscopy (MP-AES)

MP-AES is an elemental analysis technique based on the principles of atomic emission. The principle of this technique is similar to any other emission technique such as flame emission or the well-known ICP-AES (Kamala, Balaram et al. 2014). The technique relies on a microwave and magnetically excited nitrogen plasma heated to around 5000 K and is formed within a quartz torch. All samples are in liquid form or digested into solution and therefore energy from the torch is used for atomisation and excitation of the sample. However, this limits samples to soluble or digestible catalysts whereas inductively coupled plasma optical emission spectrometers can analyse solid samples via a laser ablation system.

Atomisation of the sample is facilitated by the high temperatures from this plasma source which also leads to a high population of excited states. This gives MP-AES a higher sensitivity over lower temperature techniques such as flame atomic absorption spectrometers. The diagram below (Figure 3.2) shows the basic principles behind MP-AES from the introduction of a liquid sample to the nitrogen plasma. After excitation, electrons relax into lower quantised energy levels releasing photons of defined energies and wavelengths which are characteristic for each

element. One of the main benefits of this type of technique is the ability to analyse each wavelength individually and sequentially using a monochromator detector and mirror grating. This, along with the high intensities observed, leads to a high sensitivity and low interference for each element.

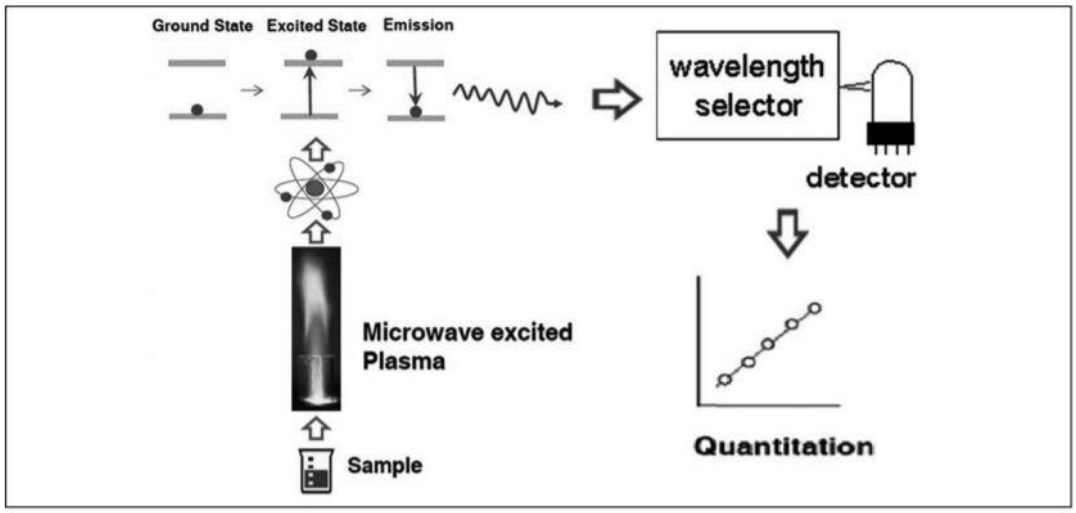


Figure 3. 2. Schematic diagram explains the principle of microwave plasma atomic emission spectrometry (MP-AES) (Balaram, Vummiti et al. 2014).

It is also possible to use multiple emission wavelengths for each element. This is useful when analysing solutions comprising many different elements, such as Cu, Fe, Mn or Zn, (Li, Simmons et al. 2013) as interference from nearby wavelengths can occur, leading to false positives and concentrations.

In this project, MP-AES was used in order to identify if any unreacted Fe form was left on the solution after the experimental process of the chemical co- precipitation method of the graphene sheets by iron oxide nanoparticles. Multiple samples were prepared for MP-AES analysis according to the following procedure. A small volume of the solution (2-3 ml) before the magnetic separation of the iron oxide@graphene sheets was filtered using PTFE syringe filter (0.22 μm) in order to get only the possible unreacted Fe into the solution as the lateral size of the graphene sheets that used are larger than 0.3 μm. The dried magnetic nanohybrids (~50 mg) was placed into a volumetric flask (50 ml) and submerged in freshly prepared *aqua regia* (10 ml). These samples were left for 24 hours to allow any metal ions to leach into solution. Samples were then diluted using deionised water (50 ml) and filtered using PTFE syringe filters (0.22 μm). Samples were then analysed using an Agilent MP-AES 4100.

### 3.2.4. Optical Microscopy

The evaluation of particle dispersion was carried out by Optical Microscope with a system in transmitted light configuration. In this project, graphene nanofillers (GNPs, FLG, GNPs-COOH, FLG-COOH and rGO) and magnetic graphene nanohybrids (MNPs@GNPs, MNPs@FLG, MNPs@FLG and MNPs@rGO) were dispersed using a range of concentrations into two main epoxy matrices which are described in the section of the Materials (3.1). The dispersion state before and after the curing process were viewed under a Nikon Eclipse LV100 optical microscope using the x10 and x50 objective lens. In the uncured stage, all the images were captured one day after the mixture process, following a rheological study. The analysis was done on a small droplet of the epoxy suspension placed on a microscope slide with a glass cover slip of 0.2 mm thickness. Many images were captured through the area of cover slip in order to provide a representable picture of the dispersion state of the filler. The NIS elements D was used in order to capture and adjust the images.

### 3.2.5. Scanning Electron Microscopy (SEM) and Transmission Electron Microscopy (TEM)

Scanning Electron Microscopy (SEM) and Transmission Electron Microscopy (TEM) are the most versatile methods for the investigation of materials down to the atomic scale.

For the filler powders samples, SEM and TEM were conducted in order to obtain information about the sample's surface topography, composition and particle size, respectively. The morphology of the nanofillers has been studied by Scanning Electron Microscopy (SEM) analysis using a Zeiss Sigma HD Field Emission Gun Analytical SEM. To avoid charging during electron irradiation, the samples (starting materials-powders and graphene/epoxy composites) have been sputter coated with an overlayer of Au-Pd alloy (BIO-RAD SC500). A 20-30 nm thick layer of AuPd is uniformly applied to the sample surface. Secondary electron images were acquired at 5 kV with an in-lens detector. Semi-quantitative chemical analysis was performed at the same beam energy by energy dispersive spectroscopy (EDS) using two X-MaxN 150 EDS detectors.

Transmission electron microscope (TEM) analyses of the powder samples were conducted on a Jeol JEM-2100 LaB6 Transmission Electron Microscope fitted with Oxford Instruments X-MaxN 80 EDS analyser. The samples were dispersed in ethanol using an ultra-sonic bath for 2-3 mins and then transferred to 300 Mesh Copper grids (AGS147-3) covered with Holey Carbon Film. This procedure allowed the better separation of agglomerations in individual

particles for easier observation and size quantification of them. The analysis of the TEM images for measuring the size distribution of the nanoparticles was proceeded by software ImageJ. To gain reliable results, the particle size distribution was evaluated by measuring the length of 100 nanoparticles from different TEM images (more than three). ImageJ was used to measure the thickness of the graphene sheets, getting the average of 10 measurements which run through the graphene layer. For each image, the calibration was done by matching the straight-line tool with the scale bar.

The microstructure analysis of graphene-based epoxy composites was performed by SEM analysis. The composites were frozen in liquid nitrogen and then broken manually. After the Au-Pd coating with the same apparatus (BIO-RAD SC500), the fracture surface of the samples was investigated by Scanning Electron Microscopy (SEM) analysis using a Zeiss Sigma HD Field Emission Gun Analytical SEM.

### 3.2.6. Fundamental principles of Raman Spectroscopy

Raman spectroscopy has become an important tool in the field of vibrational spectroscopy and is complementary to infrared absorption spectroscopy. Infrared absorption detects vibrations due to a change of the molecular dipole moment while Raman scattering results from the change of the polarizability (Lindon, Tranter et al. 2016).

Raman spectroscopy is a fast, nondestructive, and high-resolution, providing detailed information about chemical structure and identity, phase and polymorphism, molecular interactions and crystallinity (Bîru and Iovu 2018). The principle of this technique is based on the characteristic of inelastic scattering that occurs when a monochromatic laser light interacts with a material. Following the quantum theory, the energy of the incident light E can be expressed:

$$E = hv_0 \qquad (3.6)$$

Where $v_0$is the vibrational frequency and h is is the Planck's constant.

The photons in the light beam interact with the electrons in the molecule. If the photon energy matches the energy gap between the ground and the exited state of the molecule, the energy is absorbed to promote the molecule to the excited state. However, it can also excite the molecule to a 'virtual state'. The virtual state is not stable and will immediately re-radiate to a lower excited or ground state (Li 2015).

The incident ($E_i$) and scattered photon energy ($E_s$) can be obtained by (Gong 2013):

$$\omega = \frac{E_i - E_s}{hc} = \frac{\Delta v_0}{c} \qquad (3.7)$$

where c represents the speed of light, and $\Delta v_0$ denotes the frequency change of the incident photon and scattered photon. ω is the corresponding wavenumber shift, referred to as 'Raman shift' (Raman wavenumber), with a unit of $\Delta cm^{-1}$ but usually used as $cm^{-1}$.

If the scattered energy comprises radiation at the incident frequency, is called as Rayleigh or elastic scattering (ω=0), which occurs when only electron-cloud distortion is involved in scattering. Rayleigh scattering is filtered out and discarded. The fraction of photons scattered from molecular centres with less energy than they had before the interaction is called Stokes scattered photon (ω>0). When the energy of scattered photons is more than that of the incident photons is called anti-Stokes scattered photon (ω<0). This is because of scattering of photons from molecules that are in high vibrational states. A simple energy diagram of energy level of Raman scattering presented bellow in Figure 3.3.

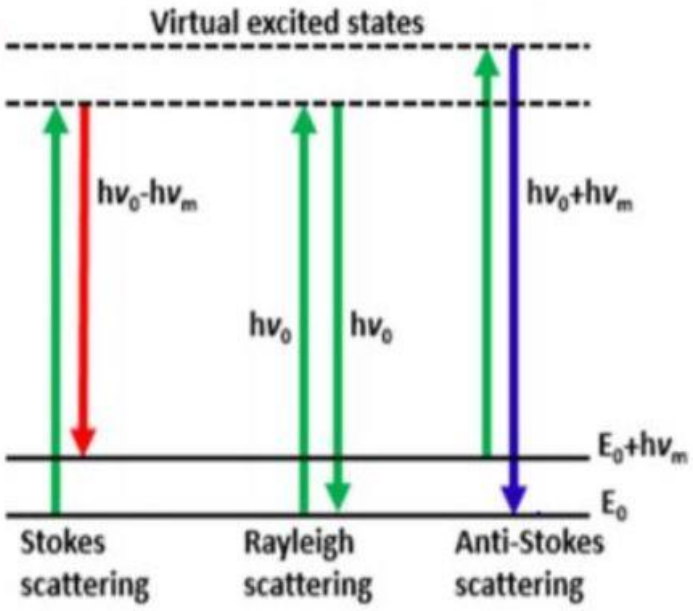


Figure 3. 3. Diagram of the Rayleigh scattering, Raman Stokes mode, Raman anti-Stokes mode and resonance Raman scattering (Lohumi, Kim et al. 2017).

### 3.2.6.1. Raman Spectroscopy of Graphene and Graphene oxide

Raman spectroscopy has played an important role in the structural characterization of graphitic materials (Lespade, Al-Jishi et al. 1982, Ferrari and Robertson 2000, Ferrari, Meyer et al. 2006, Ferrari 2007, Dresselhaus, Dresselhaus et al. 2013) and has also become a powerful tool for understanding the behaviour of electrons and phonons in graphene aimed at gaining a better

understanding of the information on graphene that we can get from Raman spectroscopy studies.

The most prominent features in the Raman spectra of monolayer graphene are the G band appearing at 1582 $cm^{-1}$ (graphite) and the G′ band at about 2700 $cm^{-1}$ using laser excitation at 2.41 eV (Figure 3.4. (a)). In the case of a disordered sample or at the edge of a graphene sample, we can also see the disorder-induced D-band, at about half of the frequency of the G′ band (around 1350 $cm^{-1}$ using laser excitation at 2.41 eV) (Malard, Pimenta et al. 2009).

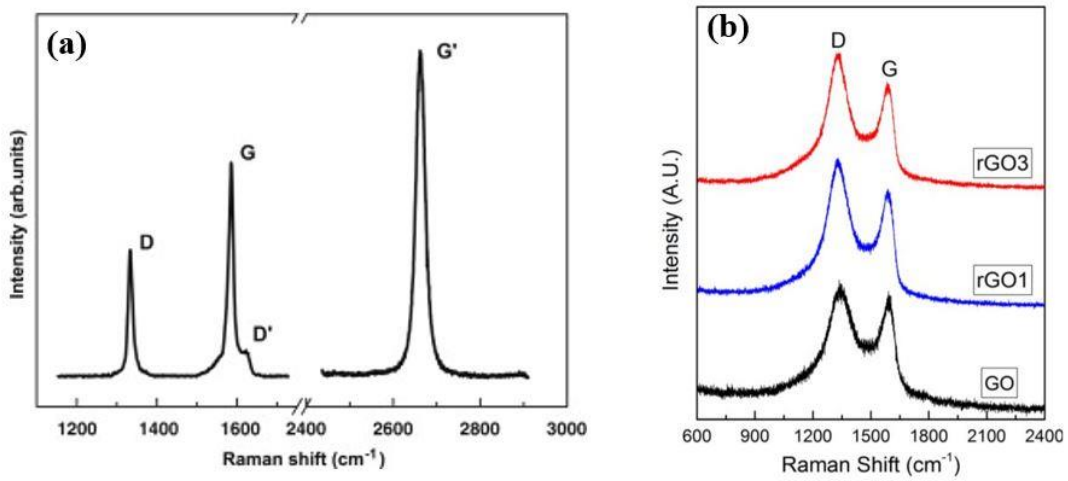


Figure 3. 4. Raman spectrum of a graphene edge, showing the main Raman features, the D, G and G′ bands taken with a laser excitation energy of 2.41 eV (a) (Malard, Pimenta et al. 2009). Raman spectra of GO and two types of reduced GO (rGO): $rGO_1$ which is less reduced than $rGO_3$(b) (Wei, Yu et al. 2016).

The Raman spectrum of graphene oxide (GO) and reduced GO (rGO) is different than that of graphene (Figure 3.4 (b)), since there is an absence of the 2D band due to the strong oxidation that breaks the $sp^2$ carbon network, resulting in the formation of the $sp^3$ bonds. There is also the broadening of the G band, compared to graphene and the relatives intensities of the G and D bands can be used for the evaluation of the defects that are formed during the chemical functionalisation process (Kudin, Ozbas et al. 2008).

In this study, Raman analysis for the graphene powders placed in a glass slide was performed using a Renishaw Raman Spectrometer (InVia Renishaw microspectrometer) with a HeNe excitation laser (514 nm wavelength-2400/mm). Scans were carried out with an exposure time of 10 sec and 10 accumulations, a lens with magnification of x20 was used, with a laser beam diameter on the focus point smaller than 2 μm and energy smaller than 5%. Raman study for

FLG and FLG-COOH was performed at 514 nm wavelength with a laser power of 5% and an exposure time of 30 sec with 1 accumulation using a 20x objective lens. Raman spectra were also obtained for the top surface of the composites with a HeNe laser (785 nm wavelength-1200l/mm). Raman mappings at the composite samples were performed at 785 nm wavelength using a 50xlog working distance lens with a laser power of 0.1 % in order to minimise the heating of the polymer matrix. A window with x and y values of -50 & -49 mm with exposure time of 20 (s) and 1 accumulation was used with a step of 3 μm. A Lorentzian fitting was performed with Wire$^{TM}$ software.

#### 3.2.6.2. Monitoring stress transfer processes using micro-Raman Spectroscopy

Raman spectroscopy provides a unique insight into the relationship between macroscopic deformation and the processes that occur at the molecular or microstructural level and has now revolutionized common understanding of the micromechanics of inclusions in composite materials. This physical phenomenon is due to the anharmonic nature of the chemical bonds and the consequent change of their force constant with bond axial extension.

When a carbon material is strained, the C-C bonds are distorted with changes in the bond angles to occur, which is accompanied by a change of bonding energy. When an external loading is applied to a material, the interatomic distance changes, resulting in a variation of the interatomic force and of vibrational frequency in Raman. Based on this approach, an independent calibration curve between Raman shifts and stress or strain can be constructed and this can then be used to revert to values of stress or strain in the inclusion when the latter is subjected to mechanical load by the substrate or matrix (Manikas, Carbone et al. 2019).

In this present study, Raman spectra were obtained from the graphene-based nanocomposites, during deformation and the positions of both the G and D bands were monitored as a function of strain (0-2 %). The tensile experiments were conducted using a micro-tensile tester (Deben MT 200) under the Raman microscope (InVia Renishaw microspectrometer) at 785 nm laser excitation and a laser power of 0.1 % (exposure time 20 (s) and 1 (s) accumulation). At each deformation step (every 0.5 % strain), several Raman spectra were acquired to three samples for every composite and the experimental data were fitted with Lorentzian by using Wire$^{TM}$ software.

### 3.2.7. Vibrating Sample Magnetometer (VSM)

The magnetic properties of the nanofillers were studied using Vibrating Sample Magnetometer (VSM). A vibrating-sample magnetometer (Figure 3.5.) measures the magnetic moment of a

sample when it is vibrated perpendicularly to a uniform magnetizing field (Foner 1956). The magnetic curves were obtained with 10 to 170 mg of each sample, measuring with a scaler Nimbus (ae ADAM) in a Vibrating Sample Magnetometer (Lake Shore Cryotronics 7410). Typical hysteresis curves were obtained at fields between -1T and 1T at room temperature. The absolute accuracy of the system is better than 1% of reading ±0.2 % and the reproducibility better than ±1 %. The sample was placed in a pure gelatin capsule by Agar scientific. The magnetic parameters, specifically saturation magnetization (Ms), magnetic coercivity (Hc) and remanence (Mr) were deduced from these VSM results.

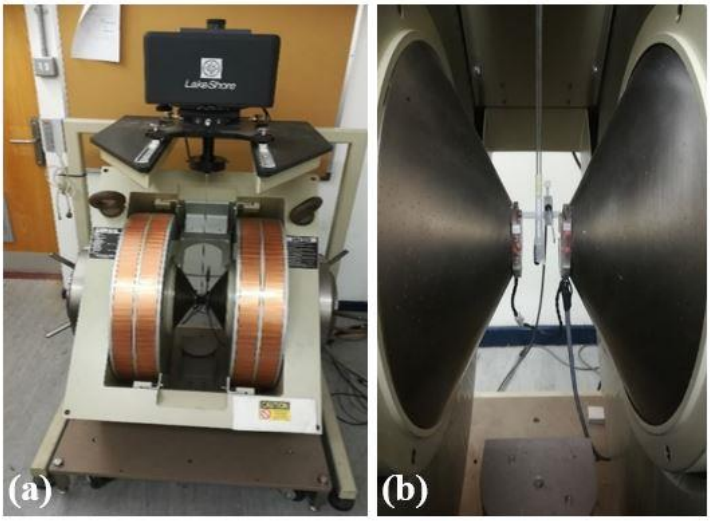


Figure 3. 5. Vibrating Sample Magnetometer (VSM) set up (a). The powder sample is placed on a gelatin capsule between the two poles (b).

### 3.2.8. Rheology Study

The properties of graphene/epoxy nanocomposites depend greatly on the degree of graphene dispersion and exfoliation in the pre-polymer at the resin preparation level. Rheology has been used in order to evaluate analytically the dispersion and the interconnection of graphene nanofillers in epoxy-based dispersions.

Steady shear experiments were conducted in Bohlin C-VOR 200 shear rheometer. Steady-state shear flow curves help us to understand how the graphene flakes dispersed in a liquid medium can orient and align under shear, providing information about the microstructure of the graphene dispersions. A parallel aluminium plate geometry (500 μm gap and 40 mm diameter) was used to analyse the dispersions. The flow properties of the graphene-based epoxy liquids were studied using the rheometer in rotational mode. Shear viscosity ($\eta$) and shear stress ($\tau$) were recorded in the shear rate range 0.15-1000 $s^{-1}$. The delay time for each step was 5 (s) and

the integration time was 5 (s). All the measurements were performed at 25 $^{o}$C and repeated three times and the average was taken with standard deviation error bars. All the rheological parameters were calculated and proceeded via the Bohlin software C-VOR 200.

### 3.2.9. Dynamical Mechanical Analysis (DMA)

Dynamic mechanical analysis (DMA) is a material characterization technique that provides information on viscoelastic properties and thermal transitions of polymers. During this technique, a sinusoidal stress or strain (in-phase component) applied to a known geometry sample and analysing the response (out-phase component) to determine the complex modulus E* and obtain a phase lag, δ between the in- and out- components. These data allow the calculation of the damping or tan delta (δ) (Menard and Menard 2002).The stress and strain can be then expressed:

$$E^* = \frac{\text{stress}}{\text{strain}} \qquad (3.8)$$

$$E' = E^* \cos\delta \qquad (3.9)$$

$$E'' = E^* \sin\delta \qquad (3.10)$$

$$tan\delta = \frac{E''}{E'} \qquad (3.11)$$

where E′ is the storage modulus representing the elastic component and E″ is termed the loss modulus (viscous component). When the phase lag δ is 0°, then it indicates a purely elastic material, and an increasing phase shift corresponds to increasing viscoelastic character of the material. The elastic (E′) and viscous (E″) modulus represent, respectively, the abilities of the material to store and lose energy that is applied from the cyclic loading. Therefore, the viscoelastic tan δ can characterize the efficiency of the material to dissipate energy (Panwar and Pal 2017). All the data can be measured as a function of temperature, time and frequency.

DMA can be used to identify the glass transition temperature ($T_g$) of a material. Although there are several thermal techniques (DSC or TMA) available to make $T_g$ measurements, by far the most sensitive technique is dynamic mechanical analysis, DMA. The $T_g$ represents a major transition for many polymers, as physical properties change drastically as the material goes from a hard glassy to a rubbery state. The thermal transitions in polymers can be described in terms of either free volume changes or relaxation times. As the free volume continues to increase with increasing temperature, the glass transition, $T_g$, occurs where large segments of

the chain start moving (Menard and Menard 2002). Here, the $T_g$ was estimated on temperature when tanδ reached its peak. The value of $T_g$ is directly related with the crosslink density (Suresh Kumar and Subramanian 2018). Crosslinking is very important for the mechanical properties of the polymer; therefore, the effect that the incorporation of the nanofillers will have on the degree of the crosslinking of the resultant composites was investigated.

DMA measurements were performed using Perkin Elmer DMA model 8000. Bar specimen dimensions were ~17 mm x 5 mm x 2 mm. The dimensions value measured using a micrometre. Single cantilever bending mode at 1Hz were applied for all specimen, over a temperature range of room temperature to 140 $^oC$ at a heating rate of 3 $^oC$/min. The strain was kept constant at 0.05 mm and more than five specimens were measured for every batch. At room temperature, strain multiplex measurements were also performed using a strain range 0.001-1 mm with a constant frequency 1 Hz. The analysis was performed using the Pyris software. All the samples were kept to a desiccator in order to avoid any moisture absorption.

### 3.2.10. Tensile testing

Tensile tests of the nanocomposites were performed in an MTS® 858 Mini Bionix machine. MTS is a hydraulic testing machine with excellent force and displacement sensitivity, suitable for testing of a wide range of materials. The films were cut in strips of ~3 cm x 3 mm, while their thickness was ~0.3 mm. They were placed in specific grips of MTS, designed for thin films. The displacement rate of the tensile experiments was 5 mm/min and for each film type, more than 5 strips were tested. Strain was measured by an in-built digital function of MTS machine, based on displacement of grips and samples' dimensions.

### 3.2.11. Thermal Gravimetric Analysis (TGA)

TGA provides a quantitative measurement of the mass change in materials associated with transitions and thermal degradation. By monitoring the weight of a sample within a furnace, thermal effects that cause a weight change can be identified and studied. This is perfect for the thermal analysis of a material’s decomposition temperature, thermal stability, adsorption and desorption, dehydration, and combustion. The TGA curve represents the percent mass (weight) loss or its derivative versus temperature when the sample is heated at a uniform rate (heating rate) in a specific environment. The change in mass over specific temperature ranges provides an indication of the composition of the sample, including volatiles such as water and solvents, and inert additives or fillers, as well as indications of thermal stability (ASTM E1131).

Perkin Elmer TGA/DSC $3^+$ Mettler Toledo was used to obtain information on the thermal stability of nanofillers and the nanofiller-based epoxy composites. The samples measured in on aluminium oxide crucibles using a sample weight of ~100-150 mg and were heated from 25 $^oC$ to 800 $^oC$ at the heating rate of 5 $^oC$/min under oxygen atmosphere (only for the powders fillers) and nitrogen atmosphere (for graphene-based epoxy composites). More than three measurements were repeated for every material.

# Chapter 4 Synthesis of iron oxide nanoparticles and study into the effect of graphene support on magnetic properties

## 4.1. Introduction

Here, we present the chemical analysis of as-received materials. Also, we study the effect of different graphene morphologies on a simple, efficient, reproducible and one-step scalable procedure for the synthesis of iron oxides/graphene composite. A chemical *in situ* deposition of iron oxide nanoparticles onto three different graphene sheets (GNPs, FLG and rGO) has been achieved in the presence of water-soluble iron salts under mild conditions. The structural characteristics of graphene/magnetic nanoparticles (MNPs) composites have been studied in detail, exploring the growth mechanism of MNPs over the functionalised graphene surface. Owing to the experimental difficulty in controlling particles sizes, the current study investigates the relationship between the particle size and the magnetic properties of the nanocomposites.

## 4.2. Experimental

The coating process of graphite nanoplatelets (GNPs), few layer graphene (FLG) and partially reduced graphene oxide (rGO) (materials details in Chapter 3) with iron oxide nanoparticles has been achieved by a facile co-precipitation method (Wu, Ladani et al. 2015). As mentioned in Chapter 3, the GNPs and FLG from Haydale, UK, were produced using a plasma functionalization process. The GNPs and FLG were functionalised by plasma treatment in oxygen, providing –COOH groups on the surface (GNPs-COOH and FLG-COOH, respectively). The graphene source (0.225 g) was dispersed in distilled water (250 mL) using an ultra-sonic bath for 20 min, into which $FeCl_3$ (0.225 g) was added whilst stirring. The mixture was vigorously stirred for 15 min whilst heating to 50 $^oC$. To control the reaction kinetics and limit oxidation of the formed nanoparticles, the synthesis was performed in an oxygen-free environment under $N_2$ gas. The nitrogen atmosphere ($N_2$) not only protects against critical oxidation of the iron oxide nanoparticles, but also reduces the particle size (Majidi, Zeinali Sehrig et al. 2016), in comparison with methods without oxygen removal. Then, $FeSO_4.7H_2O$ (0.18 g) was added, with continuous stirring under a $N_2$ atmosphere for 30 min. Next, $NH_4OH$ (5 mL) aqueous solution was added to precipitate ferric and ferrous salts. The pH value plays an important role on controlling the size of the nanoparticles (Kim, Zhang et al. 2001). The pH value of the mixture was continuously checked by pH test strips and kept at ~10 and the reaction carried out at 50 $^oC$ for 30 min under vigorous magnetic stirring. The magnetic nano-hybrids (MNPs@graphene) were obtained by magnetic separation using a

simple magnet, washed with distilled water and ethanol for more than five times in order to stabilise at pH=7, and finally dried overnight under vacuum at 50 °C. Figure 4.1 represents a typical fabrication procedure of iron oxide-coated GNPs.

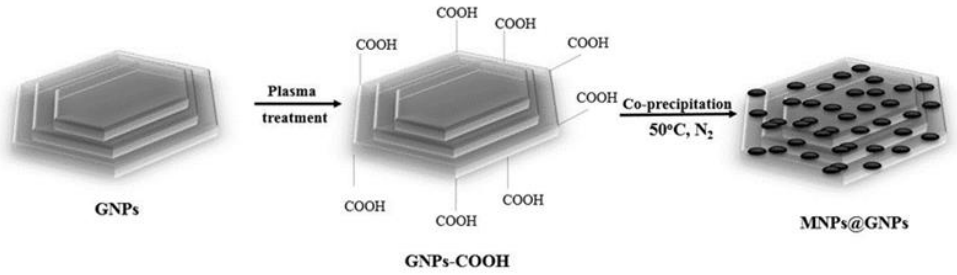


Figure 4. 1. Fabrication procedure of the MNPs@GNPs. The similar synthesis route followed for FLG-COOH and rGO.

In a co-precipitation method, the reaction mechanism can be simplified as:

$$Fe^{2+} + 2Fe^{3+} + 8OH^{-} \rightleftarrows Fe(OH)_2 + 2Fe(OH)_3 \rightarrow Fe_3O_4 + 4H_2O \quad (1)$$ (Wu, Wu et al. 2015)

During the experimental procedure of the first graphene source (GNPs), MNPs@GNPs were obtained in the form of a flaky powder after the vacuum process because the graphene nanoplatelets tend to agglomerate after the removal of the water solution due to the strong Van der Waals forces among individual graphene nanosheets. In order to avoid this effect, a freeze-dry process was used for the FLG and rGO. A shock cooling of the aqueous solution was fabricated by placed it in a freezer (-80 °C). Then, freeze-drying method can help to prevent the possible restacking and agglomeration of graphene sheets and form a more interconnected and porous network which is composed of randomly oriented, crinkly sheets (Xu, Pan et al. 2015). By the end of the experiment, the solution of MNPs@graphene washed several times with distilled water in order to secure the pH=7 and placed into plastic containers (25 mL). The samples were frozen for 24 hrs and then dried for three days in a ScanVac CoolSafe freeze dryer. A noticeable less dense powder was obtained by this method.

## 4.3. Results and Discussion

### 4.3.1. Structural Analysis

#### 4.3.1.1. X-ray Photoelectron Spectroscopy (XPS)

X-ray Photoelectron spectroscopy (XPS) scans in the C1s, O1s and Fe2p regions were recorded for all the materials. Firstly, the XPS data are presented for GNPs, plasma-functionalized GNPs

(GNPs-COOH) and MNPs@GNPs. In detail, the C1s scan of GNPs-COOH (Figure 4.2 (a)) showed the presence of C-C bonding of GNPs at 284.3 eV (peak 1) binding energy attributed to the graphene structure (Kang and Khondaker 2014). This sample is predominantly graphitic in nature and fits derived from a pure graphite reference (cluster cleaned HOPG) (Morgan 2017) were used as the basis for the graphitic contribution to the C (1s) envelope. The remaining signal can be attributed to carbon-oxygen functionalities, which have been fitted with peaks of similar full width at half maximum (FHWM). Specifically, a peak at 285.6 eV (peak 2) have been attributed to defects in the carbon nanotube structure ($sp^3$ hybridization) as well as the peaks at 286.3 eV (peak 3), 288.1 eV (peak 4) and 289.3 eV (peak 5), corresponding to carbon atoms attached to oxygen groups, -C-O, -C=O and –COO (O–C=O), respectively (Zhou, Song et al. 2011, Zhang, Huang et al. 2016). Finally, the $\pi$–$\pi*$ transition loss peak was detected at 291.3 eV (peak 6), which indicates that the delocalized $\pi$ conjugation is restored in graphene sheets (Lin, Chen et al. 2013). Similar results are obtained for the C1s scan of MNPs@GNPs (Figure 4.2 (b)). Any peak at 283.3 eV contributed to Fe-C bonds (Zhou, Song et al. 2011), has not been observed in the C1s scan of MNPs@GNPs, which provides evidence for a no covalent bonding.

Regarding the O1s scan of GNPs-COOH (Figure 4.2 (c)) was fitted to four peaks: peak 1 at 532.1 eV corresponding to the oxygen with a double bond to carbon (-C=O), peak 2 at 533.3 eV corresponding to oxygen with a single bond to carbon (-C-O) (Pantea, Darmstadt et al. 2001), peak 3 at 535.9 eV corresponding to the oxygen atoms absorbed on the graphene surface (Plomp, Su et al. 2009), and peak 4 at 538 eV originates from oxygen of the residual ambient air. After the plasma process, the O1s peak of GNPs-COOH mainly comes from the residual epoxy groups C-O and carbonyl groups C=O, which is consistent with the analysis on the C1s spectrum (Figure 4.2 (a)). Comparing with the O1 scan of MNPs@GNPs (Figure 4.2 (d)), there is an extra peak at 530.1 eV (peak 5) revealing the presence of lattice oxygen within iron oxide nanoparticles (Fe-O) (Bhuvaneswari, Pratheeksha et al. 2014). The peak 1 has been shifted at 531.2eV. This binding energy could be attributed to the functional group O-C=O, which is also found in the C1s scan of GNPs-COOH (Figure 4.2 (a)) but does not appear in the O1s scan of GNPs-COOH because its binding energy is very close to the peak of oxygen group –C=O (532.1 eV). However, this energy can be caused by the bonds between the magnetic nanoparticles and the graphene sheets (Fe-O-C) as the binding energy of O1s in Fe–O–C bond can present in the range of 531–533 eV (Kataby, Cojocaru et al. 1999). Also, a reduction in the

intensity of peak 1 and peak 2 was observed, which would be consistent with the attachment of the iron oxide nanoparticles on the graphene surface.

It has been shown in previous studies that the peak positions of $Fe2p_{1/2}$ and $Fe2p_{3/2}$ depends on the ionic states of Fe. Moreover, the position of satellite peaks for $Fe2p_{1/2}$ and $Fe2p_{3/2}$ are very sensitive to the iron oxidation states, therefore these peaks have been used for the qualitative determination of the ionic states of the iron (Radu, Iacovita et al. 2017). From the Fe2p spectra (Figure 4.2. (c)), the $Fe2p_{1/2}$ and $2p_{3/2}$ peaks are located at 724.46 eV and 710.89 eV, respectively, in addition with the satellite peaks at 719. 1 eV (peak 1) and 733.3 eV (peak 2) and with the absence of the satellite peak at 715 eV for Fe(II), indicating that the surface of the sample looks primarily comprised of a Fe (III) phase (Biesinger, Payne et al. 2011), either hematite (α-Fe2O3) or maghemite ($\gamma$-$Fe_2O_3$). However, it is possible the sample surface is oxidised slightly from Fe (II) to Fe (III) when placed it under air (Santoyo Salazar, Perez et al. 2011) as a result no satellite peak of Fe (II) was observed. Regarding the study of the McIntyre and Zetruk (McIntyre and Zetaruk 1977), the shape of the main Fe2p3/2 line is clearly narrow for the maghemite ($\gamma$-$Fe_2O_3$) while the Fe2p3/2 peak for the α-form has two distinct peaks separated by ~1 eV. The Fe2p3/2 peak of the produced nanoparticles is a simple narrow peak (Section 1, appendix Figure 4.1.), confirming the absence of the hematite ($\alpha$-$Fe_2O_3$). This observation has been clarified by the position of Fe2p1/2 at 724.46 eV, suggesting the allotropic form of maghemite ($\gamma$-$Fe_2O_3$) (Radu, Iacovita et al. 2017).

Furthermore, no peak at 707.5 eV attributed to the iron atoms in Fe-C bonds is present, which confirms no formation of Fe-C bonds again (Li, Xu et al. 2005). The interaction between the iron oxide nanoparticles and the graphene sheets can be divided into chemical bonding (Subrahmanyam, Manna et al. 2010) and physical adsorption (Ihiawakrim, Ersen et al. 2013). The physical adsorption (non-covalent bonding) , especially the van der Waals force (Lu, Mao et al. 2009) or the electrostatic force (Ding, Li et al. 2015) can result in a weaker interaction but may preserve the $sp^2$ hybridization of carbon atoms and the unique intrinsic properties of the graphene sheets, while the chemical bond (covalent bonding) can lead to much stronger interaction and as a result modify the geometric and structural properties of graphene. The possible chemical covalent bonds between iron oxide nanoparticles and graphene may be that iron and carbon atoms are connected by oxygen atoms to form Fe–O–C bonds (Kataby, Cojocaru et al. 1999), and/or a direct Fe–C bond (Adenier, Bernard et al. 2001) . In the XPS results, there was no strong evidence for a direct covalent bonding either Fe-O-C or Fe-C. This allows the assumption that the positively charged magnetic nanoparticles can attract with

negatively charged GNPs-COOH sheets through electrostatic interaction. By this non-covalent bonding, the nanoparticles were intimately distributed and anchored on the surface of GNPs-COOH. This formation mechanism of iron oxide nanoparticles onto the graphene has also been reported recently by Chen et al. (2019), resulting in no morphological changes on the magnetic nanoparticles after the attachment on the graphene surface. The XPS spectra survey of the MNP@GNPs (Figure 4.2 (f)) shows the presence of the iron, oxygen and carbon, confirming the successful anchoring of iron oxide nanoparticles into the GNPs.

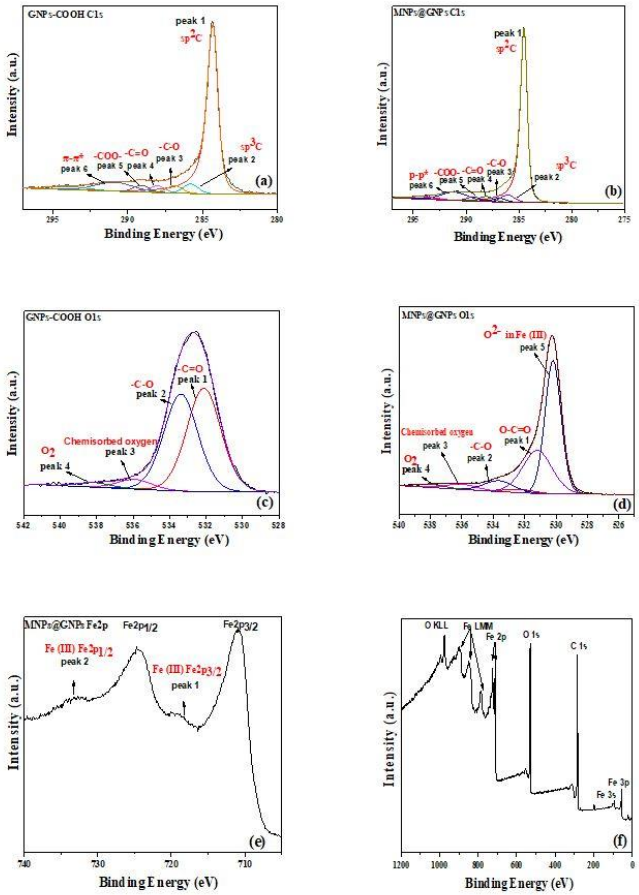


Figure 4. 2. XPS C1s scan of GNPS-COOH (a), C1s scan of MNPs@GNPs (b), O1s scan of GNPs-COOH (c), O1s scan of MNPs@GNPs (d), Fe2p scan of MNPs@GNPs (e) and survey of MNPs@GNPs (f).

XPS spectra surveys are presented in the appendix section 1 for: GNPs and GNPs-COOH (Figure 4.2. (a), (b)), FLG and FLG-COOH (Figure 4.3. (a), (b)) and MNPs@FLG (Figure 4.3. (c)). Relating to MNPs@FLG, the XPS spectra survey scan shows the typical characteristic peaks of carbon (~282 eV), oxygen (531 eV) and iron elements (711 eV and 725 eV). No differences were found on the C1s scans between the FLG-COOH and MNPs@FLG.

Comparing the O1s scan of FLG-COOH and MNPs@FLG (Section 1, appendix Figure 4.4. (a), (b)), the deposition of iron oxide nanoparticles has been confirmed with the extra peak (peak 5) at 530.1 eV revealing the presence of lattice oxygen within iron oxide nanoparticles (Fe-O). The peak 1 has been shifted at 531.3 eV (O-C=O) at a lower intensity and the absence of peak 2 (-C-O) was observed. The Fe2p scan gave similar results for MNPs@FLG, confirming mainly the allotropic form of Fe (III).

The XPS data for rGO are presented in Figure 4.3. C1s scans for rGO and MNPs@rGO (Figure 4.3 (a), (b)) were fitted with similar satellite peaks, as shown previously. O1s scan of rGO (Figure 4.3 (c)) was fitted to three peaks: peak 1 (530.5 eV) is assigned to double bonded oxygen (C=O) (Sakorikar, Kavitha et al. 2017), peak 2 (532 eV) is for oxygen atoms with two bonds to carbon (C-O-C) and peak 3 (533.5eV) is for oxygen atoms with one bond to carbon (C-OH) (Pantea, Darmstadt et al. 2001). The most important observation is that the addition of the iron oxide nanoparticles results in a decrease of the C1s and O1s signals corresponding to the functional group O–C=O (peak 4) in C1s scan (Zhou, Song et al. 2011) and peak 2 (C-O-C) which has shifted at 531.6 eV and peak 3 (C-OH) in O1s scan, marked with black arrows. The peak 1* of the O1s at 530.16 eV corresponding to metal oxide and may cause the absence of the peak at 530.5 eV (C=O), marked by a black arrow. This would be consistent with the attachment of the iron oxide nanoparticles on the graphene surface. The nanoparticles are replacing the above-mentioned functional groups and attach at the defect sites in the graphene lattice. In that way, the defects act as anchoring centres for the particles. Any peak at 283.3 eV contributed to Fe-C bonds, has not been observed in the C1s scan of MNPs@rGO. From the Fe2p scan of MNPs@rGO (Figure 4.3 (e)), similar results were obtained with MNPs@GNPs and MNPs@FLG. No peak at 707.5 eV attributed to the iron atoms in Fe-C bonds is present, which again confirms no formation of Fe-C bonds (McIntyre and Zetaruk 1977). Due to the absence of strong evidence for a direct chemical bonding, the precipitated nanoparticles may be anchored to rGO structure with the surface oxygen-containing groups via electrostatic bonding.

Finally, a XPS survey scan is presented, illustrating the presence of iron, oxygen and carbon elements (Figure 4.3 (f)). Table 1 lists the elementary compositions of the surfaces of the samples (more information for the at % of every functional group is included on the appendix-Table 4.1, Section 1).

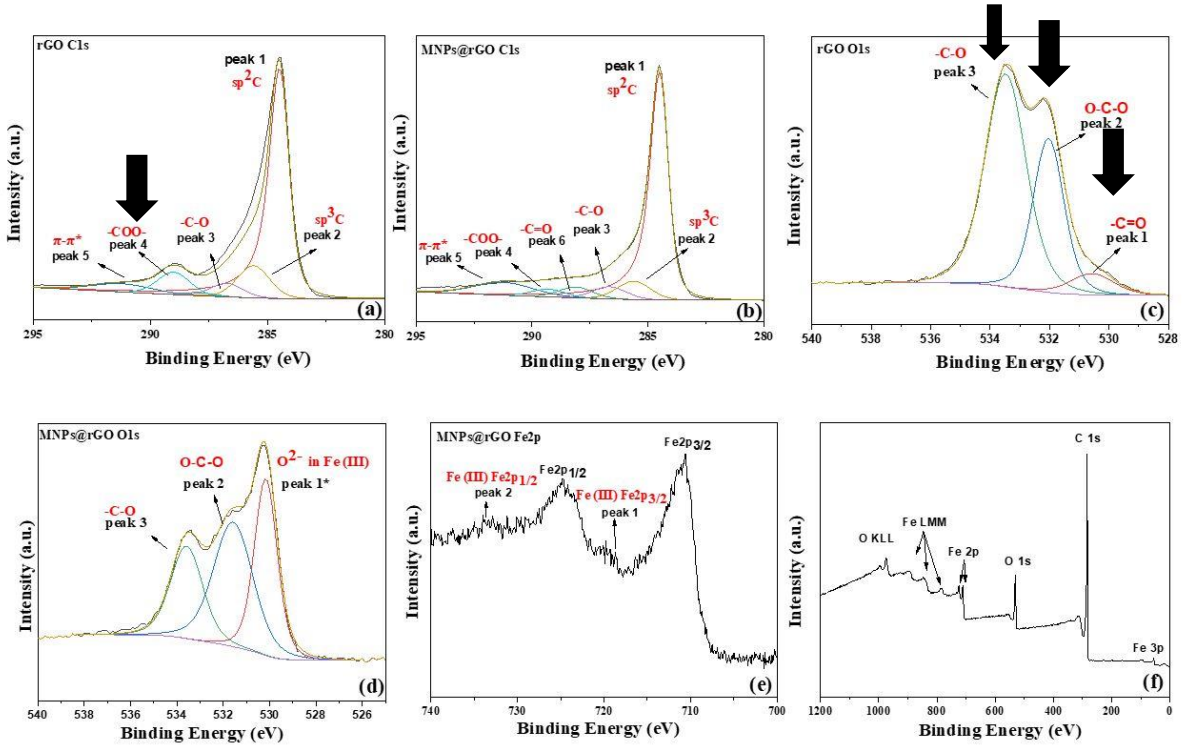


Figure 4. 3. XPS C1s scan of rGO (a), C1s scan of MNPs@rGO (b), O1s scan of rGO (c), O1s scan of MNPs@rGO (d), Fe2p scan of MNPs@rGO (e) and survey of MNPs@rGO (f).

Table 4. 1. Atomic and weight percentage of surface element composition for all the samples.

| **Sample** | **Element (at %)** | | | | | | **(wt. %)** | | |
|---|---|---|---|---|---|---|---|---|---|
| | Carbon (C1s) | Oxygen (O1s) | Iron (Fe2p) | Silicon (Si2p) | Sulfur (S2p) | Chlorine (2p) | C | O | Fe |
| **GNPs** | 96.27 | 3.54 | - | 0.19 | - | | 95.32 | 4.67 | - |
| **GNPs-COOH** | 93.41 | 6.44 | - | 0.15 | - | | 91.58 | 8.41 | - |
| **MNPs@GNPs** | 61.03 | 22.84 | 16.13 | - | - | | 36.62 | 18.27 | 45.09 |
| **FLG** | 99.02 | 0.98 | - | - | - | | 98.69 | 1.30 | - |
| **FLG-COOH** | 94.39 | 5.61 | - | - | - | | 92.65 | 7.34 | - |
| **MNPs@FLG** | 78.85 | 14.68 | 6.47 | - | - | | 61.33 | 15.22 | 23.44 |
| **rGO** | 88.07 | 11.33 | - | 0.24 | 0.09 | | 85.35 | 14.64 | - |
| **MNPs@rGO** | 87.94 | 9.81 | 1.76 | - | 0.25 | 0.24 | 80.51 | 11.97 | 7.50 |

### 4.3.1.2. X-ray diffraction (XRD)

For a more accurate structural analysis of the attached material, X-ray diffraction (XRD) was used to identify the crystalline structure of the products. Initially, structural characterisation of as-received GNPs, GNPs-COOH, FLG, FLG-COOH and rGO was carried out and presented

at Figure 4.4 (a). The GNPs shows a typical sharp diffraction peak at 26.45°, which is attributed to the (002) plane of the graphite structure (JCPDS card 00-041-1487). The crystallographic planes (100), (101), (004) and (110) generated the weaker peaks at 2θ=42.36°, 44.47°, 54.52° and 77.38°, respectively. After the plasma treatment, this sharp diffraction peak remains unchanged indicating that the high-crystalline nature of graphene has not been affected significantly. Four more peaks are shown on both of two patterns at 2θ=42.3°, 44.3°, 54.5°, 77.4° that correspond to the graphite planes (100), (101), (004) and (110), respectively. Figure 4.4. (b) gives a clear idea of the crystalline structure for FLG, FLG-COOH and rGO. In detail, a broad peak at 25.6° and a peak at 44.6° are presented, which are related to the (002) and (101) graphite planes (JCPDS card 01-077-7164), respectively. Interestingly, there is no C (002) diffraction peak in the XRD pattern of rGO due to the absence of the stacking morphology of rGO (thickness <3 nm). The crystal size, L, is related to the thickness of the platelets and can be calculated using the Scherrer equation (Scherrer 1912). Hence, the crystal domain size of the GNPs and FLG is calculated as:

$$L = \frac{K\lambda}{\beta \cos\theta} \qquad (4.1.)$$

where,

L is a measure of the volume-averaged size of the ordered crystalline domains, K is a dimensionless shape factor, with a value close to unity. The shape factor has a typical value of about 0.9 (Monshi, Foroughi et al. 2012). λ is the X-ray wavelength (λ=1,548Å), β is full width at half maximum intensity (FWHM) of the diffraction peak, which is calculated by a Gaussian fitting using the origin software and θ is the angular position of the peak. The (002) peak of XRD for GNPs is located at a 2θ of 26.45° with a full width at half maximum (FWHM) of 0.46± 0.003°, estimating a thickness of 18 nm, which is on the range that specified by the supplier (>50 nm). Similar thickness was calculated for the GNPs-COOH (18.72 nm) and hence, these samples are well characterized as graphite nanoplatelets consisting of several graphene layers. The thicknesses for FLG, FLG-COOH were found at 2.71 nm and 2.35 nm, respectively. These results are in a good agreement with the suggested values by the supplier (~2 nm).

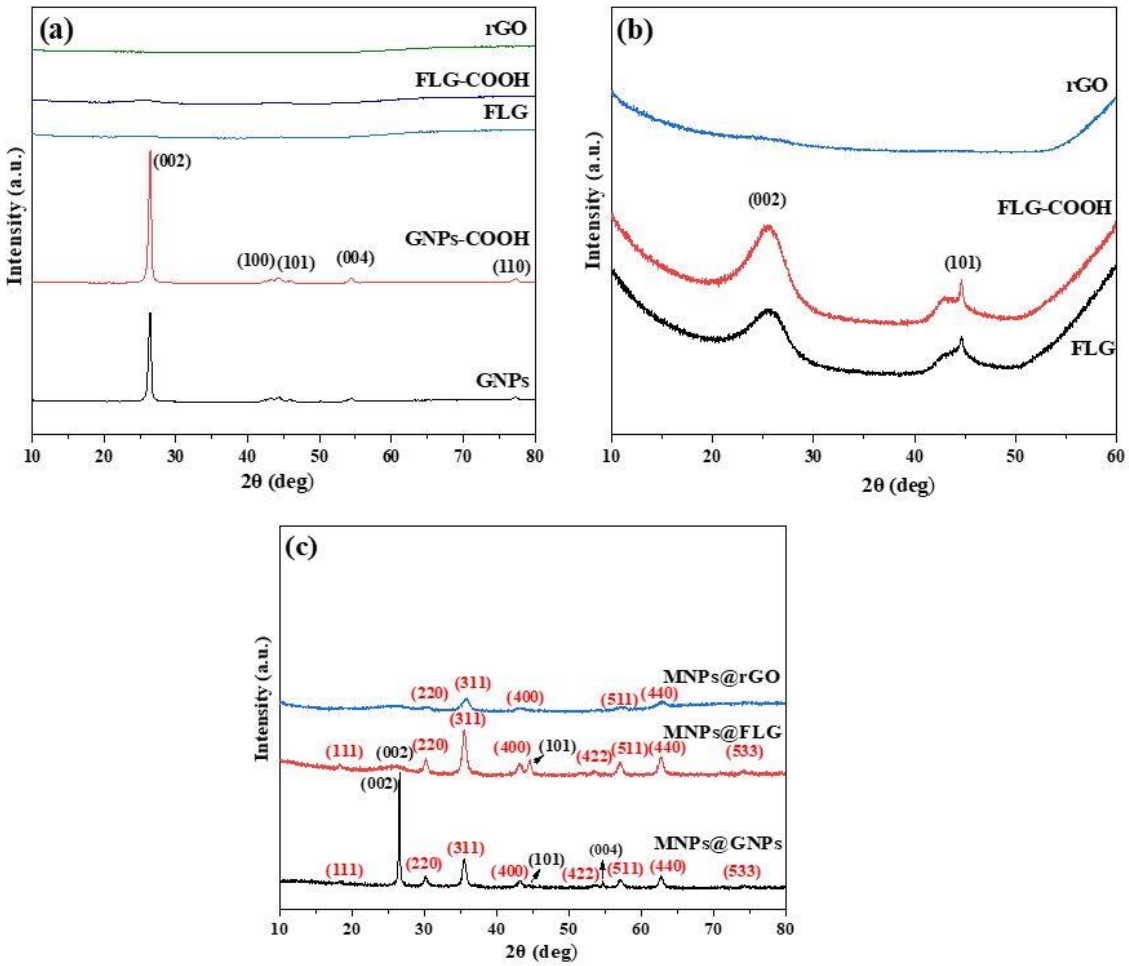


Figure 4. 4. XRD spectra of GNPs, GNPs-COOH, FLG, FLG-COOH and rGO (a), (b), and MNPs@GNPs, MNPs@FLG and MNPs@rGO (c).

According to the third pattern (Figure 4.4 (c)), the peaks in the range of $18^o$ <2θ< $80^o$ correspond to a cubic structure for spinel phases of maghemite ($\gamma$-$Fe_2O_3$) (JCPDS card 00-039-1346) and/or magnetite ($Fe_3O_4$) (JCPDS card 01-084-2782). No other peaks from other oxide phases, such as hematite ($\alpha$-$Fe_2O_3$), were noticed. In addition to these peaks, two additional peaks were observed for the MNPs@GNPs and MNPs@FLG at ~$26^o$ (002) and $44.6^o$ (101) corresponding to the graphite structure, indicating the coexistence of the magnetic nanoparticles and graphene in the hybrid. The absence of the sharp peak at ~$26^o$ for FLG, FLG-COOH and rGO suggests the disappearance of long stacking order (Zhang, Wang et al. 2011) and on the other hand the sharp peaks of the magnetic nanoparticles show high crystalline structure and high phase purity (Zhou, Song et al. 2011). Moreover, a much broader peak at ~$26^o$ for FLG-COOH was noticed after the anchoring of iron oxide nanoparticles which could be due to the fact that iron oxide plays a role of spacer to prevent excessive restacking of the FLG during the drying step (Baaziz, Truong-Phuoc et al. 2014). It is important to mention that

the lattice parameters of the magnetite and maghemite phases are very close and difficult to differentiate (Kim, Nunnery et al. 2010). However, the maghemite phase is known to exhibit a few extra peaks, which may possibly be used to distinguish it from the magnetite phase (Kim, Suh et al. 2012). For instance, the peak at 14.95 $^{o}$ related to the (110) plane of maghemite ($\gamma$-$Fe_2O_3$) is not apparent in the diffraction spectra and regarding the JCPDS card 01-084-2782, this peak is not exhibited in magnetite ($Fe_3O_4$) spectra, indicating that the phase of the iron oxide nanoparticles is $Fe_3O_4$ (magnetite). Moreover, it is noticed that the peaks for MNPs@rGO are fitted better to the structure of inverse spinel ferrite of magnetite (JCPDS file no. 19-0629) (Erdem, Erdem et al. , Santoyo Salazar, Perez et al. 2011). All the characteristic planes of magnetite and graphite have been labelled with red and black colour, respectively.

Using the Scherrer equation (4.1), the crystal domain size was determined by estimating the (FWHM) of the main characteristic peak of magnetite phase (311) for $2\theta=35.5^{o}$. Hence, the crystal nanoparticle size of MNPs@GNPs, MNPs@FLG and MNPs@rGO was found 14.55 nm, 11.94 nm, 7.29 nm, respectively. These values will be compared with the average size determined by TEM (Section 3.3.3). As mentioned above, XRD patterns of maghemite and magnetite are practically identical and hence XRD diffraction cannot be used alone to distinguish between the two phases. Therefore, taking into consideration also the XPS results, it is safe to assume that the produced nanoparticles is a mixed phase of $\gamma$-$Fe_2O_3$/$Fe_3O_4$. Indeed, the high instability of magnetite ($Fe_3O_4$, containing $Fe^{2+}$ and $Fe^{3+}$ in the 1:2 ratio) in air causes the NPs to undergo a partial oxidation to maghemite ($\gamma$-$Fe_3O_2$), ending up with a core−shell structure in which the thickness of the oxidized layer is a function of the particle size (Frison, Cernuto et al. 2013).

#### 4.3.1.3. Raman spectroscopy

Raman spectra (514 nm excitation) of GNPs, GNPs-COOH, and MNPs@GNPs are plotted at Figure 4.5 (a). Specifically, there are three characteristic peaks centered near 1360 $cm^{-1}$, 1580 $cm^{-1}$ and 2700 $cm^{-1}$ in the Raman scattering spectra, which can be attributed to the D band, G band and 2D or G' band, respectively (Kudin, Ozbas et al. 2008). The D band is associated to the disorder in graphitic structure, while G band is mainly assigned to the in-plane displacement of carbon atoms in hexagonal carbon sheets. The 2D band has been used for the evaluation of the number of layers (less than 5). For nanographites with over 5 layers, the Raman spectrum becomes hardly distinguishable from that of bulk graphite (Ferrari, Meyer et al. 2006). The intensity ratio $I_D/I_G$ is a useful indicator to evaluate the size of $sp^2$ domains and the structural disorder of the graphene nanosheet (Dresselhaus, Jorio et al. 2010). Both of GNPs and plasma-

treated GNPs (GNPs-COOH) showed a sharp peak mainly for the G, and very small peaks for D and 2D bands with the intensity of G band (~1580 $cm^{-1}$) to be higher than D band (~1360 $cm^{-1}$). These Raman spectra are very similar with a typical Raman spectra of graphite, as reported by Ferrari et al (Ferrari 2007). There results clarified the purity of GNPs, but also the presence of some possible defects on GNPs surface before the use of plasma treatment. These defects could be attributed by the small content of oxygen (3.54 at %) which was identified by XPS results. The amount of defects present in graphene is directly proportional to the intensity of the D band (Hazarika, Deka et al. 2017). Here the amplitude of the D band is the same for both of pristine GNPs and GNPs-COOH, indicating that the plasma process was not significantly destructive to the graphene surface. This was also confirmed by XRD results.

By conducting a Gaussian fit on the D and G bands, no difference to the $I_D/I_G$ was found after the attachment of the iron oxide nanoparticles. It is known that the 2D band (named as G' band) is the most prominent band observed in graphite samples and is due to the second order of D band (Ferrari 2007). In the case of GNPs@MNP's, a slight shift to a lower wavenumber is observed for 2D band, indicating interactions between the graphene nanoplatelets and the magnetic nanoparticles (Castarlenas, Rubio et al. 2014). Additionally, the location of the G peak has been used to reveal the interaction between the metal nanoparticles and the graphene sheets (Subrahmanyam, Manna et al. 2010). The G peak of MNPs@GNPs has been shifted to 1574.97 $cm^{-1}$. Generally, the shift of the G peak in Raman spectra of carbon-based composites with nanocrystals suggests a charge transfer between the carbon materials and nanocrystals (Kitaura, Imazu et al. 2008). Figure 4.5 (b) shows that the magnetic nanoparticles induced red-shift of G band by ~ 6 $cm^{-1}$ in MNPs@GNPs, suggesting the charge transfer from graphene sheets to iron oxide nanoparticles. This may also be caused due to the stress-induced hardening by the attached magnetic nanoparticles (Sun, Zhang et al. 2016). The peak at 667 $cm^{-1}$ (Figure 4.5 (c)) is associated with the strong peak of magnetite ($Fe_3O_4$) (Panta and Bergmann , Chourpa, Douziech-Eyrolles et al. 2005).

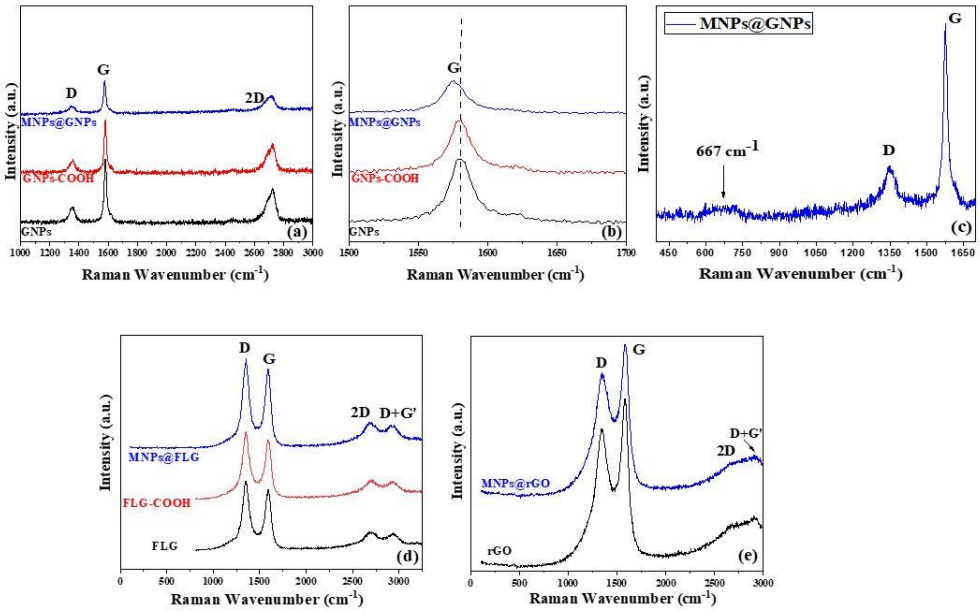


Figure 4. 5. Raman spectra of GNPs, GNPs-COOH, and MNPs@GNPs (a), (b) and (c), FLG, FLG-COOH and MNPs@FLG (d), rGO and MNPs@rGO (e) at 514 nm excitation.

Raman analysis was performed for FLG, FLG-COOH and MNPs@FLG (Figure 4.5 (d)). Comparing with pristine graphene, which has two sharp peaks for the G and 2D bands with no D band, here it is presented two very sharps peaks for the G (1590 $cm^{-1}$) and D (1347 $cm^{-1}$) with the intensity of D band to be higher than G band. Similar Raman spectra were obtained in the literature (Wei, Yu et al. 2016). Also, a peak at 2932 $cm^{-1}$ is detected, known as D+G' band (Wu, Lin et al. 2018), which is corresponded to the graphitization (Moon, Lee et al. 2010). Here, no difference on D+G' band is performed after the plasma process and the chemical deposition with iron oxide nanoparticles; hence, no changes on the graphitic structure. The absence of Raman bonds of iron oxide nanoparticles in MNPs@FLG might be attributed to lower concentration of the magnetic nanoparticles in every graphene sheet. Since a uniform dispersion of the magnetic nanoparticles was achieved on MNPs@FLG, as proved in SEM micrographs (Section 4.3.3), the concentration percentage of the nanoparticles per graphene surface is lower, and hence they may not be detected by the Raman. Similar spectra are represented for rGO and MNPs@rGO (Figure 4.5 (e)). Specifically, there are two sharp peaks for the G (1581 $cm^{-1}$) and D (1345 $cm^{-1}$) with the intensity of G band to be higher than D band as well as the D+G' band (2923 $cm^{-1}$), as reported in the literature (Zhang, Zou et al. 2016, Muzyka, Drewniak et al. 2018). No differences are found on the Raman bands after the magnetic deposition.

#### 4.3.1.4. Thermogravimetric analysis (TGA)

Figure 4.6 (a)- (d) shows the thermogravimetric analysis (TGA) curves of GNPs-COOH and MNPs@GNPs (a) - (b) and FLG-COOH and MNPs@FLG (c) - (d) in air atmosphere. All these TGA curves demonstrate a typical thermal decomposition process in air atmosphere. A detailed analysis of all the weight loses are shown at Figure 4.6 for the GNPs-COOH, MNPs@GNPs (b) and FLG-COOH, MNPs@FLG (d), respectively. This analysis was used in order to evaluate the mass ratio between the magnetic nanoparticles and the graphene nanofillers.

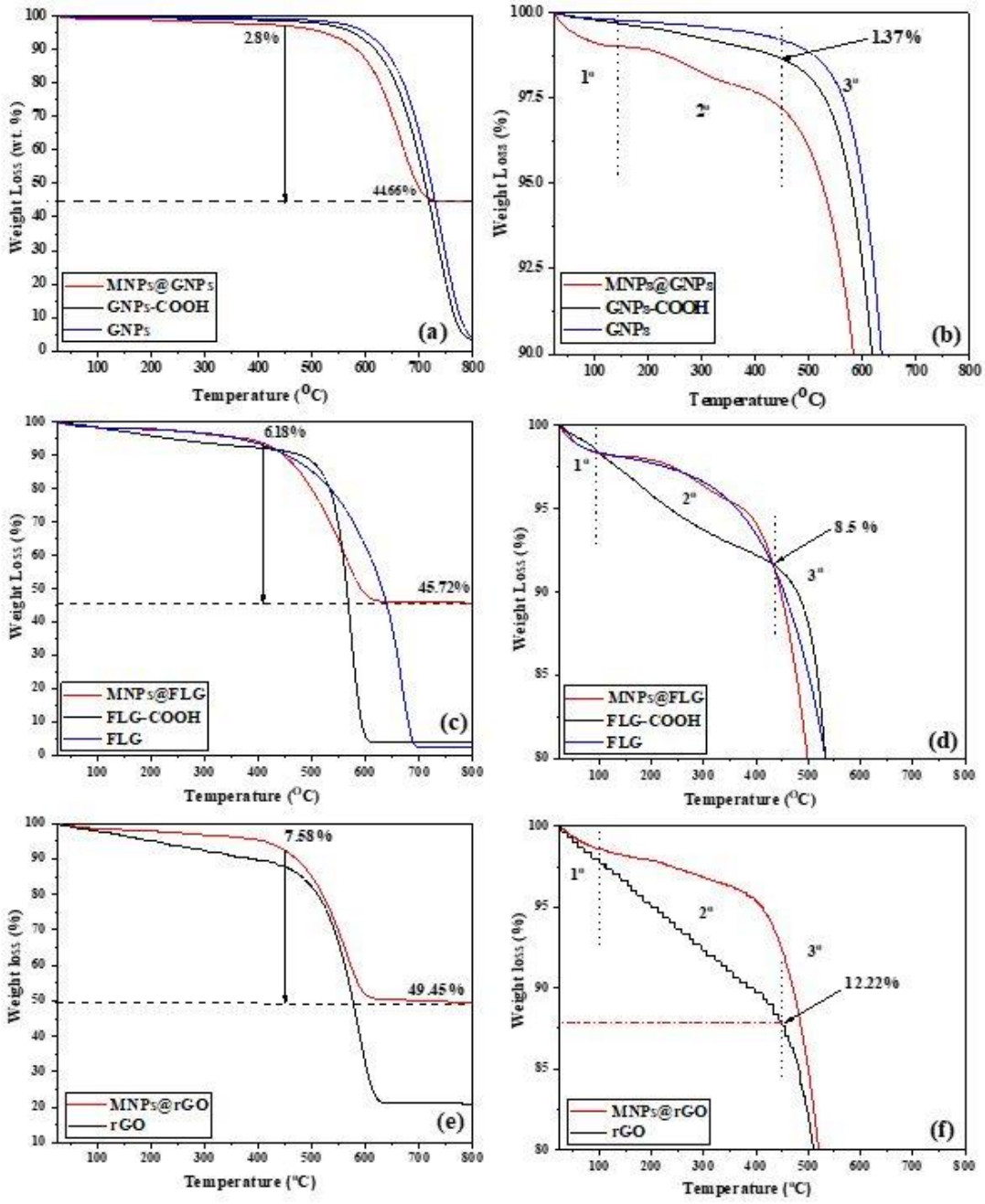


Figure 4. 6.TGA curves of GNPs, GNPs-COOH and MNPs@GNPs (a)-(b), FLG, FLG-COOH and MNPs@FLG (c)-(d) and rGO and MNPs@rGO (e)-(f) in air atmosphere.

When pure graphite is heated in air, there is almost no mass loss of the pristine graphite before 700 °C in air atmosphere, and the complete oxidation and decomposition of pristine graphite occurred after 900 °C (Zhang, Wen et al. 2018). Recently, Kanel et al. (Viculis, Mack et al. 2005) achieved an intercalation and exfoliation of pure graphite to produce graphite nanoplatelets (GNPs) and the thermal decomposition of the later starts in a lower temperature (500 $^{o}$C) than the pure graphite (650 $^{o}$C) due to the greatly reduced van der Waal interactions that occurred in GNPs. Here, the graphite nanoplatelets (GNPs) show a similar behaviour and are stable in air until approximately 450 $^{o}$C, as represented in Fig. 4.6 (a). Figure 4.6 (b) shows all the weight losses in detail. Firstly, one small loss (1$^{o}$) is attributed to the evaporation of absorbed water until 150 $^{o}$C and then a gradual weight loss (2$^{o}$) observed from 200 °C to 450 °C might have resulted from the decomposition of carboxyl, hydroxyl, and epoxy groups at the edge and basal planes, respectively, giving a total loss of 1.37% (Huang, Zhu et al. 2014, Rajagopalan and Chung 2014). Finally, the main loss (3$^{o}$) occurred in the range 450-750 $^{o}$C in which the graphene sheets were burnt as a result the release of CO that is generated from the Bouduard reaction ($C+CO_2 \rightarrow 2CO$) (Lahijani, Zainal et al. 2015) between graphene and $CO_2$ and the decomposition of unstable oxygenated carbon species (Becerril, Mao et al. 2008). Similar thermal decomposition behaviour is observed with FLG-COOH and rGO, as illustrated by the Figure 4.6 (c)-(d) and (e)-(f), respectively. Comparing with the GNPs-COOH, it was noticed that FLG-COOH is less stable as the decomposition starts earlier for 10$^{o}$ (~440 $^{o}$C), with a total loss of 8.5% until this temperature. Although the XPS results of GNPs-COOH and FLG-COOH show similar oxygen contents at wt.% (Table 4.1, 8.41 and 7.34 wt.%, respectively), here the higher total mass of FLG-COOH before 450 $^{o}$C can be attributed only to the water absorption and the presence of more oxygen groups. Hence, the higher oxygen content results in a less stable material, which has been reported in the past (Kuila, Mishra et al. 2013). In the case of rGO (Figure 4.6 (e)-(f)), similar oxygen content was found for both of two techniques.

Similar thermal decomposition patterns to that of the GNPs-COOH and FLG-COOH are observed for the as-prepared magnetic graphene nanohybrids; by the final residual weight percentages, the content of magnetic nanoparticles in the graphene nanohybrids can be estimated by TGA. Before ~450 $^{o}$C, the loss is estimated to 2.8%, 6.18% and 7.58% for MNPs@GNPs, MNPs@FLG and MNPs@rGO until 450 $^{o}$C, respectively. The weight change between 400 and 800 °C is ascribed to the combustion of graphene. Thus, the main residues after 600 $^{o}$C is attributed to the magnetic nanoparticles and has been calculated about 41.86%, 39.54% and 41.87% for MNPs@GNPs, MNPs@FLG and MNPs@rGO, respectively.

### 4.3.2. Quantitative analysis by Microwave Plasma-Atomic Emission Spectrometry (MP-AES analysis)

MP-AES was used in order to identify any unreacted Fe remaining in the solution after the chemical deposition method. Under optimum conditions, the analyte calibration curve was obtained after preparing a series of standards (10 ppm, 30 ppm, 50 ppm) with increasing analyte Fe concentration. The calibration curve was found to have good linearity and correlation coefficient. A blank run was performed using deionised water. The analysis was performed in two different batches: the first one was a small volume of solution after the end of the experiment which was filtered using a 0.25 μm filter in order to ensure that only unreacted iron nanoparticles can pass into the solution. The second one was the dried sample which has been digested in aqua regia to obtain an actual metal loading. All the samples (MNPs@GNPs, MNPs@FLG, MNPs@rGO) were analysed and two measurements were performed in order to control the accuracy of the results. Representable results are shown on the Table 4.2. No Fe was found in the solutions and the dried samples gave ~28 wt. %, 18.66 wt. % and 16 wt. % of Fe, for MNPs@GNPs, MNPs@FLG and MNPs@rGO, respectively. The theoretical percentage value of Fe was estimated:33.55 % wt. Due to the absence of unreacted Fe by the solution, this confirms that most of synthesized iron nanoparticles have been attached to the graphene surface. In the case of FLG and rGO, lower values of Fe were found. MP-AES measures only atomically dispersed species, hence the iron oxide nanoparticles that may also have been filtered out, they will not be detected by the MP-AES instrument.

Table 4. 2. Analytical results for Fe concentration in MNPs@GNPs, MNPs@FLG and MNPs@rGO after MP-AES determination.

| | **Samples** | **Fe (371.993 nm) ppm (mg/l)** | **Fe (wt. %)** |
|---|---|---|---|
| **solution** | MNPs@GNPs | 0 | 0 |
| **dried sample** | MNPs@GNPs | 46.1 | 28 |
| **solution** | MNPs@FLG | 0 | 0 |
| **dried sample** | MNPs@FLG | 31.1 | 18.6 |
| **solution** | MNPs@rGO | 0 | 0 |
| **dried sample** | MNPs@rGO | 26.6 | 16 |

### 4.3.3. Morphological Analysis

The morphological study of the prepared samples was carried out by Scanning Electron Microscopy (SEM). Figure 4.7 shows the morphology and structure of GNPs, GNPs-COOH,

MNPs@GNPs (a-c) and FLG, FLG-COOH and MNPs@GNPs (d-f) in magnification of x50.000. In GNPs, the graphene sheets are randomly oriented, giving rise to petal-like shaped agglomerates with many of the platelets folded. The microstructure of the plasma treated-GNPs appears similar in detail to the untreated GNPs, which are comparable to the previous literature (Zaldivar, Nokes et al. 2014). They confirm and provide clear views of corrugated surface with rough edges (white circles) at nanoscale. Similar observations for GNPs and GNPs-COOH (supplied by Haydale) are recorded by Taylor et al. (Chong, Hinder et al. 2016). The authors found that GNPs which have produced by acid exfoliation, providing trace amounts of hydroxyl and carbonyl functional groups on the GNPs surface, showed a more wrinkle surface comparing with the plasma-proceed materials. Wrinkles can be observed on these materials due to the local strains and electrostatic repulsion caused by the presence of the oxygen functional groups (Ivanovskaya, Wagner et al. 2012). Such rough and wrinkled surface assists the physical interference and plays an important role on the attachment of the MNPs. Figure 4.7. (c) shows that the GNPs are densely covered with sphere-like iron oxide nanoparticles. The majority of the magnetic nanoparticles are uniformly distributed on the GNPs although some clustering of the nanoparticles has been observed. This phenomenon, which has been explained in the literature is due to strong magnetic dipole–dipole attractions between particles combined with van der Waals force and high surface energy (Lalatonne, Richardi et al. 2004, Xia, Wang et al. 2012). When magnetic nanocrystals dispersed in a solution, there are two major types of attractive forces: van der Waals and dipolar interactions. It has been reported that in the case of weak dipolar interactions, large isotropic van der Waals interactions occur when nanocrystal contact distance is short, resulting in the formation of aggregated clusters. These clusters exhibit large dipole moments compared with a single particle. On the other hand, for weak van der Waals interactions, the strength of the dipolar moments controls the formation of randomly chain-like aggregates. Comparing with the thick cakes of graphite nanoplatelets in GNPs, Figure 4.7 (d)- (e) show the thin large flakes of few layer graphene (FLG) with a wrinkled morphology. In Figure 4.7 (e), randomly aggregated, thin, crumpled sheets closely associated with each other forming a disordered structure, without clear differences after the plasma treatment. A uniform distribution of MNPs appeared on the FLG (Figure 4.7 (f)), achieving much less agglomerations.

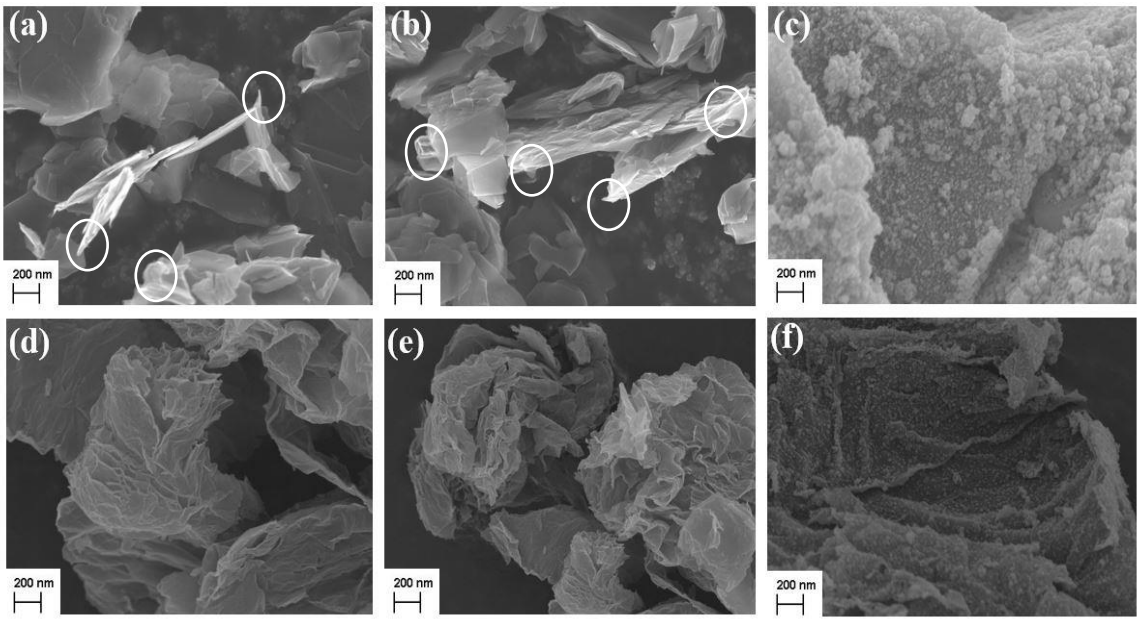


Figure 4. 7. SEM images of GNPs (a), GNPs-COOH (b), MNPs@GNPs (c), FLG (d), FLG-COOH (e) and MNPs@FLG (f). The rough edges of GNPs and GNPs-COOH are highlighted with white circles.

Figure 4.8 (a)- (b) show the morphological structure of rGO and MNPs@rGO in magnification of x25.000 (a), x30.000 (b-c) and x50.000 (d). Specifically, the rGO exhibits a highly porous structure containing open edges with wrinkles and folding on its surfaces. Also, it can be seen by Figure 4.8 (b) that rGO were highly interconnected to each other's to form a complete networked structure with hollow interior and contains large numbers of sub-micrometer pores. The grafting of iron oxide nanoparticles by rGO are shown in Figure 4.8 (c). Due to the small size of nanoparticles, a higher magnification analysis (x50.000) (Figure 4.8 (d)) has been used and the MNPs can been observed as bright dots. The high surface area of graphene plays a critical role in suppressing MNP aggregation as they separately attach to the graphene sheets, leading to their surface active sites being exposed to a higher level of air (Tung, Chien et al. 2019). Using three different planar sizes; GNPs (> 5 μm), FLG (> 8 μm), rGO (~40 μm), the MNPs are shown a better dispersion on rGO, in which no aggregations were observed.

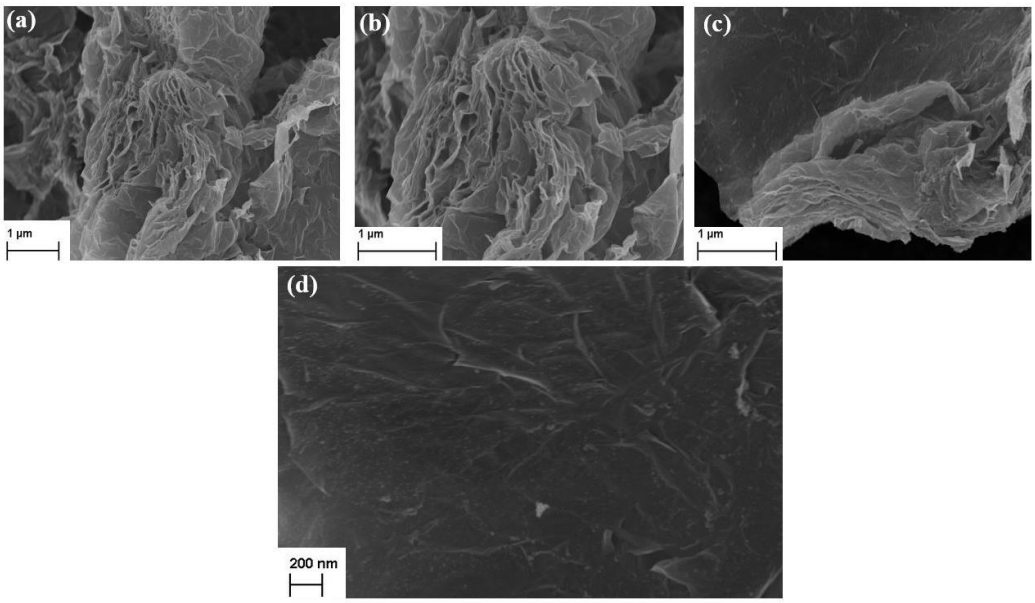


Figure 4. 8. SEM images of rGO (a)-(b), MNPs@rGO (c)-(d).

To further characterize the structures of as received-graphene materials and the magnetic nanoparticles attached on the graphene surface in more detail, TEM analysis was conducted. Low magnification of TEM micrographs (Figure 4.9. (a) and (b)) show the stack morphology of the GNPs and GNPs-COOH with a relatively smooth surface but rough edges, respectively. In order to measure the thickness of GNPs and GNPs-COOH, we focused on wrinkle-like regions (Gong 2011). In an average of three TEM images, the selected wrinkled areas were measured by ImageJ in order to identify the thickness of graphene. For instance, a high magnification TEM image used (Section 2- appendix Figure 4.5. (a)) and the thickness of the GNPs-COOH was estimated with an average of 4.2±1.47 nm and similarly the thickness of GNPs was found ~5.98±2.37 nm. These results are different to the XRD calculations by Scherrer equation, however the results from the two techniques are not expected to be equal. XRD is a bulk averaging technique that measures the size of diffracting crystalline domains (crystallite) while on TEM analysis, we focused only- as mentioned above in wrinkle regions and for graphite nanoplatelets (more than 10 layers), these features are difficult to be distinguished. After the co-precipitation treatment, Figure 4.9 (c) confirmed that the magnetic nanoparticles attached into the GNPs surface, creating some local agglomerations, as observed by SEM images. Spherical iron oxide nanoparticles grew on the surface of GNPs with a large size distribution ranging from 10 nm to 30 nm, giving an average of 27.5±7.99 nm (Figure 4.9. (d)). Figure 4.9 (e) and (f) shows that some of the magnetic nanoparticles deposited onto the graphene sheets and some anchored onto the edges as marked by the black arrow on the Figure 4.9 (e). A high magnification TEM image of MNPs@GNPs (Figure 4.9 (e)) shows the high

crystalline structure of the magnetic nanoparticles. The lattice fringe spacing between two adjacent crystal planes of an individual particle was determined to be 0.25 nm, which corresponds to the (311) lattice plane of cubic $Fe_3O_4$ (Iyengar, Joy et al. 2016). Also, the crystal planes of GNPs are identified clearly in Figure 4.9 (e) and (f), giving a thin layer of 4.89 nm. A selected area electron diffraction data (see appendix information, Section 2-Figure 4.5. (b) and (c)) confirms the presence of well-defined six diffraction rings which matches well to the major d-spacings of magnetite ($Fe_3O_4$) (Kemp, Ferguson et al. 2016). Taking into consideration the XPS and XRD results, the information from the electronic diffraction pattern, allows us to deduce that the prepared iron oxide nanoparticles are mainly magnetite ($Fe_3O_4$) which is further oxidized to maghemite ($Fe_2O_3$).

Comparing with GNPs, FLG and FLG-COOH characterized by crumpled and wavy sheets like images, as shown by Figure 4.10 (a)- (b), respectively. The higher transparency areas indicate the presence of few layers' graphene. Dark areas indicate the thick stacking nanostructure of several graphene layers, as shown in the case of GNPs. The thickness of FLG and FLG-COOH was estimated at 4.26±1.30 nm and ~2.9±0.9 nm, which are relevant to XRD results (2.71 nm and 2.35 nm, respectively). Figure 4.10 (c) and (d) showed spherical and uniform diameter of 14.14±3.9 nm which is in a good agreement with the XRD result (11.94 nm). The particles are crystalline as seen in the lattice fringes (Figure 4.10 (e)) with a d-spacing of 0.48 nm which is very close to the (111) plane reflection of magnetite ($Fe_3O_4$). A selected area electron diffraction data (see appendix information-Figure 4.6. (b) and (c)) confirms the presence of well-defined six diffraction rings which matches well to the major d-spacings of magnetite ($Fe_3O_4$) (Kemp, Ferguson et al. 2016).

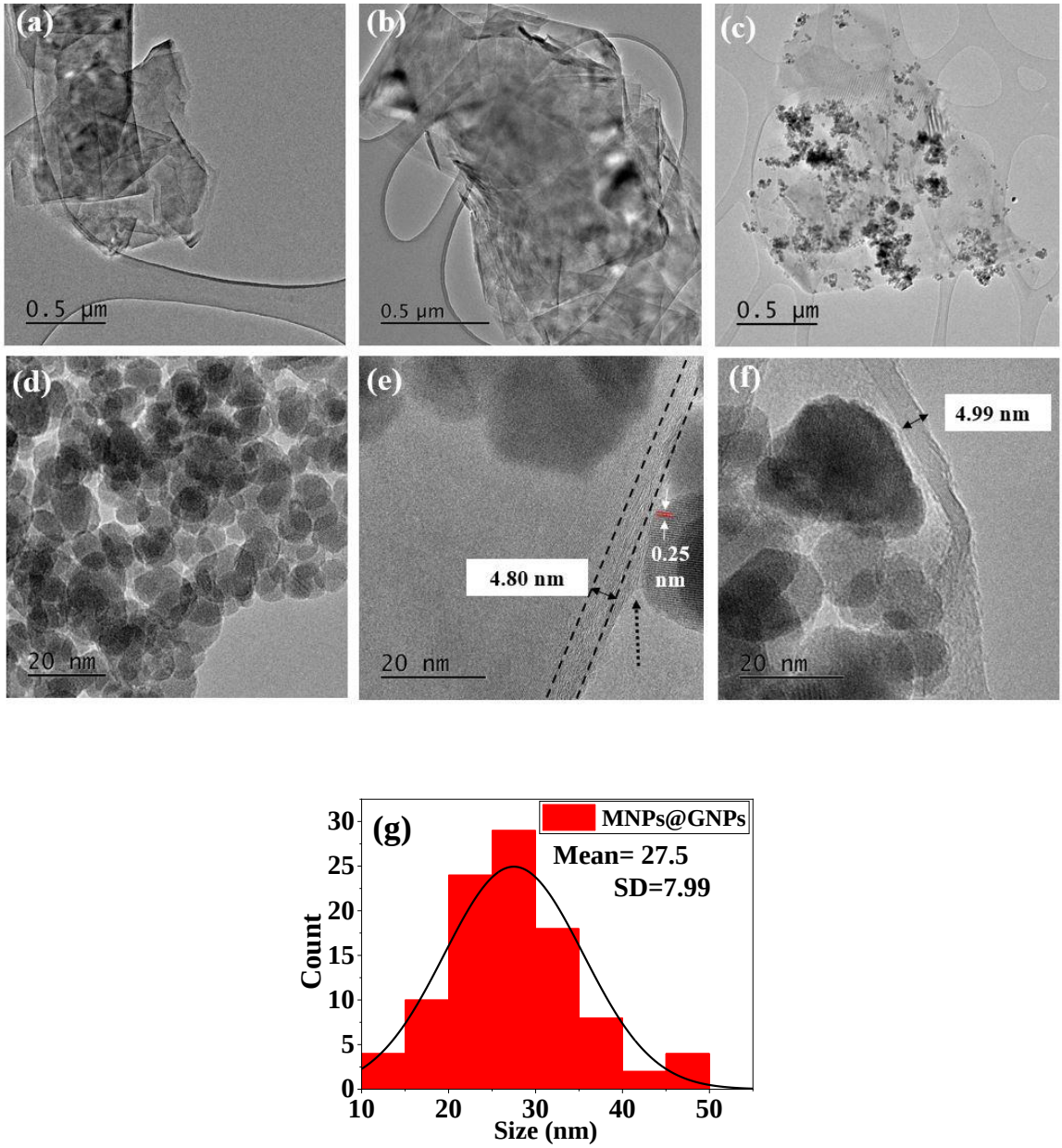


Figure 4. 9. Typical TEM images of GNPs (a), GNPs-COOH (b) and MNPs@GNP's (c), (d), (e), (f) and the size distribution of the iron oxide nanoparticles (g). The black arrow on the image (e) shows the anchor of MNPs on the edges of GNPs.

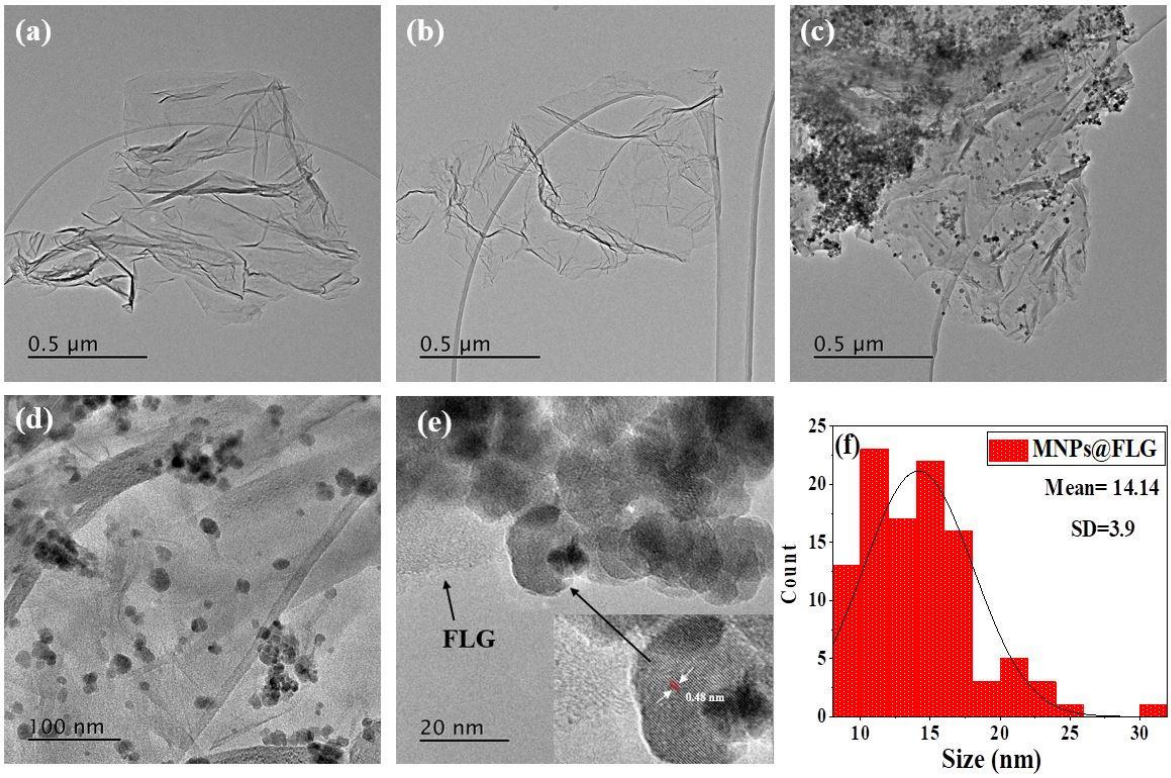


Figure 4. 10.Typical TEM images of FLG (a), FLG-COOH (b) and MNPs@FLG (c), (d) and (e). The inset on the image (e) show the crystalline morphology of the MNPs. The black arrows show the surface of FLG and the MNPs. The size distribution of the iron oxide nanoparticles is presented at (f)

TEM images of rGO (Figure 4.11. (a)- (b)) indicate a significantly larger surface area of high transparency of delaminated graphene layers (of about one to few layer thickness) with some corrugations and scrolling sheets. A two-dimensional ultrathin flexible structure with thickness of 1 nm was observed (Section 2, appendix-Figure 4.7. (a)). A wavy structure was identified by the TEM (inset on the appendix-Figure 4.7. (a)), which can contribute to the presence of defects on the surface of rGO. Figure 4.11 (c) and (d) showed the deposition of the magnetic nanoparticles with an average size of 11.51±3.77 nm, which is very close to the calculated size of XRD results (7.29 nm). Table 4.3. summarises the thickness of all the graphene materials and the size of the MNPs, obtained by XRD and TEM. Interestingly, few cubic MNPs were observed which are highlighting by the red circles on Figure 4.11 (d). It has been reported that sphere-like nanoparticles commonly consist of agglomerates of variously sized cubic nanoparticles (Li, Kartikowati et al. 2017). It can be assumed that the higher content of oxygen functional groups that presented in the surface of rGO increases the adhesive forces between the molecules of iron oxide, which arise the surface energy of the nanoparticles and minimise their surface area, resulting in the formation of crystals with a different shape.

Table 4. 3. d-spacing, full width half maximum (FWHM) of (002) for GNPs, GNPs-COOH, FLG, and FLG-COOH and (311) peaks for MNPs@graphene. Size measurements from XRD and TEM analysis. The d-spacing of graphene-based materials was not calculated after the nanoparticle attachment as no shift was found on the XRD graphs.

| | | | Thickness (nm) | | Size of MNPs (nm) | |
|---|---|---|---|---|---|---|
| **Samples** | **d-spacing (nm)** | **FWHM (º)** | **XRD** | **TEM** | **XRD** | **TEM** |
| **GNPs** | 0.339 | 0.46±0.003 | 18 | 5.98±2.37 | - | - |
| **GNPs-COOH** | 0.3338 | 0.44±0.003 | 18.72 | 4.2±1.47 | - | - |
| **FLG** | 0.3548 | 3.07±0.102 | 2.71 | 4.26±1.30 | - | - |
| **FLG-COOH** | 0.3694 | 3.47±0.07 | 2.35 | 2.8±0.9 | - | - |
| **rGO** | - | - | - | 1.73±0.49 | - | - |
| **MNPs@GNPs** | - | 0.61±0.006 | - | - | 14.55 | 27.5±7.99 |
| **MNPs@FLG** | - | 0.70±0.007 | - | - | 11.94 | 14.14±3.9 |
| **MNPs@rGO** | - | 1.25±0.017 | - | - | 7.29 | 11.51±3.77 |

The strong anchoring of the nanoparticles on the edges of the rGO can been seen by Figure 4.11 (e), in which MNPs have been attracted on the wrinkles of graphene. The inset in Figure 4.11 (e) confirms the highly crystalline character of the MNPs with a d-spacing of 0.48 nm which corresponds to the (111) plane reflection of magnetite ($Fe_3O_4$). The electron diffraction was carried out and confirms the presence of magnetite ($Fe_3O_4$) phase (Section 2, appendix-Figure 4.7. (b) and (c)). For all the magnetic nanocomposites, no $Fe_3O_4$ nanoparticles were observed outside of graphene sheets, indicating that $Fe_3O_4$ nanospheres combined well with graphene sheets in the hybrid.

Overall, the successful coating of the MNPs was achieved on the surface of GNP-COOH, FLG-COOH and rGO. Some areas of the graphene sheets are shown a heterogeneous distribution of the MNPs. It has been noticed that the presence of wrinkles and rough edges facilitates the adsorption of the MNPs, which has been reported also by Mata et al. (2017) for the decoration of rGO with gold nanoparticles. Wrinkled graphene has been used as a scaffold to attach nanoparticles, such as core-shell $SnO_2$ (Zhou, Liu et al. 2014), Pt-Au alloy nanoparticles (Jang, Kim et al. 2015) or $Fe_3O_4$ (Guoxin and Xu 2015). Here, large agglomerations of MNPs were found close to, or at, the edges or wrinkles of the graphene surface (appendix-Figure 4.8 (a)-(c)). The rough edges and wrinkles presence is due to crystalline defects in the graphene sheets and the high concentration of NPs in or close to this area can be explained as a combination of electrostatic interactions, overlapping of the extended π-orbital of graphene with the d orbitals

of the metal NPs and/or allocation of particles at the defects of graphene sheet (Lim, Jung et al. 2015).

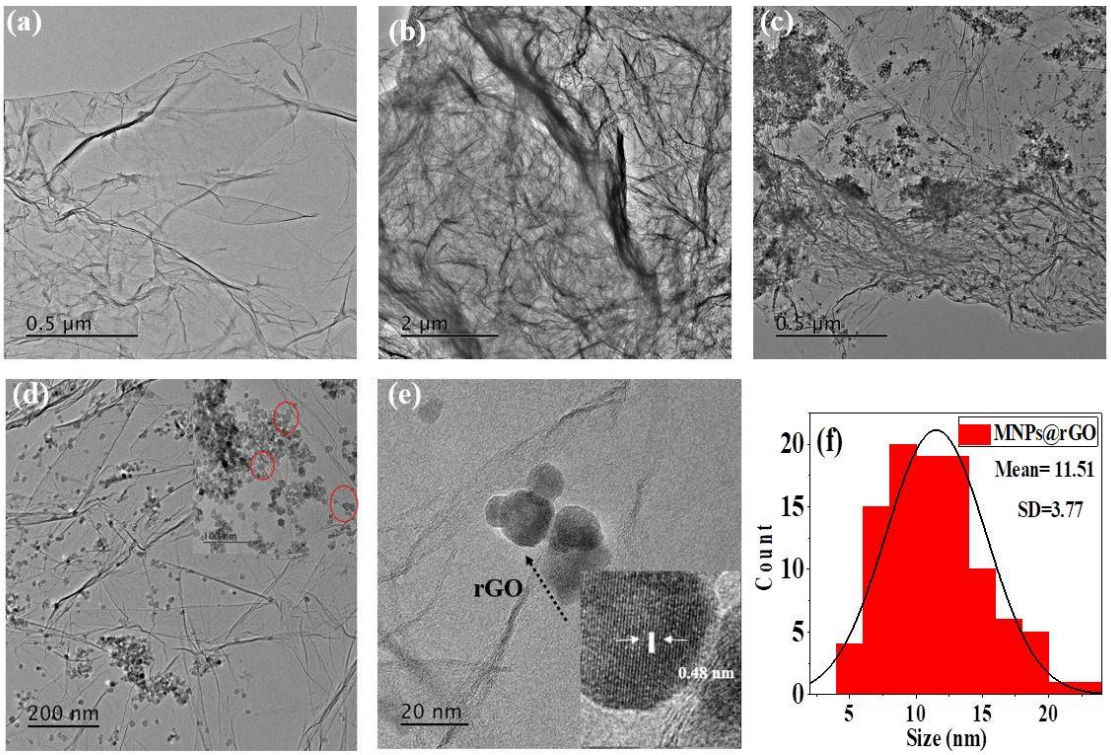


Figure 4. 11. Typical TEM images of rGO (a), (b) and MNPs@rGO (c), (d), and (e). The inset on the image (d) shows the crystalline morphology of the MNPs and the size distribution of the iron oxide nanoparticles is presented at (f). The red circles show the cubic nanoparticles.

One main challenge of the in situ chemical deposition of iron oxide nanoparticles into the graphene surface is the control of the nanoparticle size distribution. It is of great interest according to the fact that MNPs with narrow size distribution allow to get more insight into the chemical and physical processes which arise during the subsequent application of such material (Baaziz, Truong-Phuoc et al. 2014). Especially in the magnetic field applications, the magnetic moment of Fe clusters also varies remarkably depending on the Fe size (Li, Kartikowati et al. 2017) and for this reason iron oxide nanoparticles required with a homogenous size distribution due to the fact that the magnetic behaviour of iron oxide MNPs changes as a function of volume. Studies for a controllable size distribution have been reported in the past with altering the feeding materials, such as the starting material of $Fe^{3+}$ (Yang, Zhang et al. 2009) or the graphene loadings (Zubir, Yacou et al. 2014). In detail, the concentration of the Fe precursor influenced both the density and size of the magnetite sphere. More ferric ions will generate more $Fe_3O_4$ nanocrystallites to increase both density and size of $Fe_3O_4$ nanoparticles (Zhou, Zhu et al. 2010). Here, a reduced size distribution was presented with a size order: GNPs-

COOH>FLG-COOH>rGO. Following the same synthesis parameters for all the magnetic nanocomposites, the only factors that can affect the size of nanoparticles are the dimensions of the graphene and the structural defects obtained by the plasma process and the reduction treatment (for the case of rGO). This means that the nanoparticles tend to grow in a smaller size when a large specific surface area occurs. It is known that a nanoparticle can be made of one crystal or an agglomeration of more than one crystal, and nanoparticles are larger than crystals, indicating that each nanoparticle is composed of more than one crystal (Naghdi, Rhee et al. 2016). Hence, the higher surface area of FLG and rGO provides less crystal agglomerations of MNPs, giving a narrow size distribution.

### 4.3.4. Magnetic properties

The magnetization curves of the $Fe_3O_4$, $Fe_2O_3$, GNPs-COOH, FLG-COOH, rGO and as synthesised magnetic samples were recorded by Vibrating Sample Magnetometer (VSM) at room temperature and presented in Figure 4.12. Their magnetic parameters are given in the Table 4.4. As shown in Figure 4.12 a) and b), all the magnetic hysteresis loops were S-like curves, except for the GNPs-COOH, FLG-COOH and rGO samples which have low magnetic susceptibility. The magnetization saturation Ms of the commercial products $Fe_3O_4$ and $Fe_2O_3$ were 88.1 emu/g and 58.46 emu/g calculated at 1T (higher magnetic fields could not be reached due to the overheating of the VSM instrument), respectively. The values of bulk magnetite ($Fe_3O_4$) and maghemite ($Fe_2O_3$) are 92 emu/g (Chen, Gao et al. 2009) and 74-80 emu/g (Shokrollahi 2017) at room temperature, respectively. The magnetization saturation of the MNPs@GNPs, MNPs@FLG and MNPs@rGO decreases as the size decreases and are well agreed with previous research works (Su, Cao et al. 2011, Fan, Gao et al. 2012, Peik-See, Pandikumar et al. 2014). These values are lower than that of the pure $Fe_3O_4$ due to the smaller size (below 50 nm) of the MNPs comparing with the higher size of the commercial product (50-100 nm) and also to the distribution and the existence of magnetically inactive graphene layers. The loop for the smallest nanohybrids exhibit no coercive field and very small remanence value. This fact indicates that the diameter of ~11 nm is very close to behaving as superparamagnets at room temperature. By the application of an external magnetic field, they become magnetized up to their saturation magnetization, and on removal of the magnetic field, they no longer exhibit any residual magnetic interaction; hence it is unlikely to agglomerate with the removal of the magnetic field. At such a small size, these nanoparticles do not exhibit multiple domains as found in large magnets; on the other hand, they become a single magnetic domain that exhibits high magnetic susceptibility. Thus, on application of a magnetic field,

these nanoparticles provide a stronger and more rapid magnetic response compared with bulk magnets with negligible remanence and coercivity (Wahajuddin 2012). Here, it is very important to mention that the formed iron oxide nanoparticles are a mixed phase of magnetite ($Fe_3O_4$)/ maghemite ($\gamma$-$Fe_2O_3$) due to the air oxidation that occurs preferentially at the surface. Pourroy et al. (2011) established that iron oxide nanoparticles below 20 nm synthesized by a similar co-precipitation approach, are nonstoichiometric magnetite throughout their entire volume. The authors proved that the quantity of maghemite ($\gamma$-$Fe_2O_3$) can reach 85% when the diameter is as low as 10 nm, as a result changing the magnetic susceptibility curve and increasing the coercivity and remanence. Therefore, it could be a reason that Ms of MNPs@GNPs (~27.5 nm) is much higher comparing the MNPs@FLG (~14 nm) and MNPs@rGO (~11.51 nm).

The magnetic nature of the nanoparticles was demonstrated by placing a permanent magnet below a distilled water dispersion of magnetic nanohybrids. Figure 4.12 (c) shows that the magnetic nanoparticles response to an external magnetic field, giving a colourless solution, demonstrating high magnetic sensitivity. This separation process shows that the graphene sheets can be manipulated by the application of an external magnetic field, providing promising magnetic applications.

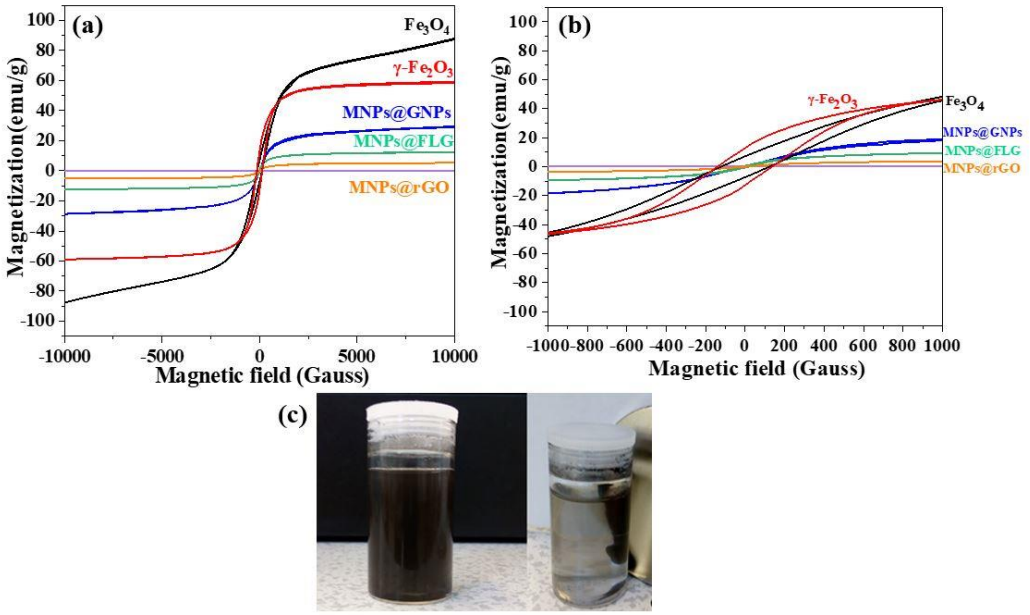


Figure 4. 12. Magnetic hysteresis cycles for $Fe_3O_4$, $Fe_2O_3$, GNPs-COOH, FLG-COOH, rGO, MNPs@GNPs, MNPs@FLG and MNPs@rGO (a), (b), and the well-dispersed solution before the magnetic separation (left) and the magnetic response of GNPs@MNPs distilled to a water dispersion (right) (c). This is a representable result. All the magnetic materials behaved similarly.

Table 4. 4. Magnetic properties measured by VSM.

| Samples | Ms(emu/g)-1T | Mr(emu/g) | Hc (mT) |
|---|---|---|---|
| Maghemite ($Fe_2O_3$) | 58.46 | 12.83 | 13.79 |
| Magnetite ($Fe_3O_4$) | 88.1 | 7.14 | 12.41 |
| GNPs-COOH | 0.035 | $9.16 \times 10^{-4}$ | 27.94 |
| MNPs@GNPs | 29.58 | 0.056 | 0.505 |
| FLG-COOH | 0.007 | 0.026 | 0.097 |
| MNPs@FLG | 12.29 | 0.564 | 1.98 |
| rGO | 0.069 | 0 | 18.58 |
| MNPs@rGO | 5.26 | 0.05 | 0 |

## 4.4. Conclusion

The in-situ growth mechanism of iron oxide nanoparticles in the range of 10-30 nm diameter on carbon support has been studied using graphene sheets with different structural surface and specific surface area. The magnetic nanoparticles have been attached successfully on GNPs-COOH, FLG-COOH and rGO through a simple and scalable co-precipitation method. Using various chemical characterization methods, it can be confirmed that that iron oxide nanoparticles is a mixed phase of magnetite ($Fe_3O_4$)/ maghemite ($\gamma$-$Fe_2O_3$). A detailed morphological analysis showed that the size and distribution of the nanoparticles can be controlled and influenced significantly by the planar size and the structural defects of the graphene surface, providing a better nanoparticle dispersion with a narrow size distribution on a higher surface area of FLG-COOH and rGO. Finally, the magnetic properties are highly influenced by the particle size with the magnetic saturation (Ms) decreasing with decreasing particle size. This is also attributed to a nonstoichiometric volume distribution of the two iron oxide phases as the size decreases. These findings suggest that considerable attention should be given to the structural features of the graphene which strongly influence the particle size, the crystallinity and the magnetic properties of formed nanoparticles. Controlling these parameters, a good balance between the effective surface area and satisfactory magnetic performance can be achieved, giving their potential for many industrial applications.

# Chapter 5 Understanding the manufacturing parameters in graphene-based epoxy nanocomposites

## 5.1. Introduction

This chapter presents the characterisation of two epoxy systems filled with five different nanofillers, GNPs, GNPs-COOH, FLG, FLG-COOH and rGO. The effect of oxygen functionalities on graphene surface, the dispersion state and the loading of the nanofiller has been investigated before and after the curing process using Optical Microscopy, Rheology and SEM. Subsequently, the thermal stability has been quantified by TGA. Finally, DMA and tensile testing were used to investigate the mechanical reinforcement achieved by the addition of the fillers in two different epoxy systems. The main purpose is to determine the influence of the degree of crosslinking on the thermomechanical properties and the interfacial strength of the interphase zone. The results are compared with micromechanical predictions based on the 'rules of mixtures' and the analytical model Halpin-Tsai.

## 5.2. Manufacturing process of graphene-reinforced epoxy nanocomposites

Nanocomposites of GNPs, GNPs-COOH, FLG, FLG-COOH and rGO with various contents (Table 5.1) were manufactured using two different mixing methods:

1. **One step method: High speed mixing method (HSM):** Graphene filler was well mixed in IN2 epoxy infusion resin, using a high-speed mixer (Dual Asymmetric Centrifuge 800.1 FVZ) with a speed of 1950 rpm/min for 5 min. Then, the mixtures were degassed for around 1hr in a vacuum chamber in order to remove any trapped air.
2. **Two-step method: High speed mixing method (HSM) and three roll mill (TRM):** For the HSM, the same procedure was followed. In order to break possible agglomerations, a calendaring process was followed. The dispersion of the filler was performed using an Exakt 80E three roll mill (Exakt GmbH) in two steps. A total of five passes were performed at varying speeds and nip gaps, to gradually breakdown the agglomerates. The roller speed refers to fastest moving roll (feed roll, $N_1$) and the rollers (central roller, $N_2$ and apron roller, $N_3$) move in relation to each other with a ratio of 1:3:9. During the first cycle, the gap size between each pair of rolls varied as a function of the steps: $N_1/N_2$ =45 μm and $N_2/N_3$=5 μm. For the second cycle, $N_1/N_2$ =15 μm and $N_2/N_3$=5 μm were used. The last cycle was repeated four times. The rolling step was 350 rpm for the first cycle and for the fourth cycles was 450 rpm. Then, the mixtures were degassed for 1hr in a vacuum chamber.

Table 5. 1. Formulation of the prepared graphene/epoxy composites.

| Materials | Loading (wt. %) |
|---|---|
| **GNPs** | 1, 2, 4 |
| **GNPs-COOH** | 1, 2, 4 |
| **FLG** | 0.25, 0.5, 1, 2 |
| **FLG-COOH** | 0.25, 0.5, 1, 2 |
| **rGO** | 0.25, 0.5 |

After the dispersion conditions, the resin dispersions were catalysed (AT30) at a ratio 100:30 (resin: hardener) for 2 min on the HSM and they were degassed again for 10 min as the gelation time of the hardener is 15-20 min. For DMA measurements, mixtures were then casted into aluminium moulds (which have been coated with a release agent supplied by Easycomposites-ELRA-01) at room temperature for 6 hrs and then cured in the oven at 60 ºC for 12 hrs. A schematic (Figure 5.1. (a)) is presented included all the steps for the fabrication of the composites. For tensile measurements, the same curing cycle process was followed. Thin films with thickness of 0.3 mm were fabricated, pouring the mixture into a pair of glass slides by a pipette and the thickness has been controlled using two cover slips between the two glass slides, as shown in Figure 5.1. (b), providing a repeatable manufacturing procedure.

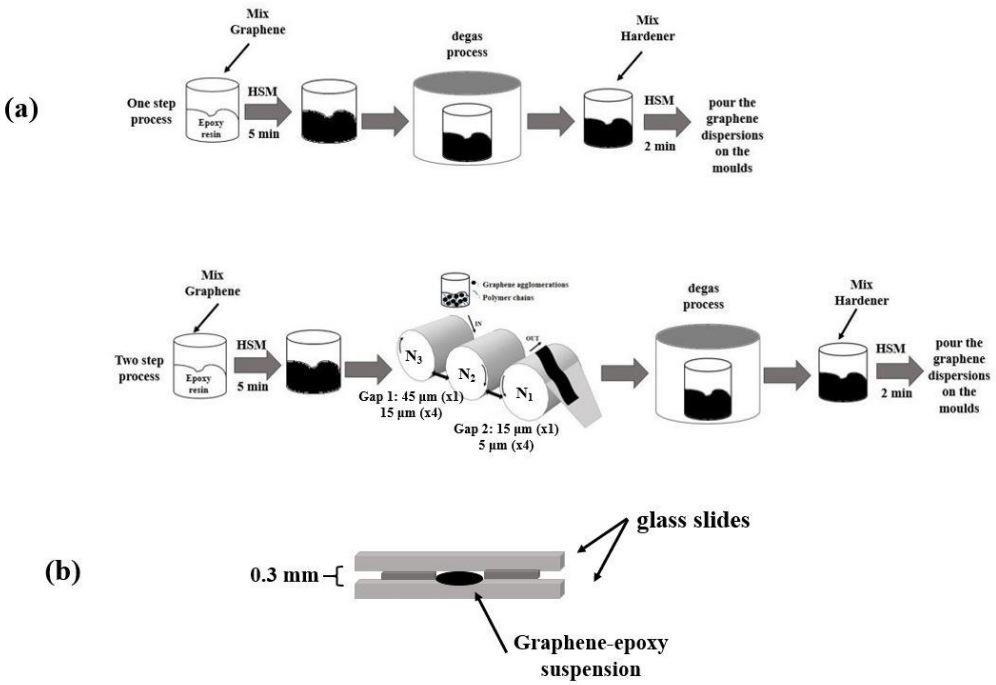


Figure 5. 1.Schematic illustration of fabrication methods (a) and sample preparation for tensile testing (b).

For the study of the cross-linking effect, Diglycidyl ether of bisphenol A (DGEBA) with two different amines (cyclohexylamine, CHA and isophorone diamine, IPD) were used, as described in Experimental chapter. FLG, FLG-COOH and rGO were mixed on the second epoxy system following the same mixing conditions at filler loadings: 1 wt.% for FLG and FLG-COOH and 0.25 wt. % and 0.5 wt. % for rGO. After mixing, the liquid suspensions were degassed for 1 hr and then poured into a Polytetrafluoroethylene (PTFE) mould (Figure 5.2. (a)). The samples were cured at 140 $^{o}$C for 12 hrs following the curing process by Putz et al (2008). Due to the highly exothermic curing reaction, air bubbles are escaped, resulting in voids through the samples' surface. For this reason, the aluminium DMA moulds were not suitable for the casting of the second epoxy system. After many trials, the large surface of PTFE moulds helped to release the gas during the curing process and proving blocks of epoxy composites without any voids (Figure 5.2 (b)). The samples were cut by a diamond tool (Struers Accutom 100) in the dimensions: 35 mm x 4 mm x 5 mm (Figure 5.2 (c)). The speed of diamond cut-off wheel was 1000 rpm.

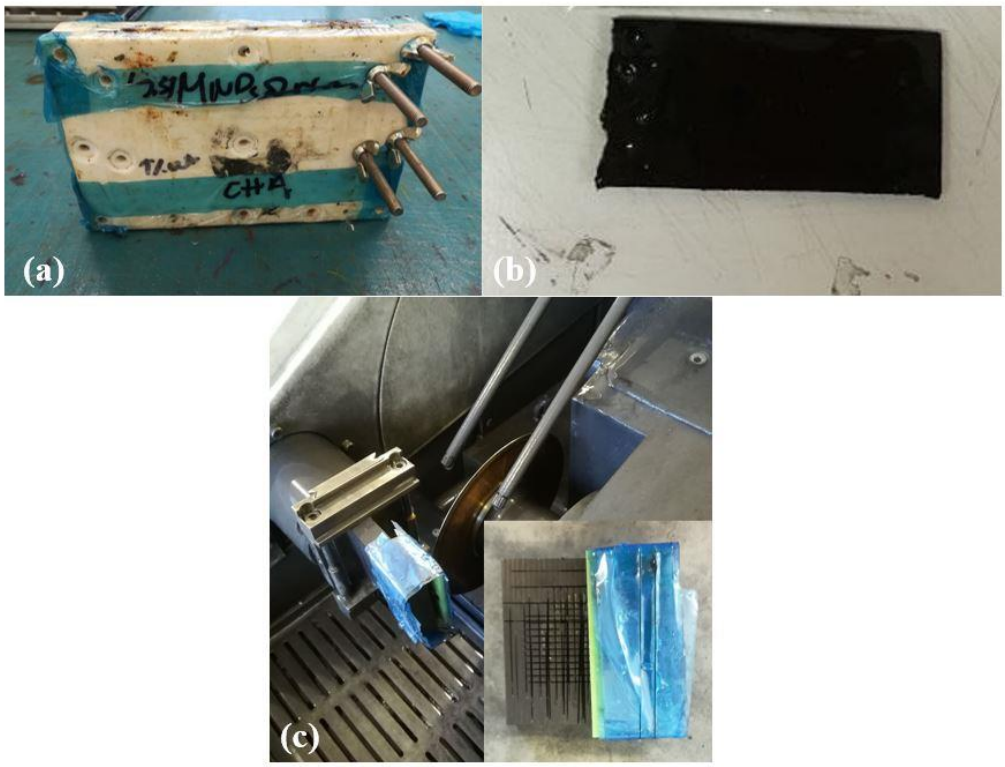


Figure 5. 2. PTFE mould used for the casting process of the second epoxy system (DGEBA) (a), an example of 1 wt. % FLG-DGEBA based composite (b) and the diamond cutting tool (c). The inset shows the way that the sample loaded on the holder in order to avoid any cracks on the samples' surface during the cutting process.

## 5.3. Dispersion study

### 5.3.1. Optical Microscope of graphene-infusion epoxy system

The analysis was performed in order to investigate the dispersion state of GNPs, FLG, plasma treated GNPs and FLG and rGO into the epoxy matrix, using three different parameters: a) nanofiller concentration, b) the dispersion state *via* the mixing methods (HSM and TRM) and c) the surface functionalization.

Figure 5.3. (a)-(f) represents the optical micrographs of GNPs/epoxy suspensions with different filler loadings (1 wt. %, 2 wt. %, 4 wt. %) at different magnification levels. In the uncured stage, the HSM was more effective mixing method provides a well-dispersed mixture at lower concentrations (1 wt.% and 2 wt.%) filler loadings, as shown in Figure 5.3. (a) and (b). Comparably, the use of TRM (Figure 5.3. (d) and (e)) creates mostly isolated aggregates, so more free space is present between the agglomerates. By increasing filler concentration to 4 wt. %, the dispersion of the nanofiller changes after the use of TRM, showing a better dispersed graphene network which can been seen clearly comparing the high magnification images. In the case of the cured stage in which the hardener mixed with graphene-epoxy suspension by HSM, surprisingly a relatively good dispersion was observed at 1 wt. % GNPs at room temperature for both of two mixing methods (Figure 5.4. (a) and (d)). Increasing the filler concentration (2 wt.%), individual large agglomerations were observed by the end of the curing process (Figure 5.4. (b) and (e)) which can be attributed to the lack of functional groups on the surface of GNPs which leads in poor compatibility between the GNPs and the epoxy matrix (Li, Young et al. 2013).When the concentration was increased further (4 wt. % (Figure 5.4. (c)), most of the observation area has been occupied by graphene fillers, especially with the use of TRM (Figure 5.4. (f)).

For the GNPs-COOH/epoxy uncured suspensions which are mixed by HSM (Figure 5.5. (a), (b) and (c)), some agglomerations were observed (highlighted by the red circles), which may be attributed to agglomerates that were present in starting powder that have not been broken down by HSM. Similar with GNPs, at low concentration (1 wt. %), a poorer dispersion state was observed by TRM (Figure 5.5. (d)). However, the big blocks of agglomerates were broken down and as a result the graphene aggregates seems to create a well-connected microstructure network. Comparing with the GNPs/epoxy composites (Figure 5.3), the plasma process seems clearly to help the dispersion of graphene fillers into the epoxy, with the increase of the nanofiller concentration. Especially, for the TRM mixed composites, the differences are more

obvious (Figure 5.5 (d)-(f)). Similar results are observed in the cured stage (Figure 5.6). The effect of the oxygen groups to the agglomerations of graphene in nanocomposites by increasing the concentration of the filler was reported by Li et al (2018). The authors compared the agglomeration factor $\eta_a$ (a term they determined by using the rules of mixtures) between the GO and base-washed GO (bwGO, lower content of functional groups) and they reported that $\eta_a$ of bwGO decreases dramatically (i.e. the degree of agglomeration increases) as bwGO loading increases; the $\eta_a$ of GO do not change until the concentration reaches at 5 wt. %. The authors suggested that there is more basal plane (edge-edge' or 'edge-plane') interactions at this high filler loading that results in the restacking of the GO. The removal of functional groups causes the flakes to re-agglomerate even at low filler loading which has been also confirmed using molecular dynamics simulations (Cha, Kyoung et al. 2016).

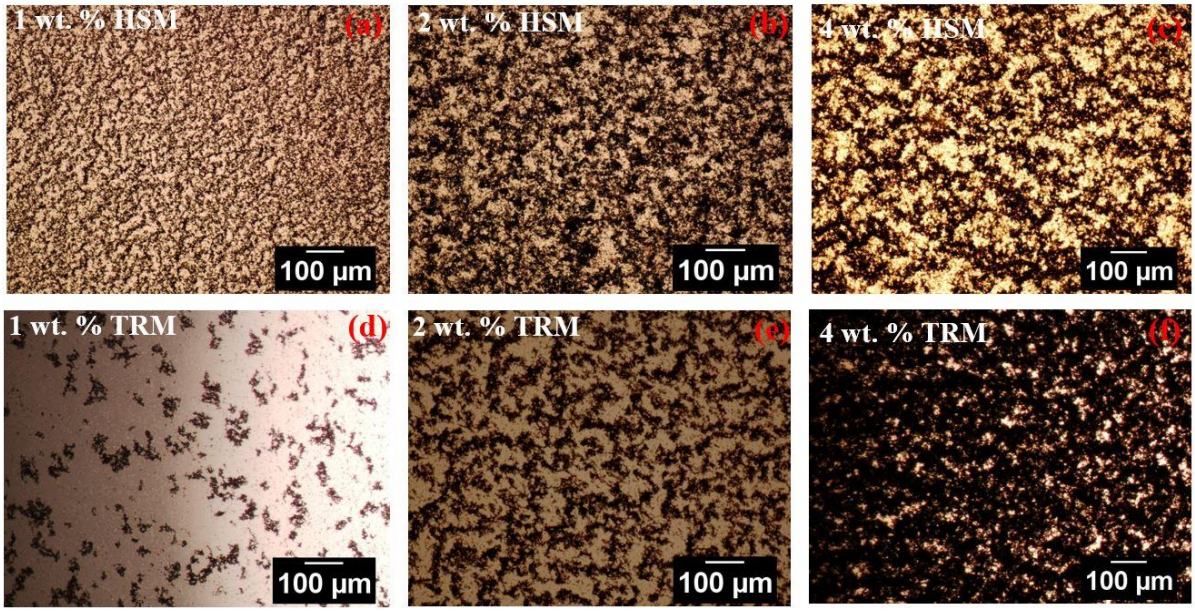


Figure 5. 3. Optical images of 1 wt. %, 2 wt. % and 4 wt. % GNPs dispersed in epoxy matrix before curing using HSM (a), (b), (c) and TRM (d), (e) and (f) (scale bar-100 µm).

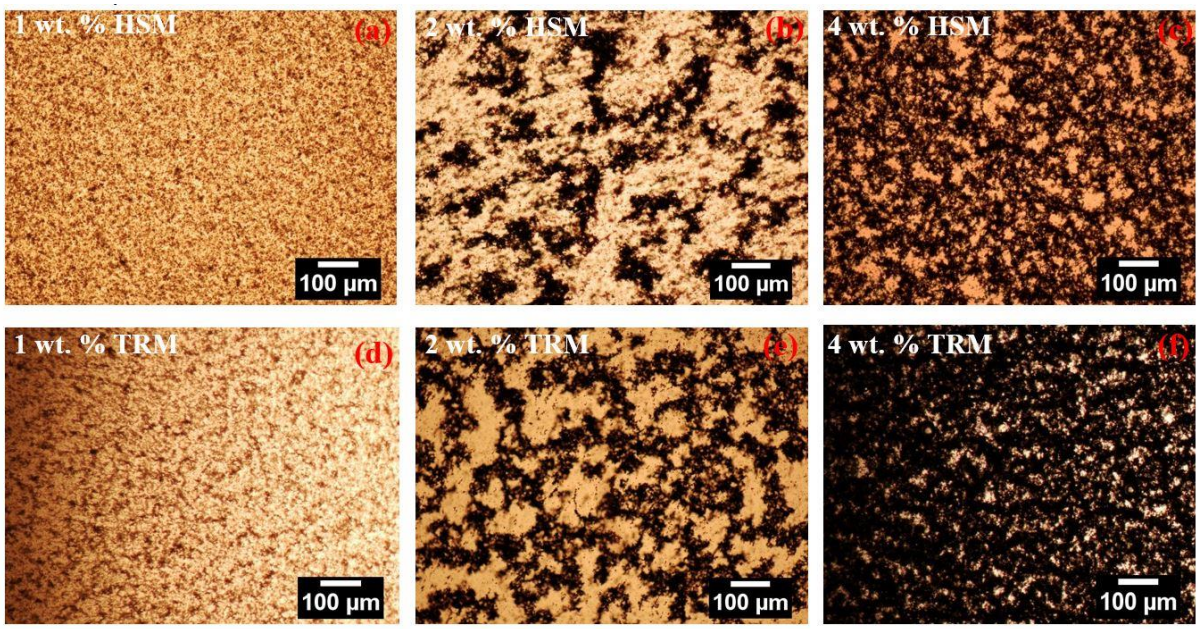


Figure 5. 4. Optical images of 1 wt. %, 2 wt.% and 4 wt. % GNPs dispersed in epoxy matrix after curing using HSM (a), (b), (c) and TRM (d), (e) and (f) (scale bar-100 µm).

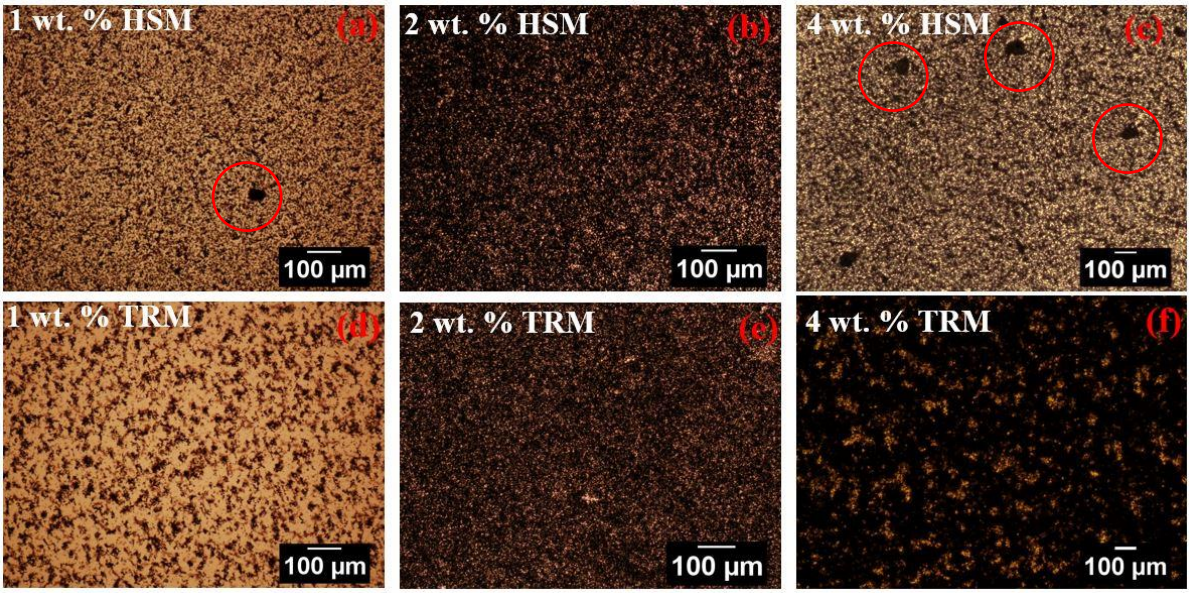


Figure 5. 5. Optical images of 1 wt. %, 2 wt. % and 4 wt. % GNPs-COOH dispersed in epoxy matrix before curing using HSM (a), (b), (c) and TRM (d), (e) and (f) (scale bar-100 µm). The red circles highlighted the agglomerations of GNPs-COOH at HSM.

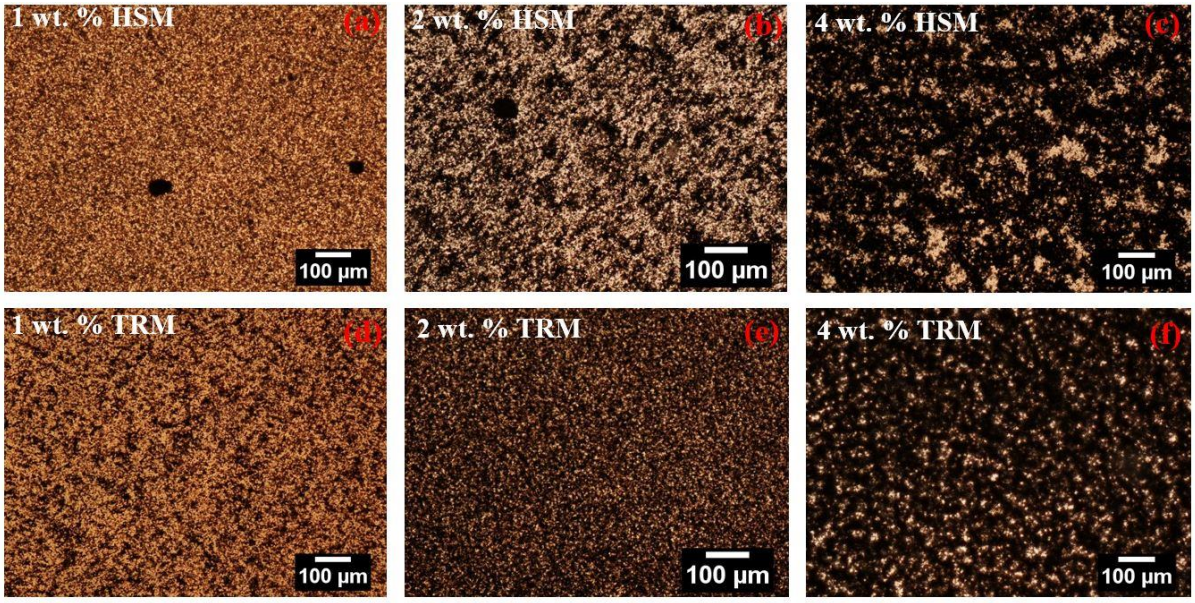


Figure 5. 6. Optical images of 1 wt. %, 2 wt.% and 4 wt.% GNPs-COOH dispersed in epoxy matrix after curing using HSM (a), (b), (c) and TRM (d), (e) and (f) (scale bar-100 µm).

Figure 5.7 and 5.8 illustrate the dispersion of FLG into the epoxy before and after the curing process, respectively. Lower concentrations were used (0.25 wt.%, 0.5 wt.%, 1 wt.% and 2 wt. %) as the viscosity increased significantly (due to higher specific surface area), providing practical difficulties for manufacturing the epoxy composites. Similar with GNPs/epoxy suspensions, a better quality of dispersion was achieved for the HSM-mixed FLG/epoxy suspensions at lower concentrations (Figure 5.7. (a), (b)), with small, isolated graphene lakes to be appeared by the use of TRM (Figure 5.7. (e)- (f)). Although, suitable shear stresses that perform through TRM can initially provide a better dispersion of nanofillers in liquid matrices, after removing by the three roll mil equipment, the absence of solvent (Caradonna, Badini et al. 2019) and the poor interfacial interactions between the non-treated nanofiller and the polymer matrix can cause re-agglomeration of the nanofiller due to the strong Van der Waal forces. By increasing the concentration of nanofiller, the viscosity greatly increases due to the restriction of the polymer chains, which hinders the re-aggregation of the graphene nanosheets. For this reason, a better dispersion occurs for higher filler loadings in the uncured stage, as shown in Figure 5.3 ((e) and (f)) and Figure 5.7 ((c) and (g)). Reaching 2 wt. % of FLG, large agglomerations were observed after HSM (Figure 5.7 (d)). The dispersion state cannot be characterized after TRM as the optical light was blocked by the higher concentration and increased dispersion (Figure 5.7. (h)). In the cured state, a well-dispersed material was observed for all the nanocomposites (Figure 5.8). This may be attributed to the extra mixing process of hardener at HSM, resulting in a better dispersion of the nanofillers that are then locked in place

by curing. The effect of nanofiller concentration was difficult to be distinguished by Optical microscope, hence SEM characterisation will be used.

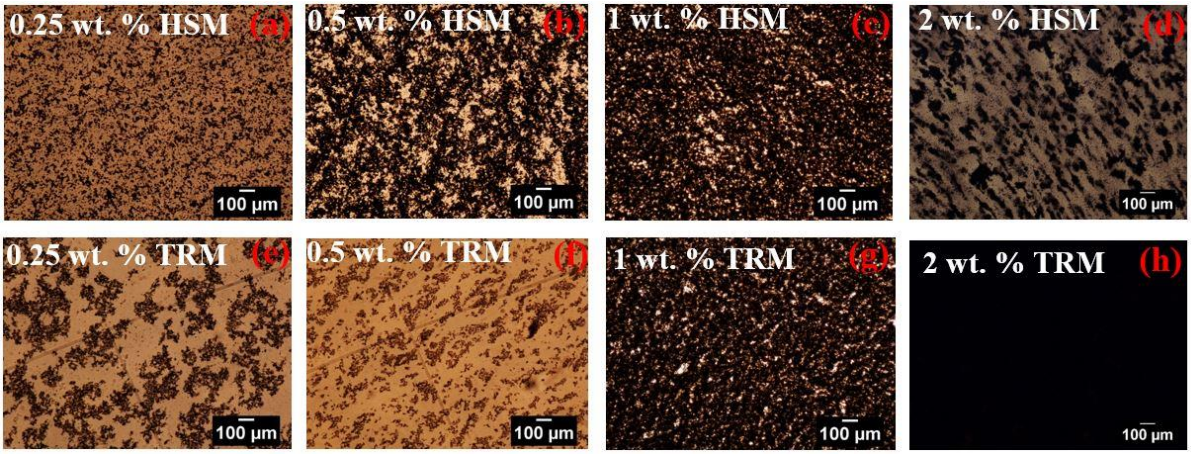


Figure 5. 7. Optical images of 0.25 wt.%, 0.5 wt. %, 1 wt. % and 2 wt. % FLG dispersed in epoxy matrix before curing using HSM (a), (b), (c) (d) and TRM (e), (f), (g) and (h) (scale bar-100 µm).

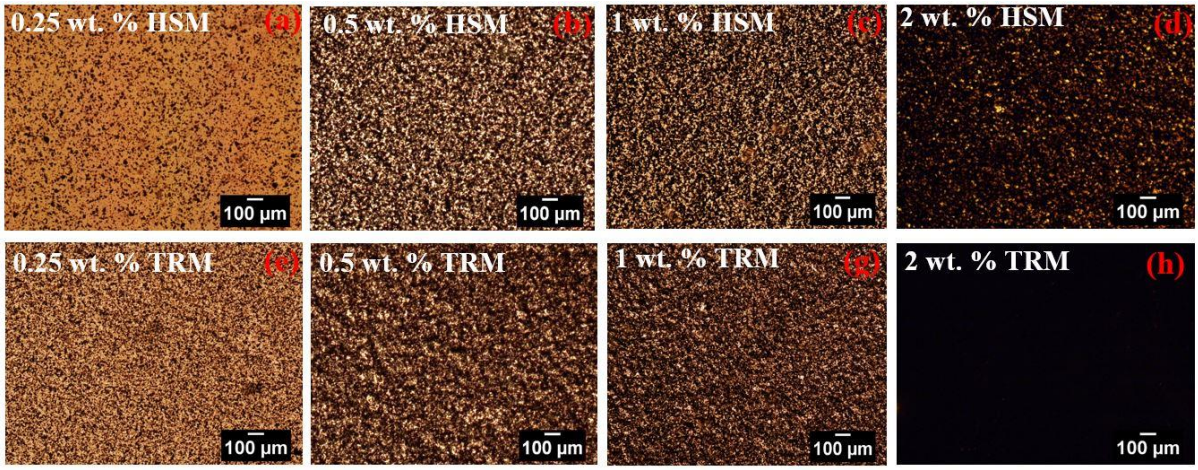


Figure 5. 8. Optical images of 0.25 wt. %, 0.5 wt. %, 1 wt. % and 2 wt. % FLG dispersed in epoxy matrix after curing using HSM (a), (b), (c) (d) and TRM (e), (f), (g) and (h) (scale bar-100 µm).

Comparing with FLG (Figure 5.7), a better dispersed nanofiller was carried with FLG-COOH, especially at the range 0.25-0.5 wt. %. This is not clear in the cured stage (Figure 5.8 and 5.10). For this reason, SEM (Section 5.3.4) are used to clarify the dispersion state in the cured stage. TRM provides a better dispersion up to 1 wt. % in both uncured and cured states (Figure 5.9 and 5.10). After its use, a network of FLG-COOH chains was created, reaching a very well dispersed material at 1 wt. % (Figure 5.9 (g) and 5.10 (g)). When the concentration reaches at 2 wt. %, a very poor dispersion state was noticed in the uncured stage (Figure 5.9 (d)-(h)). Here, it is important to highlight that the material used for 2 wt. % FLG and FLG-COOH in the uncured stage had a different batch code with the previous material, which may explain the

differences on the dispersion state. If the different batch code is a material with slightly different structural characteristics, it is possible to provide another behaviour on the dispersion degree into the polymer matrix.

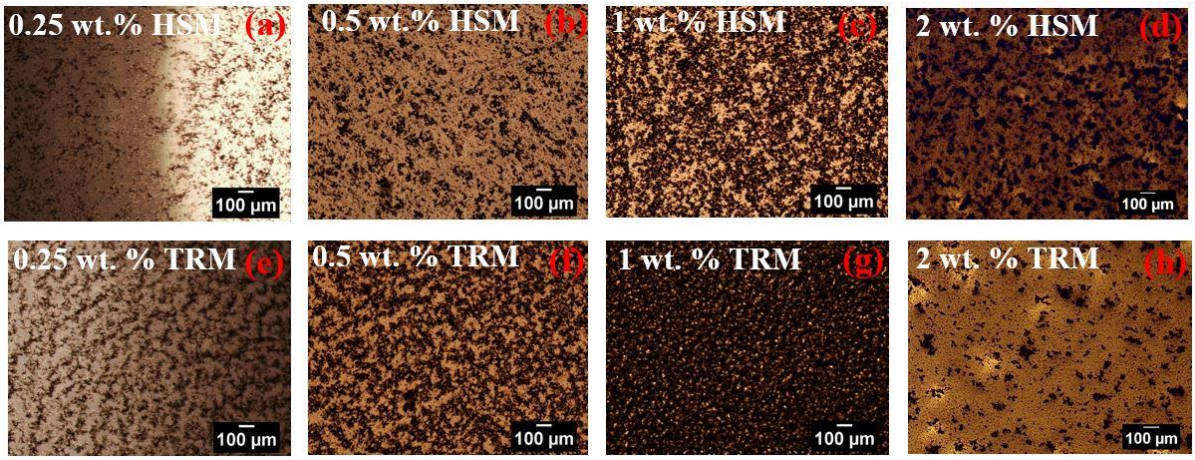


Figure 5. 9. Optical images of 0.25 wt., 0.5 wt., 1 and 2 wt. % FLG-COOH dispersed in epoxy matrix before curing using HSM (a), (b), (c) (d) and TRM (e), (f), (g) and (h) (scale bar-100 µm).

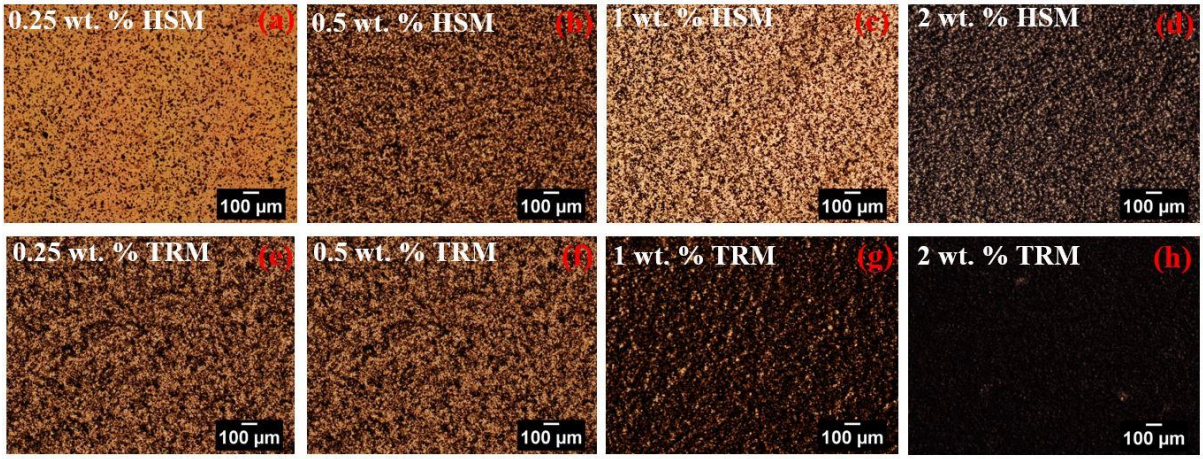


Figure 5. 10. Optical images of 0.25 wt.%, 0.5 wt. %, 1 wt. % and 2 wt. % FLG-COOH dispersed in epoxy matrix after curing using HSM (a), (b), (c) (d) and TRM (e), (f), (g) and (h) (scale bar-100 µm).

The effectiveness of TRM was confirmed with the dispersion of rGO in uncured and cured states. A large amount of agglomeration was present after HSM (Figure 5.11 and 5.12 (a) and (b)) which have been broken by the TRM (Figure 5.11 and 5.12 (c) and (d)). Small areas with agglomerations of rGO were observed in the cured stage (marked by red circles). Overall, it has been proved that TRM can be used in order to provide a high degree of dispersion for a range of graphene nanomaterials even at high filler loadings. These results are in a good

agreement with the literature (Chatterjee, Wang et al. 2012, Prolongo, Jimenez-Suarez et al. 2013, Li, Zhang et al. 2016).

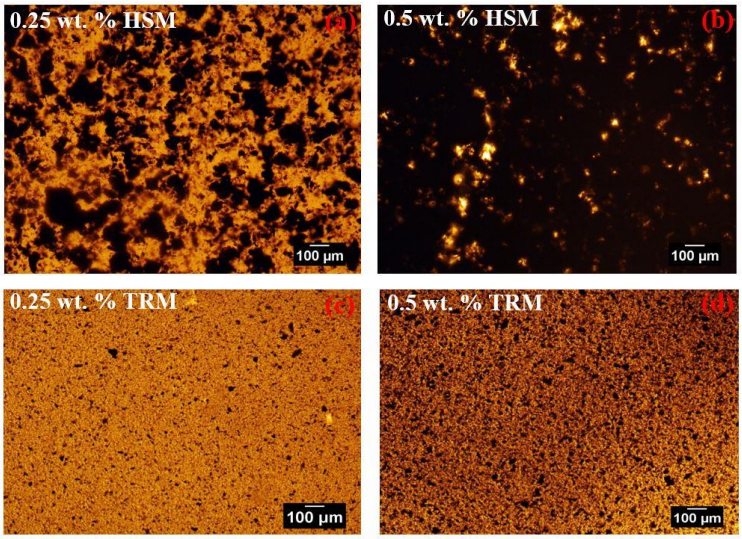


Figure 5. 11. Optical images of 0.25 wt. %, 0.5 wt.% rGO dispersed in epoxy matrix before curing using HSM (a), (b) and TRM (c), (d) (scale bar-100 µm).

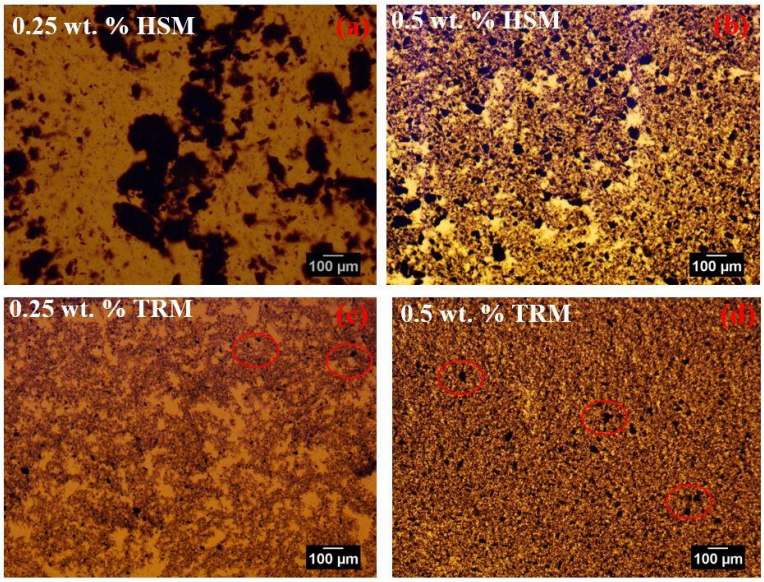


Figure 5. 12. Optical images of 0.25 wt. %, 0.5 wt. % rGO dispersed in epoxy matrix after curing using HSM (a), (b) and TRM (c), (d) (scale bar-100 µm). Small areas with agglomerations of rGO were observed in the cured stage (marked by red circles).

### 5.3.2. Optical Microscope of graphene-DGEBA system

The dispersion state of 1 wt. % FLG and FLG-COOH as well as 0.25 wt. % and 0.5 wt. % rGO mixed by HSM and TRM in the cured DGEBA epoxy system was studied using two different reagents, CHA and IPD, as shown in Figure 5.13 and 5.14 and 5.15, respectively. The

microstructure of these systems was studied only in the cured stage. Similar with the previous data, TRM provides a better dispersion state for all the materials. No differences were found on the dispersion state at two different cross-linking levels (Ξ=0 when only CHA used for the curing and Ξ=1 when only IPD used for curing).

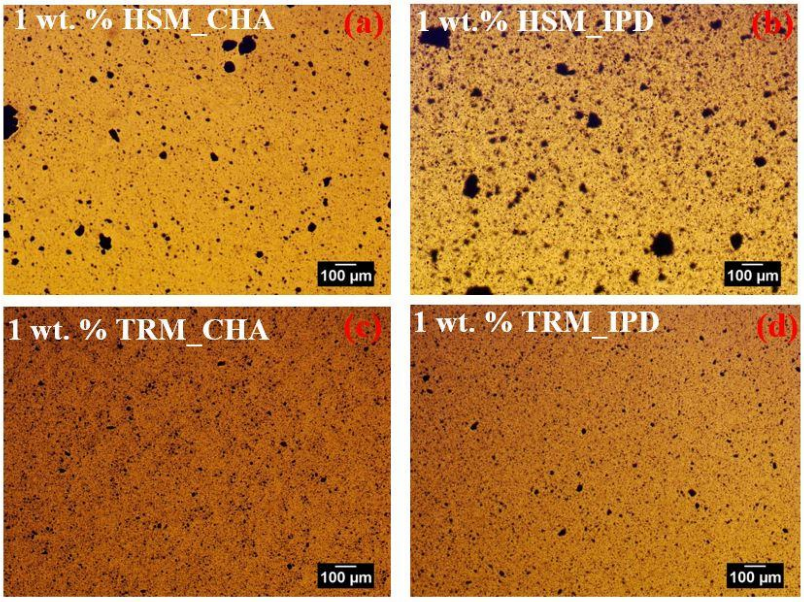


Figure 5. 13. Optical images of 1wt. % FLG dispersed by HSM and TRM in DGEBA after curing with CHA (a) and (c) and IPD (b) and (d) (scale bar-100 µm).

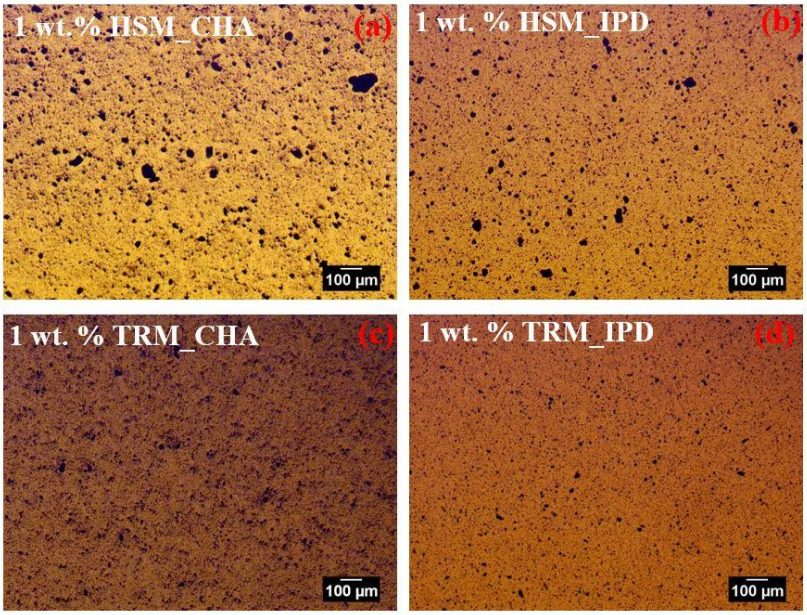


Figure 5. 14. Optical images of 1 wt. % FLG-COOH dispersed by HSM and TRM in DGEBA after curing with CHA (a) and (c) and IPD (b) and (d) (scale bar-100 µm).

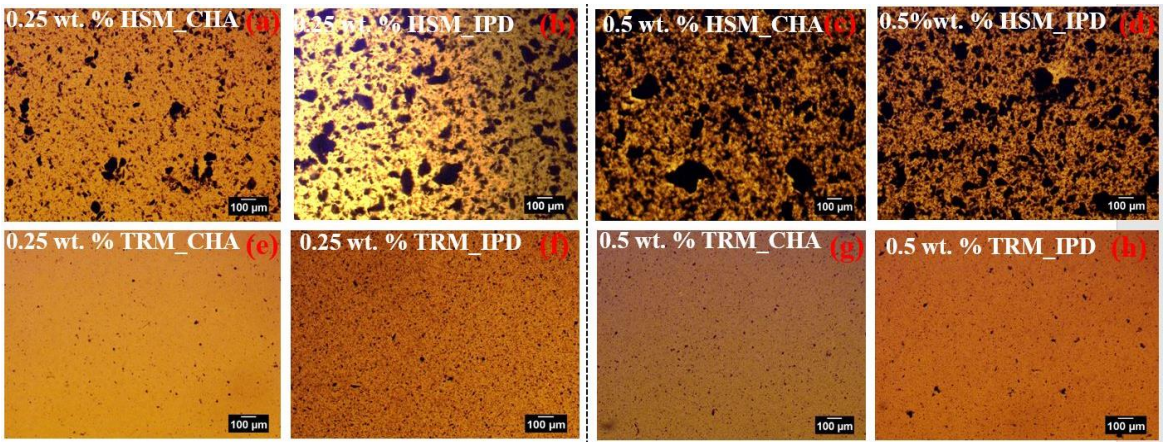


Figure 5. 15. Optical images of 0.25 wt. % and 0.5 wt. % and 1 wt. % of rGO dispersed by HSM and TRM in DGEBA after curing with CHA (a), (e), (c) and (g) and IPD (b), (f), (d) and (h) (scale bar- 100 µm).

### 5.3.3. Steady Shear Rheology

Shear steady rheology has been used in order to evaluate analytically the dispersion and the interconnection of graphene nanofillers in epoxy-based systems. The microstructure behaviour of GNPs, FLG, GNPs-COOH, FLG-COOH and rGO into the infusion epoxy matrix was studied using shear steady rheology. The power law model is employed to correlate the shear stress and the shear rate for the five different materials, by the equation (5.1) (Hatami and Ganji 2013):

$$\sigma = K\, x\, \gamma^{n} \qquad (5.1)$$

where σ is shear stress (Pa), K is flow consistency index (Pa.s$^{n}$), γ is shear rate (s$^{-1}$) and the n is flow behaviour index. For a Newtonian fluid, n=1 whereas for a pseudoplastic fluid, n<1 (George and Qureshi 2013). The fitting was performed using the Excel 'Solver' tool and the results are included in Figure 5.16. For pure epoxy resin and its suspensions, the n value is almost equal to 1, which indicates a Newtonian behaviour. Lower values of n were observed at 0.97, 0.91, 0.95, 0.96 and 0.83 for 4 wt. % GNPs/ 4 wt. % GNPs-COOH, 1 wt. % FLG, 1 wt. % FLG-COOH, 2 wt. % FLG-COOH and 0.5 wt. % rGO mixed by TRM, respectively, indicating a more like pseudoplastic behaviour of these nanofillers.

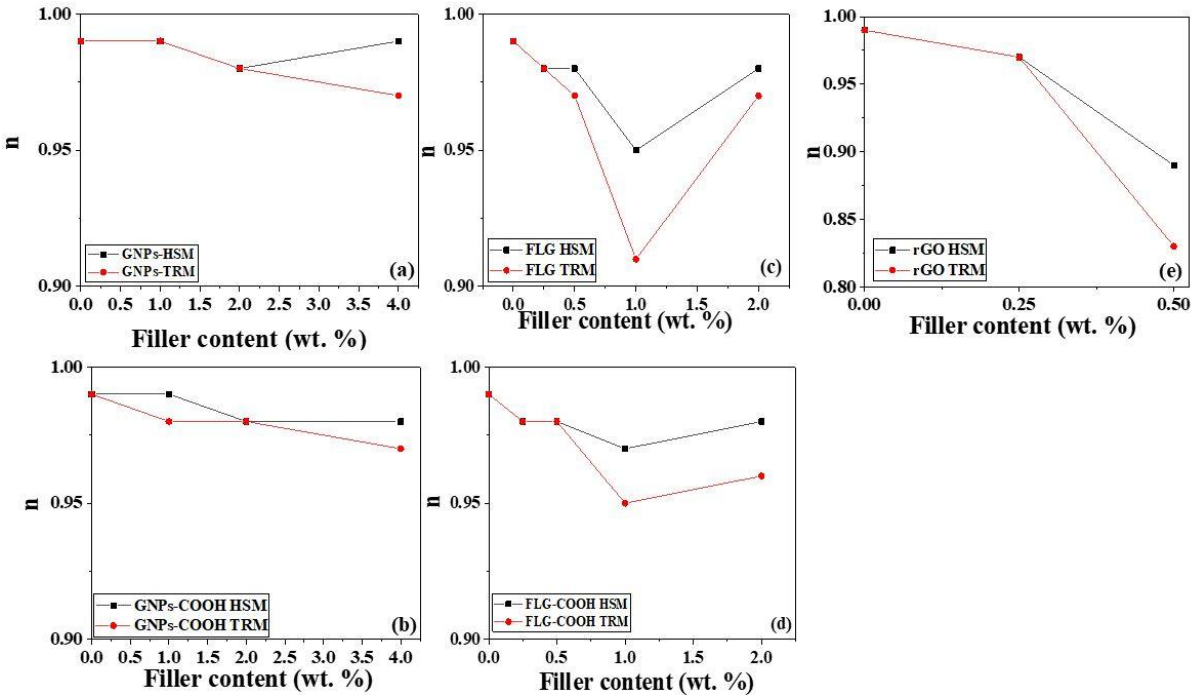


Figure 5. 16. Flow behaviour index n of GNPs (a), GNPs-COOH (b), FLG (c), FLG-COOH (d) and rGO (e) /epoxy suspensions mixed by HSM and TRM as a function of filler loading.

Figure 5.17 represents the steady-state shear flow curves of GNPs and GNPs-COOH mixed by HSM and TRM, which shows how the graphene flakes dispersed in a liquid medium can orient and align under shear. The results of the rheological analysis were presented, in terms of shear viscosity ((a) to (c)) and stress ((b) to (d)) as a function of shear rate. Both of composites show a Newtonian behaviour up to the concentration of 2 wt.% with linear shear stress profile and constant viscosity profile as a function of the applied shear rate. As mentioned in Literature review (Section 2.10), the most influential factor in dispersion is the matrix viscosity; it is a cause effect of the dispersion which becomes high when good dispersion is achieved. Considering the error bars, no significant difference on the viscosity was observed up to 2 wt. % of GNPs and GNPs-COOH by the application of TRM. This effect of TRM at low concentrations (1 wt. % and 2 wt.% of GNPs and GNPs-COOH/epoxy suspensions) were also observed by the optical microscope images (Figure 5.3 & 5.5 (d)-(e)). The liquid to solid-like behaviour which is attributed to the rheological percolation was observed at 4 wt. % for both materials. Increasing the filler loading at 4% wt., the phenomenon of shear thinning was observed for the low rates (Vallés 2017). At low shear rates, after the use of TRM, the viscosity is increased suggesting a graphene network has been formed. These results are in a good agreement with the optical micrographs (Figure 5.3 (f) and Figure 5.5 (f)) that show a well-connected microstructure network for 4% wt. GNPs and GNPs-COOH/epoxy composites

mixed by TRM. By contrast, when the shear rate is increased the graphene particles tend to reorganise and align with the flow. As a result the free space is increased, resulting in a rapid drop in the viscosity which reaches the initial level of epoxy suspensions that not showing shear thinning effect (Del Giudice and Shen 2017).

Regardless the plasma treatment effect, the GNPs-epoxy solutions gave a higher viscosity (1.4 Pa*s) compared with the plasma-treated GNPs-COOH-epoxy solutions (1.04 Pa*s) at the same low shear rate (below 1 1/s). The viscosities and rheological percolation thresholds in graphene-polymer systems are known to be strongly dependent on the interactions between the graphene and polymer as a consequence of different levels of functionalization, and the dispersion of the flakes in the matrix(Vallés, Young et al. 2014). Hence, our results indicate that a better dispersion quality may be occurred with the addition of 4 wt. % GNPs in the epoxy matrix, resulting in higher viscosity.

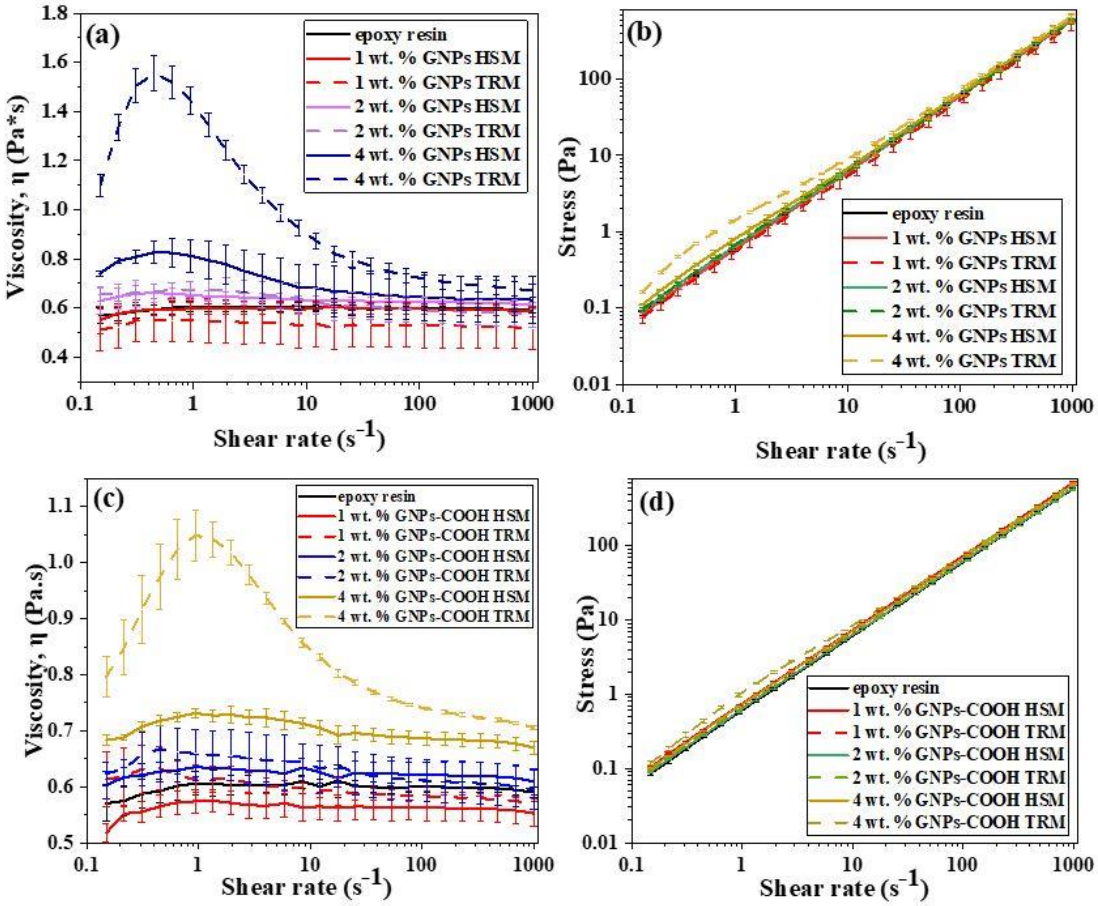


Figure 5. 17. Steady shear curves (shear viscosity and stress as a function of shear rate) of GNPs ((a)-(b)) and GNPs-COOH ((c) – (d)) dispersions into the epoxy resin at different concentrations.

Similar rheological behaviour was observed in Figure 5.18 (a) - (d) for the FLG and FLG-COOH epoxy suspensions, with the viscosity to be stable up to 0.5 wt. %. This again confirms the optical results that showed a lower dispersion state at low concentrations after using TRM (Figure 5.7 & 5.9 (e)-(f)). By increasing the concentration at 1 wt. %, shear thinning behaviour was observed by TRM, suggesting the existence of a graphene network at rest and low shear rates which breaks up into the isolated particles at higher shear rates. Here, the rheological percolation of FLG and FLG-COOH is much lower due to their high specific surface area. Moreover, at a low shear rate region (below 1 $s^{-1}$), the values of viscosity of FLG and FLG-COOH were found 6.26 Pa.s and 2.15 Pa.s for the same filler loading (1 wt. %), respectively. This showed that the FLG increases the viscosity significantly for the same filler loading, comparing with plasma-treated FLG-COOH. The addition of the plasma-treated materials did not raise the viscosity of the system as much as the untreated nanofillers. This behaviour has been explained by Vallès et al (2016) that the lower content in oxygen at graphene surface provides less electrostatic forces between the flakes and tended to show good dispersion up to high loadings.

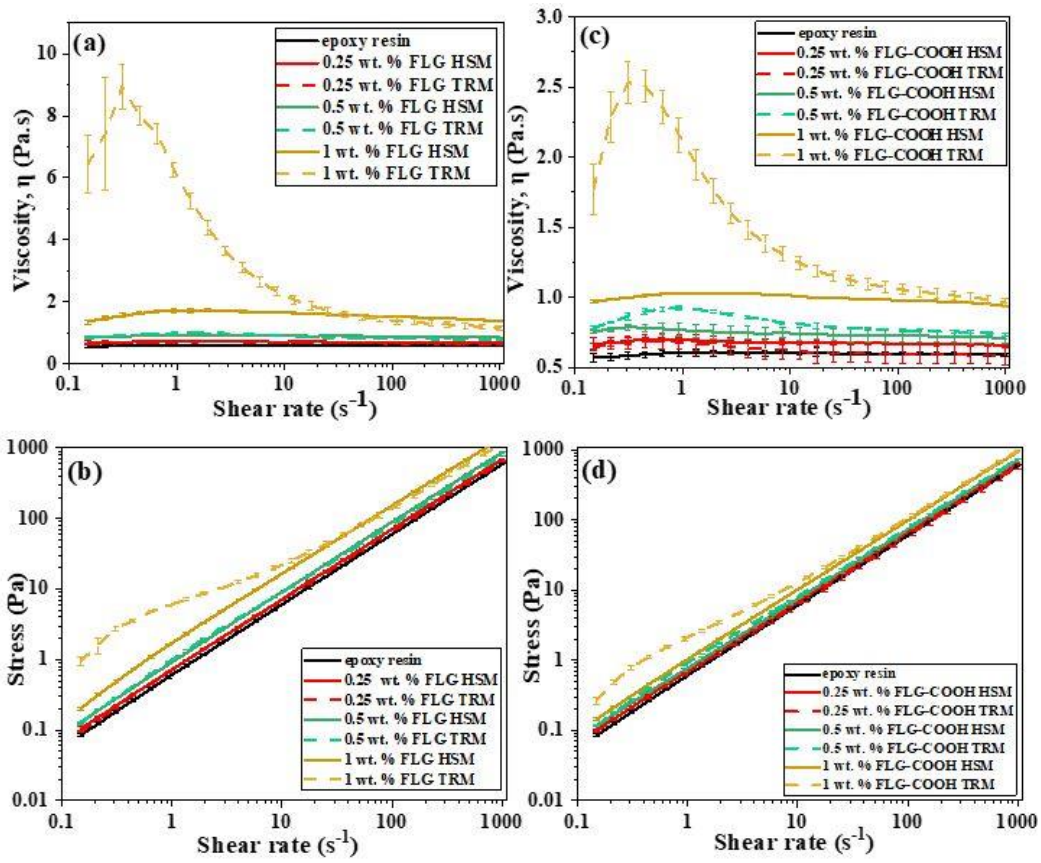


Figure 5. 18. Steady shear curves (shear viscosity and stress as a function of shear rate) of FLG ((a)-(b)) and FLG-COOH ((c) - (d)) dispersions in epoxy resin at different concentrations.

Figure 5.19 represents the steady-state shear flow curves for rGO/epoxy suspension in terms of shear viscosity (Figure 5.19 (a)) and stress (Figure 5.19 (b)) as a function of shear rate. Due to the higher aspect ratio of rGO (planar size: 40 μm), the viscosity is dramatically increased with only 0.5 wt.% rGO mixed by TRM, reaching 11.35 Pa.s at low shear rates (below 1 $s^{-1}$).

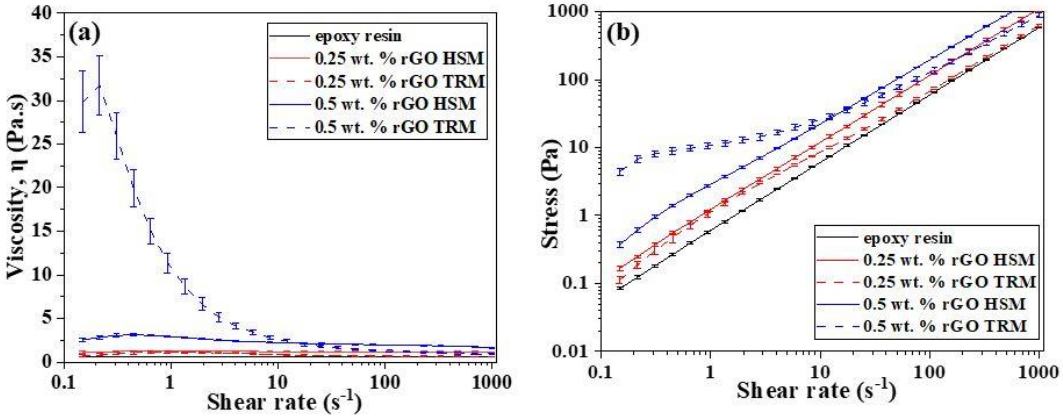


Figure 5. 19. Steady shear curves (shear viscosity and stress as a function of shear rate) of rGO ((a)-(b)) dispersions into the epoxy resin at different concentrations.

In order to investigate the exfoliation effect of processing via TRM, an integrated model was used that incorporates the physical parameters of a TRM system, the fluid dynamics of the suspension and the internal resistance to shear of the graphene nanofillers, as proposed by Palmese et al (Throckmorton and Palmese 2015). Assuming static, isobaric, laminar flow between parallel plates, the fluids shear stresses (τ) of a TRM can be approximated as a function of viscosity (μ), roller surface velocities ($u_1$ and $u_2$) and nip width (L) using the standard equation (5.2) for shear stress under Couette flow:

$$\tau = \frac{\mu(u_2 - u_1)}{L} \qquad (5.2)$$

where L=5 μm (the gap size between the center roll ($N_2$) and apron roll ($N_1$), as described in Figure 5.1. The three rollers rotate at increasing speeds: 50,150,450 rpm with surface velocities $u_2$=1932.5 mm/s and $u_1$=628 mm/s ($u_r$=r*ω with the diameter of roller r=40 mm and angular frequency $\omega = \frac{2\pi}{T}$, T is the period (measured in seconds)). For the calculations, the viscosity values (μ) at 0.93 $s^{-1}$ strain were used by the shear rheological data. The viscosities are taken at a low shear rate, which is lower than the relative one at TRM. As the epoxy liquids behave as Newtonian, the viscosity will be linearly correlated to the local shear rate. On the experimental

setup used for this experiment, roller velocities are fixed. Thus, the gap is the primary experimental control over the shear experienced by a graphite flake within the mill. On the basis of equation (5.2), when the viscosity is increased, high shear forces will be produced. Therefore, sufficient highly shear forces will be present when the rheological percolation is reached. For the highest filler loadings, the liquid shear stresses τ were calculated: 0.377 MPa (4 wt. % GNPs), 0.271 MPa (4 wt. % GNPs-COOH), 1.63 MPa (1 wt. % FLG), 0.56 MPa (1 wt. % FLG-COOH) and 2.97 MPa (0.5 wt. % rGO). These values of shear stress can be compared with literature values of graphite interlayer shear stresses (ISS) in order to identify the existence of the exfoliation or the exfoliation level. A wide range of graphite ISS values has been reported starting from 0.25 MPa (Soule and Nezbeda 1968) to 140 MPa (Liu, Zhang et al. 2012). The lower values represent the shear required to induce sliding between randomly oriented layers, whereas a higher number is required to induce sliding motion between pristine, AB-stacked layers. The application of the experimental shear forces is on the range of the reported ISS values, which supports the process of the partial exfoliation, giving graphene with a random rotational stacking. Below the rheological percolation (η=0.65 Pa.s), the shear forces (τ=~0.17 MPa) are not enough to produce any exfoliation effect.

### 5.3.4. Scanning Electron Microscopy

The roughness of the fracture surface of a specimen provides valuable information about the behaviour (i.e., brittle or ductile) of the material and the crack deviation mechanism (Ahmadi-Moghadam, Sharafimasooleh et al. 2015). When stiff graphene nanoparticles introduced to an epoxy matrix, the propagation of cracks may inhibit and thus increase the energy required for fracture. The cryo-fractured surface of pure epoxy resin was analysed by Scanning Electron Microscopy (SEM). Figure 5.20 (a) and (b) show the crack lines at low magnification (x129) and the relatively flat surface at high magnification (x10000). These lines indicate the crack propagation direction from top to bottom (Chandrasekaran, Sato et al. 2014) whereas the smooth and clean fracture surface of resin is corresponded to its brittle failure (Tao, Sun et al. 2020). By the introduction of GNPs and GNPs-COOH to the epoxy matrix, the fracture surfaces of the samples exhibit relatively rough with some river-like structures, as shown in Figure 5.20 at magnification of x5000. The distribution of 2 wt. % GNPs (Figure 5.21) and GNPs-COOH (Figure 5.22) mixed by HSM and TRM were studied here in order to evaluate the degree of the dispersion prepared by two different mixing methods and the interfacial interaction using the plasma treatment process.

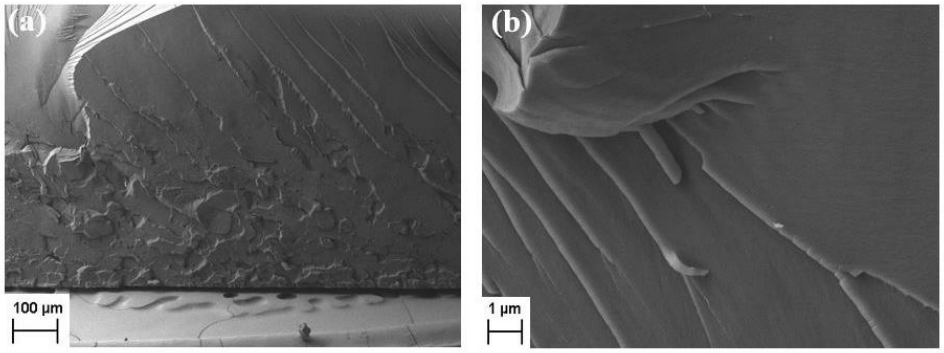


Figure 5. 20. SEM images of the pure epoxy resin at low (a) and high (b) magnification.

Individual (marked by red arrows) or agglomerated flakes (marked by yellow arrows) were observed for both of GNPs and GNPs-COOH which were pulled out from the epoxy resulting in poor interfacial adhesion and thereby making those sites susceptible to stress concentration points which promote crack propagation (Domun, Hadavinia et al. 2017). This evidence for a poor interfacial interaction can be an implication on a poor stress transfer efficiency that will affect the mechanical reinforcement. In the case of GNPs, no significant differences at surface roughness can be observed by the low-magnification SEM images (x800). Following the results by optical microscope images (Figure 5.4 (b) and (e)), although there is a more interconnecting network by the use of TRM, there are still large agglomerations of GNPs due to the poor compatibility between the GNPs (oxygen content: >3% at.) and the epoxy system. Relating to GNPs-COOH, there are still some agglomerations (inset of Figure 5.21 (b), x30000), providing the difficulty to overcome the high adhesive van der Waals forces despite the higher shear force applied by the use of TRM. However, there are also evidence of GNPs-COOH rich regions (Figure 5.22 (c) and (d)) that have been covered within epoxy resin, a feature which has not been observed in GNPs.

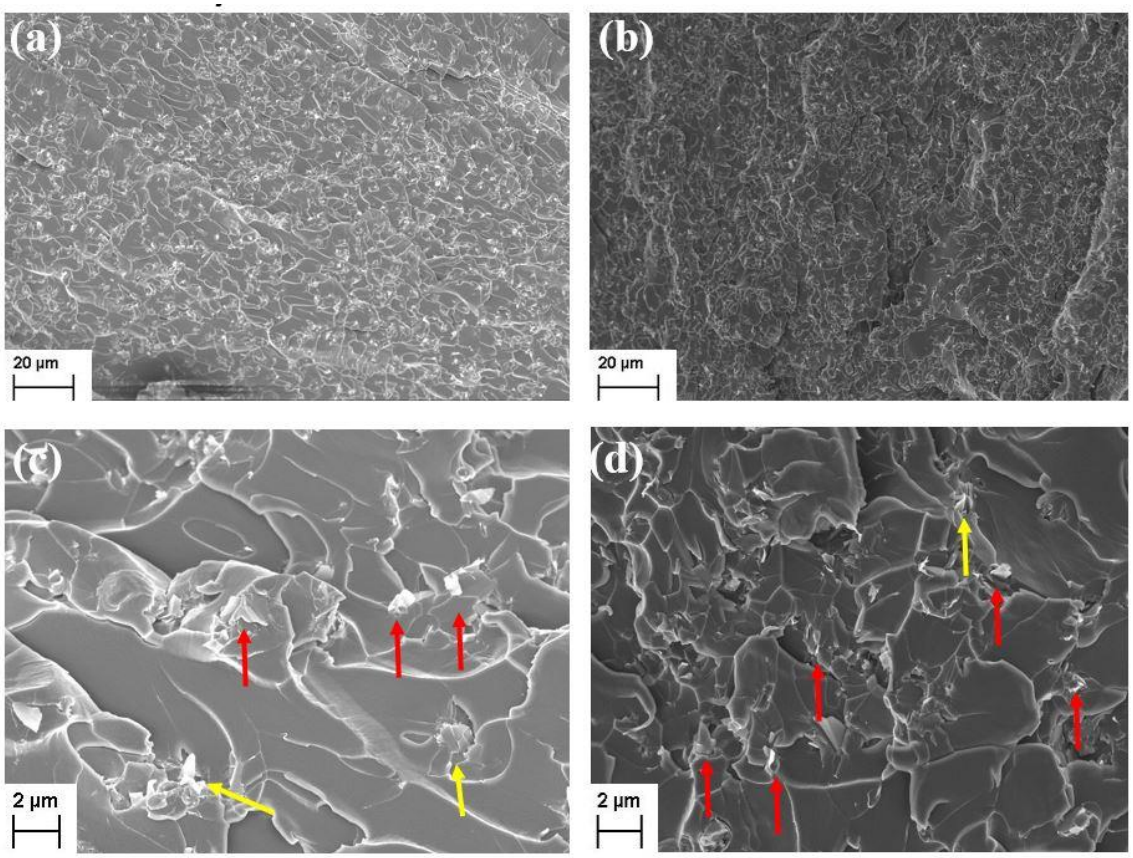


Figure 5. 21. SEM images of fracture surface of 2 wt. % GNPs/epoxy composites mixed by HSM (a), (c) and TRM (b), (d). Individual (marked by red arrows) or agglomerated flakes (marked by yellow arrows) were observed.

In Figure 5.22. (c) at x20000 and (d) at x30000, red lines show randomly dispersed GNPs-COOH that have been covered by the epoxy matrix, providing a better dispersion level after TRM. It is clear that the plasma process gives a better dispersed material, as it been proved by the optical microscope images for both of mixing methods (Figure 5.4 and 5.5. (b) and (e)).

The fracture surface of FLG and FLG-COOH/epoxy composites mixed by HSM and TRM was also explored by SEM (Figure 5.23 and 5.24, respectively). Comparing the two mixing methods, a higher surface roughness was presented at TRM-mixed samples than those from the HSM-mixed samples that could be arisen to a better distribution (Chandrasekaran, Seidel et al. 2013). Yellow arrows have been used in order to highlight the wrinkle surface of the agglomerated few layer graphene sheets. A more densely packed agglomerates were observed in the case of FLG, as shown in Figure 5.23 (c). Similar with the GNPs, this indicates a relatively week interfacial bonding between the nanofillers (FLG) and the epoxy resin. By introducing FLG-COOH into the epoxy matrix, some agglomerations were observed, but with

a careful observation (Figure 5.24 (c) and (d)), it can be seen that there is an improved interface adhesion between the FLG-COOH and the epoxy resin (marked by red arrows) in comparison with the FLG sheets that pull out from the epoxy matrix. This means that the plasma process can provide a more uniformly dispersed material that may promote the efficient local stress transfer from the matrix to the flake (Zhao, Chang et al. 2016).

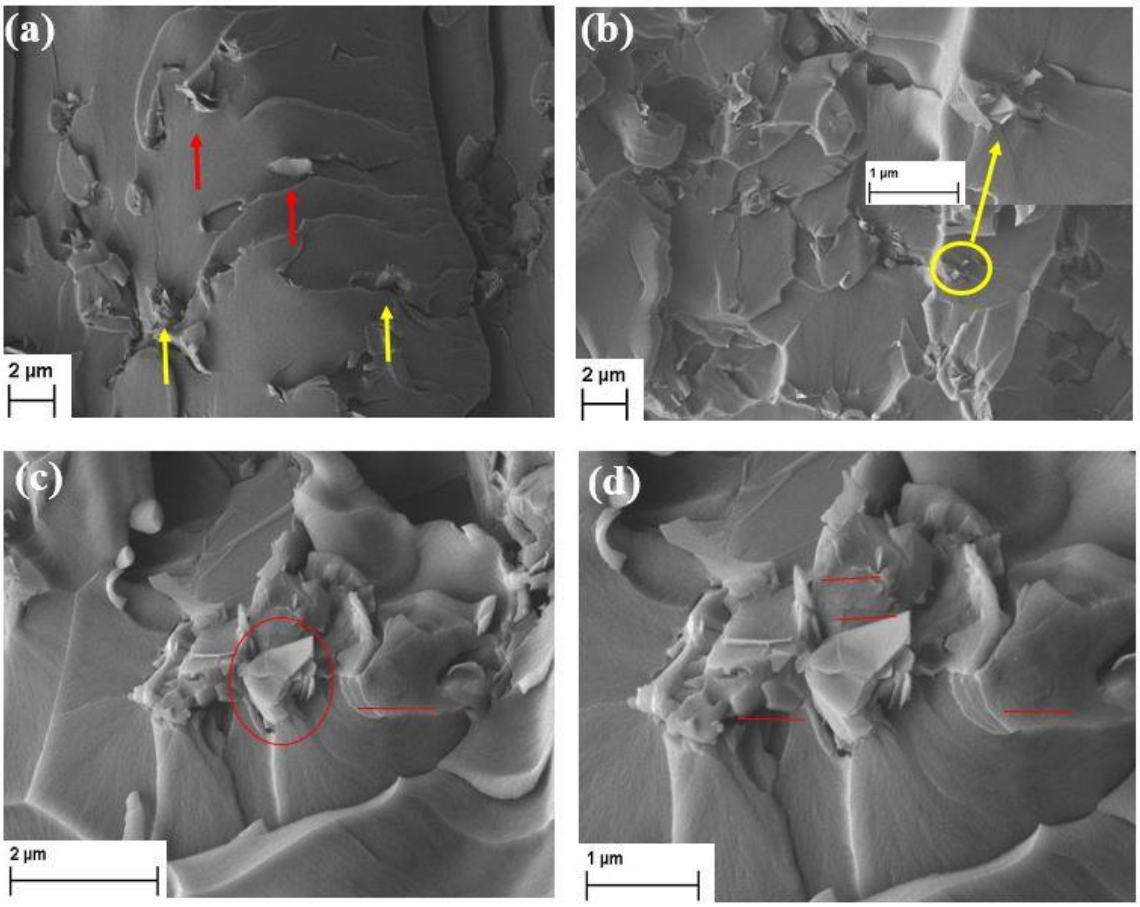


Figure 5. 22. SEM images of fracture surface of 2 wt. % GNPs-COOH/epoxy composites mixed by HSM (a), and TRM (b), (c) and (d). Individual (marked by red arrows) or agglomerated flakes (marked by yellow arrows) were observed. The red circles show some stack GNPs-COOH and the red lines indicate the presence of the GNPs-COOH that covered by epoxy resin.

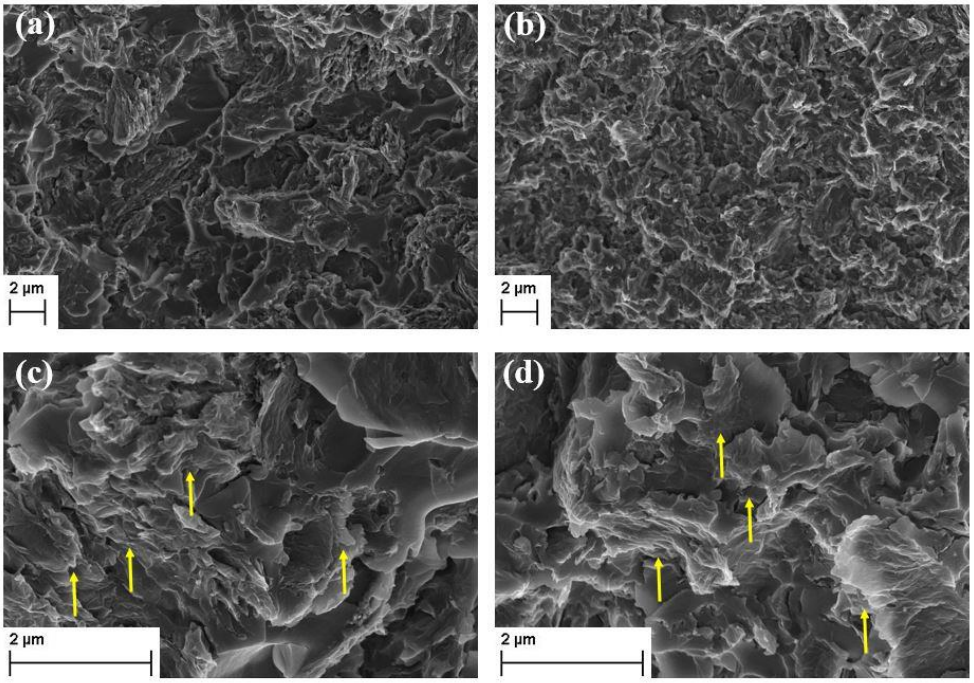


Figure 5. 23. SEM images of fracture surface of 2 wt. % FLG/epoxy composites mixed by HSM (a), (c) and TRM (b) and (d). Yellow arrows have been used in order to highlight the wrinkle surface of the agglomerated few layer graphene sheets.

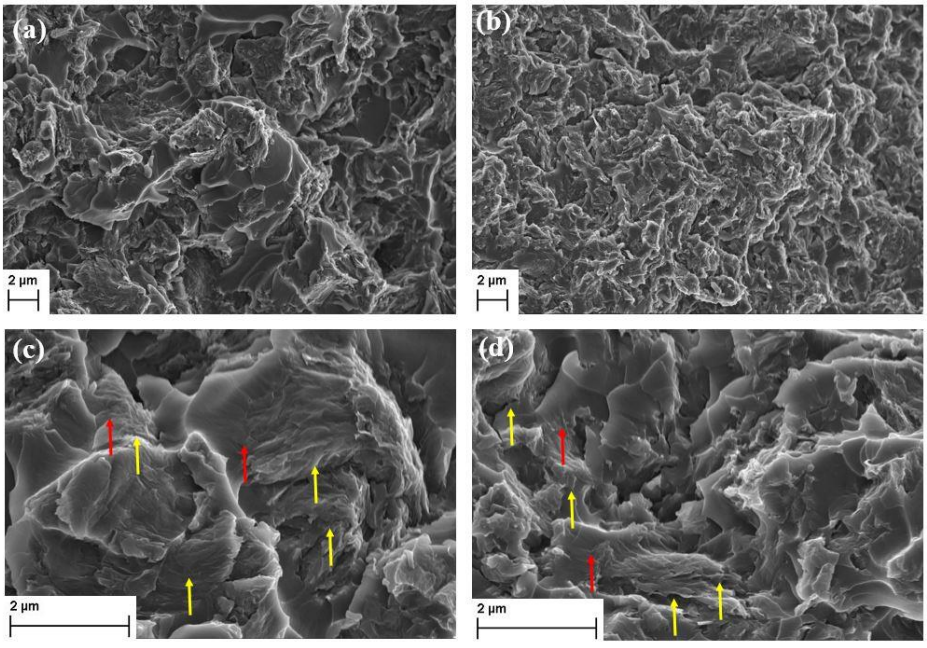


Figure 5. 24. SEM images of fracture surface of 2 wt. % FLG-COOH/epoxy composites mixed by HSM (a), (c) and TRM (b) and (d). There is an improved interface adhesion between the FLG-COOH and the epoxy resin (marked by red arrows) in comparison with the FLG sheets that pull out from the epoxy matrix.

### 5.3.5. Raman Spectroscopy

Raman spectra of pure epoxy and their composites filled with 1 wt. % GNPs (a) and GNPs-COOH (b), 1 wt. % FLG (c) and 1 wt.% FLG-COOH (d) and 0.5 wt.% rGO (e) mixed by HSM and TRM are shown in Figure 5.25. Raman spectra of neat GNPs and GNPs-COOH, FLG and FLG-COOH and rGO are included in Chapter 4. The characteristic Raman bands of the epoxy structure and graphene were detected, indicating that the two components are well-mixed. Raman bands corresponding to epoxide vibration are in the range of 1230 $cm^{-1}$ and 1280 $cm^{-1}$(marked by blue star) and other Raman peaks at 1112 $cm^{-1}$, 1186 $cm^{-1}$ and 1608 $cm^{-1}$ (marked by red stars) assigning to resin backbone vibrations (Vaskova and Křesálek 2011). By adding 1 wt. % of the GNPs and GNPs-COOH (Figure 5.25 (a) and (b)), it can be detected only the G peak (1582 $nm^{-1}$). In the case of 1 wt. % FLG, 1 wt. % FLG-COOH (Figure 5.25 (c) and (d)) and 0.5 wt.% rGO/ composites (Figure 5.25 (e)), the spectra are quite different with the broad G and D bands, and a D band (~1300 $cm^{-1}$) that is of higher intensity than the G band (~1600 $cm^{-1}$). These features with the absence of 2D band for all the materials (2700 $cm^{-1}$) are related to the formation of $sp^3$ carbon bonds by breaking the $sp^2$ carbon network (Malard, Pimenta et al. 2009).

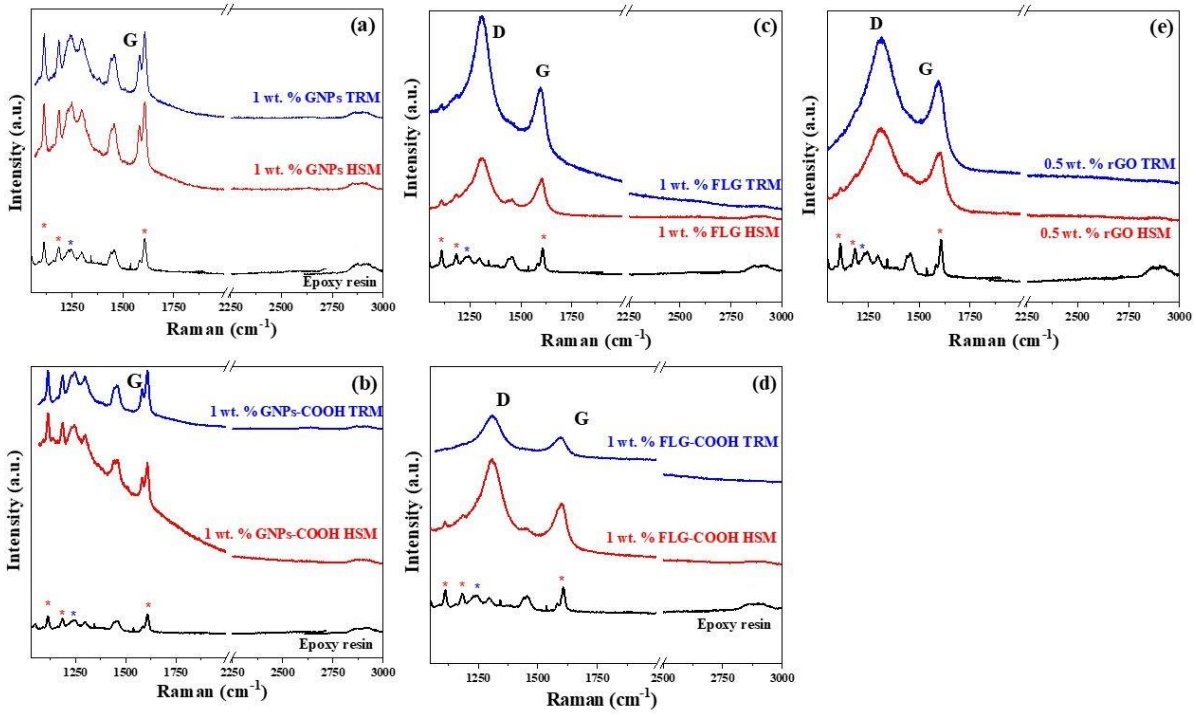


Figure 5. 25. Raman Spectra of 1 wt. % GNPs (a) and 1 wt. % GNPs-COOH (b), 1 wt. % FLG (c) and 1 wt. % FLG-COOH (d) and 0.5 wt. % rGO/epoxy composites (e) mixed by HSM and TRM methods (laser excitation: 785 nm).

### 5.3.6. Thermogravimetric analysis (TGA)

The thermal stability of the cured epoxy resin and its nanocomposites was evaluated by means of TGA. Figure 5.26 and show the TGA plots of GNPs (a), GNPs-COOH (b), FLG (c), FLG-COOH (d) and rGO (e) /epoxy composites under nitrogen atmosphere. More than three measurements were tested at TGA in samples that prepared for DMA analysis. Table 5.2 lists the main indicators including initial decomposition temperature (IDT), temperature of the maximum rate of degradation ($T_{max}$) and residual weight percentage at 450 $^{o}$C. IDT corresponded to the temperature where a 5% mass loss was accumulated ($T_{5\%}$). $T_{max}$ represented the stability at main mass loss stage which was determined at the peak of the differential thermogravimetric curves (included on the Appendix-Section 1). All the TGA curves of graphene based epoxy composites displayed only one main weight loss which takes place at around 300 $^{o}$C and 500 $^{o}$C and it is attributed to the degradation of the epoxy network (Grassie, Guy et al. 1986). At the mainstage of decomposition, sharp mass losses were observed in the epoxy and incorporated systems, with $T_{max}$ at about 325 °C. The nanofillers hardly affected the thermal behaviour at this stage. As the temperature was further increased, the samples experienced a steady mass loss stage in the range of 450 °C–800 °C. A slightly higher residue was obtained for most of the graphene/epoxy composites at 450 $^{o}$C comparing with the pure epoxy, as graphene is more stable at high temperatures, retaining its original mass in the char residue. Thus, the higher residues are attributed to the physical changes in graphene/epoxy composites, rather than chemical reaction changes in the epoxy resin (Zhang, Wang et al. 2018).

The thermal stability can be explained in terms of the nanofiller dispersion and interfacial interaction with the epoxy matrix. When an improved dispersion and strong interfacial interactions are achieved between the nanofiller and the polymer matrix, the mobility of the local matrix around the nanofillers is reduced, offering a better barrier effect which retards the volatilization of polymer decomposition products (Wan, Gong et al. 2014). Moreover, the dependence of the nanofiller loading was examined for the thermal stability of the epoxy composites.

Following the optical and SEM results, it has been proved above that the plasma-process provides a better dispersion of GNPs-COOH and FLG-COOH when mixed into the epoxy resin by HSM and TRM method. By introducing 1 wt. % GNPs-COOH, the IDT was increased at 270 $^{o}$C whereas a significant drop (250 $^{o}$C) was noticed with the addition of 1 wt.% GNPs. Increasing the concentration of GNPs at 4 wt. %, the IDT reaches the initial value of the pure

epoxy, which could be attributed to the tortuous path effect which is created by the formation of the graphene network (Huang, Lu et al. 2012). However, the addition of 4 wt. % of GNPs-COOH leads in a reduction of $10^{o}$ in comparison with the IDT of 1 wt.% GNPs-COOH (270 $^{o}$C). Although, the dispersion level is better for the GNPs-COOH/epoxy composites comparing the GNPs/epoxy composites, the drastic drop can be associated with the surface properties of the nanofiller. Specifically, this can be explained by the strong catalytic effect of GNPs-COOH due to the higher oxygen content. Similar results have been reported in the past by the work of Cheng et al (2011). The authors showed that the compatibility of GO with epoxy and dispersion were significantly improved through the hydroxyl groups on the surface of GO; however, the addition of GO decreases the IDT of epoxy, which indicating that the GO act as catalysts and facilitate the curing reaction and the catalytic effect increases with the GO contents. Similarly, Zhang et al (2018) reported that the carboxylic groups on the surface of GO can lead to decreased thermal stability of polymer nanocomposites, following an acid-catalysed degradation mechanism.

Interestingly, the TRM-mixed composites reinforced by GNPs and GNPs-COOH showed a decreased IDT (lower than the pure epoxy resin) comparing with the HSM-mixed composites, an effect which is more dominant at high filler loadings. By providing a better dispersion with TRM, the surface area of the nanomaterials was increased, which leads to more negative defects with the epoxy matrix. Hence, the cross-linking network orientation is hampered, resulting in the thermal degradation of resin at much lower temperature.

Following the same behaviour as GNPs, the IDT of FLG/epoxy composites decreased significantly for all the composites. A slight increase at ~266 $^{o}$C at higher filler loading (2 wt. %, TRM-mixed) was noticed, which will be attributed to the tortuous path effect through the better dispersion state. The initial decrease in degradation temperature is likely due to the residual oxygen functionalities on the surface of FLG (XPS:0.98% at.) and defects in the polymeric network (Chhetri, Adak et al. 2018). Moreover, the IDT of FLG-COOH/epoxy composites are lower than the pure epoxy resin, but they showed better results in comparison with FLG/epoxy composites, especially when TRM-mixed. In that case, the well dispersed material acts as a good barrier to prevent degradation of the epoxy matrix, resulting in higher degradation temperatures. Similar effect of the concentration filler was found for rGO/epoxy composites, as shown in Table 5.2.

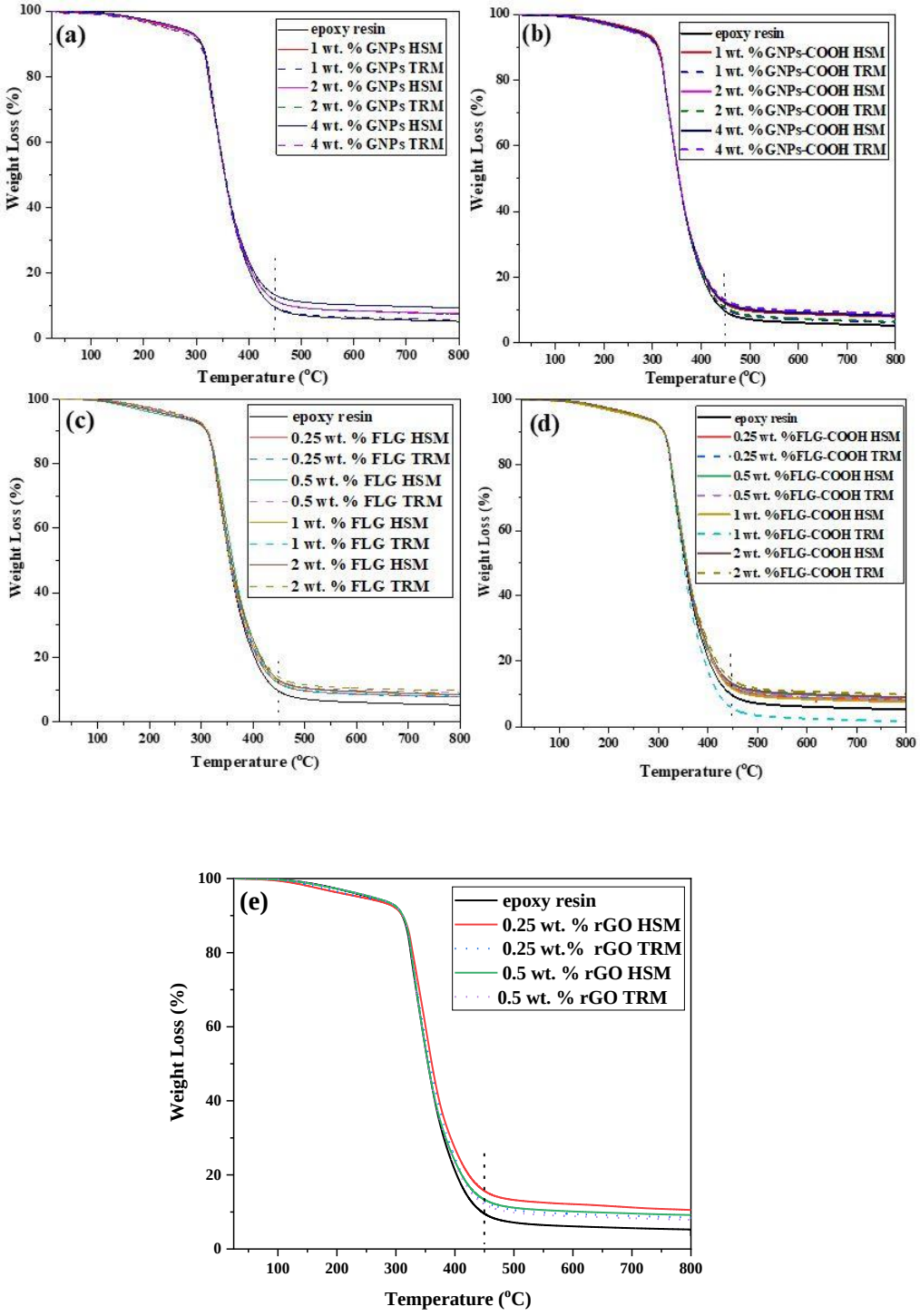


Figure 5. 26. TGA curves of the GNPs (a) and GNPs-COOH (b), FLG (c), FLG-COOH (d) and rGO (e)/epoxy composites.

Table 5. 2. Thermal properties of epoxy and its nanocomposites.

| Sample | IDT ($T_{5\%}$) | $T_{max}$ (ºC) | Residue (%) at 450ºC |
|---|---|---|---|
| **Epoxy resin** | **265.81±1.82** | **324.41±1.46** | **11.14+1.05** |
| **1 wt. % GNPs HSM** | 250.97± 0.205 | 324.71 ±1.35 | 11.70 ±0.145 |
| **1 wt. % GNPs TRM** | 259.67±1.87 | 324.82±0.325 | 9.69±0.095 |
| **2 wt. % GNPs HSM** | 256.74±4.6 | 324.26±0.47 | 11.62±0.62 |
| **2 wt. % GNPs TRM** | 238.54±0.66 | 324.93±0.095 | 11.69±0.37 |
| **4 wt. % GNPs HSM** | 264.96±0.49 | 321.80±0.2 | 13.34±0.7 |
| **4 wt. % GNPs TRM** | 236.96±6.05 | 323.57±0.55 | 11.62±2.025 |
| **1 wt. % GNPs-COOH HSM** | 270.42±2.4 | 324.34±0.46 | 11.94±0.06 |
| **1 wt. % GNPs-COOH TRM** | 259.89±0.37 | 324.60±0.065 | 10.43±2.18 |
| **2 wt. % GNPs-COOH HSM** | 256.4±0.33 | 324.54±0.05 | 12.30±0.09 |
| **2 wt. % GNPs-COOH TRM** | 253.1±4.9 | 324.03±0.69 | 10.72±1.63 |
| **4 wt. % GNPs-COOH HSM** | 260.03±3.85 | 323.58±0.19 | 12.26±1.1 |
| **4 wt. % GNPs-COOH TRM** | 251.8±6.22 | 324.43±0.3 | 12.96±0.72 |
| **0.25 wt. % FLG HSM** | 258.77±3.47 | 325.04±0.095 | 11.91±0.055 |
| **0.25 wt. % FLG TRM** | 245.25±6.27 | 327.6±±0.89 | 11.99±0.38 |
| **0.5 wt. % FLG HSM** | 213.91±0.96 | 329.96±0.74 | 13.05±0.77 |
| **0.5 wt. % FLG TRM** | 255.6±14.4 | 327.32±0.17 | 13.01±0.96 |
| **1 wt. % FLG HSM** | 243.3±0.26 | 326.61±1.085 | 12.62±0.21 |
| **1 wt. % FLG TRM** | 239.69±2.96 | 328.69±0.065 | 13.72±0.045 |
| **2 wt. % FLG HSM** | 233.14±9.9 | 327.03±1.84 | 13.03±0.8 |
| **2 wt. % FLG TRM** | 265.8±6.5 | 324.39±0.55 | 13.98±0.12 |
| **0.25 wt. % FLG-COOH HSM** | 251.35±6.21 | 325.55±1.05 | 12.16±0.03 |
| **0.25 wt. % FLG-COOH TRM** | 260.95±1.85 | 324.45±0.33 | 11.96±0.025 |
| **0.5 wt. % FLG-COOH HSM** | 262.84±6.85 | 328.18±0.65 | 12.35±0.23 |
| **0.5 wt. % FLG-COOH TRM** | 264.94±0.26 | 327.97±1.78 | 11.4±0.33 |
| **1 wt. % FLG-COOH HSM** | 250.97±8.55 | 327.12±0.17 | 11.63±0.77 |
| **1 wt. % FLG-COOH TRM** | 264.01±3.6 | 325.48±0.29 | 5.57±1.06 |
| **2 wt. % FLG-COOH HSM** | 263.55±1.58 | 327.15±0.9 | 12.83±0.07 |
| **2 wt. % FLG-COOH TRM** | 259.58±2.22 | 326.6±1.05 | 14.08±0.28 |
| **0.25 wt. % rGO HSM** | 246.78±6.08 | 330.67±3.14 | 12.88±0.85 |
| **0.25 wt. % rGO TRM** | 244.95±0.065 | 326.47±0.48 | 12.83±0.69 |
| **0.5 wt. % rGO HSM** | 254.2±4.78 | 325.39±0.19 | 12.3±0.4 |
| **0.5 wt. % rGO TRM** | 270.85±3.29 | 325.54±0.7 | 13.065±1.33 |

## 5.4. Curing study

### 5.4.1. DMA study of graphene-infusion epoxy system

As mentioned in Literature review (Section 2.11), the nanofillers can affect the curing reaction of the epoxy systems, resulting in diminished mechanical properties. Here, different manufacturing parameters, such as dispersion state, filler loading, stoichiometric ratio between the hardener and the resin and the cross-linking density have been adjusted in order to establish a better understanding of the curing effect on the mechanical properties of the final nanocomposites. DMA was used to understand how the addition of graphene materials and loading level affect the dynamic mechanical properties of the graphene-reinforced nanocomposites. The elastic and viscous responses of these epoxy nanocomposites are studied in the linear viscoelastic region (LVR) which means under low force conditions that do not destroy the polymer structure (Dunson 2017). The choice of the strain (displacement) control for applying the deforming load to the sample was selected in the range that the dynamic strain and stress show a linear relationship (Menard 2008). For all the composites, strain and stress are linearly related and the displacement of 0.05 mm was selected.

Figure 5.27, 5.28 and 5.29 illustrates the variation of storage modulus and Tg for pure epoxy and its composites reinforced with GNPs, GNPs-COOH, FLG, FLG-COOH and rGO, respectively, as a function of the filler concentration. Higher filler loadings are expected to increase the storage modulus due to the reinforcement of the graphene and confinement of the epoxy chains between the graphene particles (Wang, Drzal et al. 2015). Considering the error bars, there is not a significant mechanical reinforcement by increasing the filler loading. Similar results have been reported in the past (Li, Young et al. 2013, Vallés, Beckert et al. 2016).

As shown in Figure 5.27 (a) and (c), the addition of 1 wt. % GNPs and GNPs-COOH/epoxy composites do not seem to affect the storage modulus of epoxy resin (~5% increase for both mixing methods was achieved). In the case of GNPs, by increasing the concentration of graphite particles to 2 wt. % GNPs, a slight decrease of this property was induced which will be attributed to the poor dispersion that occurs between the nanofillers and the epoxy matrix, as proved by optical microscope images (Figure 5.4 (b) and (e) for 2 wt. % GNPs). By increasing the concentration of GNPs-COOH, an anomalous trend was observed for 2 wt. % GNPs-COOH, but then there was a slight reduced trend in storage modulus for both of mixing methods.

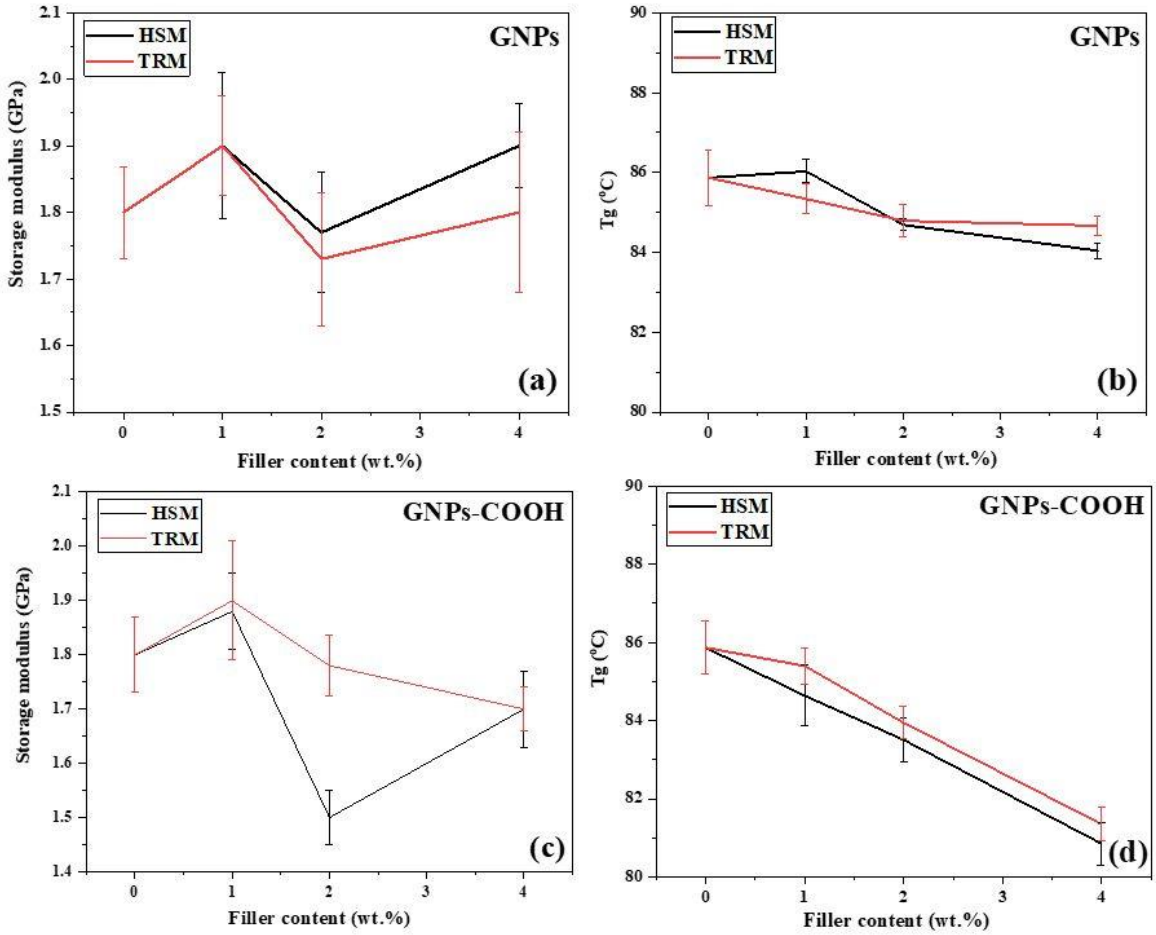


Figure 5. 27. Storage modulus at 30 °C and $T_g$ values for GNPs (a), (b) and GNPs-COOH (c), (d) - epoxy composites, respectively as a function of nanofiller concentration prepared by HSM and TRM mixing methods.

It is clear from Figure 5.27 (b) and (d) that the $T_g$ is reducing with increasing filler loading. This might explain why no further improvements in storage modulus are seen as the filler loading increases, i.e., the additional reinforcement is cancelled out by the reducing polymer properties. This is supported by the greater loss in $T_g$ observed in the plasma functionalised material (Figure 5.27 (d)), which corresponds to slightly lower storage modulus values when compared with the as received material. These results are in a good agreement with the TGA study (as shown in Table 5.2) in which at high filler loadings, there was a drop on the initial decomposition temperature (IDT) of the composites (especially the IDT for TRM-mixed materials). As the $T_g$ has been reduced with the increase of filler concentration, the cross-linking network of the epoxy system is affected, resulting to its thermal degradation at lower temperatures.

Regarding to FLG and FLG-COOH (Figure 5.28), both materials gave an increase in storage modulus of ~7-10% at 1 wt. % with no significant differences at higher nanofiller concentration and with the use of different mixing methods. By the addition of only 0.25 wt. % FLG and FLG-COOH, there was a significant drop of $T_g$ (~5 $^oC$), which shows that the nanomaterials have affected the curing reaction of the epoxy system. By increasing the filler concentration, there was a slight increase on $T_g$ (but still lower than the pure epoxy), which is attributed to the movement restriction of the polymer chains. In the case of FLG, this drop could be attributed to the formation of the agglomerations due to poor interfacial interactions that occur between the FLG and epoxy matrix as the FLG is consisted of a very low oxygen content that detected by XPS (0.98 at. %). Although, it has been showed that the TRM provides a better dispersion state of FLG in the epoxy matrix (Figure 5.8), $T_g$ values are still lower than the pristine epoxy resin. Moreover, a very well dispersed FLG-COOH into the epoxy matrix was achieved, as showed by Optical and SEM results (Figure 5.10 & 5.24, respectively), due to the interfacial interactions that occur after the plasma process and especially after mixing by TRM. This strongly recommends that a high degree of dispersion can be achieved in high levels of concentrations (as proved for 1 wt.% and 2 wt.% of FLG and FLG-COOH), but the crosslinking network can still be diminished.

Lower $T_g$ values were obtained also with rGO (Figure 5.29 (b)), with an increase of storage modulus was achieved (~14% with 0.5 wt.%), as shown in Figure 5.29 (a). The effect of reduced crosslinking density was leaded to the initial drop at IDT (Table 5.2), as supported by the TGA results for the FLG, FLG-COOH and rGO/epoxy composites with the addition of only 0.25 wt. %.

Figure 5.30 represents the changes of peak factor and tan δ $peak_{max}$ (loss factor) as a function of the filler concentration. The FWHM of the loss factor measured by Origin software via Gaussian fitting for the calculation of the peak factor (Γ). The peak factor (Γ) is defined as the full width at half maximum of the tan δ peak divided by its height, and it can be qualitatively used to assess the homogeneity of the epoxy network (Zhou, Pervin et al. 2007). It is known that the changes on the tan $\delta_{max}$ and the FWHM of the loss factor are generally correlated with the cross-linking density of the polymer (Olowojoba et al. 2017). This phenomenon is associated with a wide range of relaxation temperatures in nanocomposites as all the backbones in a polymer matrix do not have the same relaxation temperatures. If all the relaxation temperatures are very similar, then the tanδ peak is very narrow. In the case of graphene-reinforced composites, the fillers limit the mobility of neighbouring polymer chains, changing

the relaxation behaviour on comparison to the chains located far from the nanofiller interface (Surnova et al. 2019). By increasing the nanofillers, the peaks of tanδ (loss factor) become lower and broader in comparison with the pure epoxy resin (higher FWHM and peak factor). Hence, broader is the area under the tanδ peak, greater is the degree of molecular mobility, which translates in a less uniform polymer network (higher heterogeneity).

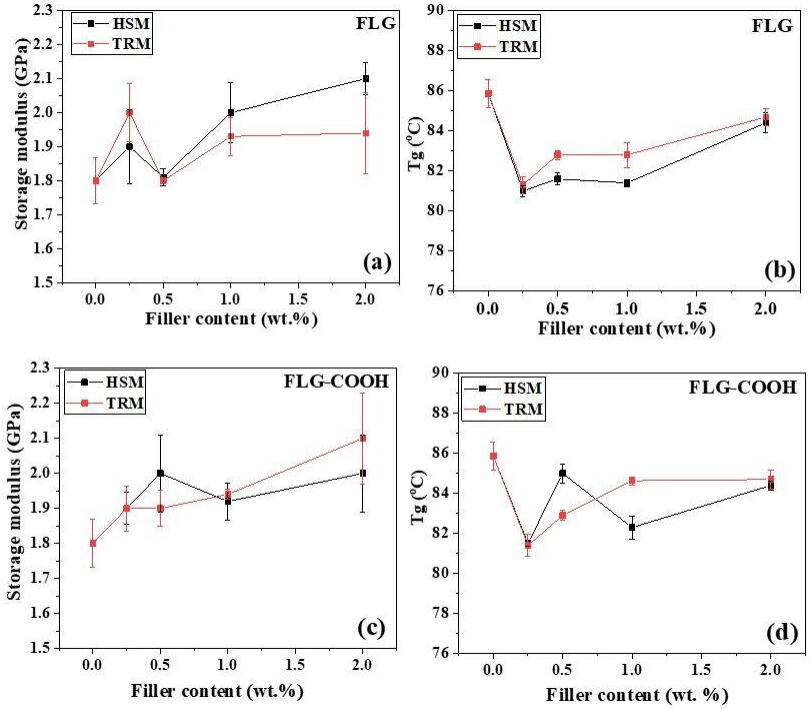


Figure 5. 28. Storage modulus at 30 °C and Tg values for FLG (a), (b) and FLG-COOH (c), (d) - epoxy composites, respectively as a function of nanofiller concentration prepared by HSM and TRM mixing methods.

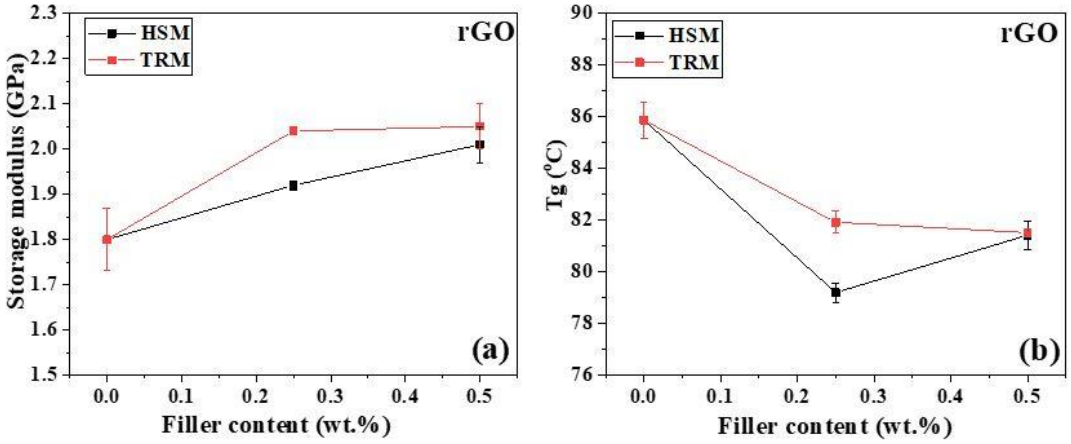


Figure 5. 29. Storage modulus at 30 °C and Tg values for rGO (a), (b) -epoxy composites, respectively as a function of nanofiller concentration prepared by HSM and TRM mixing methods.

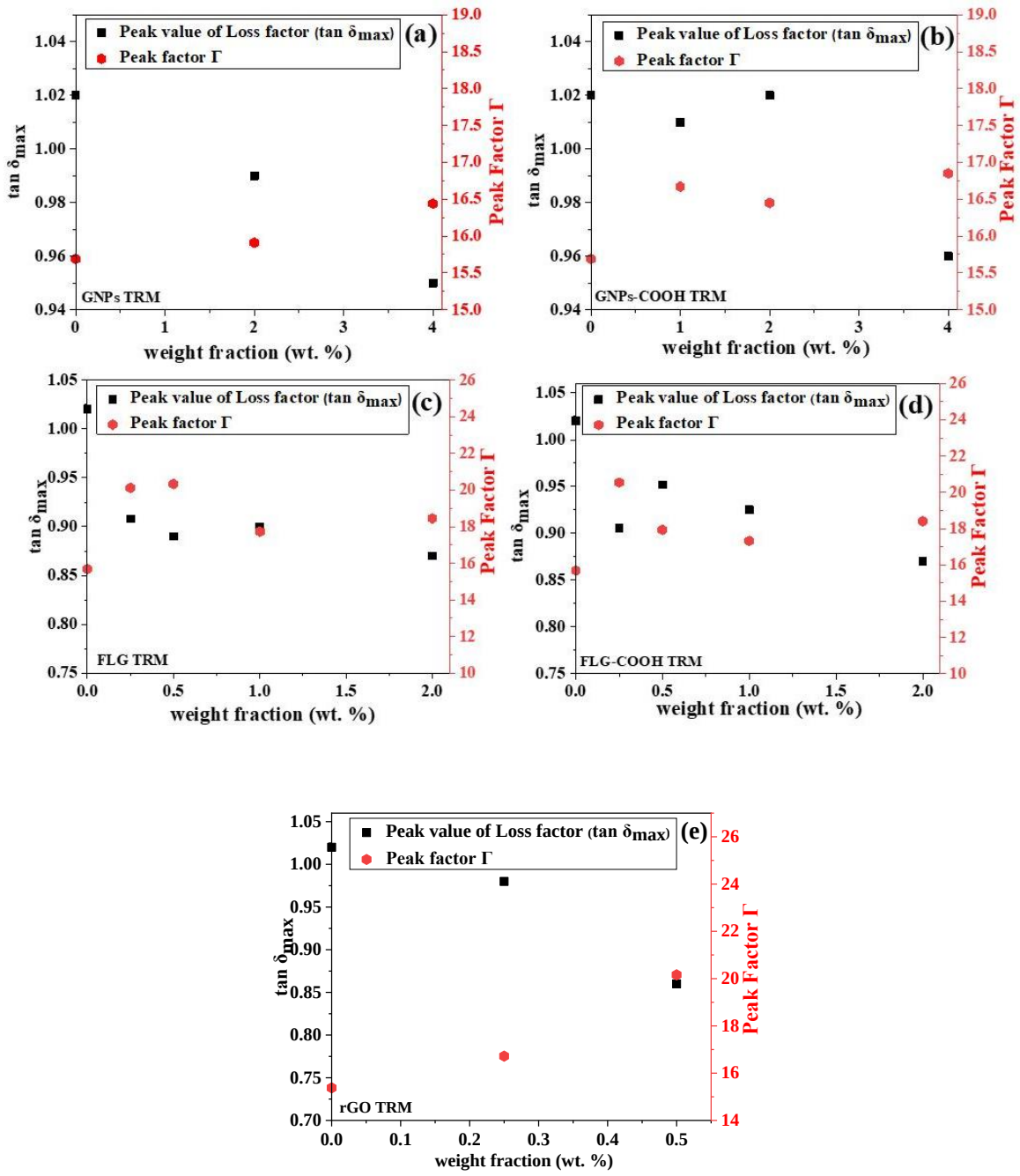


Figure 5. 30. Changes of peak factor Γ and tan δ peak $_{max}$ (loss factor) as a function of the filler concentration for GNPs (a), GNPs-COOH (b), FLG (c), FLG-COOH (d) and rGO (e). Here the results of TRM-mixed composites are presented.

The mechanism behind the reduced crosslinking in the case of FLG, FLG-COOH and rGO will be examined by adjusting the stoichiometric ratio between the hardener and epoxy resin. The stoichiometric ratio plays an important role in epoxy-based systems as it largely affects the mechanical properties, due to its influence on matrix properties and interphase characteristics (Bignotti, Pandini et al. 2011). In order to prove that the addition of fillers affected the

stoichiometry during the curing, the effect on the $T_g$ and the storage modulus was investigated of a non-stoichiometric epoxy (100:28.5, i.e., 5% less hardener). Figure 5.31 represents the storage modulus (a) and Tg values (b) of 0.25 wt. % FLG, 0.25 wt. % FLG-COOH and 0.25 wt.% rGO, when HSM-mixed with two different hardener ratios (100:30 and 100:28.5). Only the HSM method was used as similar trends were seen for both TRM and HSM. Although, the lower volume of hardener is expected to give different macromolecular structure which will affect the mechanical behaviour of pure epoxy and its composites, here no drop was noticed either for the pristine matrix, as shown in Figure 5.31 (a). Interestingly, a slightly higher storage modulus was achieved for the non-stoichiometric composites filled with FLG-COOH and rGO in comparison with the same stoichiometric filled composites. This may suggest that in the case of stoichiometric composites, the oxygen groups of the fillers surface compete with the epoxy to react initially with the hardener molecules, which leads to the unreacted hardener molecules and hence, a lower crosslinking network and a less stiff material. When the pure epoxy resin cured by using the non-stoichiometric ratio, $T_g$ was dropped for 5 $^oC$ that is comparable with the $T_g$ values of filled composites when the right stoichiometry was used (100:30). Additionally, the $T_g$ of filled composites was decreased similarly when the non-stoichiometric ratio was used (100:28.5). These results confirm that the stoichiometric composition has been disrupted in the presence of these nanofillers, with around 5% of hardener molecules not to interact with the polymer chains, resulting in a reduced cross-linking density. Similar results have been reported by Liu et al (2012) investigated the effect of nano- and micro- alumina fillers on the $T_g$ of the epoxy composites (bisphenol A-based as is the infusion resin that used in this study) and showed that aggregated nano-fillers do not allow the hardener molecules to distribute in the epoxy matrix, causing imbalanced stoichiometry between them and affecting the crosslinking density, with consequently lower $T_g$.

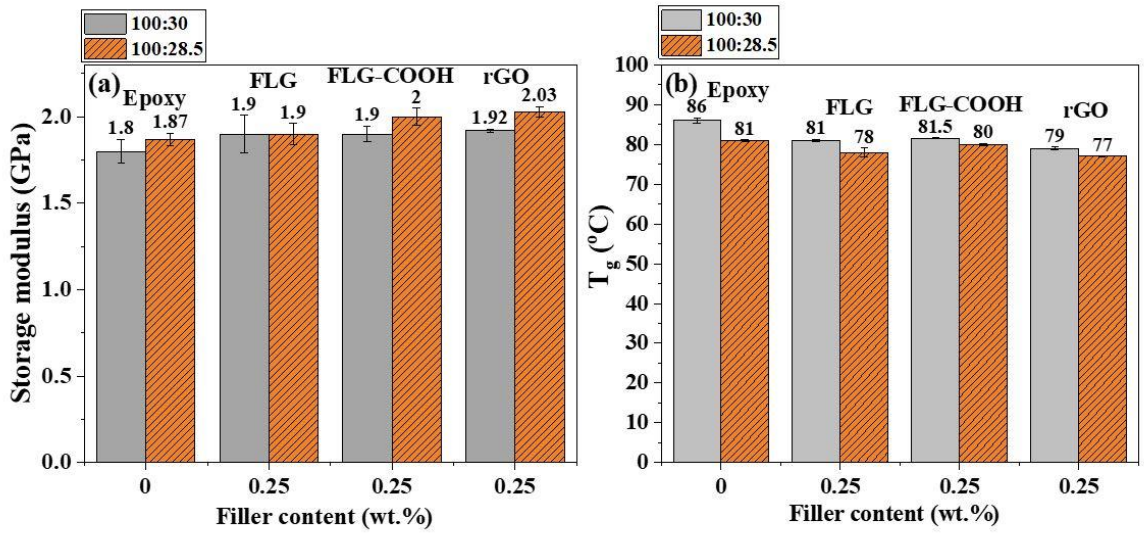


Figure 5. 31. Storage modulus at 30 °C (a) and $T_g$ values (b) for 0.25 wt. % FLG, 0.25 wt. % FLG-COOH and 0.25 wt.% rGO when HSM-mixed by ratio 100:30 (grey bars) and 100:28.5 (orange bars).

### 5.4.2. DMA study of graphene-DGEBA system

It is considered very challenging to characterize experimentally the interface region, and a computational molecular modelling has been used mainly for understanding the influence of interfacial molecular structure on bulk-level properties. A more accessible approach is to look at bulk properties that rely on interphase by studying the role of the crosslinking density on the interphase formation near the graphene sheets in a linear and highly cross-linked polymer networks. For this investigation, a model system includes diclycidyl ether of bisphenol A (DGEBA) resin cured with a combination of monoamine 'chain extender' and diamine 'cross-linker' chains while keeping the epoxide/amine stoichiometry constant (Putz, Palmeri et al. 2008). When only 'chain extender' is used (linear chains are formed) the diamine fraction is equal to 0 (Ξ=0) and when only 'cross-linker' chains are used (highly cross-linked system) the diamine fraction is equal to 1 (Ξ=1). Figure 5.32 represents the differences on the storage modulus and Tg values for 1 wt. % FLG ((a) and (b)), 1 wt. % FLG-COOH ((c) and (d)), 0.25 wt. % and 0.5 wt. % of rGO ((e) and (f)) based on a purely linear (Ξ=0) and highly cross-linked polymer (Ξ=1). There are two main findings: when a linear polymerization occurs, the storage modulus was significantly increased (~11% and 49%, respectively) by introducing *via* HSM the FLG and FLG-COOH with a dramatic drop of Tg (from 73 °C to ~50 °C) whereas the stiffness was less increased in the case of highly cross-linked composites (~4% and 16%, respectively) following a small decrease of Tg (2-3 °C). This difference on percentage increase of stiffness is attributed mainly to the low modulus of matrix of linear polymerized polymers.

The higher reinforcement level upon the addition of graphene in matrices with the lower modulus in comparison with more rigid matrices was highlighted in Literature review (Section 2.12). As the absolute modulus contribution of the nanofillers is not significant on our systems, this proves the low stress efficiency on the interphase region.

Similar results were obtained for rGO, reaching an enhancement in storage modulus of 30-34% for linear composites and 16-18% for the highly cross-linked composites. In comparison with 0.25 wt. % rGO/composites, the mechanical reinforcement was diminished when 0.5 wt.% rGO mixed by TRM for both linear and highly cross-linked. Increasing the concentration, larger is the proportion of rGO, which are well-dispersed with the polymer matrix. By achieving a better dispersion, the surface area in contact with the polymer matrix is increased, resulting in more isolated graphene sheets with the interphase zone and hence more interphase interactions, that leads to a higher decrease of $T_g$ and less stiff matrix.

The mechanical properties of the epoxy systems are strongly related with the interphase region, an interfacial region which connects the nanofillers and the matrix phases (Galpaya, Fernando et al. 2015), with the $T_g$ to be highly depend on the chain length (O'Driscoll and Sanayei 1991). The interphase can either increase $T_g$ by retarding the dynamics in systems via strong attractive interactions or decrease $T_g$ through repulsive interfacial interactions. Computational results (MD simulations) were reported similar findings in epoxy composites using graphite (Hadden, Jensen et al. 2013) or silica nanoparticles (Kim, Choi et al. 2015), demonstrating that the density of the interphase zone and interfacial strength decrease with increasing number of crosslinks. Here, linear systems have a significant drop on $T_g$, which has been recovered by increasing the cross-linking density. As the crosslinking increases, the mass density of the interphase decreases, resulting in less repulsive interactions between the filler and the polymer matrix. These results are clearly evidence of the interfacial degradation by increasing the crosslinking density.

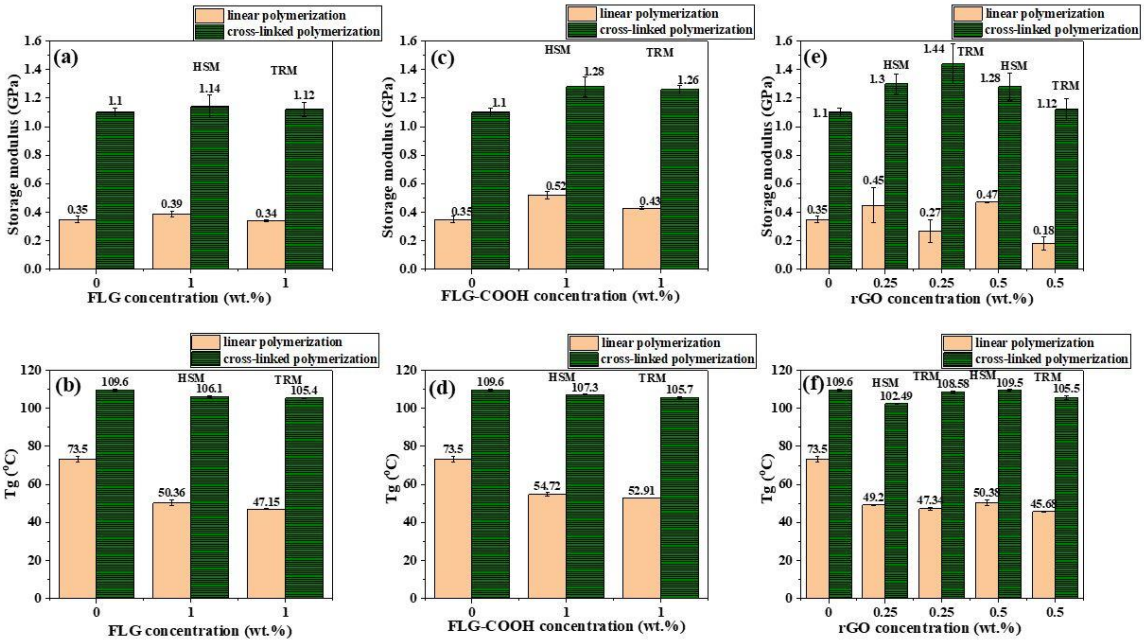


Figure 5. 32.Storage modulus at 30 °C and Tg values for 1% wt. FLG ((a) and (b)), 1 wt. % FLG-COOH ((c) and (d)), 0.25 wt. % and 0.5 wt.% of rGO ((e) and (f)) in a linear polymerization (orange bars) and highly cross-linked polymerization (green bars).

### 5.4.3. Tensile Testing

The mechanical properties of the materials were studied by tensile testing. Figure 5.33 ((a), (b)) and 5.33 ((a)) show typical stress-strain curves for the neat epoxy and composites filled with FLG, FLG-COOH and rGO, respectively, as a function of the filler loading and the mixing method. Five stress-strain curves were obtained for each loading level and mixing method for each type of filler, and representative ones are presented. Overall, the Young's modulus was increased with increasing the concentration of FLG and FL-COOH. However, no significant mechanical enhancement was observed with the large graphene flakes of rGO. The strength decreases with the nanofiller concentration, and it appears to be maintained in the case of rGO. In all cases, the strain at failure appears to be reduced by the addition of the higher concentration of fillers.

In detail, the parameters of the mechanical properties of the filled composites are tabulated in Table 5.3. The strain at failure was increased for ~34% and ~43% for 0.25 wt. % FLG and FLG-COOH mixed by HSM, respectively with a slight decrease after the application of TRM. However, the epoxy composites showed a more brittle behaviour when both of nanofillers are increased. When the concentration goes up to 2 wt. %, the strain at failure was decreased from 3.5% (neat epoxy) to 1.4% and 1.2% (FLG/epoxy composites) and to 2.3% and 1% (FLG-

COOH/epoxy composites), mixed by HSM and TRM, respectively. This brittleness behaviour was also observed by other researchers (Yasmin, Luo et al. 2006).

In general, the improvement of elastic modulus is attributed to the good dispersion of nanosize particles and good interfacial adhesion between the particles and the epoxy matrix so that the mobility of polymer chains is restricted under loading (Wu, Zhang et al. 2002). As shown in Figure 5.33 (b), increasing the nanofiller concentration, the tensile modulus was increased for ~20% for filler loading 2 wt.%. No significant differences were observed between the mixing methods as the values are close to experimental error. As mentioned above, the reduction in crosslinking density and the poor dispersion state can affect the system's performance, leading to a deterioration in the mechanical properties of the matrix polymer. Lower crosslinking density was observed by the DMA data, which can explain here the results for the tensile modulus. Therefore, a more prominent increase in modulus was detected only for 2 wt. % of FLG/epoxy composites (mixed by HSM and TRM), in which the values of $T_g$ (~84 $^oC$) are closer to the neat resin (85.8 $^oC$). Lower values in tensile strength are observed with the increase of the nanofiller (Figure 5.33 (c)) which could be attributed to the following reasons: (a) the poor interfacial interactions between the FLG and the epoxy resin, (b) possible agglomerates which act as defects and (c) the higher brittleness due to restricted chain motion which makes the samples more susceptible to defects.

For FLG-COOH (Figure 5.33 (e)) mixed by TRM the tensile modulus increased for 34% at 2 wt. %, whereas no enhancement was observed by HSM method. These results may be attributed not only to the crosslinking effect but also to the poor dispersion state that occurs in high filler loadings when mixed by HSM method. This also can be supported by the significant decrease on tensile strength that observed for the FLG-COOH/epoxy composites (Figure 5.33 (f)). Lower values on tensile strength can be attributed to presence of agglomerations that act as stress-concentration points, the insufficient load transfer from the polymer to FLG-COOH in order to reach the tensile strength of the nanofillers under loading or the general brittle material behaviour which leads to a sensitivity in defects. Lower tensile strength and strain by increasing the nanofiller were reported in the literature (Zaman, Phan et al. 2011, King, Klimek et al. 2013).

The effect of TRM method in the tensile modulus was noticed, also in the case of rGO (Figure 5.34 (b)). Although, the better dispersion, as proved by Optical microscope (Figure 5.12), gives higher stiffness comparing with the HSM-mixed composites, the mechanical reinforcement was negligible. Similarly with FLG and FLG-COOH that no improvement was found at lower

filler loadings, these results are strongly related to ‘‘cross-linking density reduction’’ effect that leads to decreased mechanical properties (Bao, Guo et al. 2011). The tensile strength was slightly improved at the higher filler loading (0.5 wt. % TRM), which attributed to the better exfoliation/dispersion of rGO based on the results of the exfoliation model; therefore, a higher surface area occurs by acting as a crack propagation barrier and improves the mechanical interlocking between the matrix and the filler (Liu, Papageorgiou et al. 2018). Finally, the strain at failure seems to decrease significantly for all the composites.

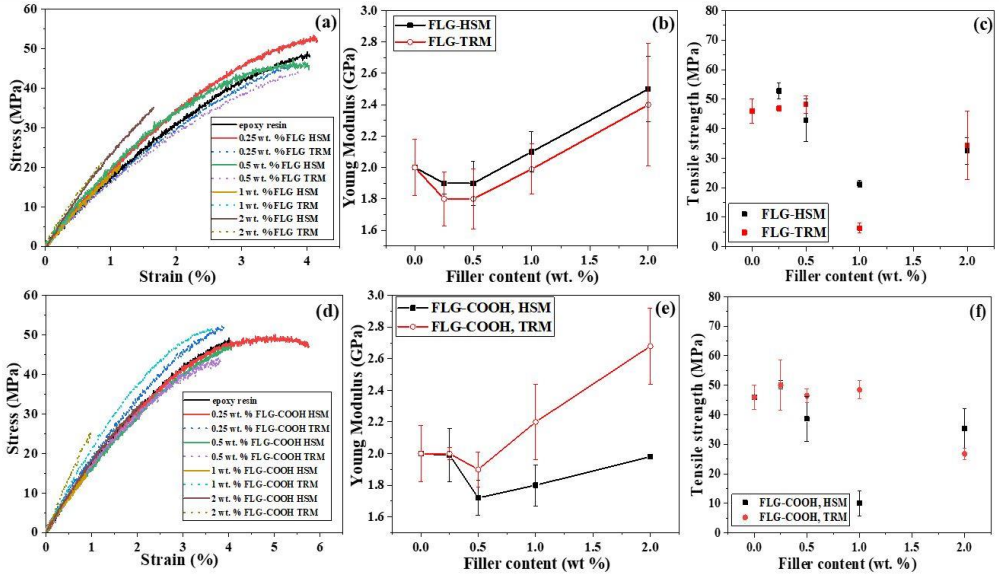


Figure 5.33. Typical stress-strain curves of FLG/epoxy composites (a), FLG-COOH/epoxy composites (d) mixed by HSM and TRM. Young’s modulus (b) and (e) as a function of filler loading of FLG and FLG-COOH epoxy composites mixed by HSM and TRM, respectively. Tensile strength (c) and (f) as a function of filler loading of FLG and FLG-COOH epoxy composites mixed by HSM and TRM, respectively.

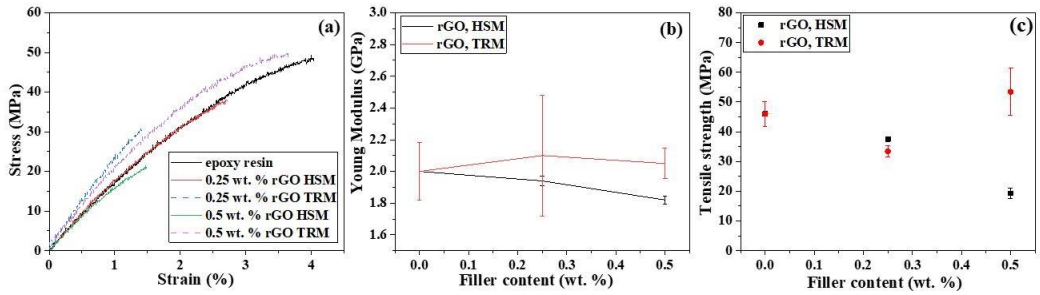


Figure 5. 34. Typical stress-strain curves of rGO/epoxy composites (a) mixed by HSM and TRM. Young’s modulus (b) as a function of filler loading of rGO/ epoxy composites mixed by HSM and TRM. Tensile strength (c) as a function of filler loading of rGO/epoxy composites mixed by HSM and TRM, respectively.

Table 5 3.Parameters of the mechanical properties

| Samples | $\sigma_{max}$ (MPa) | $\varepsilon_{max}$ | E (GPa) |
|---|---|---|---|
| **Epoxy resin** | 45.96±4.15 | 0.035±0.004 | 2±0.185 |
| **0.25% wt. FLG HSM** | 52.79±2.73 | 0.047±0.008 | 1.9±0.075 |
| **0.25% wt. FLG TRM** | 46.88±0.97 | 0.037±0.006 | 1.8±0.176 |
| **0.5% wt. FLG HSM** | 42.82±7.18 | 0.038±0.01 | 1.9±0.148 |
| **0.5% wt. FLG TRM** | 48.24±3.00 | 0.044±0.007 | 1.8±0.195 |
| **1% wt. FLG HSM** | 21.255±1.20 | 0.012±0.001 | 2.1±0.133 |
| **1% wt. FLG TRM** | 6.3±1.67 | 0.0031±0.0004 | 1.99±0.165 |
| **2% wt. FLG HSM** | 32.454±4.52 | 0.014±0.003 | 2.5±0.21 |
| **2% wt. FLG TRM** | 34.39±11.5 | 0.012±0.007 | 2.4±0.39 |
| **0.25% wt. FLG-COOH HSM** | 50.0925±1.41 | 0.05±0.015 | 1.99±0.173 |
| **0.25% wt. FLG-COOH TRM** | 50.115±8.51 | 0.042±0.014 | 2±0.046 |
| **0.5% wt. FLG-COOH HSM** | 38.613±7.62 | 0.039±0.014 | 1.72±0.117 |
| **0.5% wt. FLG-COOH TRM** | 46.46±2.29 | 0.039±0.004 | 1.9±0.11 |
| **1% wt. FLG-COOH HSM** | 10.01±4.28 | 0.005±0.002 | 1.8±0.135 |
| **1% wt. FLG-COOH TRM** | 48.44±3.06 | 0.034±0.006 | 2.2±0.24 |
| **2% wt. FLG-COOH HSM** | 35.37±6.7 | 0.023±0.004 | 1.98± 0.02 |
| **2% wt. FLG-COOH TRM** | 26.75±6.92 | 0.01±0.002 | 2.68±0.24 |
| **0.25% wt. rGO HSM** | 37.54±0.85 | 0.025±0.0009 | 1.94±0.03 |
| **0.25% wt. rGO TRM** | 33.42±1.98 | 0.015±0.001 | 2.10±0.38 |
| **0.5% wt. rGO HSM** | 19.28±1.74 | 0.012±0.002 | 1.82±0.025 |
| **0.5% wt. rGO TRM** | 49.68±2.66 | 0.029±0.002 | 2.06±0.1 |

*σmax, εmax, E are tensile strength (the stress at break in the stress-strain curve, MPa), ultimate strain and Young's modulus (the slope of the stress-strain curve in the elastic region (0-0.5% strain), GPa).

## 5.5. Mechanism of reinforcement

The mechanics of the reinforcement of polymers by graphene has been reviewed recently (Young, Kinloch et al. 2012). One of the simplest methods of evaluating the reinforcement achieved in nanocomposites is the "rule of mixtures'' whereby the effective modulus of fillers ($E_f$=$E_{eff}$), the actual modulus rather the theoretical value can be estimated by the relationship (5.3):

$$E_c = E_f V_f + E_m(1 - V_f) \qquad (5.3)$$

where $E_c$, $E_m$ are the composite modulus, the modulus of the matrix and $V_f$ and $V_m$ are the volume fractions of the filler and the matrix, respectively. The correlation of the mass fraction

$w_f$ (wt. %) with the volume fraction $V_f$ (vol. %) of the graphene nanofillers in the nanocomposites was determined using the equation (5.4) (Zhao, Zhang et al. 2010):

$$V_f = \frac{w_f \rho_p}{w_f \rho_p + (1 - w_f)\rho_g} \qquad (5.4)$$

where $\rho_p$ ~1.16 g/cm$^{-3}$(as suggested by the data sheets) and $\rho_g$ ~2.2 g/cm$^{-3}$ represent the density of epoxy resin and graphene nanofillers, respectively. The values of $E_c$ and $E_m$ are determined by the DMA data (Table 1, Appendix-Section 2). Similar analysis was performed by Young et al in the following reports (Li, Young et al. 2013, Li, Chu et al. 2018). The estimated $E_{eff}$ is shown in Table 1 (Appendix-Section 2) and Figure 5.35 shows clearly that the $E_{eff}$ drops as the nanofiller loading increases. The $E_{eff}$ were found very low comparing with the range of values reported from AFM studies on single sheets of GO (~200 GPa) (Suk, Piner et al. 2010). For instance, the very high thickness of the GNPs and GNPs-COOH leads in a poor stress transfer between the inner graphene layers due to the relatively-weak van der Waals bonding between the individual graphene layers and consequently to a reduced effective modulus and a lower mechanical reinforcement (Gong, Young et al. 2012). Ahmad et al (2017) measured the effective modulus of GNP into thermoplastic matrix (PP), using a formula which is relating to the number of layers $n_l$:

$$E_{eff} = \frac{E_g}{\frac{n_1}{2} - k_i\left(\frac{n_1}{2} - 1\right)} \qquad (5.5)$$

where $E_g$ is the Young's modulus of monolayer graphene (1050 GPa) and $k_i$ is the efficiency of stress transfer between the layers (~0.6). The thickness of graphene is taken as 0.34 nm and for thickness of nanofiller ($t_{filler}$) as calculated by the XRD data (Chapter 4, Table 4.3.) Here, the $E_{eff}$ is found: 93.83 GPa and 109.38 GPa (for GNPs and GNPs-COOH), 479.01 GPa and 530.30 GPa (for FLG and FLG-COOH) and ~444 GPa (for rGO). However, the Young's modulus ($E_{eff}$) of these materials is still lower than the calculated values which could be attributed to mainly for two reasons: (a) the random dispersion causes a reduction of the modulus by less than a factor of two, compared with a fully-aligned material (Li, Young et al. 2016). In that case, the $E_{eff}$ modulus of our materials would be reduced to around Eeff ~50 GPa and 58 GPa (GNPs and GNPs-COOH), ~255 GPa and ~283 GPa (FLG and FLG-COOH) and 237GPa (rGO) when they are oriented randomly in the epoxy matrix, (b) considering the shear-lag theory effects, as mentioned in the Literature review (Section 2.12.2), the full stress will not be carrying by 1.5 μm of each end of flake (critical length ($I_c$)= 3 μm), so the total planar size of every flake does not provide a full reinforcement. Taking into consideration that the maximum planar size of GNPs and GNPs-COOH is 5 microns (0.2- 5 μm) which is less than 2

times than the $I_c$, then the flake won't even reach the same strain as the matrix and hence the reinforcement will be minimal. In the case of GNPs and GNPs-COOH (5 μm was considered as the maximum length) is expected to get 40% of the modulus (20 GPa and 23 GPa, respectively) whereas in the case of FLG and FLG-COOH (8 μm was considered as the maximum length) is 62.5% of the total modulus (159 GPa and 177 GPa). Last, the rGO with a planar size of 40 μm is expected 92.5% of the modulus, resulting finally to 219 GPa. Considering that the interfacial interactions between the nanomaterials and the epoxy resin were not efficient and also a reduced crosslinking network was confirmed for all the composites, lower values of effective modulus were determined in comparison with the theoretical estimations.

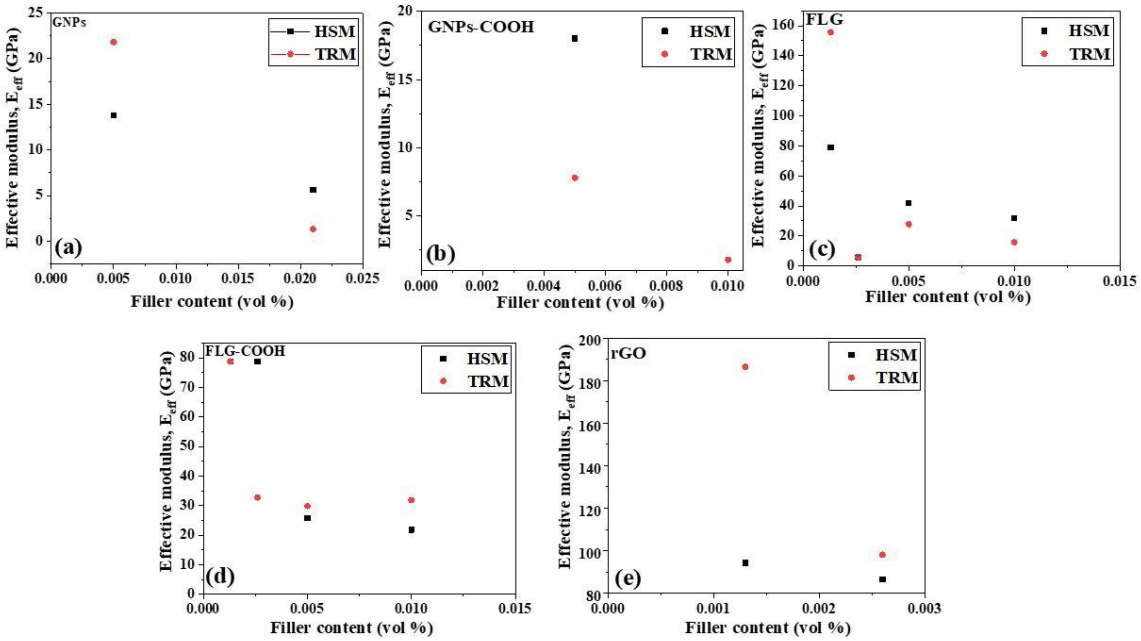


Figure 5. 28. Dependence of the effective modulus of the GNPs (a), GNPs-COOH (b), FLG (c), FLG-COOH (d) and rGO (e) reinforcement in the epoxy nanocomposites, determined from DMA measurements, upon nanofiller loading.

## 5.6. Comparison of Young's modulus between experiment and Halpin-Tsai theoretical model

The Halpin-Tsai was well established for fiber-reinforced composites and had been recently extended to CNT- and graphene-filled composites (Zhao, Chang et al. 2016). The Halpin-Tsai equations can take into account the orientation of filler towards either the longitudinal (L) or the transverse (T) directions and here was employed to theoretically predict the Young's modulus of the graphene-epoxy systems. For this reason, it was assumed that the graphene

nanofillers work as rectangular solid fibers and are dispersed separately and uniformly in the epoxy matrix. The Young's modulus of composites with randomly dispersed ($E_r$) are defined by the modified Halpin-Tsai equations (2.11)- (2.14) (as mentioned in Literature review, Section 2.12.3), with $E_f$ and $E_{matrix}$ is the Young's modulus of the nanofillers (the theoretical values have been calculated in the previous section) and the epoxy matrix (2 GPa), respectively. The values of $V_f$ were calculated by the equation (5.4). The $\xi$ is a shape parameter that takes into consideration the geometry of the nanofiller along with packaging arrangement; therefore it is related to the aspect ratio (Papageorgiou, Kinloch et al. 2017). All the parameters are included in Table 5.4.

Table 5. 4.The parameters of thickness, aspect ratio and $\xi$ that used in Halpin and Tsai model.

| Material | Thickness, nm (XRD) | Aspect ratio (s) | $\xi$ | $E_{eff}$ (GPa) |
|---|---|---|---|---|
| **FLG** | 2.71 | 2952.02 | 1968.01 | 159.4 |
| **FLG-COOH** | 2.35 | 3404.25 | 2269.05 | 176.9 |
| **rGO** | -* | 13333 | 8888.66 | 219.04 |

*due to the absence of the main peak in XRD graph, the thickness of rGO is used by the supplier data (<3 nm).

The Halpin and Tsai model was compared with the tensile data of FLG, FLG-COOH and rGO/epoxy composites, as shown in Figure 5.36. For all the materials, a difference was found between the theoretical and experimental estimations. The lower experimental values could be attributed mainly to the following reasons: (i) the poor interfacial interactions as perfect bonding between the fillers and the matrix is assumed (Yousefi, Gudarzi et al. 2013), (ii) the presence of agglomerations which leads to errors and wrong predictions (Shokrieh, Esmkhani et al. 2014) and (iii) the 'crosslinking reduction effect'.

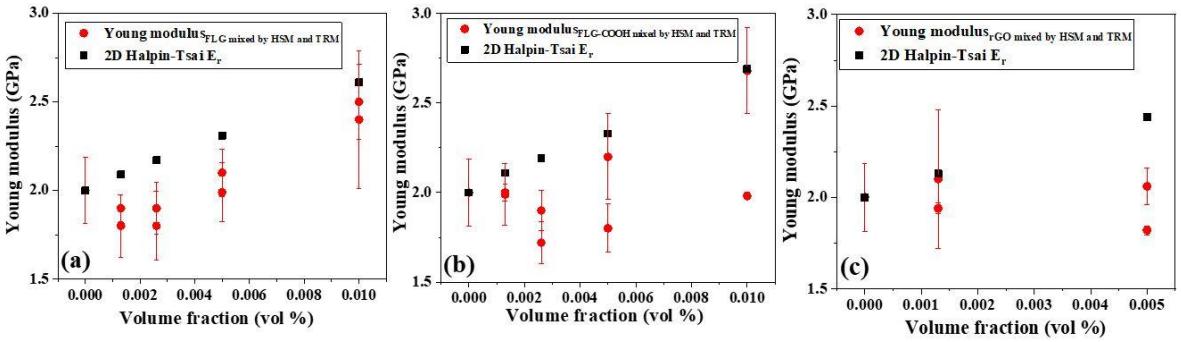


Figure 5. 29.Young modulus of FLG (a) and FLG-COOH (b) and rGO (c)/epoxy composites: Comparison of Halpin-Tsai analytical model for 2D orientation.

## 5.7. Conclusion

In this chapter, it is clear that the different structural and geometrical characteristics of graphene nanomaterials leads to a major modification of both the microstructure and mechanical properties of the polymer. The conclusions are summarized as a function of the effects of mixing methods, surface functionalization and filler loading on the dispersion state and the curing reaction of the epoxy nanocomposites:

- Plasma process provides a well dispersed material in the epoxy matrix.
- In the uncured stage, the HSM seems to be more effective at low filler loadings for GNPs, FLG, GNPs-COOH and FLG-COOH. By increasing the filler loading, TRM gives a better dispersion state, which was confirmed by rheology data. In the case of uncured rGO/epoxy suspensions, large agglomerations observed in both filler concentrations, which have been broken down using TRM.
- In the cured stage, a relatively good dispersion was achieved for all the composites under the application of TRM, as strongly supported by Optical microscope and SEM micrographs.
- A significant contribution of the curing effects into the mechanical properties was confirmed by DMA analysis. Adjusting the filler concentration, a great loss on $T_g$ and storage modulus was observed for GNPs and GNPs-COOH, which is possibly related to graphene aggregates and the catalytic effect of the oxygen groups. Adjusting the stoichiometric ratio and achieving a well-dispersed material, a reduced cross-linking density was confirmed in the case of FLG, FLG-COOH and rGO/epoxy nanocomposites. Better dispersion state leads to a high surface area of these materials that act as physical barriers, resulting in a non-stoichiometric ratio between the hardener and resin and hence, a diminished mechanical reinforcement.
- The importance of the interphase zone in the mechanical properties was evaluated by adjusting the cross-linking level. Reducing the cross-linking density, a lower stress transfer occurs on the interphase region. Moreover, higher is the dispersion state, more are the isolated graphene flakes on the interphase zone, resulting in more repulsive interactions and hence higher loss on $T_g$ and storage modulus. These results provide valuable insights for understanding the effect of graphene nanomaterials on the interphase region within the epoxy matrix and its role on the mechanical properties of the bulk nanocomposites.

- The reduced cross-linking density by the addition of the fillers was confirmed by the TGA results.
- Tensile measurements showed the Young's modulus was increased with increasing the concentration of FLG and FL-COOH. However, the mechanical enhancement for the large graphene flakes of rGO was negligible and this is attributed mainly to the reduced crosslinking density. By using the rules of mixtures, a low effective modulus was obtained for all the nanofillers, which confirms again the low mechanical reinforcement. The strength decreases with the nanofiller concentration, and it appears to be maintained in the case of rGO. In all cases, the strain at failure appears to be reduced by the addition of the higher concentration of fillers.

# Chapter 6 Magnetic Graphene-epoxy composites: Characterization and Mechanical properties. Alignment under low magnetic fields.

## 6.1. Introduction

This chapter presents the structural characterisation of epoxy resin filled with the three magnetic decorated grahene morphologies (GNPs@MNPs, MNPs@FLG and MNPs@rGO) developed in Chapter 4. The effect of the mixing method on the dispersion state of the nanofiller has been investigated before and after the curing process using Rheology, Optical Microscope, and SEM. The alignment of these nanofillers under the application of low magnetic fields was investigated using Small-Angle X-ray (SAXS), SEM and Optical Microscope. Dynamic Mechanical Analysis (DMA) and tensile testing to investigate the mechanical reinforcement achieved by the addition of the fillers before and after their alignment. Expected values obtained from micromechanics calculations using the 'rules of mixtures' and the analytical Halpin-Tsai model are compared with the data.

## 6.2. Fabrication of highly ordered epoxy composites with MNPs@graphene

### 6.2.1. Experimental

Nanocomposites of MNPs@GNPs, MNPs@FLG and MNPs@rGO with various contents (Table 6.1) were manufactured using two different mixing methods (HSM and TRM), as described in Chapter 5.

Table 6. 1. Formulation of the prepared graphene/epoxy composites

| Materials | Loading (wt. %) |
|---|---|
| **MNPs@GNPs** | 1, 2, 4 |
| **MNPs@FLG** | 0.25, 0.5, 1, 2 |
| **MNPs@rGO** | 0.25, 0.5 |

Following the data sheets, the pot-life of the epoxy is 9-14 min, the gelation time is about 2-4 hrs and a demould time of 6 hrs at 25 $^{o}$C. Therefore, the alignment of the magnetic nanohybrids was necessary to be completed prior to gelation of the epoxy resin. In the practical experiments, the mixing procedure with a stoichiometric amount of hardener (100:30, epoxy: hardener) took up to ~15 min (using the high-speed mixer for 5 min with a speed of 1950 rpm/min and degassing for 10 min) and then the solution with the use of a pipette added and cured on a microscope slide (3 x 1 in.) to a magnetic field parallel to the short edge of the slide for 2 hrs. A steel C-core electromagnet with an air gap of 30 mm between faces of 30 mm x 30 mm was

used to apply the magnetic field to the specimen. The uncured epoxy was held in position between the magnetic poles on a 3D printed plastic bracket designed to locate both the C-core and the slide. The electromagnet was energized by a software-controlled Power Supply Unit (PSU) that would allow the user to define the required magnetic field strength through the LabVIEW VI. The current was supplied by a KEPCO Bipolar power supply (400W, ±36V, ±12A) and the magnetic field was measured using a LakeShore 450 gaussmeter. More information for the development of this system is included on the ref (Dyer, Gkaliou et al. 2019). Real-time images of the alignment behaviour of the MNPs@GNPs, MNPs@FLG and MNPs@rGO in the epoxy matrix were captured using an optical microscope with 20x magnification (Leitz Wetzlar, Germany, Nikon DSLR camera) throughout the curing process, as shown in Figure 6.1 (a). Microscope image capture was controlled by the LabVIEW software at a rate of one image per minute during the curing process. This allows examination of the alignment process at any point during the curing process. For the preparation of composites for DMA and tensile testing, the solution was immediately poured into an aluminium mould and a pair of glass slides, as described in Chapter 5. Then, the nanocomposites placed under a range of magnetic fields that were applied using a DC system (Figure 6.1 (b)). The magnetic field strength employed was selected based on the theoretical modelling results, discussed below (6.2.2.). The steps of the curing cycle were at room temperature for 6 hrs and then post-cured in the oven at 60 $^{o}$C for 12 hrs.

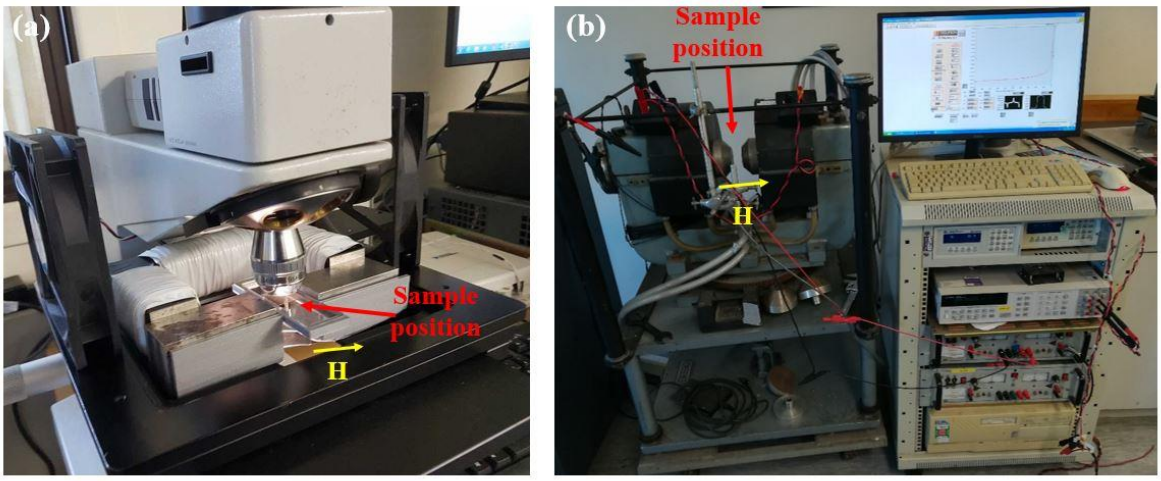


Figure 6. 1. Experimental set-up of the magnetization system comprising the plastic former, electromagnet and specimen slide holder located beneath the microscope objective (a) and DC system (b). The sample position and the direction of the magnetic field were highlighted with red and yellow arrows, respectively.

### 6.2.2. Determination of the minimum magnetic field ($H_{min}$)

In order to estimate the minimum magnetic field ($H_{min}$) required to achieve alignment in liquid epoxy resin, a method proposed by Wu et al (2016) was adopted. The method considers the planar size of the graphene, the diameter of the magnetic nanoparticles, the volume fraction of the magnetic nanoparticles on the graphene surface, the magnetic susceptibility of the hybrid material and the viscosity of the filled epoxy resin. When subjected to an external magnetic field, the magnetic moments exerted on the magnetic nanoparticles force the MNPs@graphene nanohybrids to align in the direction of the magnetic field. The minimum magnetic field ($H_{min}$) is determined by solving a torque balance equation that takes account the magnetic torque ($T_m$), gravitational torque ($T_g$) and viscous torque ($T_\eta$) acting on the magnetic graphene sheets (Jiao, Shioya et al. 2014). The magnetic torque $T_m$ of the magnetic graphene sheets can be calculated analytically by considering graphene sheets (MNPs@GNPs, MNPs@FLG and MNPs@rGO) as thin oblate spheroids with semi-major and semi-minor axes of α and b, corresponding to the radius and half thickness of a platelet (Erb, Segmehl et al. 2012):

$$T_m = \frac{2\pi\mu_0 \chi_{nh}^2}{3(\chi_{nh}+1)} [(b+d)(a+d)^2 - ba^2]H^2 sin2\theta \qquad (6.1)$$

where $\mu_0$ is the magnetic permeability of free space (1.25 x $10^{-6}$ H/m), d is the diameter of the magnetic nanoparticles, H is the external magnetic field strength, θ represents the angle between the magnetic field vector and the platelet's long axis and $\chi_{nh}$ is the volume magnetic susceptibility of the magnetic nanohybrids, which depends on the susceptibility of the magnetic nanoparticles and their fraction on the surface of the graphene sheets. The viscous torque ($T_\eta$) is proportional to the angular frequency of the platelet $\dot{\theta}$ and the viscosity of the fluid medium η:

$$T_\eta = \eta\dot{\theta}k_r \qquad (6.2)$$

where $kr=32\alpha^3/3$ is the rotational friction coefficient (Berg 2018). The dynamics of the magnetic nanohybrids is determined by a balance between the magnetic torque and the viscous torque ($T_m+T_\eta=0$) which yields $\dot{\theta} = -Asin2\theta$,

$$\text{where, } A = \frac{\pi\mu_0 \chi_{nh}^2}{16\eta(\chi_{nh}+1)\alpha^3} [(b+d)(a+d)^2 - ba^2]H^2 \qquad (6.3)$$

The time required for the rotation of the MNPs@graphene from an initial angle $\theta_1$ to a generic angular position of $\theta_2$, can be estimated using (6.4):

$$t_r = \frac{1}{2A} \ln \frac{tan\theta_1}{tan\theta_2} \quad (6.4)$$

The maximum values of the lateral size (2α) and thickness (2b) based on the supplier's data were used for the calculations. The initial viscosity of the epoxy resin was measured by the shear-steady measurements, η=0.6 Pa.s (at 0.93$s^{-1}$), but it is considered that the viscosity does not stay constant up to the gelation time. The diameter (d) of the magnetic nanoparticles is estimated by the TEM analysis. These experimental parameters are included on Table 6.2. The volume magnetic susceptibility ($\chi_{nh} = \frac{M}{H}$) is the ratio of magnetization M (magnetic moment per unit volume) to the applied magnetizing field intensity H. For this reason, the linear part of the hysteresis loops was used (Appendix, Section 1). The total volume ($V_{total}$) of the magnetic nanohybrids was calculated by using the equation (6.5):

$$V_{total} = V_{graphene} + V_{MNPs} = \frac{m_{graphene}}{d_{graphene}} + \frac{m_{MNPs}}{d_{MNPs}} \quad (6.5)$$

Where $m_{graphene}$ and $m_{MNPs}$ are estimated by the TGA results (Chapter 4, Figure 4.6). The density of graphene and the maghemite ($Fe_2O_3$) are ~2.3 g/$cm^3$ (Zielinski, Kühne et al. 2019) and 4.9 g/$cm^3$ (Coduri, Masala et al. 2020), respectively. As explained in Chapter 4, the residues on the TGA plots (after 600°C) of the magnetic nanohybrids are related to this oxidised phase of maghemite ($Fe_2O_3$). For this reason, only the phase of maghemite ($Fe_2O_3$) has been considered. However, the difference between the densities of the two phases are very small ($d_{magnetite}$=5.2 g/$cm^3$) (Ross and Bourke 2017). Following the results at Table 6.2., decreasing the size of the nanoparticles, the magnetic susceptibility becomes very small, especially for the MNPs@rGO that has a very small magnetic moment (Appendix, Section 1). There was an anomalous trend for MNPs@FLG, which may attribute to the lower fitting at hysteresis loop ($R^2$=0.96). By solving the equations (6.3) and (6.4), the minimum magnetic field strengths ($H_{min}$) required to rotate the magnetic nanohybrids from 89° to 1° within 1hr (before the gelation time) are found to be 0.69 mT, 0.77 mT and 9.94 mT for MNPs@GNPs, MNPs@FLG and MNPs@rGO, respectively.

Table 6. 2. Experimental parameters for the estimation of the magnetic field strength.

| **Materials** | **Lateral size$_{(filler)}$ (μm)** | **Thickness (nm)** | **D$_{particles}$ (nm) TEM** | **$R^2$ *** | **Volume MNPs@graphene ($cm^3$)** | **$\chi_{nh}$** | **H$_{min}$ (mT)** |
|---|---|---|---|---|---|---|---|
| **MNPs@GNPs** | 5 | < 50 | 27.5±7.99 | 0.99 | 0.059 | 1.33 | 0.67 |
| **MNPs@FLG** | 8 | 2 | 14.14±3.9 | 0.96 | 0.0034 | 2.77 | 0.77 |
| **MNPs@rGO** | 40 | < 3 | 11.51±3.77 | 0.97 | 0.0033 | 0.317 | 9.94 |

*the values of the $R^2$ estimated from the linear fitting of the VSM plots.

Following the equations (6.3) and (6.4), the rotation time can be determined including the difference between the initial angle ($\theta_1$) and the final angle ($\theta_2$), the magnetic field strength (H), the viscosity of the epoxy resin ($\eta$) and the volume fraction of the magnetic nanoparticles ($\varphi$). The relationship between the rotation time and initial angles for a magnetic field of 0.7 mT and the relationship between rotation time and magnetic field strength (0-100 mT) are presented in Figure 6.2 (a) and (b), respectively. As would be expected, the smaller the initial angle, the smaller the rotation time, as similarly reported by Wu et al (2016). Figure 6.2. (b) indicates that the rotation time significantly decreases with the increase of the magnetic field. Specifically, when the magnetic field reaches at 100 mT, the estimated rotation time decreases to 0.17 sec. Figure 6.2. (c) shows the relationship between the viscosity of the epoxy suspensions reinforced with 1, 2 and 4 wt. % MNPs@GNPs (as measured by the shear steady rheology (Section 6.3.2) and field strength required to achieve rotation in 1 hr. This shows that a minimum magnetic field (Hmin) of 1mT is necessary to orient 4 wt.% of MNPs@GNPs ($\eta$=1.36 Pa*s) in the epoxy matrix. Similar relationship between the viscosity and the magnetic field strength was found for the liquid epoxy composites filled with 1 wt.% MNPs@FLG ($\eta$=1.3 Pa*s- (Section 6.3.2). This suggest that a 1mT field is suitable for 1 wt.% MNPs@FLG, too. Whereas for the epoxy composites filled with MNPs@rGO 0.25 wt. % and 0.5 wt. % ($\eta$=0.9 Pa*s and 2.2 Pa*s, respectively (Section6.3.2), the required magnetic field strengths to achieve in 1 hr were estimated to be 12 mT and 19 mT, respectively. Hence, a magnetic field of 20 mT is needed to achieve complete orientation of the MNPs@rGO within 1hr.

Finally, the volume magnetic susceptibility ($\chi_{nh}$) of the magnetic nanoparticles plays an important role in the optimization of the alignment process. Figure 6.2 (d) gives the relationship between the volume magnetic susceptibility ($\chi_{nh}$) and the rotation time, where the volume of MNPs in the MNPs@GNPs is varied. Increasing the volume fraction of the magnetic nanoparticles, the rotation times decreases. Using the magnetic susceptibility of the bulk $Fe_3O_4$ nanoparticles ($\chi_{np} = 21$) as measured by Erb et al (Erb, Son et al. 2009), theoretical susceptibilities of the magnetic nanohybrids can been obtained from the equation (6.6):

$$\chi_{ps} = \chi_{np} * C_{np} \qquad (6.6)$$ (Erb, Segmehl et al. 2012)

where, $C_{np}$ is the volume fraction of the iron oxide nanoparticles. Here, the volume fraction of MNPs on MNPs@GNPs, MNPs@FLG and MNPs@rGO was estimated to be 25.42%, 23.52% and 25.15% by the TGA results. Using the lowest magnetic fields (Table 6.2), the maximum planar sizes and the theoretical estimations of the magnetic susceptibilities, the longest time

required for rotation of MNPs@GNPs was estimated ~9.3 min whereas the rotation time of the MNPs@FLG was found ~30 min. In the case of MNPs@rGO, the rotation time was found at 1.03 min. Hence, it has been concluded that 1 mT (for MNPs@GNPs and MNPs@FLG) and 20 mT (for MNPs@rGO) are the suitable field strengths to orient efficiently the nanomaterials into the epoxy resin in one-hour period.

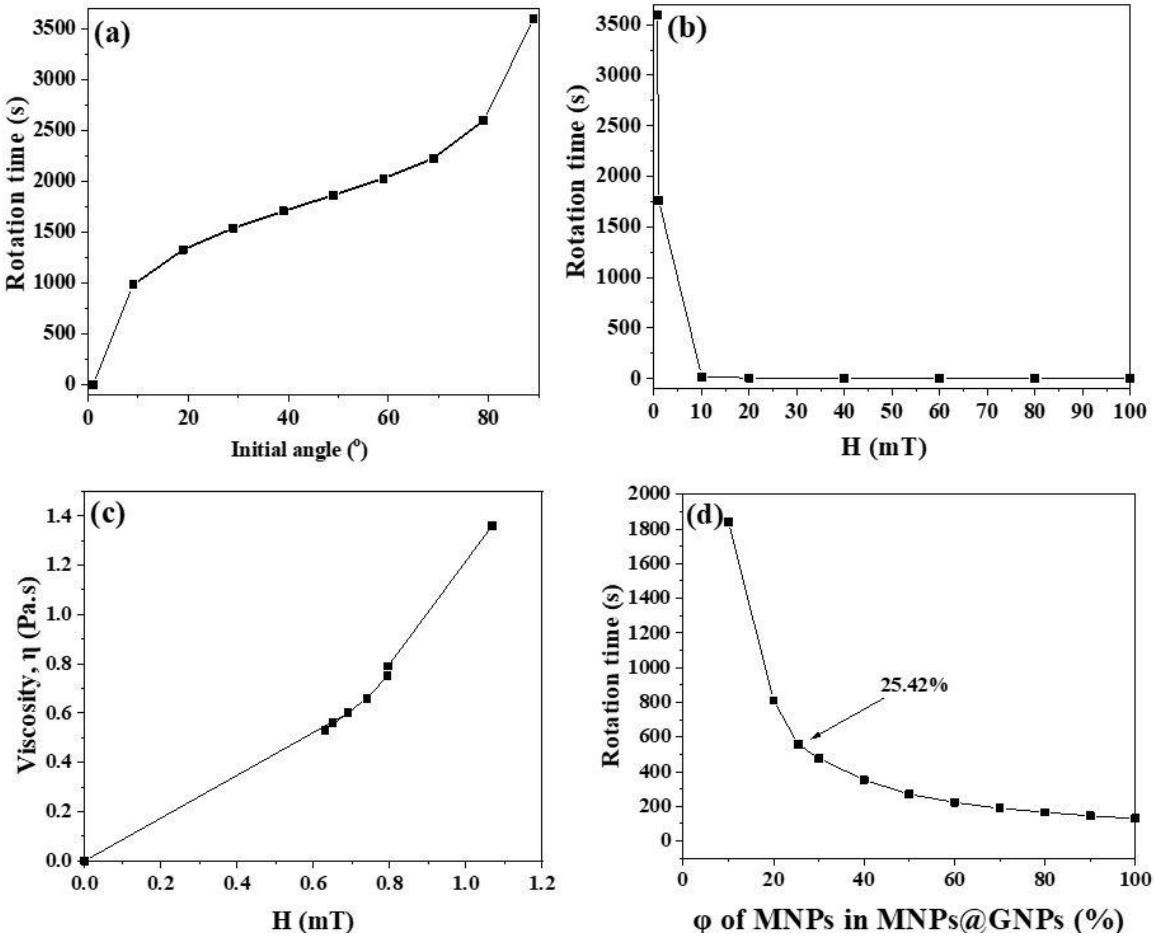


Figure 6. 2. Plots of the rotation time as a function of the initial angle for the MNPs@GNPs (a), magnetic field strength (b), viscosity of the epoxy suspensions filled with 1 wt. %, 2 wt. % and 4 wt. % MNPs@GNPs HSM and TRM mixed (c) and volume fraction of MNPs in the MNPs@GNPs.

## 6.3. Dispersion study before the alignment

### 6.3.1. Optical Microscope

The optical analysis was performed in order to investigate the dispersion state of MNPs@GNPs, MNPs@FLG and MNPs@rGO in the epoxy matrix before and after curing. Two different parameters are considered: a) nanofiller concentration and b) mixing method (HSM and TRM). Figure 6.3 (a)-(f) represents the optical micrographs of MNPs@GNPs/epoxy suspensions with different filler loadings (1 wt. %, 2 wt. %, 4 wt. %) at different magnification

levels. Large agglomerations of MNPs@GNPs were observed on the HSM-mixed suspensions (Figure 6.1 (a)- (c)), as marked by the red circles. These features were attributed to vacuum dry process that made the magnetic graphene sheets to deagglomerate with the removal of water, as explained in Chapter 4. No optical evidence of these large agglomerates is seen after TRM mixing (Figure 6.3 (d)- (f)), however, a less dispersed material was observed, performing these lake features, as observed also in Chapter 5 (Figure 5.5). Figure 6.4 illustrates the optical micrographs for 1 wt. %, 2 wt. % and 4 wt. % of MNPs@GNPs mixed by HSM ((a)- (c)) and TRM ((d)- (f)) method. It is obvious that the TRM breaks the large agglomerations of MNPs@GNPs (marked by red circles) and provides a well-dispersed graphene network for all the concentrations. The dispersion state on the TRM-mixed composites seems to improve in comparison with the uncured stage. This may be attributed to the extra mixing process of hardener at HSM, resulting in a better dispersion of the nanofillers. Similar observations were found in Chapter 5.

The freeze-drying process used for MNPs@FLG gave a more 'fluffy' material in powder form and led to the absence of flaky-shape agglomerations (as observed for the MNPs@GNPs) following mixing by HSM. Similarly with MNPs@GNPs/epoxy suspensions, the dispersion degree was worse after the use of TRM (Figure 6.5), especially at low filler loadings. When the concentration was increased to 2 wt. %, the presence of larger agglomerations was observed (Figure 6.5 (d)). However, it needs to be considered that this composite has been manufactured with material with different batch code, resulting in different agglomeration effects. Moreover, it was difficult to identify the dispersion state in the cured state and therefore SEM analysis was used (Section 6.3.3). Similar results were found for MNPs@rGO/epoxy composites (Figure 6.7 and 6.8). Overall, MNPs@FLG was dispersed better than MNPs@GNPs into the epoxy matrix, due to the different drying process. Additionally, the use of TRM was beneficial for all the nanofillers only in the cured stage, providing a higher dispersion level.

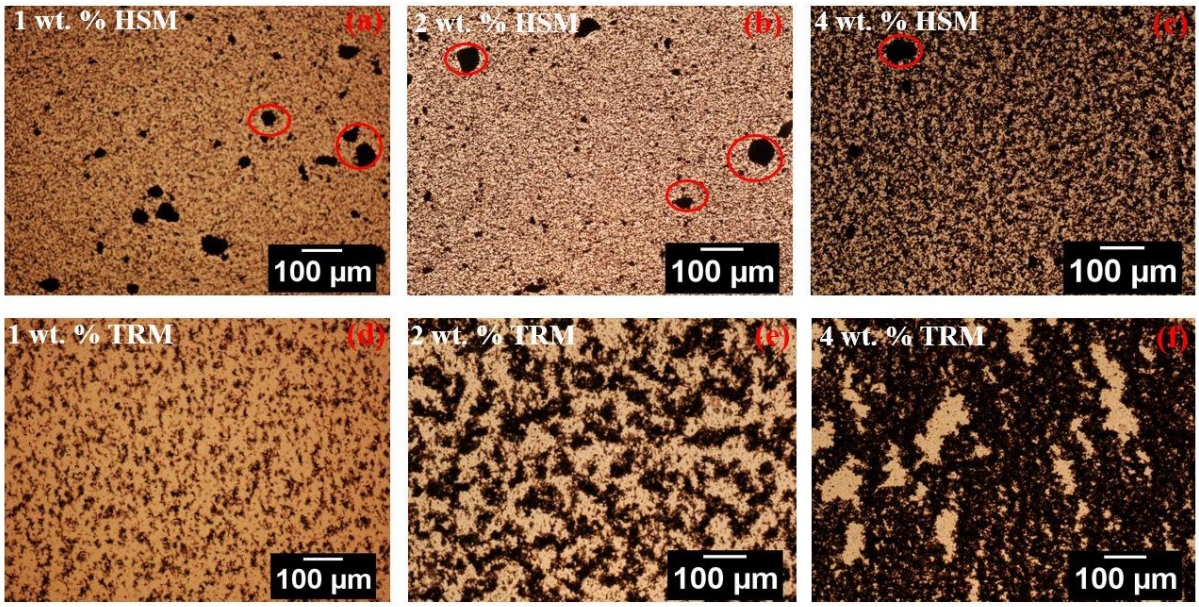


Figure 6. 3. Optical images of 1 wt. %, 2 wt. % and 4 wt. % MNPs@GNPs dispersed in epoxy matrix before curing using HSM (a), (b), (c) and TRM (d), (e) and (f) (scale bar-100 µm). Large agglomerations of MNPs@GNPs were observed on the HSM-mixed suspensions, as marked by the red circles

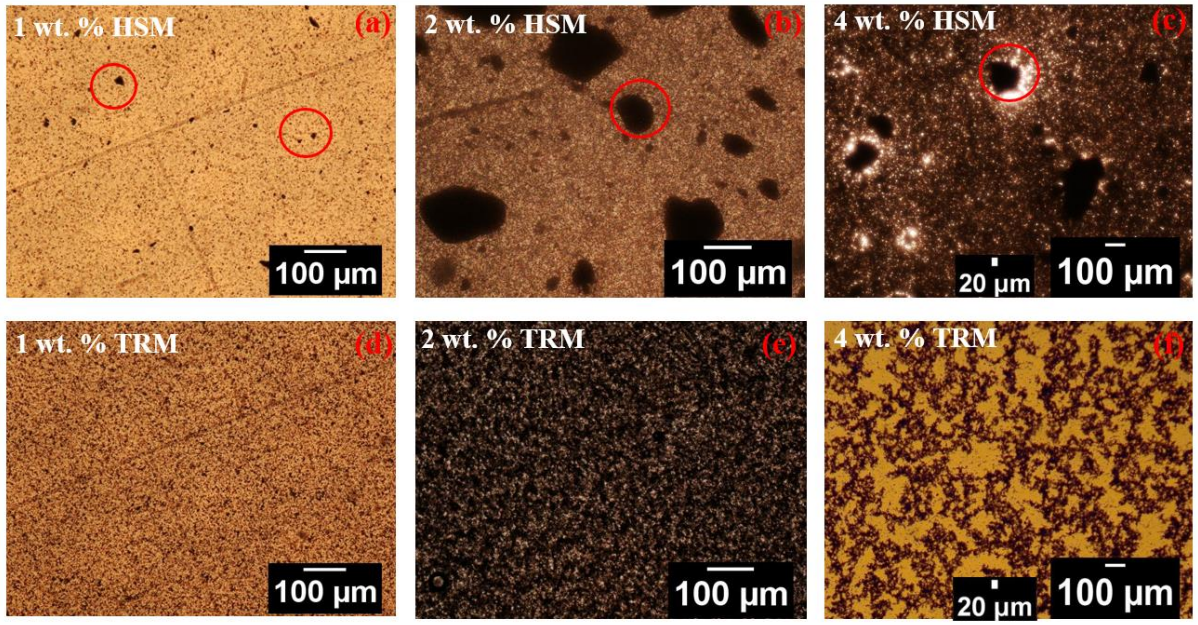


Figure 6. 4.Optical images of 1 wt. %, 2 wt. % and 4 wt. % MNPs@GNPs dispersed in epoxy matrix after curing using HSM (a), (b), (c) and TRM (d), (e) and (f) (scale bar-100 µm). The TRM breaks the large agglomerations of MNPs@GNPs (marked by red circles) and provides a well-dispersed graphene network for all the concentrations.

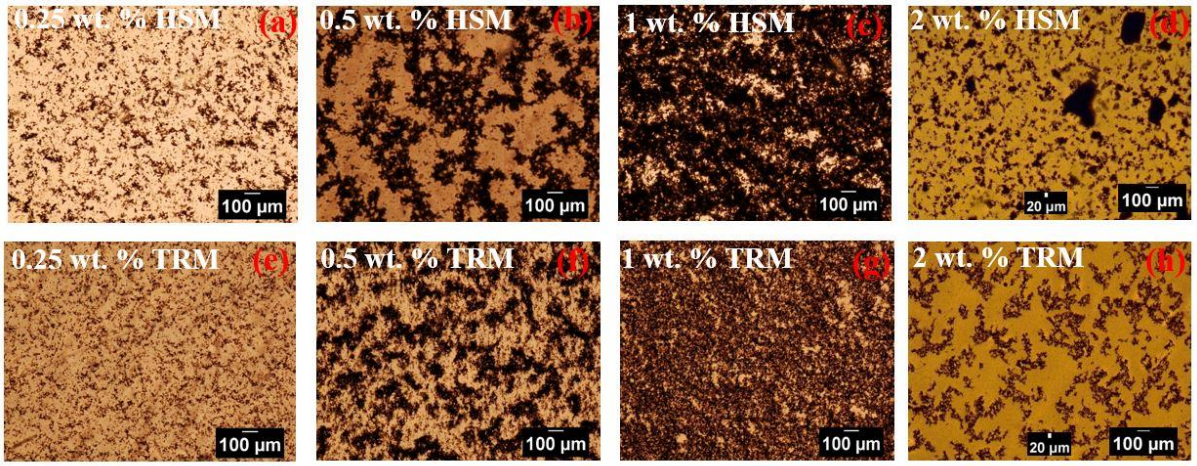


Figure 6. 5. Optical images of 0.25 wt. %, 0.5 wt. %, 1 wt. %, and 2 wt. % MNPs@FLG dispersed in epoxy matrix before curing using HSM (a), (b), (c), (d) and TRM (e), (f), (g) and (h) (scale bar-100 µm).

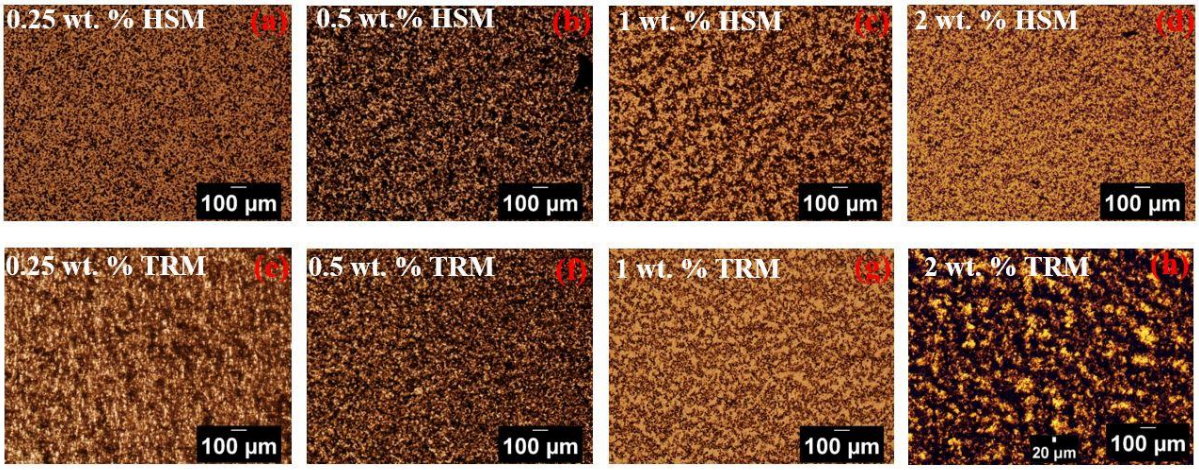


Figure 6. 6. Optical images of 0.25 wt. %, 0.5 wt. %, 1 wt. % and 2 wt. % MNPs@FLG dispersed in epoxy matrix after curing using HSM (a), (b), (c), (d) and TRM (e), (f), (g) and (h) (scale bar-100 µm).

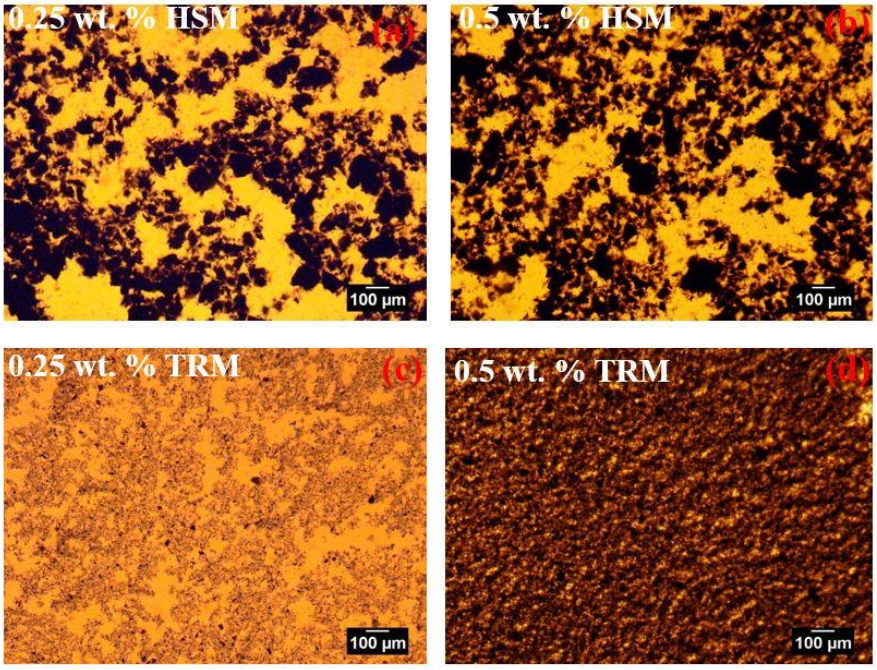


Figure 6. 7. Optical images of 0.25 wt. % and 0.5 wt. % MNPs@rGO dispersed in epoxy matrix before curing using HSM (a), (b), and TRM (c), (d) (scale bar-100 µm).

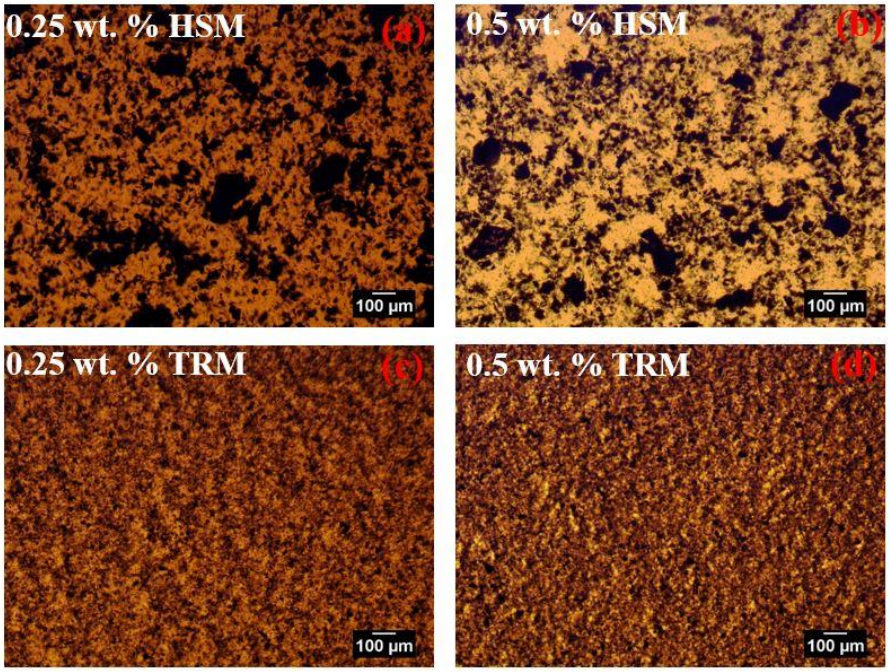


Figure 6. 8. Optical images of 0.25 wt. % and 0.5 wt. % MNPs@rGO dispersed in epoxy matrix after curing using HSM (a), (b), and TRM (c), (d) (scale bar-100 µm).

### 6.3.2. Shear-steady rheology

The dispersion state of MNPs@GNPs, MNPs@FLG and MNPs@rGO into the epoxy resin was studied using shear steady rheology. The results of the rheological analysis are presented in Figure 6.9 and 6.10, in terms of shear viscosity and stress as a function of shear rate. Similarly with the as-received materials (GNPs-COOH and FLG-COOH and rGO, as presented in Chapter 4), the MNPs@GNPs, MNPs@FLG and MNPs@rGO/epoxy suspensions show a Newtonian behaviour until the concentration of 2 wt. %, 0.5 wt.% and 0.25 wt. %, respectively. Non-newtonian behaviour was only observed at 4 wt. %, 1 wt. % and 0.5 wt. % of MNPs@GNPs, MNPs@FLG and MNPs@rGO, respectively and only after the application of TRM mixing. This suggests that the materials have reached the rheological percolation with a shear thinning behaviour seen at low shear rates (Vallés 2017). This is attributed to the creation of a well-dispersed graphene network which increases the viscosity at low shear rates. The power law model is employed to correlate the shear stress and the shear rate (Figure 6.9 (b) and (d) and Figure 6.10 (b)), by the equation (6.7) (Hatami and Ganji 2013):

$$\sigma = K\, x\, \gamma^{n} \qquad (6.7)$$

where σ is shear stress (Pa), K is flow consistency index ($Pa.s^n$), γ is shear rate ($s^{-1}$) and the n is flow behaviour index. For a Newtonian fluid, n= 1 whereas for a pseudoplastic fluid, n<1 (George and Qureshi 2013). The fitting was performed using the Excel 'Solver' tool and the results are included in Table 6.3. For pure epoxy resin and its suspensions, the n value is almost equal to 1, which indicates a Newtonian behaviour. However, lower values of n were observed at 0.95, 0.96 and 0.94 for 4 wt. % MNPs@GNPs, 2 wt. % MNPs@FLG and 0.5 wt. % MNPs@rGO mixed by TRM, respectively, indicating transition to pseudoplastic behaviour due to the better disersion state at these filler loadings. Interestingly, a decreased viscosity was found for 1 wt. % MNPs@GNPs using both mixing methods. In order to evaluate the accuracy of this results, two further batches were measured, and both gave similarly low viscosity. Zhang et al (2013) presented similar results when studying the rheological properties of graphene (Gr) and magnetic graphene sheets (Gr@Fe/$Fe_2O_3$) in a bisphenol F epoxy resin. The authors suggested that the decreased viscosity at 1% wt. Gr could be attributed to the dilution effect of graphene sheets that are not covalently bonded to the epoxy resin, resulting in a constraint release and leads to the viscosity reduction. This phenomenon was explained by Tuteja et al (2007). Another possible reason for the reduced viscosity observed could be slip or an inhomogeneous flow (Zhu, Wei et al. 2010).

In order to investigate the exfoliation effect of processing via TRM, an integrated model was used, as described in Chapter 5. By using the equation (5.2), the liquid shear stresses τ were calculated for the highest filler loadings in which the rheological percolation is reached: 0.36 MPa (4 wt. % MNPs@GNPs), 0.34 MPa (1 wt. % MNPs@FLG) and 0.58 MPa (0.5 wt. % MNPs@rGO). These stresses values are in the range of the reported ISS values, which supports the process of the partial exfoliation, giving graphene with a random rotational stacking (Soule and Nezbeda 1968, Throckmorton and Palmese 2015).

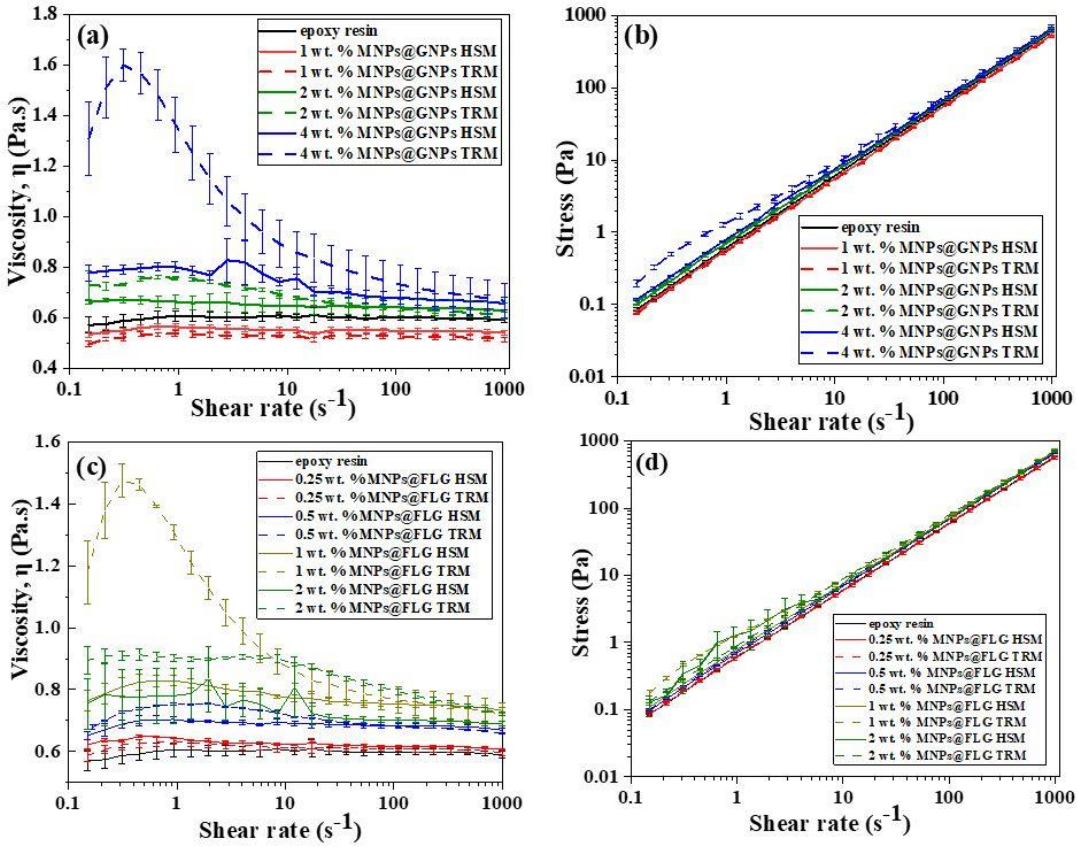


Figure 6. 9. Steady shear curves (shear viscosity and stress as a function of shear rate) of MNPs@GNPs ((a)-(b)) and MNPs@FLG ((c) – (d)) dispersions into the epoxy resin at different concentrations.

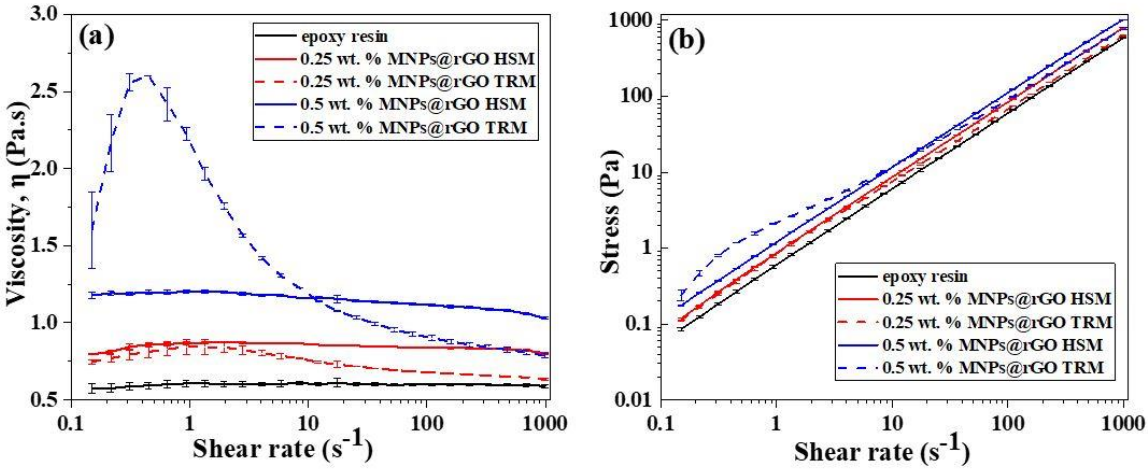


Figure 6. 10. Steady shear curves (shear viscosity and stress as a function of shear rate) of MNPs@rGO ((a)-(b)) dispersions into the epoxy resin at different concentrations.

Table 6. 3. The rheological data of pure epoxy and the liquid epoxy suspensions.

| Sample | n | K | η (0.31 $s^{-1}$) |
|---|---|---|---|
| **Epoxy resin** | 0.99 | 0.79 | 0.58 |
| **1 wt. % MNPs@GNPs HSM** | 0.99 | 0.75 | 0.54 |
| **1 wt. % MNPs@GNPs TRM** | 0.98 | 0.74 | 0.52 |
| **2 wt. % MNPs@GNPs HSM** | 0.98 | 0.83 | 0.67 |
| **2 wt. % MNPs@GNPs TRM** | 0.97 | 0.84 | 0.73 |
| **4 wt. % MNPs@GNPs HSM** | 0.98 | 0.86 | 0.79 |
| **4 wt. % MNPs@GNPs TRM** | 0.95 | 0.94 | 1.59 |
| **0.25 wt. % MNPs@FLG HSM** | 0.98 | 0.79 | 0.63 |
| **0.25 wt. % MNPs@FLG TRM** | 0.98 | 0.80 | 0.62 |
| **0.5 wt. % MNPs@FLG HSM** | 0.98 | 0.86 | 0.68 |
| **0.5 wt. % MNPs@FLG TRM** | 0.98 | 0.86 | 0.72 |
| **1 wt. % MNPs@FLG HSM** | 0.98 | 0.89 | 0.80 |
| **1 wt. % MNPs@FLG TRM** | 0.96 | 0.94 | 1.47 |
| **2 wt. % MNPs@FLG HSM** | 0.99 | 0.73 | 0.8 |
| **2 wt. % MNPs@FLG TRM** | 0.96 | 0.97 | 0.9 |
| **0.25 wt.% MNPs@rGO HSM** | 0.97 | 0.97 | 0.84 |
| **0.25 wt. % MNPs@rGO TRM** | 0.96 | 0.79 | 0.79 |
| **0.5 wt. % MNPs@rGO HSM** | 0.95 | 1.40 | 1.19 |
| **0.5 wt. % MNPs@rGO TRM** | 0.94 | 1.22 | 2.56 |

### 6.3.3. Scanning Electron Microscopy

The cryo-fracture surface of MNPs@GNPs/epoxy composites (Figure 6.11) and MNPs@FLG /epoxy composites (Figure 6.12) were analysed by Scanning Electron Microscopy (SEM). For

2 wt. % MNPs@GNPs mixed in epoxy resin by HSM, nanohybrid aggregates can be observed under SEM at low magnification (Figure 6.11 (a) and (b), x1000 and x5000), which have been marked by red arrows. The insets at Figure 6.11 (a) and (b) at a higher magnification (x5000 and x10000, respectively) demonstrate the poor dispersion of MNPs@GNPs that pull out from the epoxy matrix, which is consistent with the results of the optical microscope (Figure 6.4 (b)). Therefore, the dispersion state of MNPs@GNPs may result in poor mechanical properties, which will be examined further by the DMA measurements. In the case of TRM-mixed samples (Figure 6.11 (c) and (d), x1000 and x5000), the roughness of the fracture surface has increased significantly with no evidence of large agglomerations. These results are in good agreement with the optical micrographs (Figure 6.4 (e)). The insets at Figure 6.11 (c) and (d) (at magnification x5000 and x10000, respectively) show magnetic graphene sheets (marked by red arrows), but large aggregates are not present, indicating better dispersion.

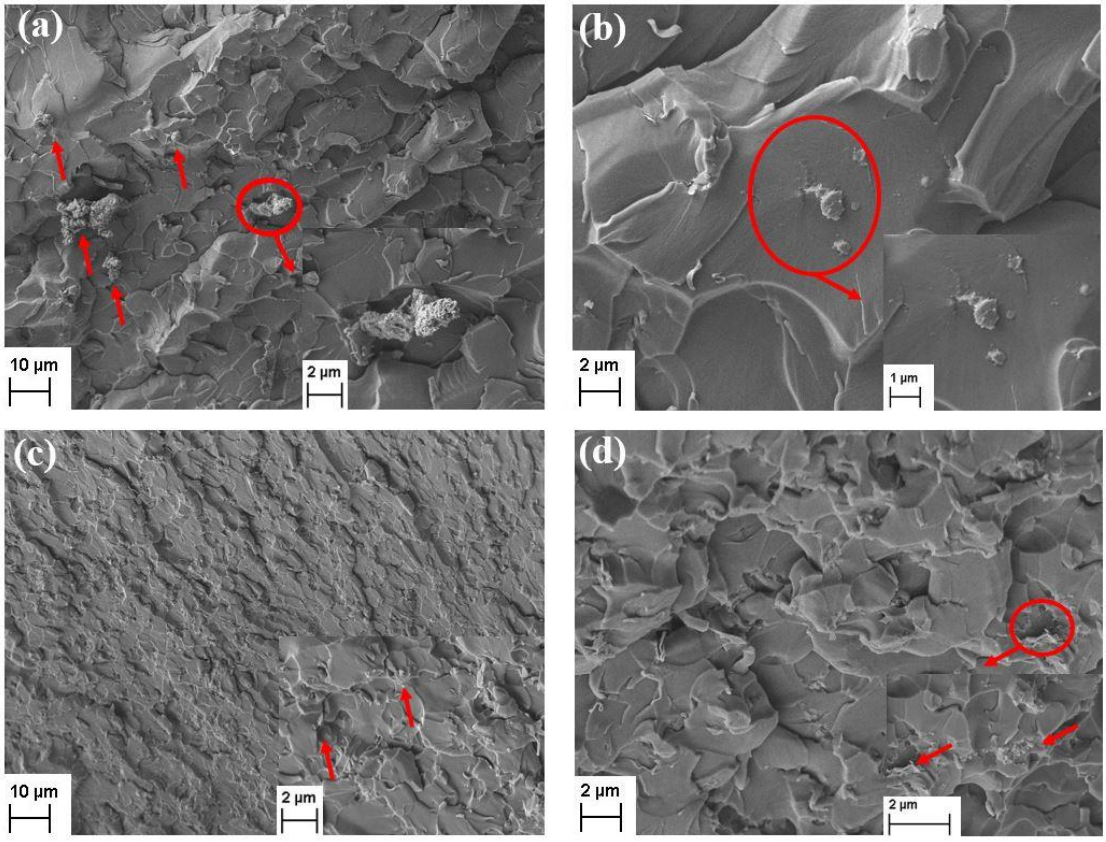


Figure 6. 11. SEM images of fracture surface of 2 wt. % MNPs@GNPs/epoxy composites mixed by HSM (a), (b) and TRM (c), (d). The insets highlighted the presence of aggregates. MNPs@GNPs aggregates have been marked by red arrows.

SEM images of 2 wt. % MNPs@FLG/epoxy composites are presented in Figure 6.12 (a) and (b) (x1000 and x10000, respectively) for HSM and Figures 6.12 (c) and (d) (x1000 and x10000,

respectively) for TRM. As with the MNPs@GNPs composites, the HSM method provides poor dispersion with some aggregates highlighted by red arrows in Figure 6.12 (b). These agglomerations may prevent the entry of hardener into the MNPs@GNPs and MNPs@FLG aggregates, which act as stress concentrations, affecting the curing degree and mechanical performance. This will be discussed later in this chapter when representing DMA analysis. By introducing the magnetic nanohybrids into the epoxy resin with the use of TRM, a uniform dispersion was achieved, as shown in Figure 6.12 (c) (x1000). It is clear by the Figure 6.12 (d) (x10000) that the epoxy resin masks the magnetic nanofillers, resulting in a greater dispersibility between the MNPs@FLG and the epoxy resin.

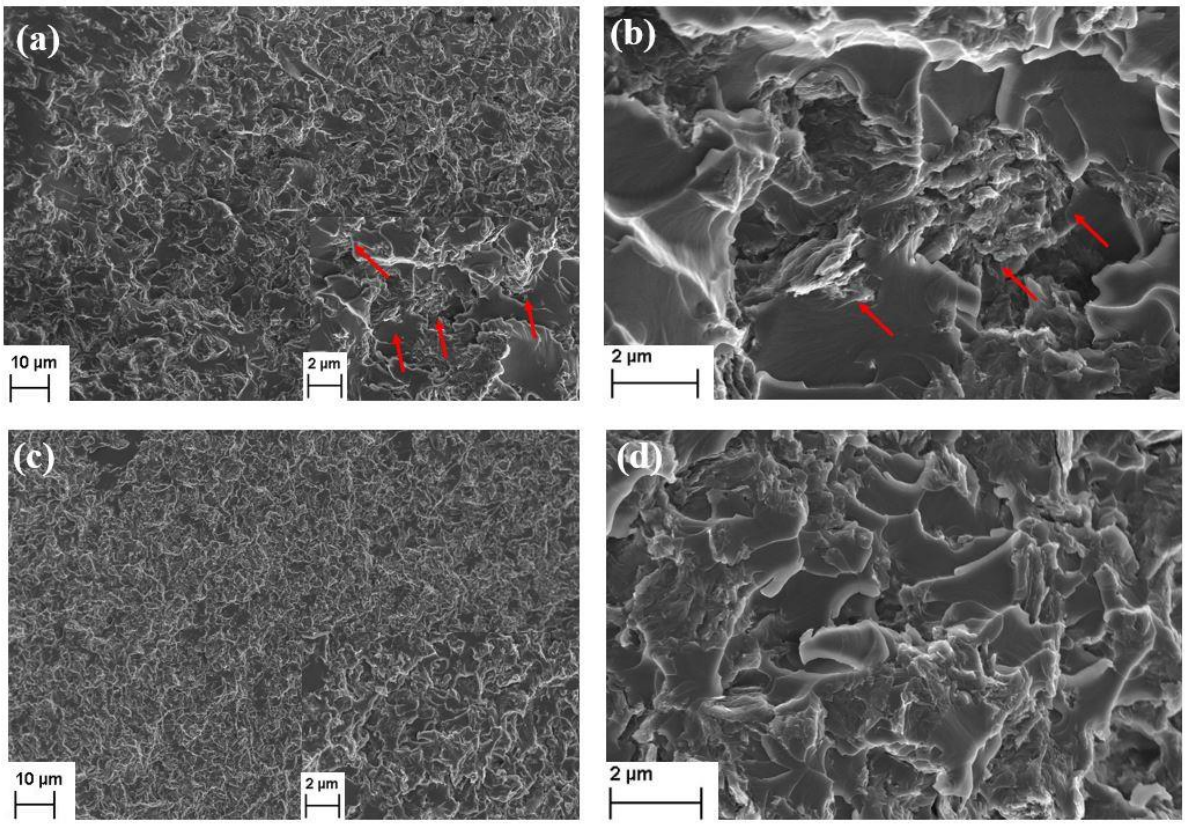


Figure 6. 12. SEM images of 2 wt. % MNPs@FLGs/epoxy composites mixed by HSM (a), (b) and TRM (c), (d). The inset of (a) and the red arrows at (a)-(b) highlighted the presence of aggregates.

### 6.3.4. Raman Spectroscopy

Raman spectra of the pure epoxy and its composites filled with 1 wt. % MNPs@GNPs (a), 1 wt. % MNPs@FLG (b) and 0.5 wt. % MNPs@rGO mixed by HSM and TRM are shown in Figure 6.13. Raman spectra of MNPs@GNPs, MNPs@FLG and MNPs@rGO powders are included in Chapter 4. Here, the Raman excitation was different (785 nm) in comparison with the Raman study of the powders (514 nm) in order to minimise the fluorescence background

by the epoxy resin. Raman spectra Raman bands corresponding to epoxide vibration are in the range of 1230 $cm^{-1}$-1280 $cm^{-1}$(marked by blue star) and other Raman peaks at 1112 $cm^{-1}$, 1186 $cm^{-1}$ and 1608 $cm^{-1}$ (marked by red stars) assigning to resin backbone vibrations (Vaskova and Křesálek 2011). By adding 1 wt. % of the MNPs@GNPs (Figure 6.13 (a)), it can be detected only the G peak (1580 $cm^{-1}$). In the case of 1 wt. % MNPs@FLG /composites and 0.5 wt. % MNPs@rGO (Figure 6.13 (b) and (c)), the spectra are quite different with the broad G and D bands, and a D band (~1315 $cm^{-1}$) that is of higher intensity than the G band (~1600 $cm^{-1}$). These features with the absence of 2D band for all the materials (2700 $cm^{-1}$) are related to the formation of $sp^3$ carbon bonds by breaking the $sp^2$ carbon network (Malard, Pimenta et al. 2009).

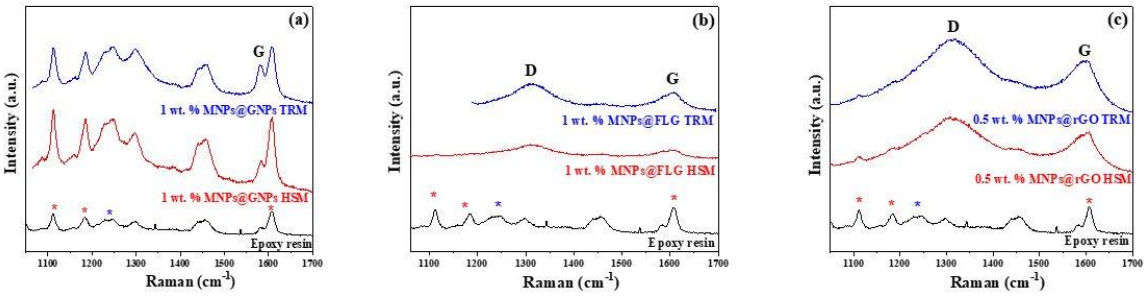


Figure 6. 13. Raman Spectra of 1 wt. % MNPs@GNPs (a), 1 wt. % MNPs@FLG (b) and 0.5 wt. % MNPs@rGO (c)/epoxy composites mixed by HSM and TRM methods (laser excitation: 785 nm).

## 6.4. Alignment of magnetic nanohybrids (MNPs@graphene) under low magnetic fields

The alignment of magnetic graphene sheets in the epoxy matrix was experimentally investigated by Optical microscope, Scanning Electron Microscope (SEM) and Small-angle X-ray diffraction (SAXS). The alignment efficiency of the magnetic nanohybrids in the presence of an external magnetic field was studied by changing the dispersion state, the magnetic field strength and the nanofiller concentration.

Figure 6.14 shows the real-time growth and alignment at the various times of 0, 1, 10, 30, 60, 120 min in the presence of a magnetic field (100 mT), as observed by the optical-magnetic system (Figure 6.14 (a)) for 1 wt.% MNPs@GNPs dispersed into the epoxy resin by HSM ((a)-(f)) and TRM ((g)-(l)). Before the application of the magnetic field (0 min), the magnetic nanohybrids are randomly dispersed (Figure 6.14 (a) and (g)) and when the magnetic field is applied, chain like clusters of nanofillers begin to be formed in the first minute (Figure 6.14. (b) and (h) for HSM and TRM-mixed samples, respectively). These observations confirmed

the above theoretical modelling results, which proved that the rotation time for MNPs@GNPs at 100 mT is 0.17 sec. More investigation will be performed by SEM in order to confirm the presence of oriented graphene sheets into the epoxy matrix. Within a very short time (10 min), the magnetic clusters are connecting (marked by red circles) and the length of the clusters keeps increasing steadily until 30 min, creating epoxy-rich regions and magnetic clusters-rich regions along the applied field direction. In order to evaluate the effect of MNPs@GNPs concentration, different MNPs@GNPs content (1 wt. %, 2 wt. % and 4 wt. %) were prepared. Increasing the concentration, the length of the aligned chains was increased (as observed in Figure 6.15).

With a better dispersion state achieved using the TRM method, thinner magnetic clusters are formed into the epoxy matrix (Figure 6.14 ((g)-(l))). No particle movement was noticed after the time of 60 min for both mixing methods, suggesting that the magnetic field can be removed after one-hour without effecting the alignment achieved. Hence, magnetic graphene sheets have formed stable magnetic clusters during the curing process of the epoxy system (before reaching the gelation time), providing an easy and scalable manufacturing method.

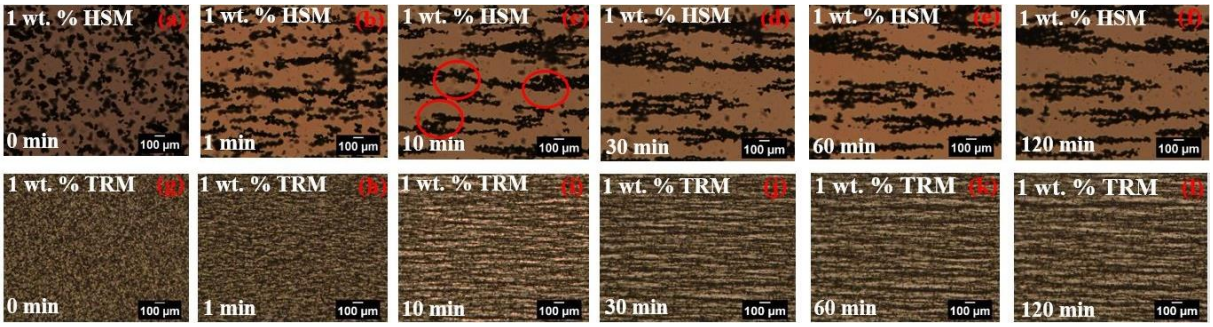


Figure 6. 14. Optical microscope images of 1 wt. % MNPs@GNPs mixed by HSM ((a)-(f)) and TRM ((g)-(l)) and their alignment into the epoxy resin under the application of 100 mT magnetic field after a time of 0 min, 1 min, 10 min, 30 min, 60 min and 120 min.

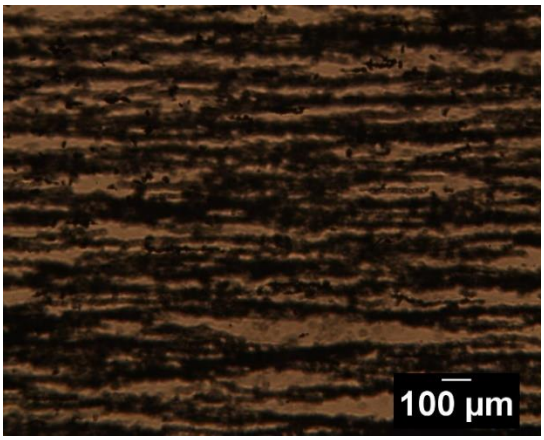


Figure 6. 15. Optical microscope image of 2 wt. % MNPs@GNPs mixed by HSM aligned at 100 mT.

To investigate the effect of magnetic-field intensity, the alignment of 1 wt. % MNPs@GNPs mixed by TRM was examined within a range of field strengths (0.5 mT to 100 mT). As shown in Figure 6.16 (a) and (b), there is no optical evidence for an alignment of the magnetic clusters under the application of the magnetic fields 0.5 mT and 1mT, respectively. However, there is a slight difference in dispersion state at 1 mT. After 10mT, the nanofillers start to form magnetic chains that become longer, wider and more separated as the magnetic field increases.

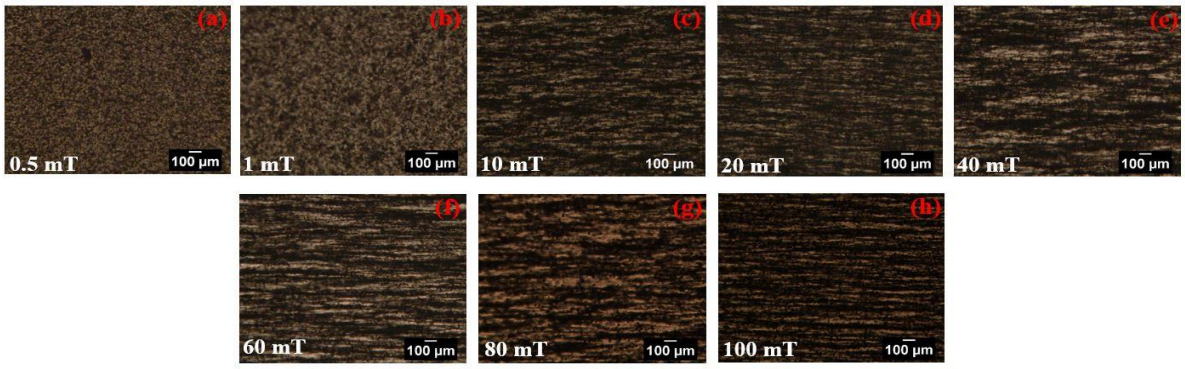


Figure 6. 16. Optical microscope images of 1 wt. % MNPs@GNPs mixed by TRM under the application of various magnetic field: 0.5 mT (a), 1 mT (b), 10 mT (c), 20 mT (d), 40 mT (e), 60 mT (f), 80 mT (g) and 100 mT (h) at a real-time of 60 min.

In the case of MNPs@FLG (Figure 6.17), the contribution of the aspect ratio was examined. Although, the aspect ratio of MNPs@FLG is higher (XRD data; thickness: 2.35 nm) than that one of MNPs@GNPs (XRD data; thickness: 18 nm), the rotation time has not changed significantly. Specifically, it was found to be 0.21 sec (using the theoretical model) under the application of 100 mT. However, the rotation time of MNPs@rGO (thickness: < 3 nm) was estimated at 35.63 sec, which is due to their higher planar size of 40 μm. Therefore, the larger graphene sheets should be harder to rotate in the resin (longer rotation time) as well as the magnetic moment will be increased in order to align them, as proved by the theoretical model for the MNPs@rGO.

Here, a different microstructure was observed by the optical microscope, providing a denser aligned material. The alignment of the MNPs@FLG was exhibited in the direction of the magnetic field (100 mT) at 10 min (Figure 6.17 (c)). After 30 min, evidence of aligned clusters was difficult to be noticed, as shown in Figure 6.17 (d)), without obvious differences on the length of the cluster after the duration of 60 min and 120 min (Figure 6.17 (e) and (f)). Red

arrows were used to highlight the direction of the magnetic clusters. The lack of alignment evidence by using optical microscope was found for TRM-mixed sample (Figure 6.17 (g)-(l)).

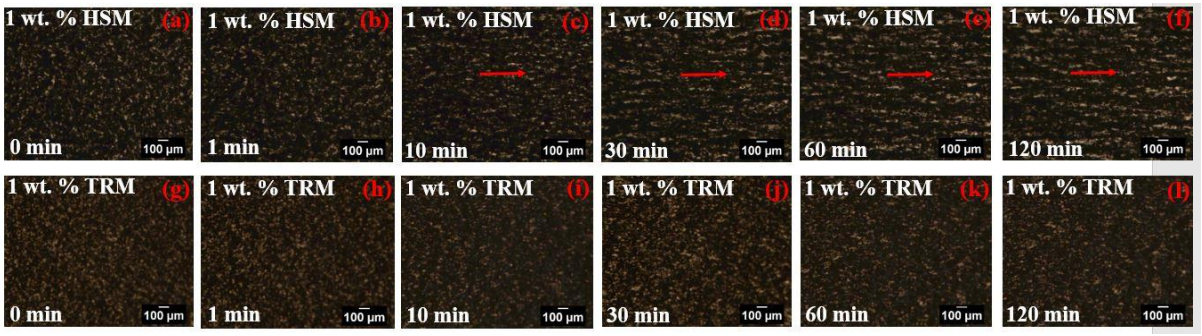


Figure 6. 17. Optical microscope images of 1 wt. % MNPs@FLG mixed by HSM ((a)-(f)) and TRM ((g)-(l)) and their alignment into the epoxy resin under the application of 100 mT magnetic field after a time of 0 min, 1 min, 10 min, 30 min, 60 min and 120 min. The red arrows indicate the direction of the magnetic clusters.

In order to study the effect of the magnetic field and filler concentration, two different magnetic fields (1 mT and 100 mT) were applied at three different concentrations (0.25 wt.%, 0.5 wt. % and 1 wt. %) of MNPs@FLG composites. Figure 6.18 presents the optical images of the alignment achieved under these experimental conditions. Similarly, with the MNPs@GNPs, any alignment can be confirmed optically at the lower magnetic field (1 mT) whereas large agglomerations of MNPs@FLG observed in the direction of the highest magnetic field (100 mT), especially for 0.25 and 0.5 wt. % (Figure 6.18. (d) and (e), respectively).

Raman spectroscopy was performed for 1 wt. % MNPs@FLG at 0 mT, 1 mT and 100 mT by mapping the relative intensity of the MNPs@FLG Raman bands over a mesoscopic area of the specimens. As shown in Figure 6.19 (Raman maps (a) and (b)), a well-dispersed MNPs@FLG can been observed after the use of TRM. With the use of 1mT (Raman maps (c), (d)), the distribution of the magnetic graphene sheets was changed, which is more obvious (Raman maps (e), (f)) with the highest magnetic field (100mT). Although, Raman showed that a poorer dispersion state occurs by the application of the magnetic field, no clear evidence of alignment was obtained. For this reason, SEM and SAXS (Small angle X-ray Scattering) analysis will be used.

Overall, small and thick graphene sheets (MNPs@GNPs) showed a higher migration behaviour (less drag forces under the applied magnetic field), performing the distinct lines of aligned ordered structures whereas the alignment of the thinner and larger flakes (MNPs@FLG) was

difficult to identify it under the optical microscope. Higher is the planar size of the nanofiller, more are the drag forces, providing a denser material on the optical microscope.

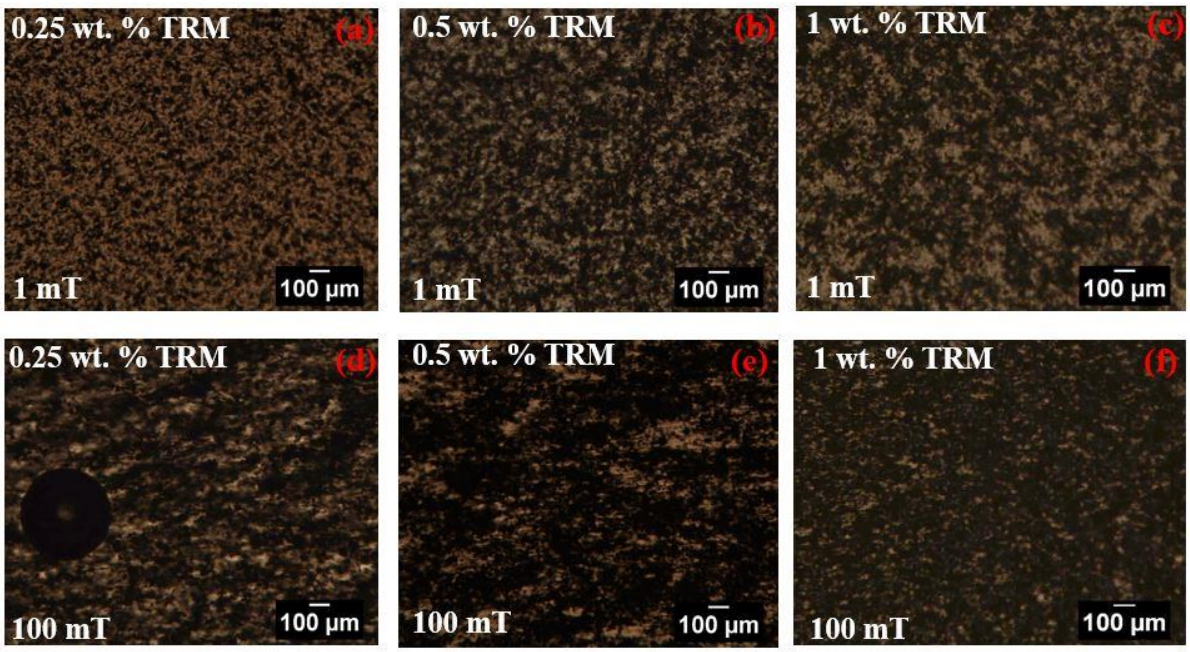


Figure 6. 18.Optical microscope images of 0.25 wt.% (a), (d), 0.5 wt. % (b), (e), and 1 wt. % (c), (f) of MNPs@FLG mixed by TRM under the application of 1 mT and 100 mT at a real-time of 60 min.

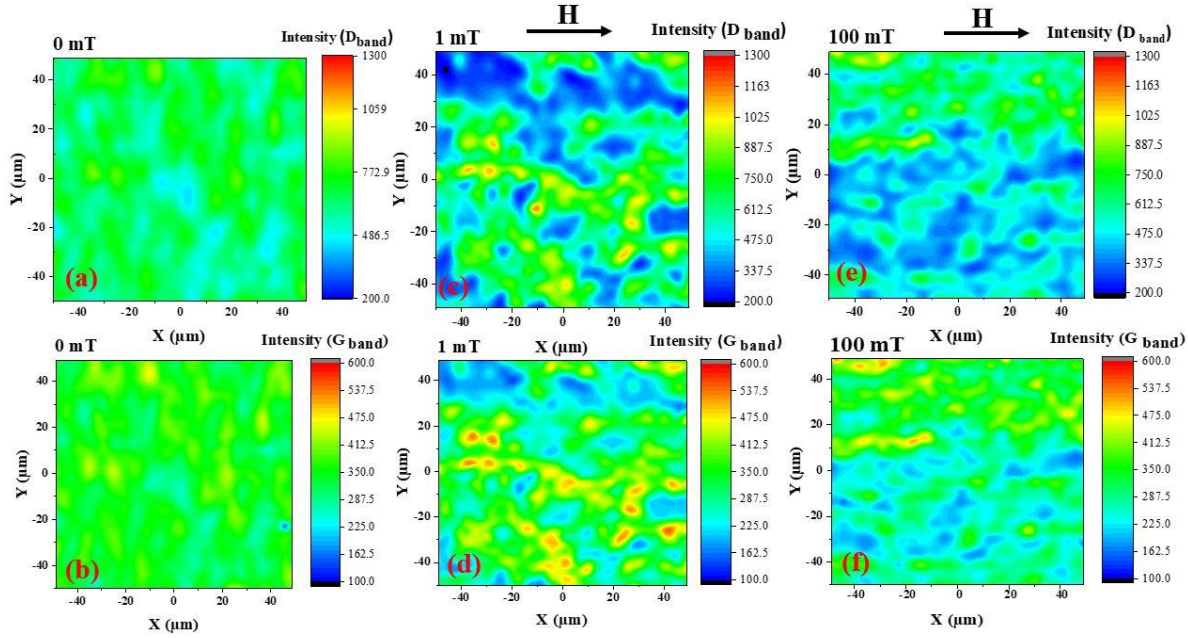


Figure 6. 19.Maps of normalized intensity ratio of 1 wt. % MNPs@FLG D-band at 1312 $cm^{-1}$((a), (c), and (e)) and G-band at 1609 $cm^{-1}$((b), (d) and (f)) to epoxy system, showing the distribution of MNPs@FLG in nanocomposites under the application of 0 mT, 1 mT and 100 mT field strength. The black arrow indicates the direction of the magnetic field.

Figure 6.20 represents the real-time images at the various times (0, 1, 10, 30, 60, 120 min) for the alignment of 0.25 wt. % MNPs@rGO/epoxy composite under a 7 mT magnetic field, after mixing with HSM ((a)-(f)) and TRM ((g)-(l)). Large agglomerations were observed for the HSM-mixed composite and no indication of alignment can be seen. There is also no indication of alignment in the case of the TRM-mixed composite and dispersion quality appears to reduce with time in the magnetic field. Increasing the concentration, it was difficult to identify any alignment observation, especially at TRM (Figure 6.21 (a)- (b)). The effect of the magnetic field was studied using two different magnetic fields: 15 mT and 30 mT (Figure 6.21 (c) and (d)). It can be seen clearly that an alignment occurs on this high magnetic fields, which are in a good agreement with the results of the theoretical model.

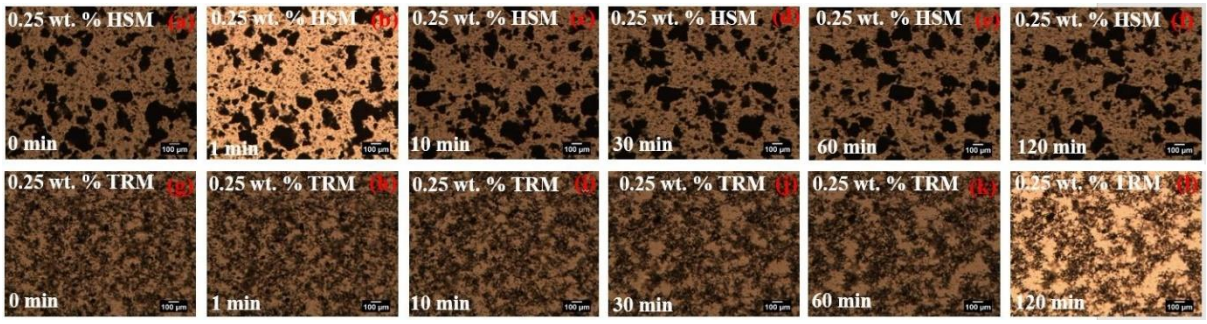


Figure 6. 20.Optical microscope images of 0.25 wt.% MNPs@rGO mixed by HSM ((a)-(f)) and TRM ((g)-(l)) and their alignment into the epoxy resin under the application of 7 mT magnetic field after a time of 0 min, 1 min, 10 min, 30 min, 60 min and 120 min.

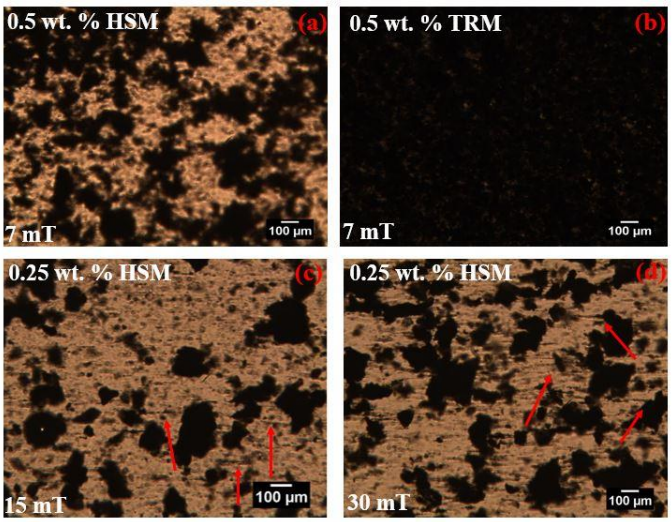


Figure 6. 21. Optical microscope image of 0.5 wt. % MNPs@rGO mixed by HSM (a) and TRM (b) aligned at 7 mT, 0.25 wt. % MNPs@rGO mixed by HSM aligned at 15 mT (c) and 30 mT (d). Aligned MNPs@rGO are observed, which has been highlighted by red arrows.

The distribution and orientation of GNPs-COOH and MNPs@GNPs in the epoxy resin was evaluated also using Scanning Electron microscopy (SEM) of samples fractured after immersion in liquid nitrogen. The images of GNPs-COOH were included in order to control any preferable alignment under the applied magnetic field. Images of the fractured surfaces of pure epoxy, 1 wt. % GNPs-COOH (mixed by HSM) and 1 wt. % MNPs@GNPs (mixed by HSM and TRM)/epoxy composites are presented in Figure 6.22. Comparing with the very smooth surface of the epoxy resin (Figure 6.22 (a)), the epoxy composite containing 1 wt. % GNPs-COOH (mixed by HSM) exhibits a relatively rough surface with river-like patterns in the direction of the fracture growth (Figure 6.22 (b)). No preferred alignment of the GNPs-COOH sheets was found when a relatively high magnetic field (100 mT) was applied, and a similar fracture surface is seen (Figure 6.22 (c)). When 1 wt. % MNPs@GNPs are randomly dispersed using HSM into the epoxy matrix (Figure 6.22 (d)) and (g)), large agglomerations were found (marked by yellow arrows) and no indication of alignment can be seen (at 0 mT). By contrast, the HSM nanocomposites subjected to the magnetic field of 100 mT (Figure 6.22 (e)) and (h)), the orientation of the magnetic nanohybrids is revealed (marked by yellow arrows) and magnetic clusters formed along the direction of the magnetic field can be seen. The incorporation of MNPs@GNPs into the epoxy matrix when mixed by TRM and aligned at the same field strength leads in a rougher fracture surface (Figure 6.22 (f)), making less identical its alignment. This is due to the initial better dispersion of the nanofiller, resulting in thinner aligned clusters (as seen in the optical microscope image, Figure 6.14) and hence less smooth epoxy-rich regions. SEM micrograph at a higher magnification (Figure 6.22 (i), 5000 X) shows the MNPs@GNPs (marked by yellow arrows) are connected and aligned parallel to the applied magnetic field direction.

Following the theoretical calculations (Section 5.3.2), it is expected that the MNPs@GNPs would be aligned along the direction of 1 mT. Although, the optical microscope images showed no alignment at this low magnetic field strength (Figure 6.16 (b)), SEM analysis was performed in the fractured surface of 1 wt.% MNPs@GNPs (mixed by TRM) in order to investigate any possible filler orientation. As shown in SEM images (6.23 (a)-(c)), the magnetic graphene sheets formed small chain-like clusters and oriented parallel to the direction of the magnetic field (marked by yellow arrows), confirming the results of the theoretical model.

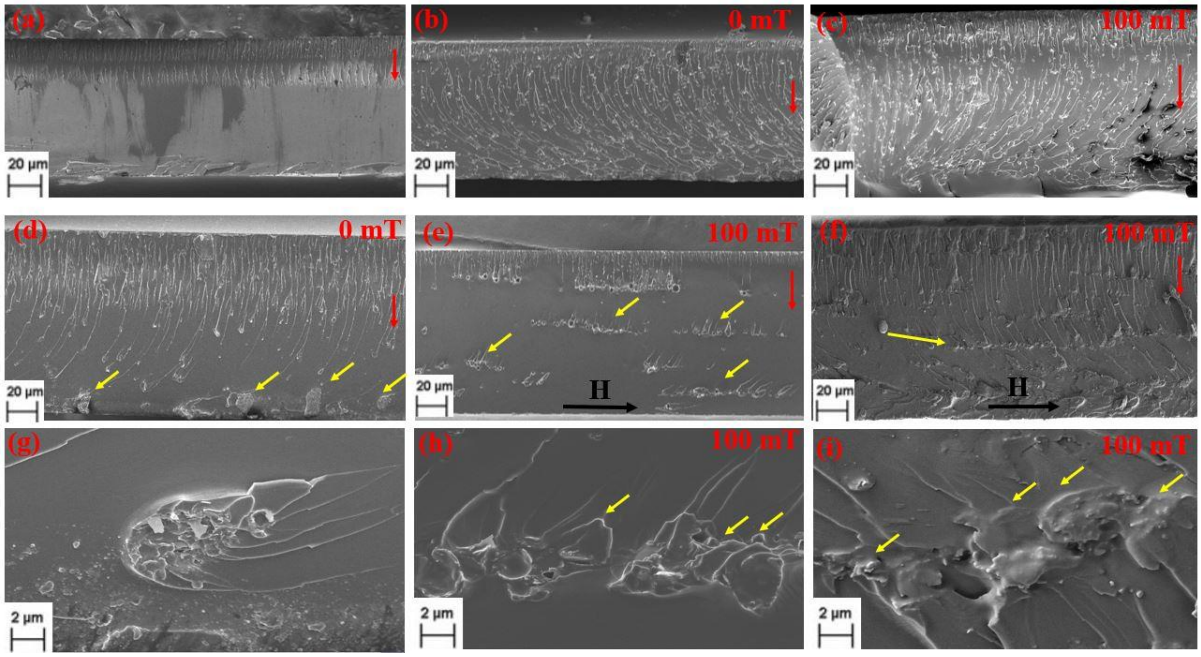


Figure 6. 22. SEM images of fracture surface of pristine epoxy resin (a), 1 wt. % GNPs-COOH/epoxy composite mixed by HSM with no magnetic field application (b), 1 wt. % GNPs-COOH/epoxy composite mixed by HSM at 100 mT (c), 1 wt. % MNPs@GNPs/epoxy composite mixed by HSM with no magnetic field application (d) and (g), 1 wt. % MNPs@GNPs/epoxy composite mixed by HSM at 100 mT (e) and (h) and 1 wt.% MNPs@GNPs/epoxy composite mixed by TRM at 100 mT (f) and (i). The direction of the magnetic field is indicated by black arrow while the yellow arrows indicate the random dispersed and aligned MNPs@GNPs. The red arrows used for the direction of the crack propagation of the fracture surfaces.

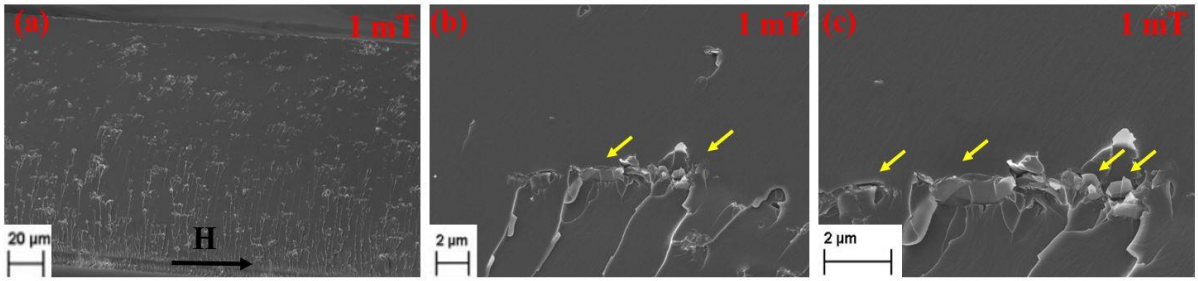


Figure 6. 23. SEM images of fracture surface of 1 wt. % MNPs@GNPs/epoxy composite (mixed by TRM) at 1 mT (a)-(c)). The direction of the magnetic field is indicated by black arrow while the yellow arrows indicate the orientation of MNPs@GNPs.

The distribution and orientation of FLG-COOH and MNPs@FLG is evaluated by SEM in Figure 6.24. A homogeneous dispersion was achieved using TRM for both FLG-COOH (Figure 6.24 (a) and (d)) and MNPs@FLG (Figure 6.24 (b) and (e)). The orientation of 1 wt. % MNPs@FLG was confirmed, as shown in Figure 6.24 (f), with a number of flakes appeared

to be oriented (marked by yellow arrows) under the direction of the applied magnetic field (100 mT). However, agglomerated graphene sheets can be seen more clearly at the higher magnification image at 10000 X (Figure 6.25 (b)) when compared with the random dispersed material (Figure 6.25 (a)). These results are in good agreement with the Raman mappings. Moreover, Figure 6.26 (a) shows the well dispersed MNPs@FLG when mixed by HSM and some evidence of aligned graphene sheets under the application of 100 mT (Figure 6.25 (b)). Similarly, the orientation of MNPs@FLG under low magnetic field (1 mT) was confirmed by Figure 6.26 (c)- (d), in which agglomerated chains of graphene sheets are formed in the direction of the external magnetic field. Although, the optical images did not give the proof of alignment, these SEM results allow us to confirm the orientation of MNPs@FLG under the applied magnetic fields.

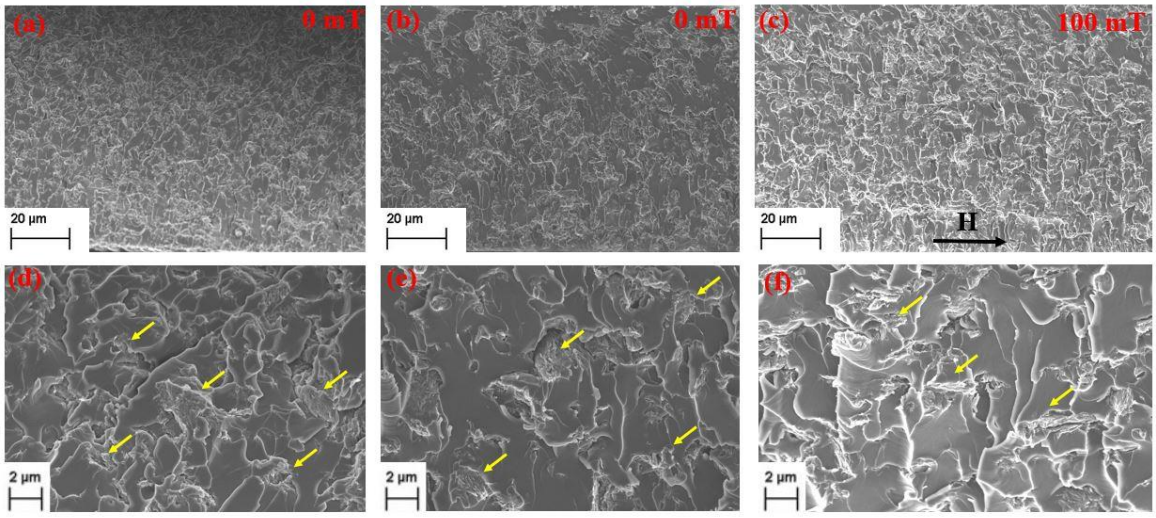


Figure 6. 24. SEM images of fracture surface of 1 wt. % FLG-COOH mixed by TRM (a) and (d) with no magnetic field application, 1 wt. % MNPs@FLG/epoxy composite mixed by TRM with no magnetic field application (b) and (e) and 1 wt. % MNPs@FLG/epoxy composite mixed by TRM at 100 mT (c) and (f). The direction of the magnetic field is indicated by black arrow while the yellow arrows indicate the random dispersed and aligned MNPs@FLG.

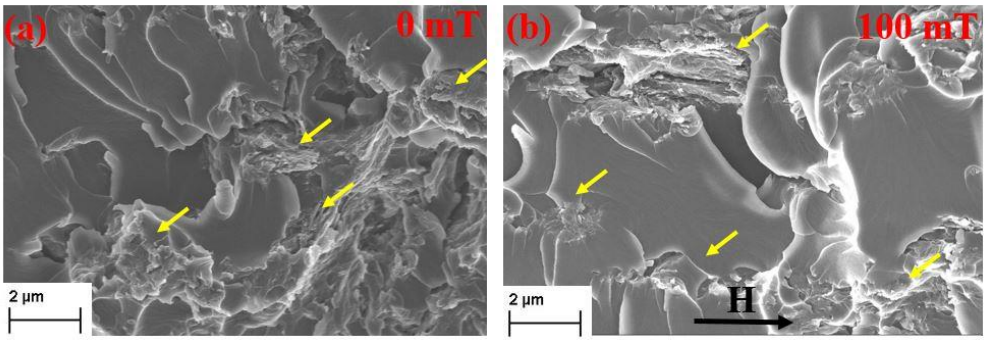


Figure 6. 25. SEM micrographs of 1 wt.% MNPs@FLG/epoxy composites mixed by TRM at 0 mT (a) and 100 mT (b). The direction of the magnetic field is indicated by black arrow while the yellow arrows indicate the random dispersed and aligned MNPs@FLG.

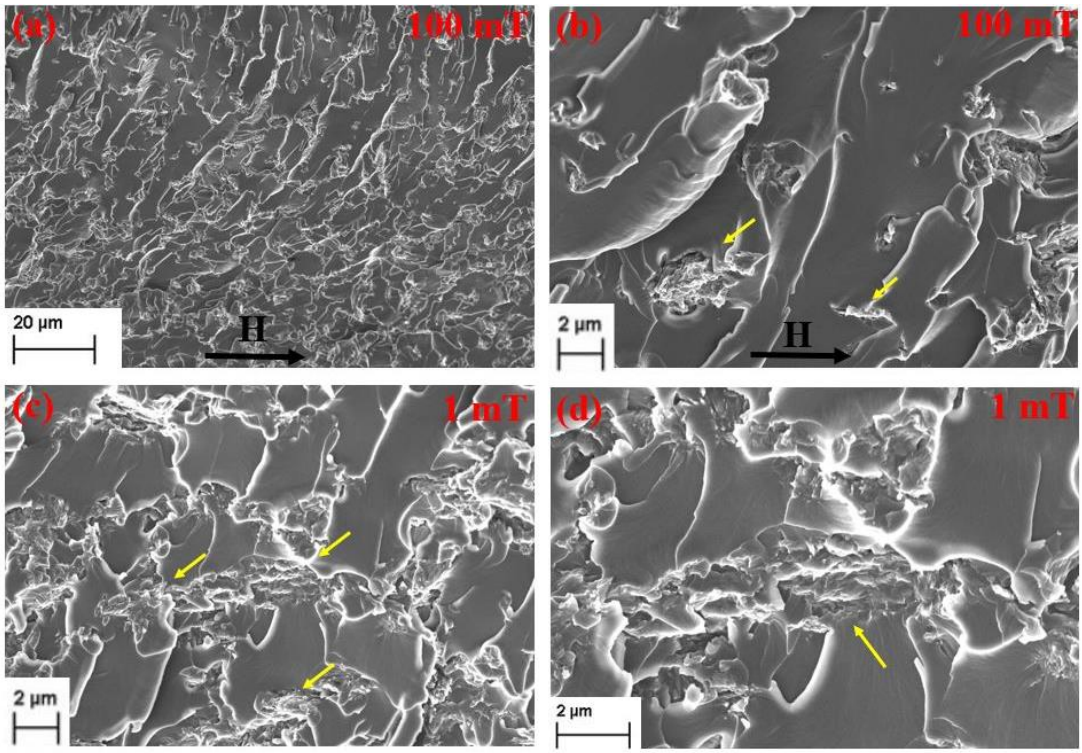


Figure 6. 26. SEM micrographs of 1 wt. % MNPs@FLG/epoxy composites mixed by HSM at 100 mT (a)-(b), 1 wt.% MNPs@FLG/epoxy composites mixed by TRM at 1mT (c)-(d). The direction of the magnetic field is indicated by black arrow while the yellow arrows indicate the aligned MNPs@FLG.

To quantitatively evaluate the alignment quality of MNPs@GNPs and MNPs@FLG, 2D Small-angle X-ray Scattering (SAXS) was used. The Cartesian coordinate system with the X, Y and Z axes in which the specimens were analysed is defined at Figure 6.27. Figure 6.27 shows the azimuthal plots of the 2D SAXS patterns of the aligned magnetic nanoparticles (MNPs@GNPs) chain-like structure, when the X-ray beam was aligned orthogonal ($\varphi=90^{o}$, perpendicular to the top surface of the sample and therefore perpendicular to alignment

direction, z-axis) and parallel (0°, perpendicular to the fractured surface of the sample, y-axis) to the magnetic field direction. In order to confirm that any anisotropic scattering originated only from the aligned nanohybrids, the X-ray beam exposed to the epoxy matrix as well as to the randomly dispersed 1 wt. % MNPs@GNPs/epoxy composites, providing a plateau line, as shown in Figure 6.27. A plateau was exhibited also for 1 wt. % GNPs-COOH/epoxy composite after exposure to 100 mT, confirming the random orientation of GNPs-COOH under the application of a magnetic field. When the X-ray beam is in a perpendicular direction to the magnetic chains, the 2D SAXS pattern has two peaks at φ=90° and φ=270°, whereas when the sample is shifted to 90° (the magnetic chains are in an orthogonal direction to the magnetic field), the peaks shifted also to 0° and 180°. Moreover, when the X-ray is parallel to the magnetic field (y-axis), the measurements give an isotropic scattering single, confirming that the magnetic graphene sheets are oriented parallel to the magnetic field.

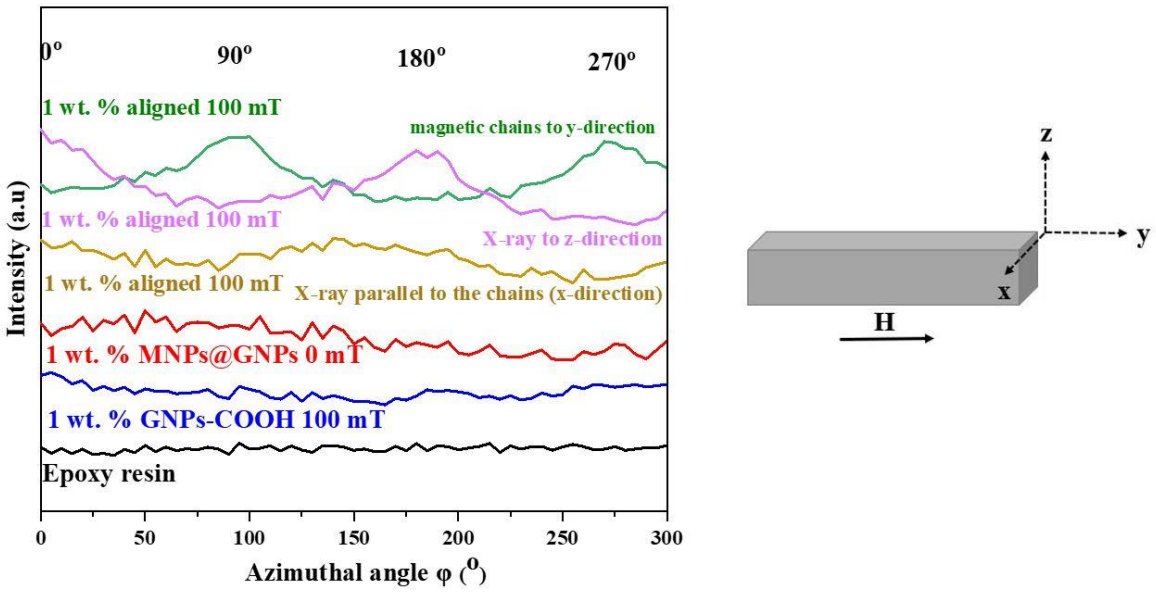


Figure 6. 27. Azimuthal plots of for 2D SAXS images of pure epoxy resin, 1 wt. 5 GNPs-COOH/epoxy composite prepared at 100 mT and 1 wt. % MNPs@GNPs prepared at 0 mT and 100 mT Schematic illustration of the Cartesian coordinate system that represents the directions (z- and y-) that used in SAXS analysis. The black arrow shows the direction of the applied magnetic field (H).

In order to investigate quantitatively the effect of the magnetic-field strength, composite films of 1 wt. % MNPs@GNPs mixed by TRM were prepared varying the intensity of the magnetic field (0.5 mT, 1mT, 10 mT, 20 mT, 40 mT, 60 mT, 80 mT, 100 mT). Figure 6.28 (a) represents the azimuthal angle (φ) plots of the 2D SAXS patterns measured with the X-ray beam orthogonal to the alignment direction (z-direction) and yields an anisotropic pattern for all the

magnetic fields. Although, a minimum magnetic field ($H_{min}$) of 1 mT found by the theoretical model that is necessary for the orientation of MNPs@GNPs, here the SAXS results proved that a reasonable alignment can been achieved at 0.5 mT. The Cinader and Burghardt equation was used by Boothroyd et al (2018) (as described in Chapter 3) was used in order to estimate the orientation factor. A perfect orientation corresponds to a factor equal to 1 (when the graphene sheets are perfectly flat) whereas a completely random orientation possesses to a factor of 0 (Li, Young et al. 2015). It was found that the orientation factor remains stable at around ~0.53 at all field strengths (Figure 6.28 (b)). These results are equivalent or better which have achieved at much lower field strengths compared with SAXS orientation factors reported for magnetically aligned graphene of 0.45 at 500 mT (Lu, Feng et al. 2017) and 0.3 at 100 mT(Wu, Ohtani et al. 2014). However, the authors of the two above references have achieved a better orientation factor (~0.8) but only with the application of very high magnetic fields (6-10 T) due to the absence of the magnetic nanoparticles, resulting in manufacturing methods that are not cost-effective and easy for scalable applications. Moreover, these orientation factors are comparable to the results for graphene orientation induced in composites using alternative techniques such as, shear and relaxation processing (orientation factor by SAXS analysis: 0.27 to 0.47 at 0.01 and 0.3 s−1 shear) (Boothroyd, Johnson et al. 2018). To add this, an orientation factor of 0.8 and 0.54 using the Raman spectroscopy has been reported by Li et al (2016) for aligned GO/PVA and GO/ epoxy nanocomposites manufactured by hot pressing. The main limitation of this alignment technique is that the orientation is reduced at 0.38 by increasing the nanofiller loading (5 wt. % GO). Also, no preferred alignment was observed in the case of GO/epoxy nanocomposites.

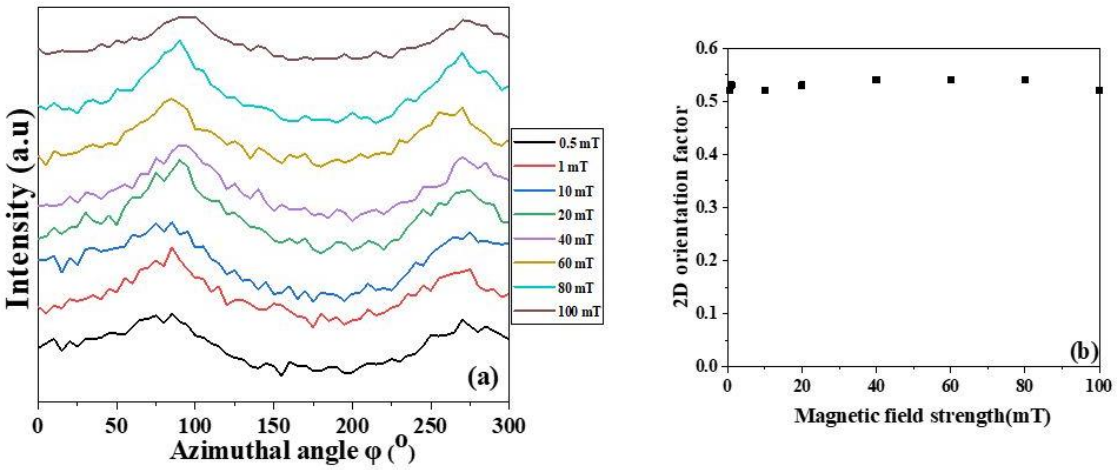


Figure 6. 28. 1 wt. % MNPs@GNPs/epoxy composites prepared by varying magnetic-field strength (b), the 2D orientation factor vs magnetic field strength.

Relating to the nanofiller concentration effect, composites with different MNPs@GNPs content (mixed by HSM) were analysed (0.2 wt. %, 0.5 wt. %, 0.8 wt. %, 1 wt. %, 2 wt. %, 4 wt. %), as shown in Figure 6.29. The azimuthal plot shows that the peak heights reduce with filler loading (due to less energy scattering), however, even at very low concentrations (0.2 wt. % and 0.5 wt. %) the orientation factor is maintained. Increasing the concentration up to 4 wt. %, large agglomerations occurred (as confirmed by the Optical microscope), that probably will affect the alignment process resulting in a poorer orientation of MNPs@GNPs. However, the orientation factor reaches at 0.56, demonstrating that the present method potentially can achieve aligned composite materials even at high concentrations.

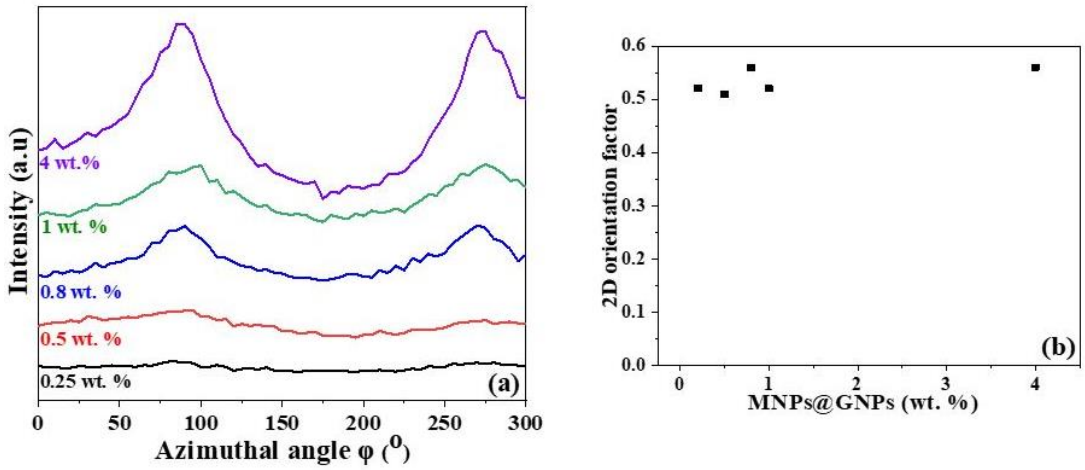


Figure 6. 29. MNPs@GNPs/epoxy composites aligned at 100 mT varying by the concentration filler (a) and the 2D orientation factor vs the concentration filler (b).

A similar anisotropic behaviour was confirmed also for 0.5 wt. % MNPs@FLG/epoxy composite aligned under the application of 1 mT and 100 mT. Figure 6.30 (a) shows the azimuthal plots of the 2D SAXS patterns of the aligned magnetic nanoparticles (MNPs@FLG), when the X-ray was aligned orthogonal. No anisotropic scattering was originated for the FLG-COOH sheets prepared without an external magnetic field and after exposed to 1 mT. Similar isotropic pattern was observed for the composite film when the highest magnetic field (100 mT) is applied. Hence, the anisotropic patterns are related to the magnetic graphene sheets (MNPs@FLG) that have been aligned in the direction of the field. Figure 6.30 (b) represents the azimuthal plots of the 2D SAXS patterns of the aligned MNPs@FLG at 100 mT in various concentrations (0.25 wt. %, 0.5 wt. %, 1 wt. %.). As shown in Figure 6.30 (c), similar orientation factors were achieved for both magnetic fields (1 mT and 100 mT), confirming again the calculations of the theoretical model. No difference was found on the orientation

factor between the mixing methods for both materials, giving a factor of ~0.5 by analysing the 2D SAXS plots (Appendix, Section 1-Figure 6.2).

Overall, these experimental studies and the theoretical modelling on the formation of aligned graphene sheets in both the liquid epoxy matrix and the epoxy nanocomposites have confirmed that a high degree of alignment may be achieved by using the process conditions that described in the experimental part.

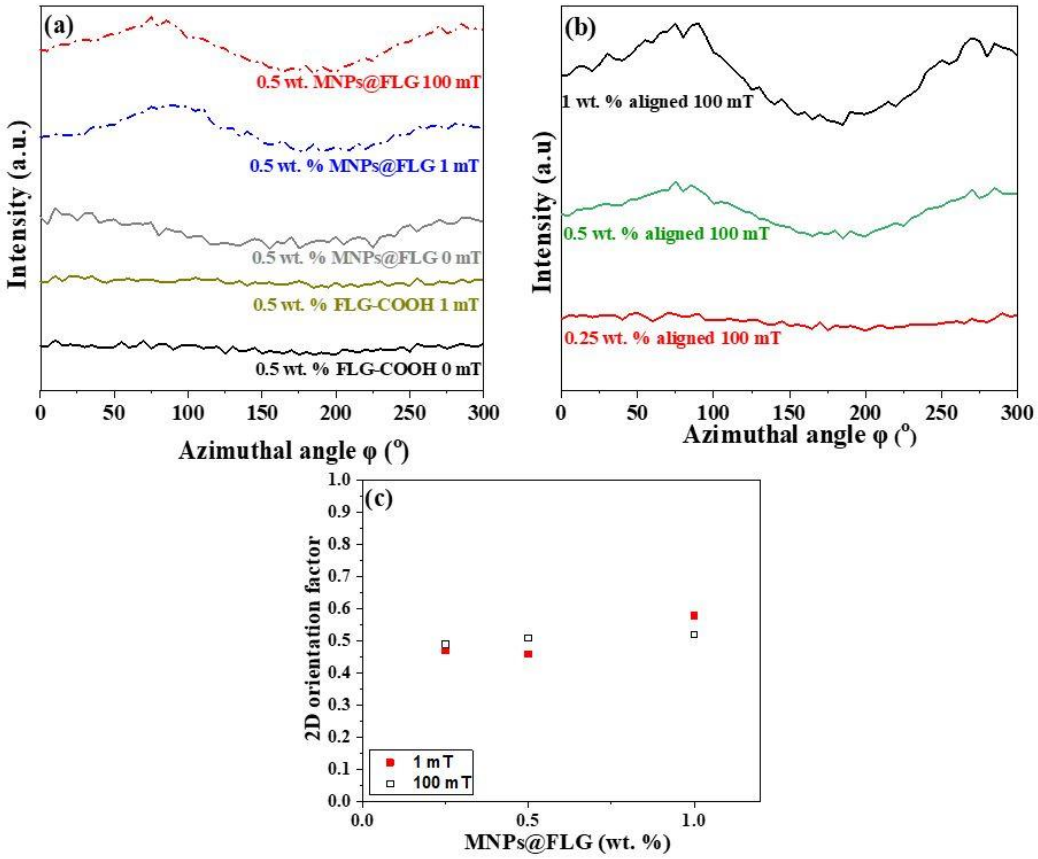


Figure 6. 30. Azimuthal plots of for 2D SAXS images of 1 wt. % FLG-COOH/epoxy composite prepared at 0 mT and 1 mT and 1% wt. MNPs@FLG prepared at 1 mT and 100 mT (a), 1 wt. % MNPs@FLG/epoxy composites prepared by varying filler concentration and magnetic field strength (b), and the 2D orientation factor vs the concentration filler at two different magnetic fields (1 mT and 100 mT) (c).

## 6.5. The effect of alignment into the mechanical properties of magnetic@graphene based composites

### 6.5.1. Monitoring stress transfer processes using micro-Raman spectroscopy

The samples of MNPs@FLG (1 wt. % mixed by TRM at 0 mT, 1 mT and 100 mT) with the higher planar size were strained in situ under a Raman spectrometer and the characteristic shifts of the Raman bands were recorded with increasing strain. The slope of the band shifts versus strain represents the stress transfer efficiency between the matrix and the filler. For each composite, three samples were measured and the data points in Figure 6.31 represent the mean values for all the specimens used for each type of composite. It was shown that the flakes display very low D and G band shifts, indicating the significantly lower stress transfer efficiency due to the low effective modulus of FLG ($E_{eff}$) within the epoxy matrix, in comparison with the pristine graphene (−60 cm−1/% strain for the 2D band that corresponds to a modulus of 1050 GPa) (Gong, Kinloch et al. 2010). Here, the planar size of the measured material (MNPs@FLG <8 μm) is significantly below than the critical length (Ic>10 μm) (Anagnostopoulos et al. 2015), which makes difficult to achieve a stress transfer efficiency from polymer matrix to the nanofiller. Although, these band shifts are lower than the reported Raman results of GO/polymer composites (Li, Young et al. 2013, Li, Young et al. 2016), there is still an improvement on Raman shifts for the aligned MNPs@FLG/epoxy composites, especially at higher magnetic field (Figure 6.31 (e) and (f)). These results showed that the aligned graphene sheets can be deformed better when they are on the tensile direction giving a higher band shift. Hence, an efficient stress transfer can travel between the polymer matrix and aligned graphene sheets as monitored by Raman spectroscopy, which is crucial to improving the mechanical properties of polymer nanocomposites.

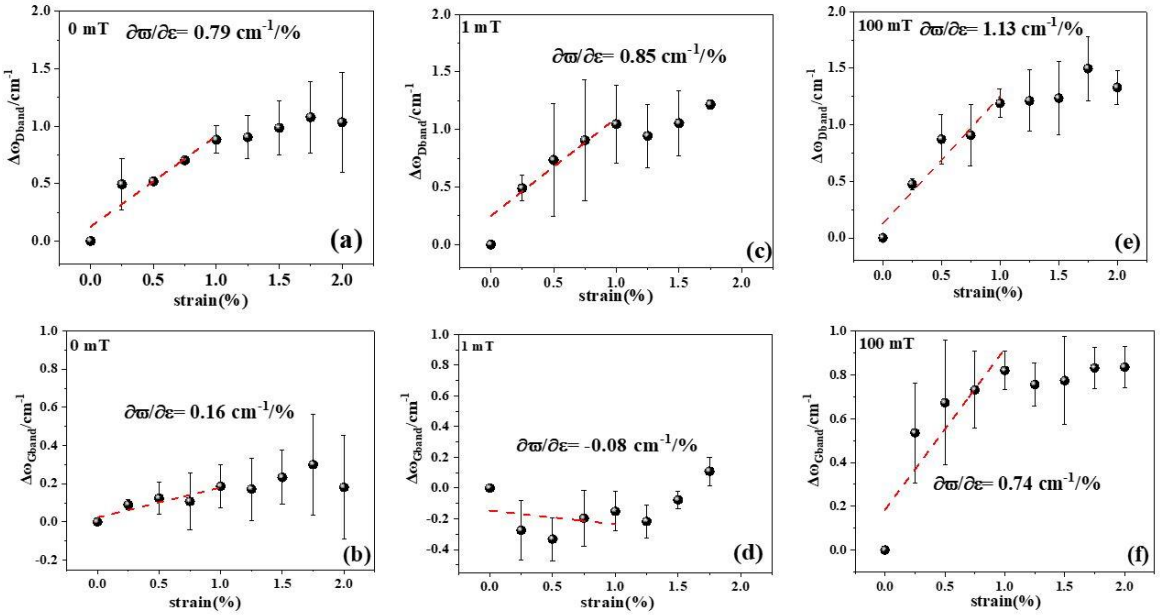


Figure 6. 31. D and G Raman band shifts of 1 wt. % MNPs@FLG/epoxy composites when randomly dispersed ((a)-(b)), aligned at 1 mT ((c)-(d)) and at 100 mT ((e) and (f)), respectively against the composite strain.

### 6.5.2. Tensile testing

The mechanical properties of the materials were studied by tensile testing. Figure 6.32 shows typical stress-strain curves for the neat epoxy and composites filled with MNPs@FLG when randomly dispersed (a) and aligned under the applied magnetic field (1 mT) (b) as a function of the filler loading and the mixing method. Five stress-strain curves were obtained for each loading level and mixing method for each type of filler, and representative ones are presented.

The parameters of the mechanical properties of the filled composites can be tabulated in Table 6.4. Overall, no significant improvement was noticed for the Young's modulus of randomly dispersed materials, by increasing the nanofiller loading when compared with the pure epoxy resin. On the other hand, the tensile strength and the strain at failure were decreased with the increase of the nanofiller loading, with the TRM-mixed composites to show lower values for tensile strength and strain at failure for all the composites comparing with the HSM-mixed composites.

In the case of HSM-mixed composites, the presence of agglomerations was observed by SEM micrographs (Figure 6.12 (a)-(b)) at high filler loadings which can cause the lower strain at failure and decreased tensile strength (Papageorgiou, Kinloch et al. 2017). However, a well-dispersed material is performed after the use of TRM (as shown in SEM images-Figure 6.12

(c)-(d)). By achieving a better dispersion, the surface area of the nanohybrids has been increased, resulting in more isolated graphene sheets in the interphase zone. However, a relatively weak interface (as proved by the stress transfer study) existing between MNPs@FLG and epoxy resin, resulting in the decreased trend on tensile strength and elongation at break. Additionally, the reduction in crosslinking density (as proved by DMA analysis in Section 6.5.3) may have made the epoxy matrix more flexible and the presence of any defects will deteriorate the ultimate mechanical properties (Olowojoba, Kopsidas et al. 2017).

After the alignment at 1 mT, the Young modulus has been increased for all the HSM-mixed composites in the range of 5-10% in comparison with the random dispersed composites. Only the lowest concentration at 0.25 wt. % gave an increase of 30%. The improved stiffness is related to the orientation of the MNPs@FLG under the direction of the magnetic field which is the same direction as the tensile tests were performed. However, there was no orientation reinforcement on the Young modulus of the TRM-mixed composites. This may be attributed to that some iron nanoparticles have been removed by the graphene surface during the TRM process, leading to a less efficient alignment. This can be supported especially for the composite with filler concentration up to 1 wt. %, in which a partial exfoliation may occur due to the high viscosity (as proved by the exfoliation model). Although still below the pure epoxy values, considerably higher stress (~36 and 40% for HSM and TRM) and strain (3% for both of two mixing methods) at break were found for 2 wt. % MNPs@FLG aligned at 1 mT comparing with the random dispersed nanofiller. Similar results were obtained by Xia et al (2018) that showed an increase of ~5% at Young modulus on aligned GNPs (10 wt. %, dimensions: 25 μm and 6 nm) into an epoxy matrix by the application of electric field (Joule heating).In this paper, the authors reported a significant decreased value of Tg for the aligned GO/epoxy composite (using DSC measurements),which has been attributed to the formation of small agglomerates and microvoids that hinder the crosslinking network. However, the reduced crosslinking density of the epoxy resin has not been considered as a reason for the small increase on the mechanical properties.

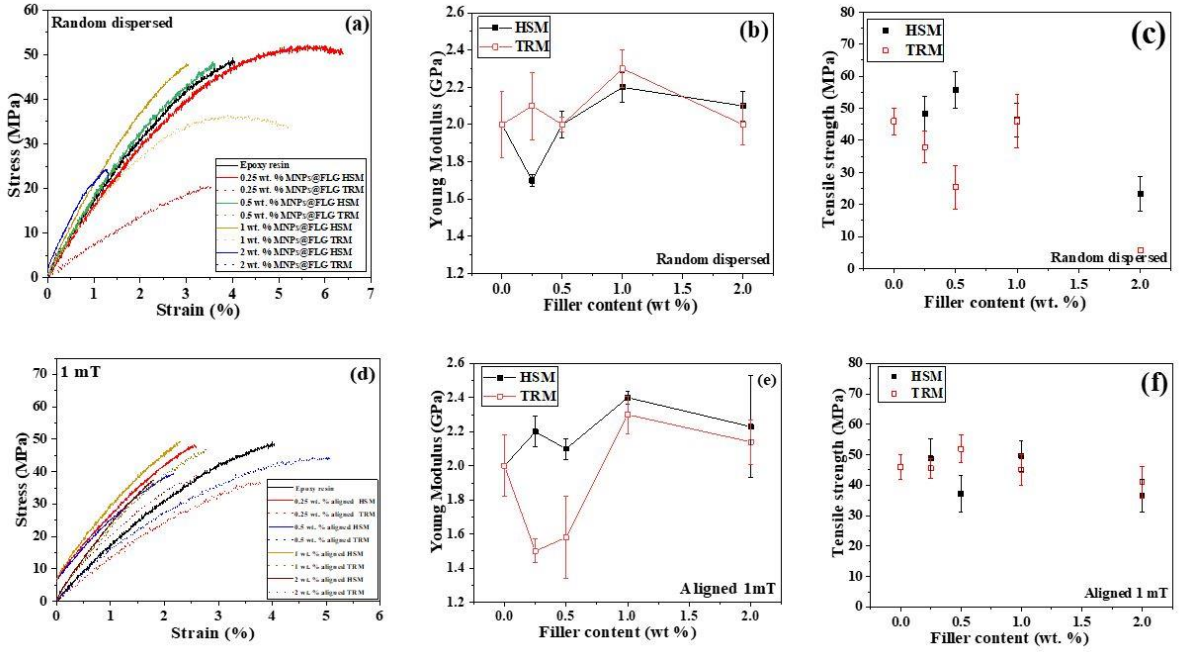


Figure 6. 32.Typical stress-strain curves from: MNPs@FLG/epoxy composites when randomly dispersed (a), MNPs@FLG/epoxy composites when aligned under the application of 1 mT (d) mixed by HSM and TRM. Young's modulus (b) and (e) as a function of filler loading for MNPs@FLG/epoxy composites when randomly dispersed and MNPs@FLG/epoxy composites when aligned under the application of 1 mT mixed by HSM and TRM, respectively. Tensile strength (c) and (f) as a function of filler loading for MNPs@FLG/epoxy composites when randomly dispersed and MNPs@FLG/epoxy composites when aligned under the application of 1 mT mixed by HSM and TRM, respectively.

Figure 6.33 shows typical stress-strain curves for the neat epoxy and composites filled with MNPs@rGO when randomly dispersed (a) and aligned under the applied magnetic field (7 mT) (b) as a function of the filler loading and the mixing method. By increasing the concentration, a noticeable improvement on Young modulus and tensile strength was noticed for TRM-mixed composites in comparison with the HSM-mixed samples when randomly dispersed (Figure 6.33 (b)- (c)), which will be attributed to the better dispersion, as shown in optical microscope images (Figure 6.8). Lower values for the strain at failure in comparison with the pure epoxy, were obtained. This can be attributed to the lower cross-linking network as lower Tg values were found for all the composites (Section 6.5.3). The effect of the orientation on the tensile properties of MNPs@rGO/epoxy composites was illustrated in Figure 6.33 (e) and (f). In the case of HSM-mixed epoxy composites, Young modulus was increased for ~10% and ~41% (Figure 6.33 (e)) and a great enhancement on strain at break was noticed (Figure 6.33 (f), ~30%

and ~50%) for 0.25 wt. % and 0.5 wt. %, respectively. Similarly with MNPs@FLG, no mechanical improvement was noticed for the TRM-mixed composites.

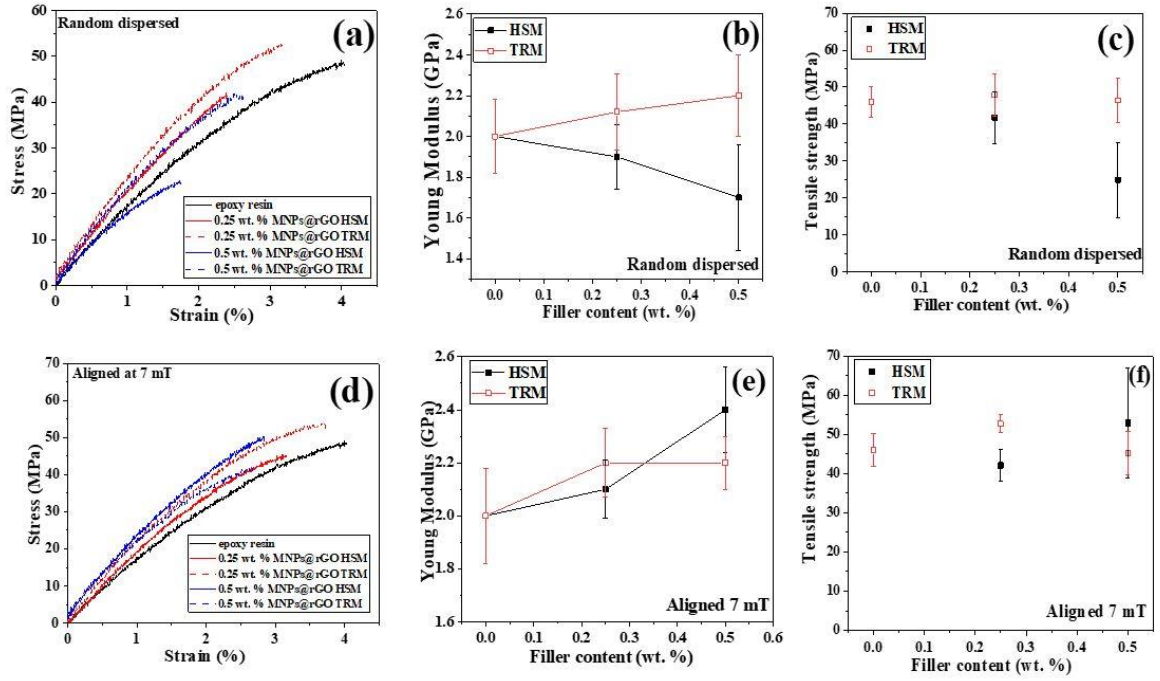


Figure 6. 33. Typical stress-strain curves from: MNPs@rGO/epoxy composites when randomly dispersed (a), MNPs@FLG/epoxy composites when aligned under the application of 7 mT (d) mixed by HSM and TRM. Young's modulus (b) and (e) as a function of filler loading for MNPs@FLG/epoxy composites when randomly dispersed and MNPs@rGO/epoxy composites when aligned under the application of 7 mT mixed by HSM and TRM, respectively. Tensile strength (c) and (f) as a function of filler loading for MNPs@rGO/epoxy composites when randomly dispersed and MNPs@rGO/epoxy composites when aligned under the application of 7 mT mixed by HSM and TRM, respectively.

Table 6. 4. Parameters of the mechanical properties

| Samples | $\sigma_{max}$ (MPa) | $\varepsilon_{max}$ | E (GPa) |
|---|---|---|---|
| **Epoxy resin** | 45.96±4.15 | 0.035±0.004 | 2±0.185 |
| **0.25 wt. % MNPs@FLG HSM** | 48.33±5.37 | 0.049±0.011 | 1.7±0.03 |
| **0.25 wt. % MNPs@FLG TRM** | 37.87±4.92 | 0.029±0.011 | 2.1±0.18 |
| **0.5 wt. % MNPs@FLG HSM** | 55.71±5.57 | 0.045±0.007 | 2±0.07 |
| **0.5 wt. % MNPs@FLG TRM** | 25.4±6.74 | 0.015±0.004 | 2±0.045 |
| **1 wt. % MNPs@FLG HSM** | 46.31±5.22 | 0.0314±0.004 | 2.2±0.081 |
| **1 wt. % MNPs@FLG TRM** | 45.96±8.29 | 0.03±0.01 | 2.3±0.10 |
| **2 wt. % MNPs@FLG HSM** | 23.34±5.51 | 0.011±0.0025 | 2.1±0.082 |
| **2 wt. % MNPs@FLG TRM** | 5.71±0.72 | 0.003±0.0004 | 2±0.11 |
| **0.25 wt. % aligned 1mT HSM** | 48.74±6.51 | 0.025±0.003 | 2.2±0.09 |
| **0.25 wt.% aligned 1 mT TRM** | 45.6±3.22 | 0.051±0.009 | 1.5±0.07 |
| **0.5 wt. % aligned 1 mT HSM** | 37.22±6.06 | 0.021±0.0049 | 2.1±0.061 |
| **0.5 wt. % aligned 1 mT TRM** | 51.96±4.44 | 0.05±0.006 | 1.58±0.24 |
| **1 wt. % aligned 1 mT HSM** | 49.62±4.97 | 0.03±0.0065 | 2.4±0.04 |
| **1 wt. % aligned 1 mT TRM** | 45.09±5.08 | 0.03±0.006 | 2.3±0.11 |
| **2 wt. % aligned 1 mT HSM** | 36.58±5.26 | 0.03±0.01 | 2.23±0.3 |
| **2 wt. % aligned 1 mT TRM** | 40.98±5.21 | 0.03±0.01 | 2.14±0.13 |
| **0.25 wt. % MNPs@rGO HSM** | 41.76±6.97 | 0.024±0.007 | 1.9±0.16 |
| **0.25 wt. % MNPs@rGO TRM** | 47.95±5.74 | 0.0033±0.009 | 2.12±0.185 |
| **0.5 wt. % MNPs@rGO HSM** | 24.9±10.15 | 0.019±0.019 | 1.7±0.26 |
| **0.5 wt. % MNPs@rGO TRM** | 46.4±5.9 | 0.028±0.009 | 2.2±0.2 |
| **0.25 wt. % MNPs@rGO aligned 7 mT HSM** | 42.13±3.96 | 0.034±0.01 | 2.1±0.11 |
| **0.25 wt. % MNPs@rGO aligned 7 mT TRM** | 52.71±2.29 | 0.036±0.002 | 2.2±0.13 |
| **0.5 wt. % MNPs@rGO aligned 7 mT HSM** | 52.9±14.04 | 0.029±0.0098 | 2.4±0.16 |
| **0.5 wt. % MNPs@rGO aligned 7 mT TRM** | 45.3±5.6 | 0.028±0.005 | 2.2±0.1 |

*σmax, εmax, E are tensile strength (the stress at break in the stress-strain curve, MPa), ultimate strain and Young's modulus (the slope of the stress-strain curve in the elastic region (0-0.5% strain), GPa).

### 6.5.3. Dynamic Mechanical Analysis (DMA)

DMA was used in order to understand how the MNPs@GNPs, MNPs@FLG and MNPs@rGO affect the viscoelastic properties of the magnetic graphene-reinforced nanocomposites before and after the alignment. An extended study was reported in the literature, providing strong evidence *via* DMA measurements about the positive effect on the thermo-mechanical properties of aligned nanofillers, such as SWCNTs (Camponeschi, Vance et al. 2007, Malkina, Mahfuz et al. 2013) or MWCNTs (Abdalla, Dean et al. 2010), in an epoxy matrix by using high external magnetic fields (1T-25T). However, there is no reported work how the magnetic control of graphene nanofillers can influence the dynamic mechanical properties of thermosetting polymer composites.

Figure 6.34 illustrates the values of storage modulus at 30$^{o}$C and tan delta for pure epoxy and MNPs@GNPs/epoxy composites (mixed by HSM and TRM) at different filler loadings (1 wt. %, 2 wt. %, 4 wt. %) before the alignment ((a) and (b)) and after aligned in two different magnetic fields: at 100 mT ((c) and (d)) and at 1 mT ((e) and (f)). As Figure 6.34 (a) shows, no improvement was induced by the increase of the nanofiller concentration; although a well dispersed material was achieved by TRM method, as confirmed by Optical microscope images (Figure 6.4) and SEM micrographs (Figure 6.11), the TRM-mixed composites showed a lower increase on the storage modulus comparing with those that are HSM-mixed. It is clear by Figure 5.27 (b) that the Tg of TRM-mixed composites are lower than the pure epoxy resin and also lower than the HSM-mixed composites until 2 wt. % which leads to the interruption of the crosslinking polymer network and results at decreased values of modulus. By increasing the concentration at 4 wt. %, there is a modest enhancement of Tg that reaches the Tg of the epoxy resin (85.8 $^{o}$C), which can be explained by the movement restriction of the polymer chains.

After the alignment of MNPs@GNPs under the applied magnetic fields, there is no significant differences on the storage modulus of aligned graphene/nanocomposites (Figure 6.34 (c) and (e)). In the section 6.5.2., Raman spectroscopy proved a low stress transfer of random dispersed MNPs@FLG (> 8 μm) that have a planar size higher than the MNPs@GNPs (0.3-5 μm). In the case of MNPs@GNPs, the flake won't even reach the same strain as the matrix and hence the reinforcement will be minimal without making any difference when it is aligned. However, an improvement of Tg was observed for TRM-mixed composites for both magnetic fields in comparison with the values of random dispersed materials, as shown in Figure 6.34 (d) and (f). When the randomly MNPs@GNPs dispersed on epoxy resin by TRM affects its curing, however by aligning it, a less distributed material was achieved in the direction of magnetic

fields (as proved by Optical microscopy and Raman mappings), resulting in less defects with the polymer chains. In the case of HSM-mixed composites, at higher filler loadings large agglomerations are formed under the direction of the applied magnetic fields (as shown in the optical microscope images) that interrupt the crosslinking density and leads in a slightly lower Tg values (~84 $^{o}$C).

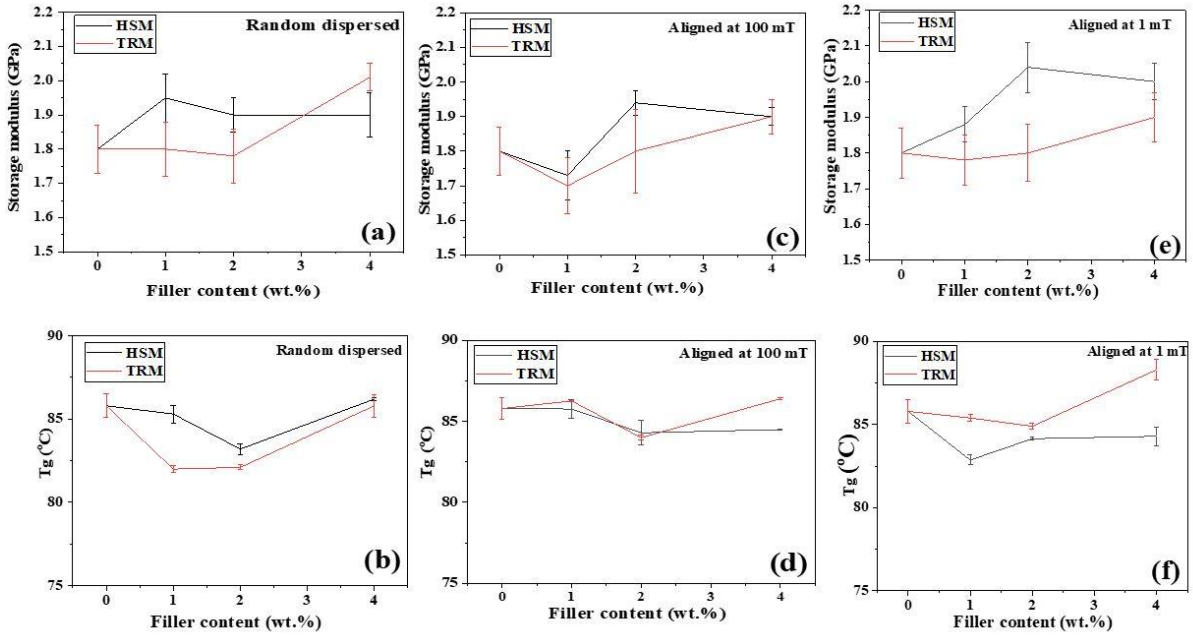


Figure 6. 34. Storage modulus at 30 $^{o}$C and Tg values of MNPs@GNPs prepared by HSM and TRM as a function of the filler concentration when randomly dispersed ((a)- (b)), aligned at 100 mT ((c)-(d)) and aligned at 1 mT ((e)- (f)).

The alignment effect on the thermo-mechanical properties of MNPs@FLG/epoxy nanocomposites prepared by HSM and TRM at different filler loadings (0.25 wt. %, 0.5 wt. %, 1 wt. % and 2 wt. %) was studied under the lowest magnetic field strength (1 mT). Figure 6.35 shows the values of storage modulus (at 30 $^{o}$C) and Tg for MNPs@FLG/epoxy composites when randomly dispersed ((a) and (b)) and aligned at 1 mT ((c) and (d)). An initial drop at the storage modulus was observed, which is attributed to the significant reduced Tg (Figure 6.35 (d)) that leads to a lower cross-linking polymer network and hence to diminished mechanical properties, as proved in Chapter 5. By increasing the filler loading, there was a constant rise on stiffness for TRM-mixed nanocomposites with a slight lower storage modulus for the 2 wt. % HSM-mixed epoxy composite, which could be attributed to the poorer dispersion state, as shown by the SEM micrographs.

Relating to the aligned MNPs@FLG-epoxy nanocomposites, a positive effect was achieved in comparison with the random dispersed materials by the storage modulus to be raised ~7-11% for both mixing methods with 0.25 wt. %. However, increasing the nanofiller loading no positive effect was achieved; specifically, a drop at storage modulus (12-15%) was noticed at 0.5% and 1 wt. %. These results have been attributed to the lower Tg values after the alignment process. Increasing the nanofiller concentration, the formation of agglomerations occurs due to the possible weak interfacial interactions between the filler and the matrix that lead to a lower dispersion degree under the application of the magnetic field (as proved by Raman mappings). By increasing the concentration at 2 wt. %, no difference was found for both of storage modulus and Tg.

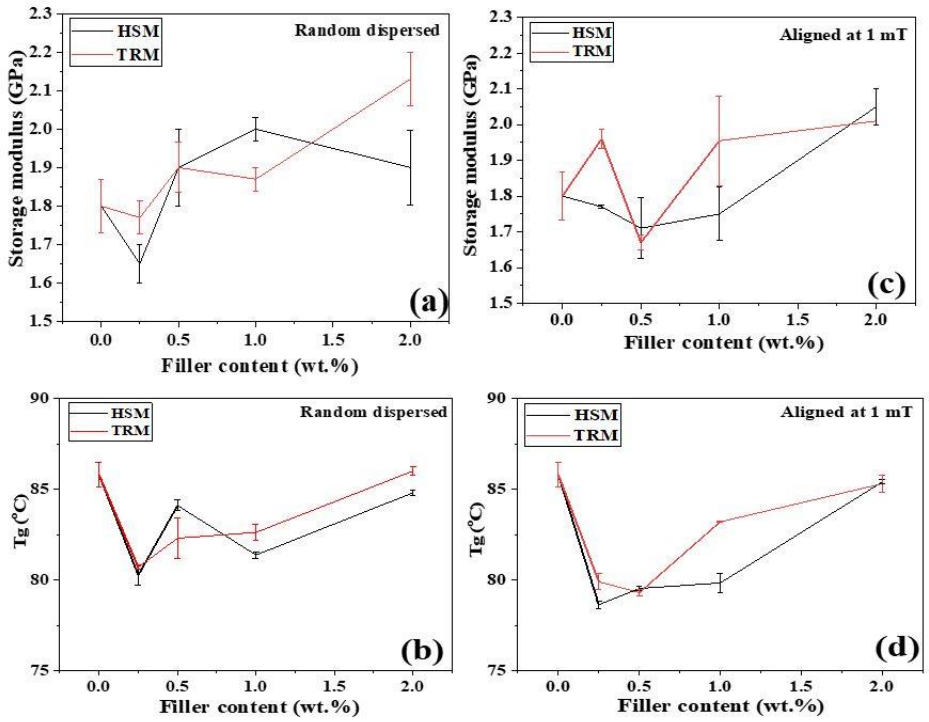


Figure 6. 35.Storage modulus at 30 °C and Tg values of MNPs@FLG prepared by HSM and TRM as a function of the filler concentration when randomly dispersed ((a)- (b)) and aligned at 1 mT ((c)-(d)).

Figure 6.36 shows the values of storage modulus (at 30 °C) and Tg for MNPs@rGO/epoxy composites when randomly dispersed ((a) and (b)) and aligned at 7 mT ((c) and (d)). All the composites showed Tg values lower than the pure epoxy resin, confirming the reduced cross-linking density. Moreover, 16% increase on storage modulus achieved with 0.25 wt. % filler loading (Figure 6.36 (a)), with no more improvement to be performed by increasing the concentration. Similarly with MNPs@FLG, no significant effect was found after the alignment

with the Tg values to be lower than the pure epoxy resin. Hence, although MNPs@rGO has a length higher than the critical length ($l_c$), the cross-linking effect and its non-fully orientation (more than 10 mT is needed regarding the theoretical model) can be attributed to the insufficient dynamic mechanical properties.

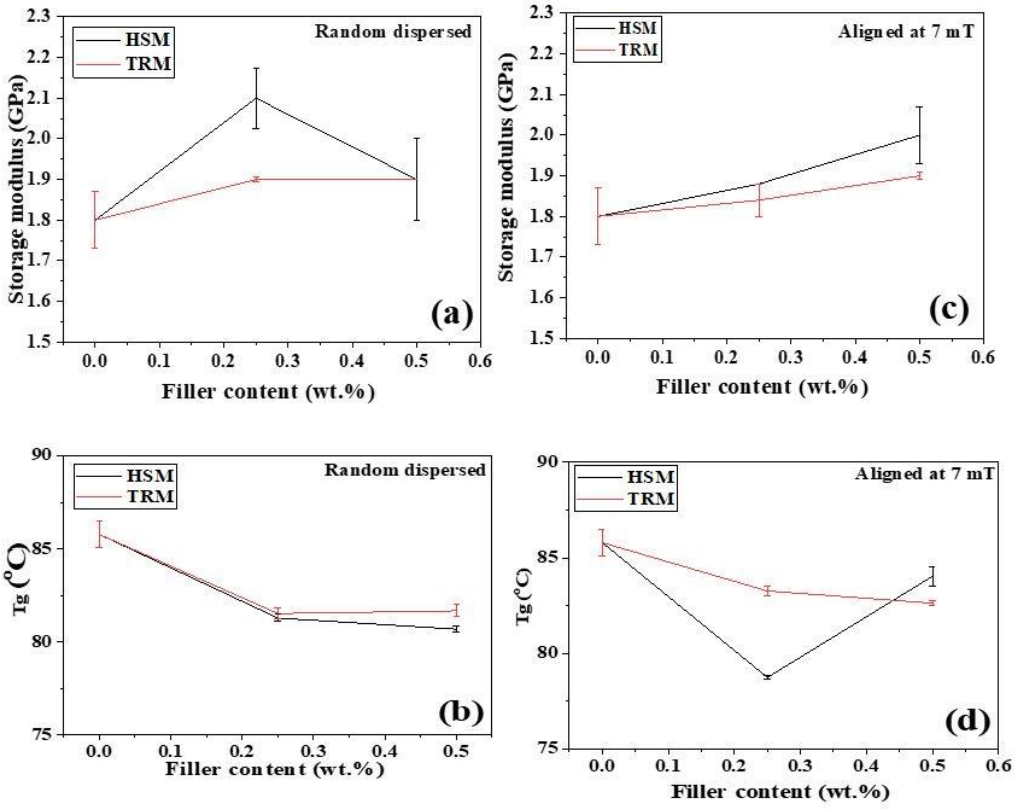


Figure 6. 36. Storage modulus at 30 °C and Tg values of MNPs@rGO prepared by HSM and TRM as a function of the filler concentration when randomly dispersed ((a)- (b)) and aligned at 7 mT ((c)-(d)).

Other reasons that can explain these results are:

- Interfacial interactions: A relative weak interface between the nanofiller and the polymer matrix can lead to a low stress transfer loading. The importance of orientation as well as the interfacial interactions between the filler and the polymer matrix was reported by Yousefi et al (2013) who studied the alignment of GO and reduced graphene oxide (rGO) sheets into the epoxy matrix. As mentioned in Literature review, a self-alignment of rGO was achieved through the strong covalent bonds between the rGO and the epoxy network, resulting to remarkable mechanical properties.
- Possible wrinkles in the graphene surface: the wrinkles can be formed under the application of the magnetic field, resulting in the misalignment of the flakes (Li, Young

et al. 2013), especially in the case of very thin flakes. Any misorientation can result in a proportionate reduction in the effective modulus of graphene and hence to a reduced stiffness of the polymer composite.

- The low values of effective modulus ($E_{ff}$) of MNPs@GNPs, MNPs@FLG and MNPs@rGO (Table 6.1 in Appendix, Section 3), which were calculated using the rules of mixtures, as described in Chapter 5.

### 6.5.4. Comparison of Young's modulus between experiment and Halpin-Tsai theoretical model

To study the distribution of MNPs@FLG and MNPs@rGO in epoxy resin, the Halpin–Tsai equation was used to simulate the modulus of the graphene/epoxy nanocomposites. The modulus $E_r$ and $E_{||}$ for the Young's moduli of the nanocomposite with randomly and unidirectionally distributed nanofiller are calculated as described in Chapter 5. The latter refers to aligned parallel to the surface of the sample and it can be estimated by the following equation:

$$E_{II} = E_m \frac{1+\eta_L \xi V_f}{1-\eta_L V_f} \quad \text{.....(6.8)}$$

For the Young's modulus of randomly dispersed materials, the theoretical effective modulus ($E_{eff}$) of FLG-COOH and rGO were used ($E_{eff}$=176.9 GPa and $E_{eff}$=219.04 GPa, respectively), as calculated in Chapter 5. However, for the calculation of Young modulus of aligned sheets, the $E_{eff}$ of FLG-COOH and rGO were atrributed to the values of aligned graphene sheets, considering the shear-lag effects ($E_{eff}$=331.43 GPa and $E_{eff}$=410.7 GPa, respectively). The values of $V_f$ were calculated by the equation (5.4) in Chapter 5. All the parameters are included in Table 5.4 in Chapter 5.

The Halpin and Tsai model were compared with the tensile data of MNPs@FLG and MNPs@rGO/epoxy composites for random dispersion and fully orientation of the nanofillers, as shown in Figure 6.37. The experimental data are agreed well with the prediction based on the random dispersion of both of nanofillers (Figure 6.37 (a) and (c)). Additionally, as shown in Figure 6.37 (b), the theoretical simulation for 2D-aligned parallel distribution shows good consistency with the experimental results collected from the resulting composite films, which apparently indicates that the MNPs@FLG are preferentially parallel to the surface. However, increasing the concentration at 2 wt. %, the experimental value was lower than the theoretical estimation which will be attributed to the presence of agglomerations which leads to errors and

wrong predictions for high filler content (Shokrieh, Esmkhani et al. 2014). Similar results were obtained for MNPs@rGO (Figure 6.37 (d)), confirming again the orientation of MNPs@rGO under the low magnetic field (7 mT). Apart from the preferable orientation of the nanomaterials, this model further suggests this is the upper pound prediction for the mechanical reinforcement, which fits well with our experimental data.

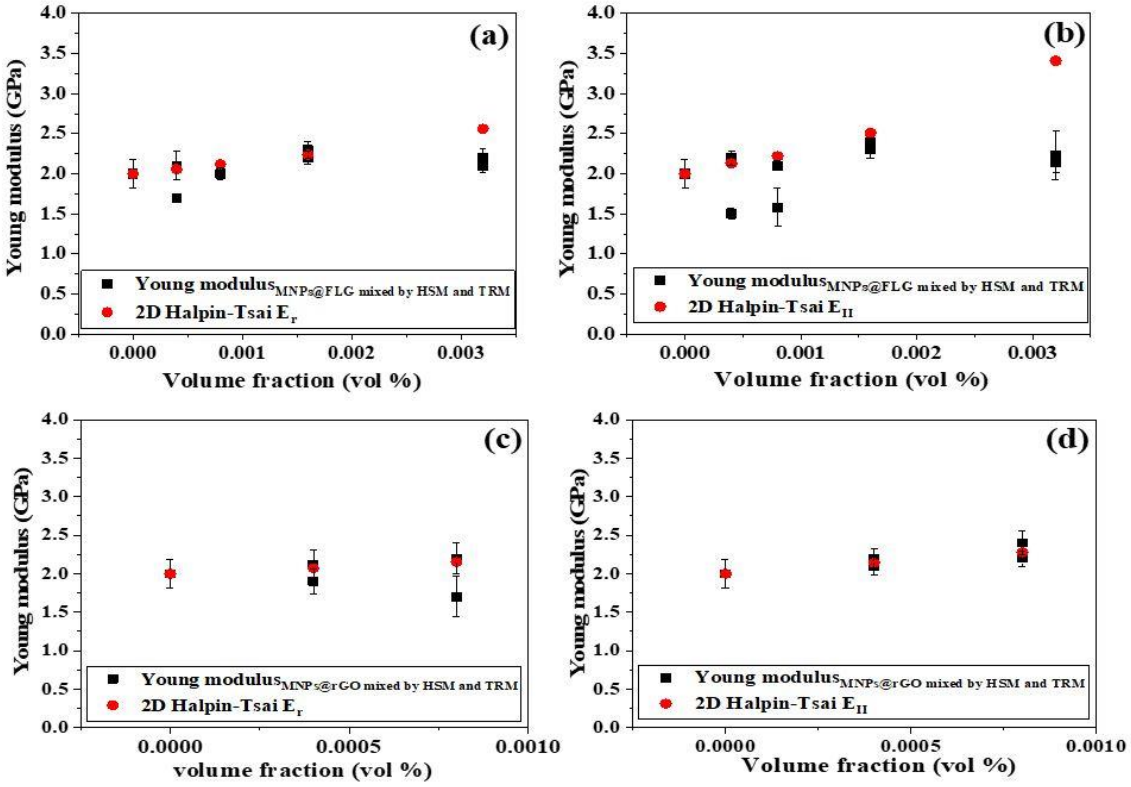


Figure 6. 37. Young modulus of MNPs@FLG (a), (b) and MNPs@rGO (c), (d)/epoxy composites: Comparison of Halpin-Tsai analytical model for random and 2D perfect orientation, respectively.

## 6.6. Conclusions

In this chapter, a new insight was studied into the microstructure and mechanisms of reinforcement in epoxy system reinforced with aligned graphene nanomaterials under the application of low magnetic fields. The conclusions are summarized as a function of the effects of dispersion state, filler loading and magnetic alignment on the main properties of composites:

- A high dispersion degree was achieved for all the composites with the use of TRM in the uncured and cured stage, as confirmed by the rheology data, optical microscope and SEM.
- Both of theoretical and experimental studies confirmed the orientation of the magnetic flakes, prior the gelation time, into the epoxy nanocomposites under low magnetic

fields. The theoretical model identifies the key parameters influencing the alignment process, including the viscosity of the suspension determined by Rheology, the strength of the magnetic field, the dimensions (i.e., planar size and thickness) of the graphene nanofillers, the diameter of the magnetite nanoparticles, and the magnetic susceptibility of the nanohybrids.

- The theoretical estimations were proved further through the extended quantitative investigation of the magnetic alignment using 2D SAXS. The following insights were gleaned: a) the MNPs@graphene are oriented parallel to the applied magnetic field, b) under optimal conditions, an efficient orientation can be achieved with an orientation factor of ~0.5, c) effects of magnetic intensity, filler concentration and dispersion state on the orientation order are clarified. These results confirmed that the present method is applicable for the alignment of magnetic graphene flakes under very low magnetic fields (1mT) in a range of filler concentrations.
- Raman spectroscopy has been demonstrated that under the magnetic field, it is possible to follow stress transfer between the polymer matrix to the MNPs@FLG reinforcement from stress-induced shifts of the Raman bands.
- Moreover, an improved Young modulus was achieved under the application of low magnetic fields. Specifically, the Young modulus of MNPs@FLG has been increased for all the HSM-mixed composites in the range of 5-10%. By using the rules of mixtures, a low effective modulus was obtained for all the nanofillers, which confirms the reason for not achieving higher mechanical reinforcement. However, in the case of aligned of MNPs@rGO, Young modulus reached an increase of ~41%. The tensile data agreed well with the theoretical estimations by the Halpin-Tsai model, confirming the 2D orientation distribution under the magnetic field.
- Although, a better dispersion has been achieved, this enhancement was not observed at TRM-mixed composites. As proved by the exfoliation model, a partial exfoliation may occur especially at high filler loadings due to the increased viscosity. This might lead to a loss of the magnetic nanoparticles under the shear forces of TRM and hence, a less efficient orientation.
- Moreover, the alignment efficiency has not been found by the DMA data. This might attribute to the following reasons: (a) a less distributed material into the epoxy resin, which was identified by Raman mappings even by the use of low magnetic fields (b) a reduced crosslinking density was proved by the reduced Tg values and TGA data. As

descripted in Chapter 5, the lower crosslinking density leads to an insufficient stress transfer, resulting in a negative effect on the mechanical properties.

# Chapter 7 Conclusions and suggestions for future work

## 7.1. Conclusions

The effect of surface functionalization by plasma treatment has improved the dispersion of graphene in both uncured and cured states for the infusion epoxy system presented. In the uncured state optical microscopy suggests that HSM is more effective than TRM for low filler loadings of GNPs, FLG, GNPs-COOH and FLG-COOH. As the filler loading increases the TRM begins to give a better dispersion state than the HSM, which was confirmed by optical microscopy and Rheology data. In the cured stage, a relatively good dispersion was achieved for all the composites under the application of TRM, as strongly supported by Optical microscope and SEM micrographs. A significant contribution of the curing effects on the mechanical properties was confirmed by DMA analysis, showing significant reductions in $T_g$ and storage modulus. This results from the catalytic effect of the oxygen groups and the physical barriers between reacting components created by high surface area flakes. This leads to a non-stoichiometric ratio which reduces cross-link density and therefore diminishes mechanical reinforcement. The presence of reduced cross-linking density was also supported by the observation of lower thermal stability, as shown in TGA results. The effect of diminishing properties with increasing filler loading in thermoset systems is commonly reported in the literature and often it is hypothesised that this results from agglomeration (in the case of modulus) and catalytic effects (in the case of $T_g$) with little supporting evidence. The results in this thesis show that the cure effects leading to reduced cross-linking density can play a significant role in both cases.

The effect of different graphene morphologies on the growth mechanism of magnetic nanoparticles (MNPs) by co-precipitation was investigated. A detailed chemical analysis confirmed that the iron oxide nanoparticles is a mixed phase of magnetite ($Fe_3O_4$)/ maghemite ($\gamma$-$Fe_2O_3$). The dispersion of MNPs was studied by SEM and TEM images, which proved a better nanoparticle dispersion with a narrow size distribution on a higher surface area material (FLG-COOH and rGO). It was found that as the size of the nanoparticles decreases, the ratio of magnetite to maghemite decreases, which leads to a lower magnetic saturation (Ms).

Good dispersion was achieved for MNPs@GNPs, MNPs@FLG and MNPs@rGO epoxy nanocomposites before and after curing and confirmed by Optical microscopy, Rheology and SEM. The orientation of MNPs@GNPs and MNPs@FLG and MNPs@rGO into the epoxy resin was characterized by real-time optical microscopy, which showed that nanofillers are

successfully aligned under the application of low magnetic fields. The role of the dispersion state, filler concentration and field strength were examined, and the main conclusions are: 1) the better dispersion achieved by TRM leads to a well-dispersed network of thinner magnetic clusters, 2) higher filler loadings result in longer aligned chains, 3) higher magnetic fields result in poorer dispersion (due to greater particle migration). The alignment was further validated by 2D Small-angle X-ray scattering (SAXS), confirming that the magnetic graphene sheets are oriented parallel to the magnetic field.

The positive effects of orientation on the mechanical reinforcement were demonstrated by Raman spectroscopy, showing greater stress transfer efficiency in aligned MNPs@FLG materials. The alignment of the magnetic nanohybrids, significantly improved the Young's modulus of the nanocomposites by 5-10% (for MNP@FLG) and 41% (for MNP@rGO) when compared with nanocomposites containing randomly-oriented nanohybrids. The tensile testing data were compared well with the theoretical estimations by the Halpin-Tsai model, further confirming the orientation of the nanofillers under the magnetic field. However, this enhancement was not observed at TRM-mixed composites and this might attribute to a loss of the magnetic nanoparticles under the shear forces of TRM and hence, a less efficient orientation. DMA data were not able to show an anisotropic reinforcement on the thermo-mechanical properties of the epoxy composites. These results are attributed mainly to the length scale effects, the less distributed material under the applied magnetic fields, the poor stress transfer (as proved by Raman) and the reduced cross-linking density.

## 7.2. Future work

In Chapter 4, the distribution of iron oxide nanoparticles on the graphene nanomaterials was performed, starting with the same concentration of iron source. It will be very interesting to optimize the alignment conditions of the magnetic nanohydrids into the epoxy system, by changing the feeding parameters of the co-precipitation method. The goal of this study will be to examine the selection of anisotropic particles within the optimum size range enables minimum use of the iron oxide nanoparticles and achieve less defects on the graphene surface with a perfect alignment into the epoxy systems.

In Chapter 5, a better understanding of the manufacturing parameters in graphene-based epoxy nanocomposites and their influence on the mechanical properties was presented. In our systems, repulsive interfacial interactions were observed as the $T_g$ was decreased for both linear and highly cross-linked systems, resulting in a low stress transfer and hence low mechanical reinforcement. A better interaction between the nanofillers and the matrix in the interface leads

to efficient energy transfer, while the excellent properties of nanofillers should be maintained. More investigation is needed to explore the mechanism on mechanical reinforcement when covalent bonding occurs on the interphase zone, using different cross-linking levels and understand better its effect on the mechanical properties of the DGEBA-grafted graphene/ epoxy composites. This work will give an understanding of the interphase of graphene-based composites and also will provide an indication for the effects of the modification of nanofillers on the interphase zone.

In the Chapter 6, Raman spectroscopy showed a better stress transfer under the applied magnetic field between the polymer matrix to the MNPs@FLG reinforcement from stress-induced shifts of the Raman bands. More investigation is needed to explore the stress transfer on the individual magnetic nanoparticles in comparison with the magnetic nanohybrids (MNPs@graphene) when are randomly and oriented dispersed on the epoxy system under the application of magnetic field. This study will present a better understanding of the effects both of magnetic nanoparticles and nanohybrids on the mechanical reinforcement of the epoxy system.

Also, the positive effect of the orientation efficiency was not observed by the TRM-composites at tensile measurements. The effect of the shear forces on the surface of dried magnetic nanohybrids after processing with TRM, can be evaluated by chemical characterizations, such as TGA and XPS in order to identify any possible changes on the mass concentration of the two components (magnetic nanoparticles and graphene sheets). Also, the morphological analysis could be evaluated by SEM or TEM in order to check if the distribution of the magnetic nanoparticles has been affected.

Moreover, all the magnetic nanohybrids have leaded to lower $T_g$ values when randomly dispersed, resulting in a lower crosslinking network and dominated the bulk mechanical properties. The effect of the cross-linking density in the mechanical properties of magnetic nanofillers reinforced on DGEBA system with different cross-linking levels before and after the alignment could be explored using DMA and DSC analysis. This study will give a new insight of the graphene orientation in the mechanical properties of the epoxy composites.

Apart from the mechanical properties of the aligned graphene/epoxy nanocomposites, it will be very interesting to be investigated the synergetic effect of the graphene sheets on the fracture efficiency of carbon fibers/epoxy nanocomposites, when the graphene sheets are aligned perpendicular direction with the carbon fibers. Also, Impedance Spectroscopy measurements

will be useful for potential applications in order to check if the aligned graphene sheets reduce the high electrical resistivity of the epoxy matrix.

## References


Abdalla, Mohamed, Derrick Dean, Merlin Theodore, Jennifer Fielding, Elijah Nyairo, and Gary Price. 2010. 'Magnetically processed carbon nanotube/epoxy nanocomposites: Morphology, thermal, and mechanical properties', *Polymer*, 51: 1614-20.

Aboutalebi, Seyed Hamed, Mohsen Moazzami Gudarzi, Qing Bin Zheng, and Jang-Kyo Kim. 2011. 'Spontaneous formation of liquid crystals in ultralarge graphene oxide dispersions', *Advanced Functional Materials*, 21: 2978-88.

Achee, Thomas C., Wanmei Sun, Joshua T. Hope, Samuel G. Quitzau, Charles Brandon Sweeney, Smit A. Shah, Touseef Habib, and Micah J. Green. 2018. 'High-yield scalable graphene nanosheet production from compressed graphite using electrochemical exfoliation', *Scientific reports*, 8: 14525.

Acocella, Maria Rosaria, C Esposito Corcione, Antonella Giuri, M Maggio, A Maffezzoli, and G Guerra. 2016. 'Graphene oxide as a catalyst for ring opening reactions in amine crosslinking of epoxy resins', *RSC advances*, 6: 23858-65.

Adenier, Alain, Marie-Claude Bernard, Mohamed M Chehimi, Eva Cabet-Deliry, Bernard Desbat, Olivier Fagebaume, Jean Pinson, and Fetah Podvorica. 2001. 'Covalent modification of iron surfaces by electrochemical reduction of aryldiazonium salts', *Journal of the American Chemical Society*, 123: 4541-49.

Affdl, JC Halpin, and JL Kardos. 1976. 'The Halpin-Tsai equations: a review', *Polymer Engineering & Science*, 16: 344-52.

Agubra, Victor A, Peter S Owuor, and Mahesh V Hosur. 2013. 'Influence of nanoclay dispersion methods on the mechanical behavior of E-glass/epoxy nanocomposites', *Nanomaterials*, 3: 550-63.

Ahmad, Siti Rohana, Chengzhe Xue, and Robert J Young. 2017. 'The mechanisms of reinforcement of polypropylene by graphene nanoplatelets', *Materials Science and Engineering: B*, 216: 2-9.

Ahmadi-Moghadam, B, M Sharafimasooleh, S Shadlou, and F Taheri. 2015. 'Effect of functionalization of graphene nanoplatelets on the mechanical response of graphene/epoxy composites', *Materials & Design (1980-2015)*, 66: 142-49.

Ahmadi-Moghadam, B, and F Taheri. 2014. 'Effect of processing parameters on the structure and multi-functional performance of epoxy/GNP-nanocomposites', *Journal of Materials Science*, 49: 6180-90.

Anagnostopoulos, George, Charalampos Androulidakis, Emmanuel N Koukaras, Georgia Tsoukleri, Ioannis Polyzos, John Parthenios, Konstantinos Papagelis, and Costas Galiotis. 2015. 'Stress transfer mechanisms at the submicron level for graphene/polymer systems', *ACS applied materials & interfaces*, 7: 4216-23.

Annamalai, M, S Mathew, M Jamali, D Zhan, and M Palaniapan. 2012. 'Elastic and nonlinear response of nanomechanical graphene devices', *Journal of Micromechanics and Microengineering*, 22: 105024.

Baaziz, Walid, Lai Truong-Phuoc, Cuong Duong-Viet, Goergian Melinte, Izabela Janowska, Vasiliki Papaefthimiou, Ovidiu Ersen, Spyridon Zafeiratos, Dominique Begin, and Sylvie Begin-Colin. 2014. 'Few layer graphene decorated with homogeneous magnetic Fe 3 O 4 nanoparticles with tunable covering densities', *Journal of Materials Chemistry A*, 2: 2690-700.

Bacon, G. E. 1961. 'Graphite: An Ideally Imperfect Material', *Nature*, 189: 522-22.

Bacon, GE. 1956. 'A method for determining the degree of orientation of graphite', *Journal of Applied Chemistry*, 6: 477-81.

Bagri, Akbar, Cecilia Mattevi, Muge Acik, Yves J Chabal, Manish Chhowalla, and Vivek B Shenoy. 2010. 'Structural evolution during the reduction of chemically derived graphene oxide', *Nature chemistry*, 2: 581-87.

Balandin, Alexander A, Suchismita Ghosh, Wenzhong Bao, Irene Calizo, Desalegne Teweldebrhan, Feng Miao, and Chun Ning Lau. 2008. 'Superior thermal conductivity of single-layer graphene', *Nano letters*, 8: 902-07.

Balaram, V., Dharmendra Vummiti, Princie Roy, C. Taylor, C. T. Kamala, Manavalan Satyanarayanan, K. Prasenjit, K. Subramanyam, A. K. Raju, and Abburi Krishnaiah. 2014. 'Microwave plasma

atomic emission spectrometry (MP-AES): a new analytical tool for geochemical studies', *Atomic Spectroscopy*, 35: 65-78.

Bao, Chenlu, Yuqiang Guo, Lei Song, and Yuan Hu. 2011. 'Poly (vinyl alcohol) nanocomposites based on graphene and graphite oxide: a comparative investigation of property and mechanism', *Journal of Materials Chemistry*, 21: 13942-50.

Bao, Chenlu, Yuqiang Guo, Lei Song, Yongchun Kan, Xiaodong Qian, and Yuan Hu. 2011. 'In situ preparation of functionalized graphene oxide/epoxy nanocomposites with effective reinforcements', *Journal of Materials Chemistry*, 21: 13290-98.

Becerril, Héctor A, Jie Mao, Zunfeng Liu, Randall M Stoltenberg, Zhenan Bao, and Yongsheng Chen. 2008. 'Evaluation of solution-processed reduced graphene oxide films as transparent conductors', *ACS nano*, 2: 463-70.

Behabtu, Natnael, Jay R Lomeda, Micah J Green, Amanda L Higginbotham, Alexander Sinitskii, Dmitry V Kosynkin, Dmitri Tsentalovich, A Nicholas G Parra-Vasquez, Judith Schmidt, and Ellina Kesselman. 2010. 'Spontaneous high-concentration dispersions and liquid crystals of graphene', *Nature nanotechnology*, 5: 406-11.

Berg, H.C. 2018. *Random Walks in Biology: New and Expanded Edition* (Princeton University Press).

Berger, Claire, Zhimin Song, Xuebin Li, Xiaosong Wu, Nate Brown, Cécile Naud, Didier Mayou, Tianbo Li, Joanna Hass, and Alexei N Marchenkov. 2006. 'Electronic confinement and coherence in patterned epitaxial graphene', *Science*, 312: 1191-96.

Bhuvaneswari, Subramani, Parakandy Muzhikara Pratheeksha, Srinivasan Anandan, Dinesh Rangappa, Raghavan Gopalan, and Tata Narasinga Rao. 2014. 'Efficient reduced graphene oxide grafted porous Fe 3 O 4 composite as a high performance anode material for Li-ion batteries', *Physical Chemistry Chemical Physics*, 16: 5284-94.

Bianco, Alberto, Hui-Ming Cheng, Toshiaki Enoki, Yury Gogotsi, Robert H Hurt, Nikhil Koratkar, Takashi Kyotani, Marc Monthioux, Chong Rae Park, and Juan MD Tascon. 2013. "All in the graphene family–A recommended nomenclature for two-dimensional carbon materials." In.: Elsevier.

Bianco, GV, M Losurdo, MM Giangregorio, P Capezzuto, and G Bruno. 'Chemical functionalization of graphene by plasma processes'.

Biesinger, Mark C, Brad P Payne, Andrew P Grosvenor, Leo WM Lau, Andrea R Gerson, and Roger St C Smart. 2011. 'Resolving surface chemical states in XPS analysis of first row transition metals, oxides and hydroxides: Cr, Mn, Fe, Co and Ni', *Applied Surface Science*, 257: 2717-30.

Bignotti, Fabio, Stefano Pandini, Francesco Baldi, and Riccardo De Santis. 2011. 'Effect of the resin/hardener ratio on curing, structure and glass transition temperature of nanofilled epoxies', *Polymer Composites*, 32: 1034-48.

Bîru, Elena Iuliana, and Horia Iovu. 2018. 'Graphene Nanocomposites Studied by Raman Spectroscopy.' in, *Raman Spectroscopy* (IntechOpen).

Bon, Silvia Bittolo, Luca Valentini, Raquel Verdejo, Jose L Garcia Fierro, Laura Peponi, Miguel A Lopez-Manchado, and Jose M Kenny. 2009. 'Plasma fluorination of chemically derived graphene sheets and subsequent modification with butylamine', *Chemistry of Materials*, 21: 3433-38.

Boothroyd, Stephen C, David W Johnson, Michael P Weir, Carl D Reynolds, James M Hart, Andrew J Smith, Nigel Clarke, Richard L Thompson, and Karl S Coleman. 2018. 'Controlled structure evolution of graphene networks in polymer composites', *Chemistry of Materials*, 30: 1524-31.

Bose, Saswata, Arit Das, Sankhadeep Basu, and Lawrence T Drzal. 2018. 'Covalent functionalization of graphene using polyacryloyl chloride and performance of functionalized graphene–epoxy nanocomposite', *Polymer Composites*, 39: 3119-28.

Bragg, William Lawrence. 1929. 'The diffraction of short electromagnetic waves by a crystal'.

Brydson, John Andrew. 1999. *Plastics materials* (Elsevier).

Cai, Jinming, Pascal Ruffieux, Rached Jaafar, Marco Bieri, Thomas Braun, Stephan Blankenburg, Matthias Muoth, Ari P Seitsonen, Moussa Saleh, and Xinliang Feng. 2010. 'Atomically precise bottom-up fabrication of graphene nanoribbons', *Nature*, 466: 470-73.

Camponeschi, Erin, Richard Vance, Marwan Al-Haik, Hamid Garmestani, and Rina Tannenbaum. 2007. 'Properties of carbon nanotube–polymer composites aligned in a magnetic field', *Carbon*, 45: 2037-46.

Caradonna, Andrea, Claudio Badini, Elisa Padovano, and Mario Pietroluongo. 2019. 'Electrical and thermal conductivity of epoxy-carbon filler composites processed by calendaring', *Materials*, 12: 1522.

Carrot, Christian, Jean-Charles Majesté, Beatriz Olalla, and René Fulchiron. 2010. 'On the use of the model proposed by Leonov for the explanation of a secondary plateau of the loss modulus in heterogeneous polymer–filler systems with agglomerates', *Rheologica Acta*, 49: 513-27.

Castarlenas, Sonia, César Rubio, Álvaro Mayoral, Carlos Téllez, and Joaquín Coronas. 2014. 'Few-layer graphene by assisted-exfoliation of graphite with layered silicate', *Carbon*, 73: 99-105.

Cha, JinHyeok, Woomin Kyoung, Kyonghwa Song, Sangbaek Park, Taewon Lim, Jongkook Lee, and Hyunmin Kang. 2016. 'Quantitative evaluation of the dispersion of graphene sheets with and without functional groups using molecular dynamics simulations', *Nanoscale research letters*, 11: 136.

Chandra, Vimlesh, Jaesung Park, Young Chun, Jung Woo Lee, In-Chul Hwang, and Kwang S Kim. 2010. 'Water-dispersible magnetite-reduced graphene oxide composites for arsenic removal', *ACS nano*, 4: 3979-86.

Chandrasekaran, Swetha, Narumichi Sato, Folke Tölle, Rolf Mülhaupt, Bodo Fiedler, and Karl Schulte. 2014. 'Fracture toughness and failure mechanism of graphene based epoxy composites', *Composites Science and Technology*, 97: 90-99.

Chandrasekaran, Swetha, Christian Seidel, and Karl Schulte. 2013. 'Preparation and characterization of graphite nano-platelet (GNP)/epoxy nano-composite: mechanical, electrical and thermal properties', *European Polymer Journal*, 49: 3878-88.

Chang, Yan-Ping, Cui-Ling Ren, Ji-Chun Qu, and Xing-Guo Chen. 2012. 'Preparation and characterization of Fe3O4/graphene nanocomposite and investigation of its adsorption performance for aniline and p-chloroaniline', *Applied Surface Science*, 261: 504-09.

Chatterjee, Sanjukta, JW Wang, WS Kuo, NH Tai, C Salzmann, WL Li, Rebecca Hollertz, FA Nüesch, and BTT Chu. 2012. 'Mechanical reinforcement and thermal conductivity in expanded graphene nanoplatelets reinforced epoxy composites', *Chemical Physics Letters*, 531: 6-10.

Chen, Jinfeng, Miao Duan, and Guohua Chen. 2012. 'Continuous mechanical exfoliation of graphene sheets via three-roll mill', *Journal of Materials Chemistry*, 22: 19625-28.

Chen, Ling, Debao Liu, and Ping Yang. 2019. 'Preparation of α-Fe 2 O 3/rGO composites toward supercapacitor applications', *RSC advances*, 9: 12793-800.

Chen, Yu-Jin, Peng Gao, Rui-Xuan Wang, Chun-Ling Zhu, Li-Jiao Wang, Mao-Sheng Cao, and Hai-Bo Jin. 2009. 'Porous Fe3O4/SnO2 core/shell nanorods: synthesis and electromagnetic properties', *The Journal of Physical Chemistry C*, 113: 10061-64.

Chhetri, Suman, Nitai Chandra Adak, Pranab Samanta, Naresh Chandra Murmu, David Hui, Tapas Kuila, and Joong Hee Lee. 2018. 'Investigation of the mechanical and thermal properties of l-glutathione modified graphene/epoxy composites', *Composites Part B: Engineering*, 143: 105-12.

Chong, HM, SJ Hinder, and AC Taylor. 2016. 'Graphene nanoplatelet-modified epoxy: effect of aspect ratio and surface functionality on mechanical properties and toughening mechanisms', *Journal of Materials Science*, 51: 8764-90.

Chourpa, Igor, Laurence Douziech-Eyrolles, Lazare Ngaboni-Okassa, Jean-François Fouquenet, Simone Cohen-Jonathan, Martin Soucé, Hervé Marchais, and Pierre Dubois. 2005. 'Molecular composition of iron oxide nanoparticles, precursors for magnetic drug targeting, as characterized by confocal Raman microspectroscopy', *Analyst*, 130: 1395-403.

Clausi, Marialaura, M Gabriella Santonicola, and Susanna Laurenzi. 2016. "Steady-shear rheological properties of graphene-reinforced epoxy resin for manufacturing of aerospace composite films." In *AIP Conference Proceedings*, 020024. AIP Publishing LLC.

Coduri, Mauro, Paolo Masala, Lucia Del Bianco, Federico Spizzo, Davide Ceresoli, Carlo Castellano, Serena Cappelli, Cesare Oliva, Stefano Checchia, and Mattia Allieta. 2020. 'Local Structure and Magnetism of Fe2O3 Maghemite Nanocrystals: The Role of Crystal Dimension', *Nanomaterials*, 10: 867.

Cooper, CA, RJ Young, and M Halsall. 2001. 'Investigation into the deformation of carbon nanotubes and their composites through the use of Raman spectroscopy', *Composites Part A: Applied Science and Manufacturing*, 32: 401-11.

Cooper, G, and A Kelly. 1969. 'Role of the interface in the fracture of fiber-composite materials.' in, *Interfaces in Composites* (ASTM International).

Dai, Jin-Feng, Guo-Jian Wang, Lang Ma, and Cheng-Ken Wu. 2015. 'Surface properties of graphene: relationship to graphene-polymer composites', *Rev. Adv. Mater. Sci*, 40: 60-71.

De Silva, KKH, H-H Huang, RK Joshi, and M Yoshimura. 2017. 'Chemical reduction of graphene oxide using green reductants', *Carbon*, 119: 190-99.

Del Giudice, Francesco, and Amy Q Shen. 2017. 'Shear rheology of graphene oxide dispersions', *Current opinion in chemical engineering*, 16: 23-30.

Dervishi, Enkeleda, Zhongrui Li, Fumiya Watanabe, Abhijit Biswas, Yang Xu, Alexandru R Biris, Viney Saini, and Alexandru S Biris. 2009. 'Large-scale graphene production by RF-cCVD method', *Chemical communications*: 4061-63.

Dikin, Dmitriy A, Sasha Stankovich, Eric J Zimney, Richard D Piner, Geoffrey HB Dommett, Guennadi Evmenenko, SonBinh T Nguyen, and Rodney S Ruoff. 2007. 'Preparation and characterization of graphene oxide paper', *Nature*, 448: 457-60.

Ding, Jie, Baojun Li, Yushan Liu, Xiaoshe Yan, Sha Zeng, Xudong Zhang, Lifen Hou, Qiang Cai, and Jianmin Zhang. 2015. 'Fabrication of Fe 3 O 4@ reduced graphene oxide composite via novel colloid electrostatic self-assembly process for removal of contaminants from water', *Journal of Materials Chemistry A*, 3: 832-39.

Domun, Nadiim, Homayoun Hadavinia, Tao Zhang, Gholamhossein Liaghat, Samireh Vahid, Chris Spacie, Keith R Paton, and Toby Sainsbury. 2017. 'Improving the fracture toughness properties of epoxy using graphene nanoplatelets at low filler content', *Nanocomposites*, 3: 85-96.

Dong, Yucheng, Ruguang Ma, Mingjun Hu, Hua Cheng, Qingdan Yang, Yang Li, and J. Antonio Zapien. 2013. 'Thermal evaporation-induced anhydrous synthesis of Fe3O4-graphene composite with enhanced rate performance and cyclic stability for lithium ion batteries', *Physical chemistry chemical physics : PCCP*, 15.

Dresselhaus, Mildred S, Gene Dresselhaus, Ko Sugihara, Ian L Spain, and Harris A Goldberg. 2013. *Graphite fibers and filaments* (Springer Science & Business Media).

Dresselhaus, Mildred S, Ado Jorio, Mario Hofmann, Gene Dresselhaus, and Riichiro Saito. 2010. 'Perspectives on carbon nanotubes and graphene Raman spectroscopy', *Nano letters*, 10: 751-58.

Dumee, Ludovic, Aaron Thornton, Kallista Sears, Jürg Schütz, Niall Finn, Steven Spoljaric, Robert Shanks, Chris Skourtis, Mikel Duke, and Stephen Gray. 2012. 'In situ small angle X-ray scattering investigation of the thermal expansion and related structural information of carbon nanotube composites', *Progress in Natural Science: Materials International*, 22: 673-83.

Dunson, Debra. 2017. 'Characterization of Polymers using Dynamic Mechanical Analysis (DMA)'.

Dyer, Christopher, Kyriaki Gkaliou, Philip Anderson, Christopher Harrison, Mark Eaton, and Jeremy Hall. 2019. 'Computer-controlled electromagnetic control and image capture system for alignment of magnetic graphene nanofillers in epoxy composites', *International Journal of Applied Electromagnetics and Mechanics*, 61: S23-S29.

El Achaby, Mounir, Fatima-Ezzahra Arrakhiz, Sebastien Vaudreuil, Abou el Kacem Qaiss, Mostapha Bousmina, and Omar Fassi-Fehri. 2012. 'Mechanical, thermal, and rheological properties of graphene-based polypropylene nanocomposites prepared by melt mixing', *Polymer Composites*, 33: 733-44.

Epp, J. 2016. 'X-ray diffraction (XRD) techniques for materials characterization.' in, *Materials characterization using Nondestructive Evaluation (NDE) methods* (Elsevier).

Erb, R. M., H. S. Son, B. Samanta, V. M. Rotello, and B. B. Yellen. 2009. 'Magnetic assembly of colloidal superstructures with multipole symmetry', *Nature*, 457: 999-1002.

Erb, Randall M, Rafael Libanori, Nuria Rothfuchs, and André R Studart. 2012. 'Composites reinforced in three dimensions by using low magnetic fields', *Science*, 335: 199-204.

Erb, Randall M, Jana Segmehl, Michalis Charilaou, Jörg F Löffler, and André R Studart. 2012. 'Non-linear alignment dynamics in suspensions of platelets under rotating magnetic fields', *Soft Matter*, 8: 7604-09.

Erdem, Sezer, Beyhan Erdem, and Ramis Mustafa Öksüzoğlu. 'Magnetic Nano-Sized Solid Acid Catalyst Bearing Sulfonic Acid Groups for Biodiesel Synthesis', *Open Chemistry*, 16: 923-29.

Fan, Wei, Wei Gao, Chao Zhang, Weng Weei Tjiu, Jisheng Pan, and Tianxi Liu. 2012. 'Hybridization of graphene sheets and carbon-coated Fe 3 O 4 nanoparticles as a synergistic adsorbent of organic dyes', *Journal of Materials Chemistry*, 22: 25108-15.

Fan, YH, SW Yu, HM Wang, YH Yao, Y Wang, and CH Wang. 2019. "Study on preparation and properties of graphene reinforced epoxy resin composites." In *IOP Conference Series: Materials Science and Engineering*, 012044. IOP Publishing.

Fang, Ming, Zhen Zhang, Jianfeng Li, Hongdong Zhang, Hongbin Lu, and Yuliang Yang. 2010. 'Constructing hierarchically structured interphases for strong and tough epoxy nanocomposites by amine-rich graphene surfaces', *Journal of Materials Chemistry*, 20: 9635-43.

Ferralis, Nicola. 2010. 'Probing mechanical properties of graphene with Raman spectroscopy', *Journal of Materials Science*, 45: 5135-49.

Ferrari, Andrea C. 2007. 'Raman spectroscopy of graphene and graphite: disorder, electron–phonon coupling, doping and nonadiabatic effects', *Solid state communications*, 143: 47-57.

Ferrari, Andrea C, JC Meyer, Vittorio Scardaci, Cinzia Casiraghi, Michele Lazzeri, Francesco Mauri, Stefano Piscanec, Da Jiang, KS Novoselov, and S Roth. 2006. 'Raman spectrum of graphene and graphene layers', *Physical review letters*, 97: 187401.

Ferrari, Andrea C, and John Robertson. 2000. 'Interpretation of Raman spectra of disordered and amorphous carbon', *Physical Review B*, 61: 14095.

Foner, Simon. 1956. 'Vibrating sample magnetometer', *Review of Scientific Instruments*, 27: 548-48.

Frank, Otakar, Georgia Tsoukleri, Ibtsam Riaz, Konstantinos Papagelis, John Parthenios, Andrea C Ferrari, Andre K Geim, Kostya S Novoselov, and Costas Galiotis. 2011. 'Development of a universal stress sensor for graphene and carbon fibres', *Nature communications*, 2: 1-7.

Frison, Ruggero, Giuseppe Cernuto, Antonio Cervellino, Oksana Zaharko, Gian Maria Colonna, Antonietta Guagliardi, and Norberto Masciocchi. 2013. 'Magnetite–Maghemite Nanoparticles in the 5–15 nm Range: Correlating the Core–Shell Composition and the Surface Structure to the Magnetic Properties. A Total Scattering Study', *Chemistry of Materials*, 25: 4820-27.

Fullerton, Robert J, Daniel P Cole, Kristopher D Behler, Sriya Das, Fahmida Irin, Dorsa Parviz, MNF Hoque, Zhaoyang Fan, and Micah J Green. 2014. 'Graphene non-covalently tethered with magnetic nanoparticles', *Carbon*, 72: 192-99.

Galindo-Rosales, Francisco J, Paula Moldenaers, and Jan Vermant. 2011. 'Assessment of the dispersion quality in polymer nanocomposites by rheological methods', *Macromolecular Materials and Engineering*, 296: 331-40.

Galpaya, Dilini GD, Joseph FS Fernando, Llew Rintoul, Nunzio Motta, Eric R Waclawik, Cheng Yan, and Graeme A George. 2015. 'The effect of graphene oxide and its oxidized debris on the cure chemistry and interphase structure of epoxy nanocomposites', *Polymer*, 71: 122-34.

Gao, Wei, Lawrence B Alemany, Lijie Ci, and Pulickel M Ajayan. 2009. 'New insights into the structure and reduction of graphite oxide', *Nature chemistry*, 1: 403.

Gao, Yun, Lu-Qi Liu, Sheng-Zhen Zu, Ke Peng, Ding Zhou, Bao-Hang Han, and Zhong Zhang. 2011. 'The effect of interlayer adhesion on the mechanical behaviors of macroscopic graphene oxide papers', *ACS nano*, 5: 2134-41.

Geim, Andre K, and Konstantin S Novoselov. 2010. 'The rise of graphene.' in, *Nanoscience and technology: a collection of reviews from nature journals* (World Scientific).

George, Herman F., and Farrukh Qureshi. 2013. 'Newton's Law of Viscosity, Newtonian and Non-Newtonian Fluids.' in Q. Jane Wang and Yip-Wah Chung (eds.), *Encyclopedia of Tribology* (Springer US: Boston, MA).

Gibson, Ronald F. 2016. *Principles of composite material mechanics* (CRC press).

Gómez-Navarro, Cristina, Marko Burghard, and Klaus Kern. 2008. 'Elastic properties of chemically derived single graphene sheets', *Nano letters*, 8: 2045-49.

Gong, Jian Ru. 2011. *Graphene: Synthesis, Characterization, Properties and Applications* (BoD–Books on Demand).

Gong, Lei. 2013. 'Deformation micromechanics of graphene nanocomposites', University of Manchester.

Gong, Lei, Ian A Kinloch, Robert J Young, Ibtsam Riaz, Rashid Jalil, and Konstantin S Novoselov. 2010. 'Interfacial stress transfer in a graphene monolayer nanocomposite', *Advanced Materials*, 22: 2694-97.

Gong, Lei, Robert J Young, Ian A Kinloch, Ibtsam Riaz, Rashid Jalil, and Kostya S Novoselov. 2012. 'Optimizing the reinforcement of polymer-based nanocomposites by graphene', *ACS nano*, 6: 2086-95.

Gou, J, J Zhuge, and F Liang. 2012. 'Processing of polymer nanocomposites.' in, *Manufacturing Techniques for Polymer Matrix Composites (PMCs)* (Elsevier).

Grassie, Norman, Marilyn I Guy, and Norman H Tennent. 1986. 'Degradation of epoxy polymers: part 4—thermal degradation of bisphenol-A diglycidyl ether cured with ethylene diamine', *Polymer degradation and stability*, 14: 125-37.

Guoxin, Hu, and Zhengxia Xu. 2015. 'Monodisperse iron oxide nanoparticle-reduced graphene oxide composites formed by self-assembly in aqueous phase', *Fullerenes, Nanotubes and Carbon Nanostructures*, 23: 283-89.

Guy, Owen J, and Kelly-Ann D Walker. 2016. 'Graphene functionalization for biosensor applications.' in, *Silicon Carbide Biotechnology* (Elsevier).

Hadden, CM, BD Jensen, A Bandyopadhyay, GM Odegard, A Koo, and R Liang. 2013. 'Molecular modeling of EPON-862/graphite composites: Interfacial characteristics for multiple crosslink densities', *Composites Science and Technology*, 76: 92-99.

Han, Joong Tark, Jeong In Jang, Haena Kim, Jun Yeon Hwang, Hyung Keun Yoo, Jong Seok Woo, Sua Choi, Ho Young Kim, Hee Jin Jeong, and Seung Yol Jeong. 2014. 'Extremely efficient liquid exfoliation and dispersion of layered materials by unusual acoustic cavitation', *Scientific reports*, 4: 5133.

Hanfland, M, H Beister, and K Syassen. 1989. 'Graphite under pressure: Equation of state and first-order Raman modes', *Physical Review B*, 39: 12598.

Hatami, M, and DD Ganji. 2013. 'Heat transfer and flow analysis for SA-TiO2 non-Newtonian nanofluid passing through the porous media between two coaxial cylinders', *Journal of Molecular Liquids*, 188: 155-61.

Haydale. 2020. 'White Paper: Up To 28% Functionalisation Through Dry Plasma HDPlas Process Offers Environmentally Friendly, Scalable Alternative to Graphene Oxide'. https://haydale.com/news/white-paper-up-to-28-functionalisation-through-dry-plasma-hdplas-process-offers-environmentally-friendly-scalable-alternative-to-graphene-oxide/.

Hazarika, Ankita, Biplab K Deka, DoYoung Kim, Kyungil Kong, Young-Bin Park, and Hyung Wook Park. 2017. 'Microwave-synthesized freestanding iron-carbon nanotubes on polyester composites of woven Kevlar fibre and silver nanoparticle-decorated graphene', *Scientific reports*, 7: 40386.

He, Fuan, Jintu Fan, Dong Ma, Liming Zhang, Chiwah Leung, and Helen Laiwa Chan. 2010. 'The attachment of Fe3O4 nanoparticles to graphene oxide by covalent bonding', *Carbon*, 48: 3139-44.

He, Hongkun, and Chao Gao. 2010. 'Supraparamagnetic, conductive, and processable multifunctional graphene nanosheets coated with high-density Fe3O4 nanoparticles', *ACS applied materials & interfaces*, 2: 3201-10.

He, Zhiping, Xiaohua Zhang, Minghai Chen, Min Li, Yizhuo Gu, Zuoguang Zhang, and Qingwen Li. 2013. 'Effect of the filler structure of carbon nanomaterials on the electrical, thermal, and rheological properties of epoxy composites', *Journal of applied polymer science*, 129: 3366-72.

Hermans, JJ, PH Hermans, D Vermaas, and A Weidinger. 1946. 'Quantitative evaluation of orientation in cellulose fibres from the X-ray fibre diagram', *Recueil des Travaux Chimiques des Pays-Bas*, 65: 427-47.

Hernandez, Yenny, Valeria Nicolosi, Mustafa Lotya, Fiona M Blighe, Zhenyu Sun, Sukanta De, IT McGovern, Brendan Holland, Michele Byrne, and Yurii K Gun'Ko. 2008. 'High-yield production of graphene by liquid-phase exfoliation of graphite', *Nature nanotechnology*, 3: 563.

Horiba. 'How long does it take to acquire a Raman spectral image?'. https://www.horiba.com/uk/scientific/products/raman-spectroscopy/raman-academy/raman-faqs/how-long-does-it-take-to-acquire-a-raman-spectral-image/.

Huang, Liang, Pengli Zhu, Gang Li, Daoqiang Daniel Lu, Rong Sun, and Chingping Wong. 2014. 'Core–shell SiO 2@ RGO hybrids for epoxy composites with low percolation threshold and enhanced thermo-mechanical properties', *Journal of Materials Chemistry A*, 2: 18246-55.

Huang, Ting, Renguo Lu, Chao Su, Hongna Wang, Zheng Guo, Pei Liu, Zhongyuan Huang, Haiming Chen, and Tongsheng Li. 2012. 'Chemically modified graphene/polyimide composite films based on utilization of covalent bonding and oriented distribution', *ACS applied materials & interfaces*, 4: 2699-708.

Hull, D. 1981. *An Introduction to Composite Materials. 1st ed.;* .

Ihiawakrim, Dris, Ovidiu Ersen, Frédéric Melin, Petra Hellwig, Izabela Janowska, Dominique Begin, Walid Baaziz, Sylvie Begin-Colin, Cuong Pham-Huu, and Rachid Baati. 2013. 'A single-stage functionalization and exfoliation method for the production of graphene in water: stepwise construction of 2D-nanostructured composites with iron oxide nanoparticles', *Nanoscale*, 5: 9073-80.

Ilnicka, Anna, Malgorzata Skorupska, Piotr Kamedulski, and Jerzy P Lukaszewicz. 2019. 'Electro-Exfoliation of Graphite to Graphene in an Aqueous Solution of Inorganic Salt and the Stabilization of Its Sponge Structure with Poly (Furfuryl Alcohol)', *Nanomaterials*, 9: 971.

Inagaki, Michio, and Feiyu Kang. 2016. *Materials science and engineering of carbon: characterization* (Butterworth-Heinemann).

Ivanov, Evgeni, Hristiana Velichkova, Rumiana Kotsilkova, Silvia Bistarelli, Antonino Cataldo, Federico Micciulla, and Stefano Bellucci. 2017. 'Rheological behavior of graphene/epoxy nanodispersions', *Applied Rheology*, 27: 1-9.

Ivanovskaya, Viktoria V, Philipp Wagner, Alberto Zobelli, Irene Suarez-Martinez, Abu Yaya, and Christopher P Ewels. 2012. 'Graphene edge structures: Folding, scrolling, tubing, rippling and twisting.' in, *GraphITA 2011* (Springer).

Iyengar, Srividhya J, Mathew Joy, Titir Maity, Jnananjan Chakraborty, Ravinder K Kotnala, and Swapankumar Ghosh. 2016. 'Colloidal properties of water dispersible magnetite nanoparticles by photon correlation spectroscopy', *RSC advances*, 6: 14393-402.

Jang, Hee Dong, Sun Kyung Kim, Hankwon Chang, Ji-Hyuk Choi, Bong-Gyoo Cho, Eun Hee Jo, Jeong-Woo Choi, and Jiaxing Huang. 2015. 'Three-dimensional crumpled graphene-based platinum–gold alloy nanoparticle composites as superior electrocatalysts for direct methanol fuel cells', *Carbon*, 93: 869-77.

Jeong, Hyung Mo, Jung Woo Lee, Weon Ho Shin, Yoon Jeong Choi, Hyun Joon Shin, Jeung Ku Kang, and Jang Wook Choi. 2011. 'Nitrogen-doped graphene for high-performance ultracapacitors and the importance of nitrogen-doped sites at basal planes', *Nano letters*, 11: 2472-77.

Jiao, Weicheng, Masatoshi Shioya, Rongguo Wang, Fan Yang, Lifeng Hao, Yue Niu, Wenbo Liu, Li Zheng, Feng Yuan, and Li Wan. 2014. 'Improving the gas barrier properties of Fe3O4/graphite nanoplatelet reinforced nanocomposites by a low magnetic field induced alignment', *Composites Science and Technology*, 99: 124-30.

Kalyon, Dilhan M, Dharmesh Dalwadi, Melek Erol, Elvan Birinci, and Christos Tsenoglu. 2006. 'Rheological behavior of concentrated suspensions as affected by the dynamics of the mixing process', *Rheologica Acta*, 45: 641-58.

Kamala, CT, V Balaram, V Dharmendra, M Satyanarayanan, KSV Subramanyam, and A Krishnaiah. 2014. 'Application of Microwave Plasma Atomic Emission Spectrometry (MP-AES) for environmental monitoring of industrially contaminated sites in Hyderabad City', *Environmental monitoring and assessment*, 186: 7097-113.

Kang, Narae, and Saiful I Khondaker. 2014. 'The impact of carbon sp2 fraction of reduced graphene oxide on the performance of reduced graphene oxide contacted organic transistors', *Applied Physics Letters*, 105: 177_1.

Kataby, G, M Cojocaru, R Prozorov, and A Gedanken. 1999. 'Coating carboxylic acids on amorphous iron nanoparticles', *Langmuir*, 15: 1703-08.

Kausar, Ayesha, Irum Rafique, and Bakhtiar Muhammad. 2016. 'Review of applications of polymer/carbon nanotubes and epoxy/CNT composites', *Polymer-Plastics Technology and Engineering*, 55: 1167-91.

Kelly, Anthony, and Norman Hillas Macmillan. 1986. 'Strong Solids', *Oxford University Press, Walton Street, Oxford OX 2 6 DP, UK, 1986.*

Kemp, Scott J, R Matthew Ferguson, Amit P Khandhar, and Kannan M Krishnan. 2016. 'Monodisperse magnetite nanoparticles with nearly ideal saturation magnetization', *RSC advances*, 6: 77452-64.

Kernin, Arnaud, Kening Wan, Yi Liu, Xuetao Shi, Jie Kong, Emiliano Bilotti, Ton Peijs, and Han Zhang. 2019. 'The effect of graphene network formation on the electrical, mechanical, and multifunctional properties of graphene/epoxy nanocomposites', *Composites Science and Technology*, 169: 224-31.

Kim, Byungjo, Joonmyung Choi, Seunghwa Yang, Suyoung Yu, and Maenghyo Cho. 2015. 'Influence of crosslink density on the interfacial characteristics of epoxy nanocomposites', *Polymer*, 60: 186-97.

Kim, Chang-Duk, Bong-Ki Min, and Woo-Sik Jung. 2009. 'Preparation of graphene sheets by the reduction of carbon monoxide', *Carbon*, 47: 1610-12.

Kim, DK, Y Zhang, W Voit, KV Rao, and Mamoun Muhammed. 2001. 'Synthesis and characterization of surfactant-coated superparamagnetic monodispersed iron oxide nanoparticles', *Journal of Magnetism and Magnetic Materials*, 225: 30-36.

KIM, GH, DK MOELLER, and YM SHKEL. 2004. 'Orthotropic polymeric composites with microstructure tailored by electric field', *Journal of composite materials*, 38: 1895-909.

Kim, Hyunwoo, Ahmed A Abdala, and Christopher W Macosko. 2010. 'Graphene/polymer nanocomposites', *Macromolecules*, 43: 6515-30.

Kim, Il Tae, Grady A Nunnery, Karl Jacob, Justin Schwartz, Xiaotao Liu, and Rina Tannenbaum. 2010. 'Synthesis, characterization, and alignment of magnetic carbon nanotubes tethered with maghemite nanoparticles', *The Journal of Physical Chemistry C*, 114: 6944-51.

Kim, Jin Ah, Dong Gi Seong, Tae Jin Kang, and Jae Ryoun Youn. 2006. 'Effects of surface modification on rheological and mechanical properties of CNT/epoxy composites', *Carbon*, 44: 1898-905.

Kim, Jiwon, Byung-seung Yim, Jong-min Kim, and Jooheon Kim. 2012. 'The effects of functionalized graphene nanosheets on the thermal and mechanical properties of epoxy composites for anisotropic conductive adhesives (ACAs)', *Microelectronics Reliability*, 52: 595-602.

Kim, Wonbaek, Chang-Yul Suh, Sung-Wook Cho, Ki-Min Roh, Hanjung Kwon, Kyungsun Song, and In-Jin Shon. 2012. 'A new method for the identification and quantification of magnetite–maghemite mixture using conventional X-ray diffraction technique', *Talanta*, 94: 348-52.

King, Julia A, Danielle R Klimek, Ibrahim Miskioglu, and Greg M Odegard. 2013. 'Mechanical properties of graphene nanoplatelet/epoxy composites', *Journal of applied polymer science*, 128: 4217-23.

Kitaura, Ryo, Naoki Imazu, Keita Kobayashi, and Hisanori Shinohara. 2008. 'Fabrication of metal nanowires in carbon nanotubes via versatile nano-template reaction', *Nano letters*, 8: 693-99.

Klimek-McDonald, Danielle R, Julia A King, Ibrahim Miskioglu, Evan J Pineda, and Greg M Odegard. 2018. 'Determination and modeling of mechanical properties for graphene nanoplatelet/epoxy composites', *Polymer Composites*, 39: 1845-51.

Kosynkin, Dmitry V, Amanda L Higginbotham, Alexander Sinitskii, Jay R Lomeda, Ayrat Dimiev, B Katherine Price, and James M Tour. 2009. 'Longitudinal unzipping of carbon nanotubes to form graphene nanoribbons', *Nature*, 458: 872-76.

Kotov, Nicholas A. 2006. 'Carbon sheet solutions', *Nature*, 442: 254-55.

Krenchel, Herbert. 1964. 'Fibre reinforcement; theoretical and practical investigations of the elasticity and strength of fibre-reinforced materials'.

Küçük, Ilknur, Halil Gevgilili, and Dilhan M Kalyon. 2013. 'Effects of dispersion and deformation histories on rheology of semidilute and concentrated suspensions of multiwalled carbon nanotubes', *Journal of Rheology*, 57: 1491-514.

Kudin, Konstantin N, Bulent Ozbas, Hannes C Schniepp, Robert K Prud'Homme, Ilhan A Aksay, and Roberto Car. 2008. 'Raman spectra of graphite oxide and functionalized graphene sheets', *Nano letters*, 8: 36-41.

Kuila, Tapas, Ananta Kumar Mishra, Partha Khanra, Nam Hoon Kim, and Joong Hee Lee. 2013. 'Recent advances in the efficient reduction of graphene oxide and its application as energy storage electrode materials', *Nanoscale*, 5: 52-71.

Lahijani, Pooya, Zainal Alimuddin Zainal, Maedeh Mohammadi, and Abdul Rahman Mohamed. 2015. 'Conversion of the greenhouse gas CO2 to the fuel gas CO via the Boudouard reaction: A review', *Renewable and Sustainable Energy Reviews*, 41: 615-32.

Lalatonne, Y, J Richardi, and MP Pileni. 2004. 'Van der Waals versus dipolar forces controlling mesoscopic organizations of magnetic nanocrystals', *Nature materials*, 3: 121-25.

Landau, LD, EM Lifshitz, and Linda E Reichl. 1981. 'Statistical physics, part 1', *Physics Today*, 34: 74.
Layek, Rama K, and Arun K Nandi. 2013. 'A review on synthesis and properties of polymer functionalized graphene', *Polymer*, 54: 5087-103.
Lee, Changgu, Xiaoding Wei, Jeffrey W Kysar, and James Hone. 2008. 'Measurement of the elastic properties and intrinsic strength of monolayer graphene', *Science*, 321: 385-88.
Lee, Jae-Ung, Duhee Yoon, and Hyeonsik Cheong. 2012. 'Estimation of Young's modulus of graphene by Raman spectroscopy', *Nano letters*, 12: 4444-48.
Lespade, P, R Al-Jishi, and MS Dresselhaus. 1982. 'Model for Raman scattering from incompletely graphitized carbons', *Carbon*, 20: 427-31.
Li, Defeng, Yuyan Liu, Haoxiang Ma, Youshan Wang, Lei Wang, and Zhimin Xie. 2015. 'Preparation and properties of aligned graphene composites', *RSC advances*, 5: 31670-76.
Li, H, T Xu, C Wang, J Chen, H Zhou, and H Liu. 2005. 'Tribochemical effects on the friction and wear behaviors of diamond-like carbon film under high relative humidity condition', *Tribology Letters*, 19: 231-38.
Li, Qi, Yufen Guo, Weiwei Li, Shengqiang Qiu, Chao Zhu, Xiangfei Wei, Mingliang Chen, Chaojun Liu, Shutian Liao, and Youpin Gong. 2014. 'Ultrahigh thermal conductivity of assembled aligned multilayer graphene/epoxy composite', *Chemistry of Materials*, 26: 4459-65.
Li, Qing, Christina W Kartikowati, Shinji Horie, Takashi Ogi, Toru Iwaki, and Kikuo Okuyama. 2017. 'Correlation between particle size/domain structure and magnetic properties of highly crystalline Fe 3 O 4 nanoparticles', *Scientific reports*, 7: 1-7.
Li, Suhao, Zheling Li, Timothy L Burnett, Thomas JA Slater, Teruo Hashimoto, and Robert J Young. 2017. 'Nanocomposites of graphene nanoplatelets in natural rubber: microstructure and mechanisms of reinforcement', *Journal of Materials Science*, 52: 9558-72.
Li, Wei, Patrick Simmons, Doug Shrader, Timothy J Herrman, and Susie Y Dai. 2013. 'Microwave plasma-atomic emission spectroscopy as a tool for the determination of copper, iron, manganese and zinc in animal feed and fertilizer', *Talanta*, 112: 43-48.
Li, Yan, Han Zhang, Emiliano Bilotti, and Ton Peijs. 2016. 'Optimization of three-roll mill parameters for in-situ exfoliation of graphene', *MRS Advances*, 1: 1389-94.
Li, Yan, Han Zhang, Maria Crespo, Harshit Porwal, Olivier Picot, Giovanni Santagiuliana, Zhaohui Huang, Ettore Barbieri, Nicola M Pugno, and Ton Peijs. 2016. 'In situ exfoliation of graphene in epoxy resins: a facile strategy to efficient and large scale graphene nanocomposites', *ACS applied materials & interfaces*, 8: 24112-22.
Li, Yunfeng, Jiahua Zhu, Suying Wei, Jongeun Ryu, Luyi Sun, and Zhanhu Guo. 2011. 'Poly (propylene)/graphene nanoplatelet nanocomposites: melt rheological behavior and thermal, electrical, and electronic properties', *Macromolecular Chemistry and Physics*, 212: 1951-59.
Li, Zheling. 2015. 'Raman Spectroscopic Studies of the Mechanics of Graphene-based Nanocomposites', University of Manchester.
Li, Zheling, Jingwen Chu, Cheng Yang, Sijia Hao, Mark A Bissett, Ian A Kinloch, and Robert J Young. 2018. 'Effect of functional groups on the agglomeration of graphene in nanocomposites', *Composites Science and Technology*, 163: 116-22.
Li, Zheling, Thomas JA Slater, Xinyu Ma, Yingjie Yu, Robert J Young, and Timothy L Burnett. 2019. 'The taxonomy of graphite nanoplatelets and the influence of nanocomposite processing', *Carbon*, 142: 99-106.
Li, Zheling, Robert J Young, and Ian A Kinloch. 2013. 'Interfacial stress transfer in graphene oxide nanocomposites', *ACS applied materials & interfaces*, 5: 456-63.
Li, Zheling, Robert J Young, Ian A Kinloch, Neil R Wilson, Alexander J Marsden, and Arun Prakash Aranga Raju. 2015. 'Quantitative determination of the spatial orientation of graphene by polarized Raman spectroscopy', *Carbon*, 88: 215-24.
Li, Zheling, Robert J Young, Neil R Wilson, Ian A Kinloch, Cristina Vallés, and Zheng Li. 2016a. 'Effect of the orientation of graphene-based nanoplatelets upon the Young's modulus of nanocomposites', *Composites Science and Technology*, 123: 125-33.
Li, Zheling, Robert Young, Neil Wilson, Ian Kinloch, Cristina Vallés, and Zheng Li. 2016b. 'Effect of the orientation of graphene-based nanoplatelets upon the Young's modulus of nanocomposites', *Composites Science and Technology*, 123: 125-33.

Li, Zheng, Rongguo Wang, Robert J Young, Libo Deng, Fan Yang, Lifeng Hao, Weicheng Jiao, and Wenbo Liu. 2013. 'Control of the functionality of graphene oxide for its application in epoxy nanocomposites', *Polymer*, 54: 6437-46.

Li, Zheng, Robert J Young, Rongguo Wang, Fan Yang, Lifeng Hao, Weicheng Jiao, and Wenbo Liu. 2013. 'The role of functional groups on graphene oxide in epoxy nanocomposites', *Polymer*, 54: 5821-29.

Liang, Jiajie, Yi Huang, Long Zhang, Yan Wang, Yanfeng Ma, Tianyin Guo, and Yongsheng Chen. 2009. 'Molecular-level dispersion of graphene into poly (vinyl alcohol) and effective reinforcement of their nanocomposites', *Advanced Functional Materials*, 19: 2297-302.

Lim, Hyunseob, Jaehoon Jung, Rodney S. Ruoff, and Yousoo Kim. 2015. 'Structurally driven one-dimensional electron confinement in sub-5-nm graphene nanowrinkles', *Nature communications*, 6: 8601.

Lin, Feng, Zhuan Zhu, Xufeng Zhou, Wenlan Qiu, Chao Niu, Jonathan Hu, Keshab Dahal, Yanan Wang, Zhenhuan Zhao, and Zhifeng Ren. 2017. 'Orientation control of graphene flakes by magnetic field: broad device applications of macroscopically aligned graphene', *Advanced Materials*, 29: 1604453.

Lin, Liangxu, Xuelin Zheng, Shaowei Zhang, and Dan A Allwood. 2014. 'Surface energy engineering in the solvothermal deoxidation of graphene oxide', *Advanced Materials Interfaces*, 1: 1300078.

Lin, Tianquan, Jian Chen, Hui Bi, Dongyun Wan, Fuqiang Huang, Xiaoming Xie, and Mianheng Jiang. 2013. 'Facile and economical exfoliation of graphite for mass production of high-quality graphene sheets', *Journal of Materials Chemistry A*, 1: 500-04.

Lindon, John C, George E Tranter, and David Koppenaal. 2016. *Encyclopedia of spectroscopy and spectrometry* (Academic Press).

Liu, Fang, Pingbing Ming, and Ju Li. 2007. 'Ab initio calculation of ideal strength and phonon instability of graphene under tension', *Physical Review B*, 76: 064120.

Liu, Gang, Hui Zhang, Dai-jun Zhang, Zhong Zhang, Xue-feng An, and Xiao-su Yi. 2012. 'On depression of glass transition temperature of epoxy nanocomposites', *Journal of Materials Science*, 47: 6891-95.

Liu, Hua, and L Catherine Brinson. 2008. 'Reinforcing efficiency of nanoparticles: A simple comparison for polymer nanocomposites', *Composites Science and Technology*, 68: 1502-12.

Liu, Lei, Donglin Xie, Muhong Wu, Xiaoxia Yang, Zhi Xu, Wenlong Wang, Xuedong Bai, and Enge Wang. 2012. 'Controlled oxidative functionalization of monolayer graphene by water-vapor plasma etching', *Carbon*, 50: 3039-44.

Liu, Mufeng, Dimitrios G Papageorgiou, Suhao Li, Kailing Lin, Ian A Kinloch, and Robert J Young. 2018. 'Micromechanics of reinforcement of a graphene-based thermoplastic elastomer nanocomposite', *Composites Part A: Applied Science and Manufacturing*, 110: 84-92.

Liu, Na, Fang Luo, Haoxi Wu, Yinghui Liu, Chao Zhang, and Ji Chen. 2008. 'One-step ionic-liquid-assisted electrochemical synthesis of ionic-liquid-functionalized graphene sheets directly from graphite', *Advanced Functional Materials*, 18: 1518-25.

Liu, Tianxi, Zishuai Zhao, Weng Weei Tjiu, Jian Lv, and Chun Wei. 2014. 'Preparation and characterization of epoxy nanocomposites containing surface-modified graphene oxide', *Journal of applied polymer science*, 131.

Liu, Yi-Tao, Xu-Ming Xie, and Xiong-Ying Ye. 2011. 'High-concentration organic solutions of poly (styrene-co-butadiene-co-styrene)-modified graphene sheets exfoliated from graphite', *Carbon*, 49: 3529-37.

Liu, Yu, Ann-Lenaig Hamon, Paul Haghi-Ashtiani, Thomas Reiss, Benhui Fan, Delong He, and Jinbo Bai. 2016. 'Quantitative study of interface/interphase in epoxy/graphene-based nanocomposites by combining STEM and EELS', *ACS applied materials & interfaces*, 8: 34151-58.

Liu, Ze, Shou-Mo Zhang, Jia-Rui Yang, Jefferson Zhe Liu, Yan-Lian Yang, and Quan-Shui Zheng. 2012. 'Interlayer shear strength of single crystalline graphite', *Acta Mechanica Sinica*, 28: 978-82.

Lohumi, Santosh, Moon S Kim, Jianwei Qin, and Byoung-Kwan Cho. 2017. 'Raman imaging from microscopy to macroscopy: Quality and safety control of biological materials', *TrAC Trends in Analytical Chemistry*, 93: 183-98.

Loos, Marcio. 2014. *Carbon nanotube reinforced composites: CNT Polymer Science and Technology* (Elsevier).

Lu, Ganhua, Shun Mao, Sungjin Park, Rodney S Ruoff, and Junhong Chen. 2009. 'Facile, noncovalent decoration of graphene oxide sheets with nanocrystals', *Nano Research*, 2: 192-200.

Lu, Xinglin, Xunda Feng, Jay R Werber, Chiheng Chu, Ines Zucker, Jae-Hong Kim, Chinedum O Osuji, and Menachem Elimelech. 2017. 'Enhanced antibacterial activity through the controlled alignment of graphene oxide nanosheets', *Proceedings of the National Academy of Sciences*, 114: E9793-E801.

Ma, Peng-Cheng, and Jang-Kyo Kim. 2011. *Carbon nanotubes for polymer reinforcement* (CRC Press).

Ma, Peng-Cheng, Naveed A Siddiqui, Gad Marom, and Jang-Kyo Kim. 2010. 'Dispersion and functionalization of carbon nanotubes for polymer-based nanocomposites: a review', *Composites Part A: Applied Science and Manufacturing*, 41: 1345-67.

Ma, Wei-Ting, S Rajesh Kumar, Chun-Ting Hsu, Chao-Ming Shih, Shiao-Wen Tsai, Chun-Chen Yang, Ying-Ling Liu, and Shingjiang Jessie Lue. 2018. 'Magnetic field-assisted alignment of graphene oxide nanosheets in a polymer matrix to enhance ionic conduction', *Journal of Membrane Science*, 563: 259-69.

Majidi, Sima, Fatemeh Zeinali Sehrig, Samad Mussa Farkhani, Mehdi Soleymani Goloujeh, and Abolfazl Akbarzadeh. 2016. 'Current methods for synthesis of magnetic nanoparticles', *Artificial cells, nanomedicine, and biotechnology*, 44: 722-34.

Malard, LM, MAA Pimenta, G Dresselhaus, and MS Dresselhaus. 2009. 'Raman spectroscopy in graphene', *Physics reports*, 473: 51-87.

Malkina, Olga, Hassan Mahfuz, K Sorge, A Rondinone, Jihua Chen, Karren More, S Reeves, and V Rangari. 2013. 'Magnetic alignment of SWCNTs decorated with Fe3O4 to enhance mechanical properties of SC-15 epoxy', *AIP Advances*, 3: 042104.

Manikas, AC, MG Pastore Carbone, CR Woods, Y Wang, I Souli, G Anagnostopoulos, M Hadjinicolaou, KS Novoselov, and C Galiotis. 2019. 'Stress transfer at the nanoscale on graphene ribbons of regular geometry', *Nanoscale*, 11: 14354-61.

Martin, CA, JKW Sandler, AH Windle, M-K Schwarz, W Bauhofer, K Schulte, and MSP Shaffer. 2005. 'Electric field-induced aligned multi-wall carbon nanotube networks in epoxy composites', *Polymer*, 46: 877-86.

McAllister, Michael J, Je-Luen Li, Douglas H Adamson, Hannes C Schniepp, Ahmed A Abdala, Jun Liu, Margarita Herrera-Alonso, David L Milius, Roberto Car, and Robert K Prud'homme. 2007. 'Single sheet functionalized graphene by oxidation and thermal expansion of graphite', *Chemistry of materials*, 19: 4396-404.

McIntyre, N. S., and D. G. Zetaruk. 1977. 'X-ray photoelectron spectroscopic studies of iron oxides', *Analytical Chemistry*, 49: 1521-29.

Menard, Kevin P. 2008. "DYNAMIC MECHANICAL ANALYSIS." In.: CRS Press.

Menard, Kevin P, and Noah R Menard. 2002. 'Dynamic mechanical analysis in the analysis of polymers and rubbers', *Encyclopedia of polymer science and technology*: 1-33.

Mermin, N David. 1968. 'Crystalline order in two dimensions', *Physical Review*, 176: 250.

Mills, SL, GC Lees, CM Liauw, and S Lynch. 2002. 'Dispersion assessment of flame retardant filler/polymer systems using a combination of X-ray mapping and multifractal analysis', *Polymer Testing*, 21: 941-47.

Mohan, Velram Balaji, Kin-tak Lau, David Hui, and Debes Bhattacharyya. 2018. 'Graphene-based materials and their composites: A review on production, applications and product limitations', *Composites Part B: Engineering*, 142: 200-20.

Monshi, Ahmad, Mohammad Reza Foroughi, and Mohammad Reza Monshi. 2012. 'Modified Scherrer equation to estimate more accurately nano-crystallite size using XRD', *World journal of nano science and engineering*, 2: 154-60.

Monteserín, Cristina, M Blanco, E Aranzabe, A Aranzabe, and JL Vilas. 2017. 'Effects of graphene oxide and chemically reduced graphene oxide on the curing kinetics of epoxy amine composites', *Journal of applied polymer science*, 134.

Moon, In Kyu, Junghyun Lee, Rodney S Ruoff, and Hyoyoung Lee. 2010. 'Reduced graphene oxide by chemical graphitization', *Nature communications*, 1: 1-6.

Morgan, David J. 2017. 'Cluster cleaned HOPG by XPS', *Surface Science Spectra*, 24: 024003.

Mullins, M. J., D. Liu, and H. J. Sue. 2018. 'Chapter 2 - Mechanical properties of thermosets.' in Qipeng Guo (ed.), *Thermosets (Second Edition)* (Elsevier).

Muzyka, Roksana, Sabina Drewniak, Tadeusz Pustelny, Maciej Chrubasik, and Grażyna Gryglewicz. 2018. 'Characterization of graphite oxide and reduced graphene oxide obtained from different graphite precursors and oxidized by different methods using Raman spectroscopy', *Materials*, 11: 1050.

Naebe, Minoo, Jing Wang, Abbas Amini, Hamid Khayyam, Nishar Hameed, Lu Hua Li, Ying Chen, and Bronwyn Fox. 2014. 'Mechanical property and structure of covalent functionalised graphene/epoxy nanocomposites', *Scientific reports*, 4: 4375.

Naghdi, Samira, Kyong Yop Rhee, Babak Jaleh, and Soo Jin Park. 2016. 'Altering the structure and properties of iron oxide nanoparticles and graphene oxide/iron oxide composites by urea', *Applied Surface Science*, 364: 686-93.

Nairn, John A. 1997. 'On the use of shear-lag methods for analysis of stress transfer in unidirectional composites', *Mechanics of Materials*, 26: 63-80.

Neto, AH Castro, Francisco Guinea, Nuno MR Peres, Kostya S Novoselov, and Andre K Geim. 2009. 'The electronic properties of graphene', *Reviews of modern physics*, 81: 109.

Nicholl, Ryan JT, Hiram J Conley, Nickolay V Lavrik, Ivan Vlassiouk, Yevgeniy S Puzyrev, Vijayashree Parsi Sreenivas, Sokrates T Pantelides, and Kirill I Bolotin. 2015. 'The effect of intrinsic crumpling on the mechanics of free-standing graphene', *Nature communications*, 6: 8789.

Nicolosi, Valeria, Manish Chhowalla, Mercouri G Kanatzidis, Michael S Strano, and Jonathan N Coleman. 2013. 'Liquid exfoliation of layered materials', *Science*, 340: 1226419.

Nobile, Maria Rossella, Marialuigia Raimondo, Khalid Lafdi, and Liberata Guadagno. 2016. "Rheological and morphological properties of graphene-epoxy nanocomposites." In *AIP Conference Proceedings*, 020143. AIP Publishing LLC.

Novoselov, Kostya S, Andre K Geim, Sergei V Morozov, D Jiang, Y_ Zhang, Sergey V Dubonos, Irina V Grigorieva, and Alexandr A Firsov. 2004. 'Electric field effect in atomically thin carbon films', *Science*, 306: 666-69.

O'Driscoll, K., and R. Amin Sanayei. 1991. 'Chain-length dependence of the glass transition temperature', *Macromolecules*, 24: 4479-80.

Olowojoba, Ganiu B, Sotirios Kopsidas, Salvador Eslava, Eduardo S Gutierrez, Anthony J Kinloch, Cecilia Mattevi, Victoria G Rocha, and Ambrose C Taylor. 2017. 'A facile way to produce epoxy nanocomposites having excellent thermal conductivity with low contents of reduced graphene oxide', *Journal of Materials Science*, 52: 7323-44.

Otari, Sachin V, Manoj Kumar, Muhammad Zahid Anwar, Nanasaheb D Thorat, Sanjay KS Patel, Dongjin Lee, Jai Hyo Lee, Jung-Kul Lee, Yun Chan Kang, and Liaoyuan Zhang. 2017. 'Rapid synthesis and decoration of reduced graphene oxide with gold nanoparticles by thermostable peptides for memory device and photothermal applications', *Scientific reports*, 7: 1-14.

Panta, PC, and CP Bergmann. 'RAMAN SPECTROSCOPY OF IRON OXIDE OF NANOPARTICLES (Fe3O4)'.

Pantea, Dana, Hans Darmstadt, Serge Kaliaguine, Lydia Sümmchen, and Christian Roy. 2001. 'Electrical conductivity of thermal carbon blacks: Influence of surface chemistry', *Carbon*, 39: 1147-58.

Panwar, Vinay, and Kaushik Pal. 2017. 'Dynamic Mechanical Analysis of Clay–Polymer Nanocomposites.' in, *Clay-Polymer Nanocomposites* (Elsevier).

Papageorgiou, Dimitrios G, Ian A Kinloch, and Robert J Young. 2017. 'Mechanical properties of graphene and graphene-based nanocomposites', *Progress in Materials Science*, 90: 75-127.

Park, Sungjin, and Rodney S Ruoff. 2009. 'Chemical methods for the production of graphenes', *Nature nanotechnology*, 4: 217.

Parvez, Khaled, Zhong-Shuai Wu, Rongjin Li, Xianjie Liu, Robert Graf, Xinliang Feng, and Klaus Mullen. 2014. 'Exfoliation of graphite into graphene in aqueous solutions of inorganic salts', *Journal of the American Chemical Society*, 136: 6083-91.

Pascault, Jean-Pierre, Henry Sautereau, Jacques Verdu, and Roberto JJ Williams. 2002. *Thermosetting polymers* (CRC press).

Paton, Keith R, Eswaraiah Varrla, Claudia Backes, Ronan J Smith, Umar Khan, Arlene O'Neill, Conor Boland, Mustafa Lotya, Oana M Istrate, and Paul King. 2014. 'Scalable production of large quantities of defect-free few-layer graphene by shear exfoliation in liquids', *Nature materials*, 13: 624.

Peik-See, Teo, Alagarsamy Pandikumar, Lim Hong Ngee, Huang Nay Ming, and Chia Chin Hua. 2014. 'Magnetically separable reduced graphene oxide/iron oxide nanocomposite materials for environmental remediation', *Catalysis Science & Technology*, 4: 4396-405.

Peres, NMR. 2009. 'The transport properties of graphene', *Journal of Physics: Condensed Matter*, 21: 323201.

Plomp, Arjan J, Dang Sheng Su, KP de Jong, and Johannes Hendrik Bitter. 2009. 'On the Nature of Oxygen-Containing Surface Groups on Carbon Nanofibers and Their Role for Platinum Deposition An XPS and Titration Study', *The Journal of Physical Chemistry C*, 113: 9865-69.

Poosala, Akkachai, Kittipong Hrimchum, Darunee Aussawasathien, and Duanghathai Pentrakoon. 2015. 'The effect of oxygen-plasma treated graphene nanoplatelets upon the properties of multiwalled carbon nanotube and polycarbonate hybrid nanocomposites used for electrostatic dissipative applications', *Journal of Nanomaterials*, 2015.

Poot, Menno, and Herre SJ van der Zant. 2008. 'Nanomechanical properties of few-layer graphene membranes', *Applied Physics Letters*, 92: 063111.

Posudievsky, Oleg Yu, Oleksandra A Khazieieva, Vsevolod V Cherepanov, Vyacheslav G Koshechko, and Vitaly D Pokhodenko. 2013. 'High yield of graphene by dispersant-free liquid exfoliation of mechanochemically delaminated graphite', *Journal of nanoparticle research*, 15: 2046.

Potts, Jeffrey R, Daniel R Dreyer, Christopher W Bielawski, and Rodney S Ruoff. 2011. 'Graphene-based polymer nanocomposites', *Polymer*, 52: 5-25.

Proctor, John E, Eugene Gregoryanz, Konstantin S Novoselov, Mustafa Lotya, Jonathan N Coleman, and Matthew P Halsall. 2009. 'High-pressure Raman spectroscopy of graphene', *Physical Review B*, 80: 073408.

Prolongo, SG, A Jimenez-Suarez, R Moriche, and A Ureña. 2013. 'In situ processing of epoxy composites reinforced with graphene nanoplatelets', *Composites Science and Technology*, 86: 185-91.

Prolongo, SG, R Moriche, A Jiménez-Suárez, M Sánchez, and A Ureña. 2014. 'Advantages and disadvantages of the addition of graphene nanoplatelets to epoxy resins', *European Polymer Journal*, 61: 206-14.

Pullicino, Edward, Wentao Zou, Matthieu Gresil, and Costas Soutis. 2017. 'The effect of shear mixing speed and time on the mechanical properties of GNP/epoxy composites', *Applied Composite Materials*, 24: 301-11.

Putz, Karl W, Marc J Palmeri, Rachel B Cohn, Rodney Andrews, and L Catherine Brinson. 2008. 'Effect of cross-link density on interphase creation in polymer nanocomposites', *Macromolecules*, 41: 6752-56.

Qian, Hui, Emile S Greenhalgh, Milo SP Shaffer, and Alexander Bismarck. 2010. 'Carbon nanotube-based hierarchical composites: a review', *Journal of Materials Chemistry*, 20: 4751-62.

Qiu, SL, CS Wang, YT Wang, CG Liu, XY Chen, HF Xie, YA Huang, and RS Cheng. 2011. 'Effects of graphene oxides on the cure behaviors of a tetrafunctional epoxy resin', *Express Polymer Letters*, 5.

Radu, T, C Iacovita, D Benea, and R Turcu. 2017. 'X-ray photoelectron spectroscopic characterization of iron oxide nanoparticles', *Applied Surface Science*, 405: 337-43.

Rahatekar, SS, KKK Koziol, SA Butler, JA Elliott, MSP Shaffer, MR Mackley, and AH Windle. 2006. 'Optical microstructure and viscosity enhancement for an epoxy resin matrix containing multiwall carbon nanotubes', *Journal of Rheology*, 50: 599-610.

Rajagopalan, Balasubramaniyan, and Jin Suk Chung. 2014. 'Reduced chemically modified graphene oxide for supercapacitor electrode', *Nanoscale research letters*, 9: 1-10.

Renteria, J, S Legedza, R Salgado, MP Balandin, S Ramirez, M Saadah, F Kargar, and AA Balandin. 2015. 'Magnetically-functionalized self-aligning graphene fillers for high-efficiency thermal management applications', *Materials & Design*, 88: 214-21.

Rosca, Iosif D, and Suong V Hoa. 2009. 'Highly conductive multiwall carbon nanotube and epoxy composites produced by three-roll milling', *Carbon*, 47: 1958-68.

Ross, P-S, and Alexandre Bourke. 2017. 'High-resolution gamma ray attenuation density measurements on mining exploration drill cores, including cut cores', *Journal of Applied Geophysics*, 136: 262-68.

Rueda, Martha Margarita, Marie-Camille Auscher, René Fulchiron, Thomas Perie, Grégory Martin, Philippe Sonntag, and Philippe Cassagnau. 2017. 'Rheology and applications of highly filled polymers: A review of current understanding', *Progress in Polymer Science*, 66: 22-53.

Sakorikar, Tushar, Maheswari Kavirajan Kavitha, Pramitha Vayalamkuzhi, and Manu Jaiswal. 2017. 'Thickness-dependent Crack Propagation in Uniaxially Strained Conducting Graphene Oxide Films on Flexible Substrates', *Scientific reports*, 7: 1-10.

Saleem, Haleema, Anjali Edathil, Thamsanqa Ncube, Jeewan Pokhrel, Sara Khoori, Akhil Abraham, and Vikas Mittal. 2016. 'Mechanical and thermal properties of thermoset–graphene nanocomposites', *Macromolecular Materials and Engineering*, 301: 231-59.

Sanchez, Vanesa C, Ashish Jachak, Robert H Hurt, and Agnes B Kane. 2012. 'Biological interactions of graphene-family nanomaterials: an interdisciplinary review', *Chemical research in toxicology*, 25: 15-34.

Santoyo Salazar, Jaime, Lucas Perez, Oscar De Abril, Lai Truong Phuoc, Dris Ihiawakrim, Manuel Vazquez, Jean-Marc Greneche, Sylvie Begin-Colin, and Genevieve Pourroy. 2011. 'Magnetic iron oxide nanoparticles in 10− 40 nm range: composition in terms of magnetite/maghemite ratio and effect on the magnetic properties', *Chemistry of materials*, 23: 1379-86.

Scherrer, Paul. 1912. 'Bestimmung der inneren Struktur und der Größe von Kolloidteilchen mittels Röntgenstrahlen.' in, *Kolloidchemie Ein Lehrbuch* (Springer).

Schwamb, Timo, Brian R Burg, Niklas C Schirmer, and Dimos Poulikakos. 2009. 'An electrical method for the measurement of the thermal and electrical conductivity of reduced graphene oxide nanostructures', *Nanotechnology*, 20: 405704.

Senthilnathan, Jaganathan, Kodepelly Sanjeeva Rao, and Masahiro Yoshimura. 2014. 'Submerged liquid plasma–low energy synthesis of nitrogen-doped graphene for electrochemical applications', *Journal of materials Chemistry A*, 2: 3332-37.

Shokrieh, MM, M Esmkhani, Z Shokrieh, and Z Zhao. 2014. 'Stiffness prediction of graphene nanoplatelet/epoxy nanocomposites by a combined molecular dynamics–micromechanics method', *Computational materials science*, 92: 444-50.

Shokrollahi, HJJOM. 2017. 'A review of the magnetic properties, synthesis methods and applications of maghemite', *Journal of Magnetism and Magnetic Materials*, 426: 74-81.

Silverson. 'Laboratory mixers;How it works'.

Singh, Virendra, Daeha Joung, Lei Zhai, Soumen Das, Saiful I Khondaker, and Sudipta Seal. 2011. 'Graphene based materials: past, present and future', *Progress in Materials Science*, 56: 1178-271.

Song, Sung Ho, Kwang Hyun Park, Bo Hyun Kim, Yong Won Choi, Gwang Hoon Jun, Dong Ju Lee, Byung-Seon Kong, Kyung-Wook Paik, and Seokwoo Jeon. 2013. 'Enhanced thermal conductivity of epoxy–graphene composites by using non-oxidized graphene flakes with non-covalent functionalization', *Advanced Materials*, 25: 732-37.

Soule, DE, and CW Nezbeda. 1968. 'Direct basal-plane shear in single-crystal graphite', *Journal of applied physics*, 39: 5122-39.

Stadler, Johannes, Thomas Schmid, and Renato Zenobi. 2011. 'Nanoscale chemical imaging of single-layer graphene', *ACS nano*, 5: 8442-48.

Stankovich, Sasha, Dmitriy A Dikin, Richard D Piner, Kevin A Kohlhaas, Alfred Kleinhammes, Yuanyuan Jia, Yue Wu, SonBinh T Nguyen, and Rodney S Ruoff. 2007. 'Synthesis of graphene-based nanosheets via chemical reduction of exfoliated graphite oxide', *Carbon*, 45: 1558-65.

Su, Jing, Minhua Cao, Ling Ren, and Changwen Hu. 2011. 'Fe3O4–graphene nanocomposites with improved lithium storage and magnetism properties', *The Journal of Physical Chemistry C*, 115: 14469-77.

Subrahmanyam, KS, Arun K Manna, Swapan K Pati, and CNR Rao. 2010. 'A study of graphene decorated with metal nanoparticles', *Chemical Physics Letters*, 497: 70-75.

Suk, Ji Won, Richard D Piner, Jinho An, and Rodney S Ruoff. 2010. 'Mechanical properties of monolayer graphene oxide', *ACS nano*, 4: 6557-64.

Sun, Renhui, Hao-Bin Zhang, Jian Yao, Dongzhi Yang, Yiu-Wing Mai, and Zhong-Zhen Yu. 2016. 'In situ reduction of iron oxide with graphene for convenient synthesis of various graphene hybrids', *Carbon*, 107: 138-45.

Surnova, Albina, Dinar Balkaev, Delus Musin, Rustem Amirov, and Ayrat M Dimiev. 2019. 'Fully exfoliated graphene oxide accelerates epoxy resin curing, and results in dramatic improvement of the polymer mechanical properties', *Composites Part B: Engineering*, 162: 685-91.

Tadmor, Zehev, and Costas G Gogos. 2013. *Principles of polymer processing* (John Wiley & Sons).

Tadyszak, Krzysztof, Jacek K Wychowaniec, and Jagoda Litowczenko. 2018. 'Biomedical applications of graphene-based structures', *Nanomaterials*, 8: 944.

Tandon, Gp P, and Gj J Weng. 1984. 'The effect of aspect ratio of inclusions on the elastic properties of unidirectionally aligned composites', *Polymer Composites*, 5: 327-33.

Tang, Long-Cheng, Yan-Jun Wan, Dong Yan, Yong-Bing Pei, Li Zhao, Yi-Bao Li, Lian-Bin Wu, Jian-Xiong Jiang, and Guo-Qiao Lai. 2013. 'The effect of graphene dispersion on the mechanical properties of graphene/epoxy composites', *Carbon*, 60: 16-27.

Tao, Lei, Zeyu Sun, Wei Min, Hanwen Ou, Liangliang Qi, and Muhuo Yu. 2020. 'Improving the toughness of thermosetting epoxy resins via blending triblock copolymers', *RSC advances*, 10: 1603-12.

Teng, Chih-Chun, Chen-Chi M Ma, Chu-Hua Lu, Shin-Yi Yang, Shie-Heng Lee, Min-Chien Hsiao, Ming-Yu Yen, Kuo-Chan Chiou, and Tzong-Ming Lee. 2011. 'Thermal conductivity and structure of non-covalent functionalized graphene/epoxy composites', *Carbon*, 49: 5107-16.

Throckmorton, James, and Giuseppe Palmese. 2015. 'Direct preparation of few layer graphene epoxy nanocomposites from untreated flake graphite', *ACS applied materials & interfaces*, 7: 14870-77.

Toh, Shaw Yong, Kee Shyuan Loh, Siti Kartom Kamarudin, and Wan Ramli Wan Daud. 2014. 'Graphene production via electrochemical reduction of graphene oxide: synthesis and characterisation', *Chemical engineering journal*, 251: 422-34.

Tong, Mingqiong, Jianda Cao, Xiaoping Chen, Huanxia Zhang, Wen Wu, and Hui Ma. 2019. 'Self-assembly of chemically modified graphene sheets in an external magnetic field', *RSC advances*, 9: 19457-64.

Trottier, Amy M, JW Zwanziger, and N Sanjeeva Murthy. 2008. 'Amorphous orientation and its relationship to processing stages of blended polypropylene/polyethylene fibers', *Journal of applied polymer science*, 108: 4047-57.

Tsoukleri, Georgia, John Parthenios, Konstantinos Papagelis, Rashid Jalil, Andrea C Ferrari, Andre K Geim, Kostya S Novoselov, and Costas Galiotis. 2009. 'Subjecting a graphene monolayer to tension and compression', *small*, 5: 2397-402.

Tung, Tran Thanh, Nguyen Viet Chien, Nguyen Van Duy, Nguyen Van Hieu, Md Julker Nine, Campbell J Coghlan, Diana NH Tran, and Dusan Losic. 2019. 'Magnetic iron oxide nanoparticles decorated graphene for chemoresistive gas sensing: The particle size effects', *Journal of colloid and interface science*, 539: 315-25.

Tuteja, Anish, Phillip M. Duxbury, and Michael E. Mackay. 2007. 'Multifunctional Nanocomposites with Reduced Viscosity', *Macromolecules*, 40: 9427-34.

Ubbelohde, A. R., F. A. Lewis, and Stuart A. Rice. 1961. 'Graphite and Its Crystal Compounds', *Physics Today*, 14: 66-68.

Vallés, Cristina. 2017. 'Rheology of graphene oxide dispersions', *Graphene Oxide: Fundamentals and Applications*: 121-46.

Vallés, Cristina, Fabian Beckert, Laura Burk, Rolf Mülhaupt, Robert J Young, and Ian A Kinloch. 2016. 'Effect of the C/O ratio in graphene oxide materials on the reinforcement of epoxy-based nanocomposites', *Journal of Polymer Science Part B: Polymer Physics*, 54: 281-91.

Vallés, Cristina, Robert J Young, Deborah J Lomax, and Ian A Kinloch. 2014. 'The rheological behaviour of concentrated dispersions of graphene oxide', *Journal of Materials Science*, 49: 6311-20.

Vaskova, Hana, and Vojtěch Křesálek. 2011. *Raman spectroscopy of epoxy resin crosslinking*.

Viculis, Lisa M, Julia J Mack, Oren M Mayer, H Thomas Hahn, and Richard B Kaner. 2005. 'Intercalation and exfoliation routes to graphite nanoplatelets', *Journal of Materials Chemistry*, 15: 974-78.

Voiry, Damien, Jieun Yang, Jacob Kupferberg, Raymond Fullon, Calvin Lee, Hu Young Jeong, Hyeon Suk Shin, and Manish Chhowalla. 2016. 'High-quality graphene via microwave reduction of solution-exfoliated graphene oxide', *Science*, 353: 1413-16.

Vryonis, Orestis, STH Virtanen, Thomas Andritsch, AS Vaughan, and PL Lewin. 2019. 'Understanding the cross-linking reactions in highly oxidized graphene/epoxy nanocomposite systems', *Journal of Materials Science*, 54: 3035-51.

Wahajuddin, Sumit Arora. 2012. 'Superparamagnetic iron oxide nanoparticles: magnetic nanoplatforms as drug carriers', *International journal of nanomedicine*, 7: 3445.

Walenta, E. 1985. 'Small angle x-ray scattering. Von O. GLATTER und O. KRATKY. London: Academic Press Inc. Ltd. 1982. ISBN 0-12-286280-5. X, 515 Seiten, geb.£ 43, 60; US $81.00', *Acta Polymerica*, 36: 296-96.

Wan, Jintao, Cheng Li, Zhi-Yang Bu, Cun-Jin Xu, Bo-Geng Li, and Hong Fan. 2012. 'A comparative study of epoxy resin cured with a linear diamine and a branched polyamine', *Chemical engineering journal*, 188: 160-72.

Wan, Yan-Jun, Li-Xiu Gong, Long-Cheng Tang, Lian-Bin Wu, and Jian-Xiong Jiang. 2014. 'Mechanical properties of epoxy composites filled with silane-functionalized graphene oxide', *Composites Part A: Applied Science and Manufacturing*, 64: 79-89.

Wang, Benjamin N, Ryan D Bennett, Eric Verploegen, Anastasios J Hart, and Robert E Cohen. 2007. 'Quantitative characterization of the morphology of multiwall carbon nanotube films by small-angle X-ray scattering', *The Journal of Physical Chemistry C*, 111: 5859-65.

Wang, Fei, Haoyu Wang, and Jian Mao. 2019. 'Aligned-graphene composites: a review', *Journal of Materials Science*, 54: 36-61.

Wang, Fuzhong, Lawrence T Drzal, Yan Qin, and Zhixiong Huang. 2015. 'Mechanical properties and thermal conductivity of graphene nanoplatelet/epoxy composites', *Journal of Materials Science*, 50: 1082-93.

———. 2016. 'Processing and characterization of high content multilayer graphene/epoxy composites with high electrical conductivity', *Polymer Composites*, 37: 2897-906.

Wang, Gongming, Fang Qian, Chad W Saltikov, Yongqin Jiao, and Yat Li. 2011. 'Microbial reduction of graphene oxide by Shewanella', *Nano Research*, 4: 563-70.

Wang, Xianbao, Haijun You, Fangming Liu, Mingjian Li, Li Wan, Shaoqing Li, Qin Li, Yang Xu, Rong Tian, and Ziyong Yu. 2009. 'Large-scale synthesis of few-layered graphene using CVD', *Chemical Vapor Deposition*, 15: 53-56.

Wang, Zepu, J Keith Nelson, Henrik Hillborg, Su Zhao, and Linda S Schadler. 2012. 'Graphene oxide filled nanocomposite with novel electrical and dielectric properties', *Advanced Materials*, 24: 3134-37.

Wei, Guidan, Ji Yu, Min Gu, and Tong Tang. 2016. 'Dielectric relaxation and hopping conduction in reduced graphite oxide', *Journal of applied physics*, 119: 224102.

Wei, Jiacheng, Rasheed Atif, Thuc Vo, and Fawad Inam. 2015. 'Graphene nanoplatelets in epoxy system: dispersion, reaggregation, and mechanical properties of nanocomposites', *Journal of Nanomaterials*, 2015.

Wei, Yi, Xiaoyu Hu, Qiuran Jiang, Zeyu Sun, Pengfei Wang, Yiping Qiu, and Wanshuang Liu. 2018. 'Influence of graphene oxide with different oxidation levels on the properties of epoxy composites', *Composites Science and Technology*, 161: 74-84.

Wick, Peter, Anna E Louw-Gaume, Melanie Kucki, Harald F Krug, Kostas Kostarelos, Bengt Fadeel, Kenneth A Dawson, Anna Salvati, Ester Vázquez, and Laura Ballerini. 2014. 'Classification framework for graphene-based materials', *Angewandte Chemie International Edition*, 53: 7714-18.

Williams, M, K Seunarine, R Gibbs, and C Spacie. 2013. 'Plasma modification of graphene and graphene like materials for component performance enhancement', *nanonewsletter*: 23.

Worsley, Kimberly A, Palanisamy Ramesh, Swadhin K Mandal, Sandip Niyogi, Mikhail E Itkis, and Robert C Haddon. 2007. 'Soluble graphene derived from graphite fluoride', *Chemical Physics Letters*, 445: 51-56.

Wu, Chun Lei, Ming Qiu Zhang, Min Zhi Rong, and Klaus Friedrich. 2002. 'Tensile performance improvement of low nanoparticles filled-polypropylene composites', *Composites Science and Technology*, 62: 1327-40.

Wu, Jiang-Bin, Miao-Ling Lin, Xin Cong, He-Nan Liu, and Ping-Heng Tan. 2018. 'Raman spectroscopy of graphene-based materials and its applications in related devices', *Chemical Society Reviews*, 47: 1822-73.

Wu, Linlin, Masataka Ohtani, Masaki Takata, Akinori Saeki, Shu Seki, Yasuhiro Ishida, and Takuzo Aida. 2014. 'Magnetically induced anisotropic orientation of graphene oxide locked by in situ hydrogelation', *ACS nano*, 8: 4640-49.

Wu, Shuying, Raj B Ladani, Jin Zhang, Ehsan Bafekrpour, Kamran Ghorbani, Adrian P Mouritz, Anthony J Kinloch, and Chun H Wang. 2015. 'Aligning multilayer graphene flakes with an external electric field to improve multifunctional properties of epoxy nanocomposites', *Carbon*, 94: 607-18.

Wu, Shuying, Raj B Ladani, Jin Zhang, Anthony J Kinloch, Zhiheng Zhao, Jun Ma, Xuehua Zhang, Adrian P Mouritz, Kamran Ghorbani, and Chun H Wang. 2015. 'Epoxy nanocomposites containing magnetite-carbon nanofibers aligned using a weak magnetic field', *Polymer*, 68: 25-34.

Wu, Shuying, Jin Zhang, Raj B Ladani, Kamran Ghorbani, Adrian P Mouritz, Anthony J Kinloch, and Chun H Wang. 2016. 'A novel route for tethering graphene with iron oxide and its magnetic field alignment in polymer nanocomposites', *Polymer*, 97: 273-84.

Wu, Wei, Zhaohui Wu, Taekyung Yu, Changzhong Jiang, and Woo-Sik Kim. 2015. 'Recent progress on magnetic iron oxide nanoparticles: synthesis, surface functional strategies and biomedical applications', *Science and technology of advanced materials*, 16: 023501.

Wu, Yingpeng, Bin Wang, Yanfeng Ma, Yi Huang, Na Li, Fan Zhang, and Yongsheng Chen. 2010. 'Efficient and large-scale synthesis of few-layered graphene using an arc-discharge method and conductivity studies of the resulting films', *Nano Research*, 3: 661-69.

Xia, Tian, Jingping Wang, Chunli Wu, Fuchang Meng, Zhan Shi, Jie Lian, Jing Feng, and Jian Meng. 2012. 'Novel complex-coprecipitation route to form high quality triethanolamine-coated Fe 3 O 4 nanocrystals: their high saturation magnetizations and excellent water treatment properties', *CrystEngComm*, 14: 5741-44.

Xia, Tian, Desen Zeng, Zheling Li, Robert J Young, Cristina Vallés, and Ian A Kinloch. 2018. 'Electrically conductive GNP/epoxy composites for out-of-autoclave thermoset curing through Joule heating', *Composites Science and Technology*, 164: 304-12.

Xu, Xingtao, Likun Pan, Yong Liu, Ting Lu, Zhuo Sun, and Daniel HC Chua. 2015. 'Facile synthesis of novel graphene sponge for high performance capacitive deionization', *Scientific reports*, 5: 8458.

Xu, Zhen, Yuan Zhang, Peigang Li, and Chao Gao. 2012. 'Strong, conductive, lightweight, neat graphene aerogel fibers with aligned pores', *ACS nano*, 6: 7103-13.

Yang, Xiaoshuang, Lixiang Yuan, Vanessa K Peterson, Andrew I Minett, Ming Zhao, Nigel Kirby, Stephen Mudie, and Andrew T Harris. 2013. 'Pretreatment control of carbon nanotube array growth for gas separation: alignment and growth studied using microscopy and small-angle X-ray scattering', *ACS applied materials & interfaces*, 5: 3063-70.

Yang, Xiaoying, Xiaoyan Zhang, Yanfeng Ma, Yi Huang, Yinsong Wang, and Yongsheng Chen. 2009. 'Superparamagnetic graphene oxide–Fe 3 O 4 nanoparticles hybrid for controlled targeted drug carriers', *Journal of Materials Chemistry*, 19: 2710-14.

Yang, Yi, Jing Cao, Ning Wei, Donghui Meng, Lina Wang, Guohua Ren, Rongxin Yan, and Ning Zhang. 2019. 'Thermal conductivity of defective graphene oxide: a molecular dynamic study', *Molecules*, 24: 1103.

Yang, Yingchao, William Rigdon, Xinyu Huang, and Xiaodong Li. 2013. 'Enhancing graphene reinforcing potential in composites by hydrogen passivation induced dispersion', *Scientific reports*, 3: 2086.

Yasmin, Asma, and Isaac M Daniel. 2004. 'Mechanical and thermal properties of graphite platelet/epoxy composites', *Polymer*, 45: 8211-19.

Yasmin, Asma, Jyi-Jiin Luo, and Isaac M Daniel. 2006. 'Processing of expanded graphite reinforced polymer nanocomposites', *Composites Science and Technology*, 66: 1182-89.

Yi, Min, and Zhigang Shen. 2015. 'A review on mechanical exfoliation for the scalable production of graphene', *Journal of Materials Chemistry A*, 3: 11700-15.

Yi, Min, Zhigang Shen, Shuaishuai Liang, Lei Liu, Xiaojing Zhang, and Shulin Ma. 2013. 'Water can stably disperse liquid-exfoliated graphene', *Chemical Communications*, 49: 11059-61.

Yi, Min, Zhigang Shen, Shulin Ma, and Xiaojing Zhang. 2012. 'A mixed-solvent strategy for facile and green preparation of graphene by liquid-phase exfoliation of graphite', *Journal of Nanoparticle Research*, 14: 1003.

Yoonessi, Mitra, James R Gaier, John A Peck, and Michael A Meador. 2015. 'Controlled direction of electrical and mechanical properties in nickel tethered graphene polyimide nanocomposites using magnetic field', *Carbon*, 84: 375-82.

Youn, Sang Cheon, Dae Woo Kim, Seung Bo Yang, Hye Mi Cho, Jae Hyun Lee, and Hee-Tae Jung. 2011. 'Vertical alignment of reduced graphene oxide/Fe-oxide hybrids using the magneto-evaporation method', *Chemical Communications*, 47: 5211-13.

Young, Robert J, Ian A Kinloch, Lei Gong, and Kostya S Novoselov. 2012. 'The mechanics of graphene nanocomposites: a review', *Composites Science and Technology*, 72: 1459-76.

Young, Robert J, and Peter A Lovell. 2011. *Introduction to polymers* (CRC press).

Young, Robert J., Mufeng Liu, Ian A. Kinloch, Suhao Li, Xin Zhao, Cristina Vallés, and Dimitrios G. Papageorgiou. 2018. 'The mechanics of reinforcement of polymers by graphene nanoplatelets', *Composites Science and Technology*, 154: 110-16.

Yourdkhani, Mostafa, and Pascal Hubert. 2013. 'Quantitative dispersion analysis of inclusions in polymer composites', *ACS applied materials & interfaces*, 5: 35-41.

Yousefi, Nariman, Mohsen Moazzami Gudarzi, Qingbin Zheng, Xiuyi Lin, Xi Shen, Jingjing Jia, Farhad Sharif, and Jang-Kyo Kim. 2013. 'Highly aligned, ultralarge-size reduced graphene oxide/polyurethane nanocomposites: mechanical properties and moisture permeability', *Composites Part A: Applied Science and Manufacturing*, 49: 42-50.

Yousefi, Nariman, Xiuyi Lin, Qingbin Zheng, Xi Shen, Jayaram R Pothnis, Jingjing Jia, Eyal Zussman, and Jang-Kyo Kim. 2013. 'Simultaneous in situ reduction, self-alignment and covalent bonding in graphene oxide/epoxy composites', *Carbon*, 59: 406-17.

Yu, Ting, Zhenhua Ni, Chaoling Du, Yumeng You, Yingying Wang, and Zexiang Shen. 2008. 'Raman mapping investigation of graphene on transparent flexible substrate: the strain effect', *The Journal of Physical Chemistry C*, 112: 12602-05.

Yuan, Hongyi, Irina J Zvonkina, Abdullah M Al-Enizi, Ahmed A Elzatahry, Jeffrey Pyun, and Alamgir Karim. 2017. 'Facile assembly of aligned magnetic nanoparticle chains in polymer nanocomposite films by magnetic flow coating', *ACS applied materials & interfaces*, 9: 11290-98.

Zaccardi, Federica, M. Gabriella Santonicola, and Susanna Laurenzi. 2018. 'Quantitative assessment of nanofiller dispersion based on grayscale image analysis: A case study on epoxy/carbon nanocomposites', *Composites Part A: Applied Science and Manufacturing*, 115: 302-10.

Zakaria, Muhammad Razlan, Muhammad Helmi Abdul Kudus, Hazizan Md Akil, and Mohd Zharif Mohd Thirmizir. 2017. 'Comparative study of graphene nanoparticle and multiwall carbon nanotube filled epoxy nanocomposites based on mechanical, thermal and dielectric properties', *Composites Part B: Engineering*, 119: 57-66.

Zaldivar, Rafael J, James P Nokes, and Hyun I Kim. 2014. 'The effect of surface treatment on graphite nanoplatelets used in fiber reinforced composites', *Journal of applied polymer science*, 131.

Zaman, Izzuddin, Hsu-Chiang Kuan, Qingshi Meng, Andrew Michelmore, Nobuyuki Kawashima, Terry Pitt, Liqun Zhang, Sherif Gouda, Lee Luong, and Jun Ma. 2012. 'A facile approach to chemically modified graphene and its polymer nanocomposites', *Advanced Functional Materials*, 22: 2735-43.

Zaman, Izzuddin, Tam Thanh Phan, Hsu-Chiang Kuan, Qingshi Meng, Ly Truc Bao La, Lee Luong, Osama Youssf, and Jun Ma. 2011. 'Epoxy/graphene platelets nanocomposites with two levels of interface strength', *Polymer*, 52: 1603-11.

Zhang, Gengyu, Mingfen Wen, Shuwei Wang, Jing Chen, and Jianchen Wang. 2018. 'Insights into thermal reduction of the oxidized graphite from the electro-oxidation processing of nuclear graphite matrix', *RSC advances*, 8: 567-79.

Zhang, Hao-Bin, Ji-Wen Wang, Qing Yan, Wen-Ge Zheng, Cao Chen, and Zhong-Zhen Yu. 2011. 'Vacuum-assisted synthesis of graphene from thermal exfoliation and reduction of graphite oxide', *Journal of Materials Chemistry*, 21: 5392-97.

Zhang, Hao-Bin, Wen-Ge Zheng, Qing Yan, Zhi-Guo Jiang, and Zhong-Zhen Yu. 2012. 'The effect of surface chemistry of graphene on rheological and electrical properties of polymethylmethacrylate composites', *Carbon*, 50: 5117-25.

Zhang, Hengji, Alexandre F Fonseca, and Kyeongjae Cho. 2014. 'Tailoring thermal transport property of graphene through oxygen functionalization', *The Journal of Physical Chemistry C*, 118: 1436-42.

Zhang, Qiangjun, Yong C Wang, Colin G Bailey, Richard KK Yuen, Joshua Parkin, Wei Yang, and Cristina Valles. 2018. 'Quantifying effects of graphene nanoplatelets on slowing down combustion of epoxy composites', *Composites Part B: Engineering*, 146: 76-87.

Zhang, Weixia, Jiecheng Cui, Cheng-an Tao, Yiguang Wu, Zhanping Li, Li Ma, Yuquan Wen, and Guangtao Li. 2009. 'A strategy for producing pure single-layer graphene sheets based on a confined self-assembly approach', *Angewandte Chemie International Edition*, 48: 5864-68.

Zhang, Wenkai, Yanshan Zhan, Xiuxiu Gao, Runming Li, Weiwei Zhu, Hao Xu, Baoying Liu, Xiaomin Fang, Yuanqing Xu, and Tao Ding. 2018. 'Effect of oxygen functionalities of graphene oxide on polymerization and thermal properties of reactive benzoxazine nanocomposites', *Macromolecular Research*, 26: 77-84.

Zhang, Xi, Ouassima Alloul, Qingliang He, Jiahua Zhu, Michael Joseph Verde, Yutong Li, Suying Wei, and Zhanhu Guo. 2013. 'Strengthened magnetic epoxy nanocomposites with protruding nanoparticles on the graphene nanosheets', *Polymer*, 54: 3594-604.

Zhang, Xiang, Ying Huang, and Panbo Liu. 2016. 'Enhanced electromagnetic wave absorption properties of poly (3, 4-ethylenedioxythiophene) nanofiber-decorated graphene sheets by non-covalent interactions', *Nano-micro letters*, 8: 131-36.

Zhang, Yanli, Yan Wang, Junrong Yu, Lei Chen, Jing Zhu, and Zuming Hu. 2014. 'Tuning the interface of graphene platelets/epoxy composites by the covalent grafting of polybenzimidazole', *Polymer*, 55: 4990-5000.

Zhang, Ying Yan, and YuanTong Gu. 2013. 'Mechanical properties of graphene: Effects of layer number, temperature and isotope', *Computational materials science*, 71: 197-200.

Zhang, Zhongshen, Linda Zou, Cyril Aubry, Mustapha Jouiad, and Zhengping Hao. 2016. 'Chemically crosslinked rGO laminate film as an ion selective barrier of composite membrane', *Journal of Membrane Science*, 515: 204-11.

Zhao, Shuai, Haiyan Chang, Shuju Chen, Jian Cui, and Yehai Yan. 2016. 'High-performance and multifunctional epoxy composites filled with epoxide-functionalized graphene', *European Polymer Journal*, 84: 300-12.

Zhao, Xin, Qinghua Zhang, Dajun Chen, and Ping Lu. 2010. 'Enhanced mechanical properties of graphene-based poly (vinyl alcohol) composites', *Macromolecules*, 43: 2357-63.

Zhao, Xingchen, Zhengming Zhang, Liaoyu Wang, Kai Xi, Qingqi Cao, Dunhui Wang, Yi Yang, and Youwei Du. 2013. 'Excellent microwave absorption property of graphene-coated Fe nanocomposites', *Scientific reports*, 3: 3421.

Zheng, Qingbin, Zhigang Li, Junhe Yang, and Jang-Kyo Kim. 2014. 'Graphene oxide-based transparent conductive films', *Progress in Materials Science*, 64: 200-47.

Zhou, Jisheng, Huaihe Song, Lulu Ma, and Xiaohong Chen. 2011. 'Magnetite/graphene nanosheet composites: interfacial interaction and its impact on the durable high-rate performance in lithium-ion batteries', *RSC advances*, 1: 782-91.

Zhou, Kangfu, Yihua Zhu, Xiaoling Yang, and Chunzhong Li. 2010. 'One-pot preparation of graphene/Fe 3 O 4 composites by a solvothermal reaction', *New Journal of Chemistry*, 34: 2950-55.

Zhou, Xunfu, Weijian Liu, Xiaoyuan Yu, Yingju Liu, Yueping Fang, Steven Klankowski, Yiqun Yang, James Emery Brown, and Jun Li. 2014. 'Tin Dioxide@Carbon Core–Shell Nanoarchitectures Anchored on Wrinkled Graphene for Ultrafast and Stable Lithium Storage', *ACS applied materials & interfaces*, 6: 7434-43.

Zhou, Yuanxin, Farhana Pervin, Lance Lewis, and Shaik Jeelani. 2007. 'Experimental study on the thermal and mechanical properties of multi-walled carbon nanotube-reinforced epoxy', *Materials Science and Engineering: A*, 452: 657-64.

Zhu, Jiahua, Suying Wei, Atarsingh Yadav, and Zhanhu Guo. 2010. 'Rheological behaviors and electrical conductivity of epoxy resin nanocomposites suspended with in-situ stabilized carbon nanofibers', *Polymer*, 51: 2643-51.

Zhu, Yanwu, Shanthi Murali, Weiwei Cai, Xuesong Li, Ji Won Suk, Jeffrey R Potts, and Rodney S Ruoff. 2010. 'Graphene and graphene oxide: synthesis, properties, and applications', *Advanced materials*, 22: 3906-24.

Zielinski, Patrik, Matthias Kühne, Daniel Kärcher, Federico Paolucci, Peter Wochner, Sven Fecher, Jakub Drnec, Roberto Felici, and Jurgen H Smet. 2019. 'Probing Exfoliated Graphene Layers and Their Lithiation with Microfocused X-rays', *Nano letters*, 19: 3634-40.

Zubir, Nor Aida, Christelle Yacou, Julius Motuzas, Xiwang Zhang, and João C. Diniz da Costa. 2014. 'Structural and functional investigation of graphene oxide–Fe3O4 nanocomposites for the heterogeneous Fenton-like reaction', *Scientific reports*, 4: 4594.

# Chapter 4 Appendix

## Section 1 Structural analysis

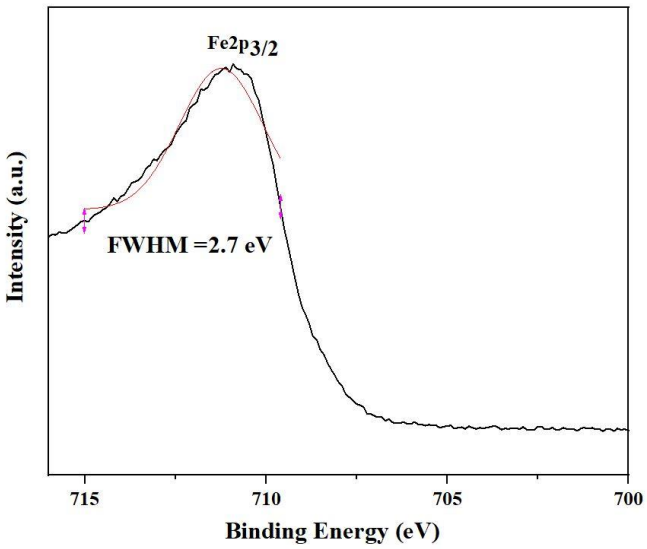


Figure 4.1. Fe2p XPS scan of MNPs@GNPs. Gaussian fitting was performed by Origin software.

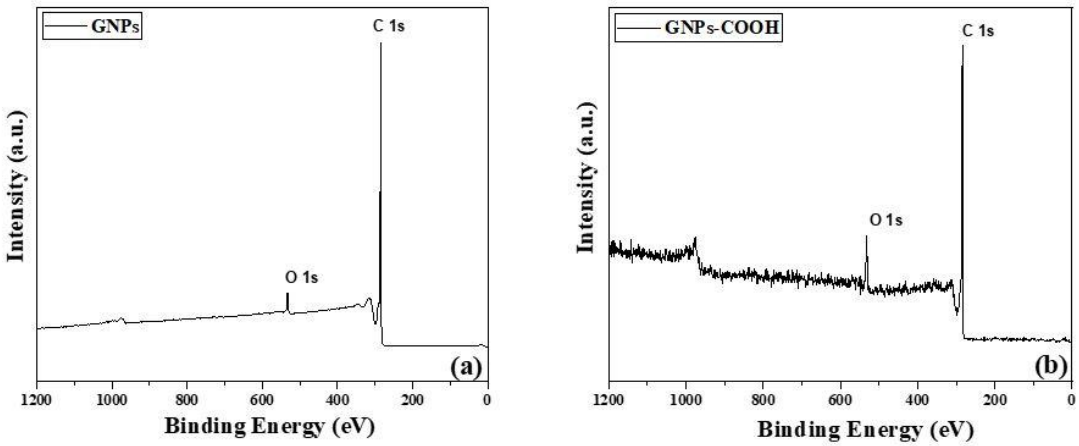


Figure 4.2. XPs survey of GNPs (a) and GNPs-COOH.

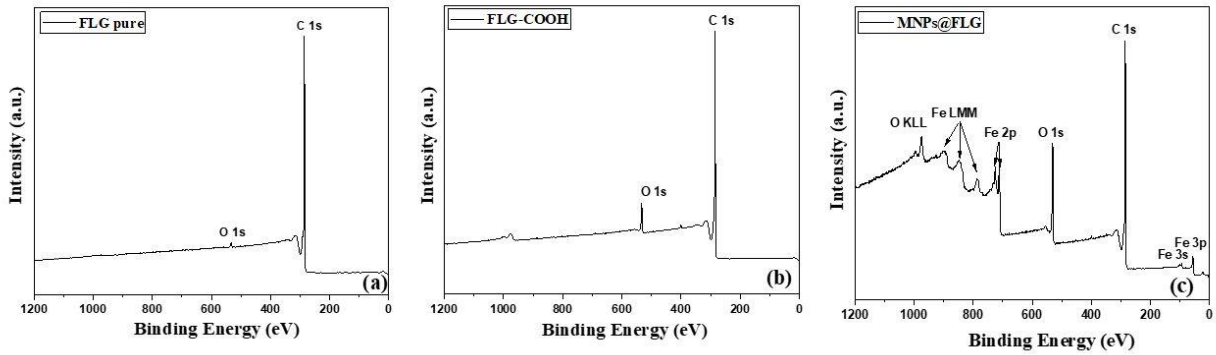


Figure 4.3. XPS survey of FLG (a), FLG-COOH (b) and MNPs@FLG (c).

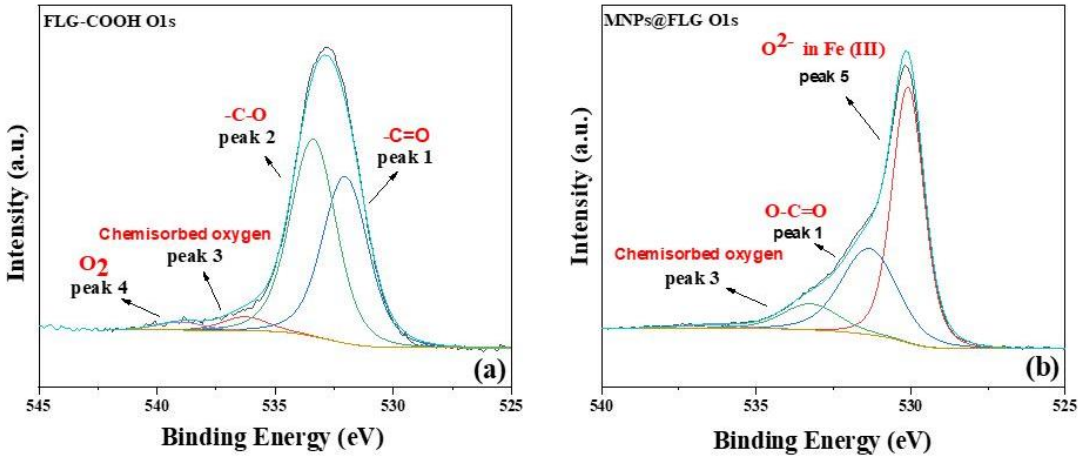


Figure 4.4. O1s scan of FLG-COOH (a), O1s scan of MNPs@FLG (b).

Table 1. Elemental composition calculated from the O1s and Fe2p high resolution XPS spectra (in atomic %).

| **Sample** | | | **Oxygen Content (at %)** | | | | | **Total** |
|---|---|---|---|---|---|---|---|---|
| | Fe-O | O-C=O | -C=O | -C-O | O-C-O | Chemisorbed oxygen | $O_2$ | |
| **GNPs** | - | - | 1.25 | 1.79 | - | 0.32 | 0.17 | 3.54 |
| **GNPs-COOH** | - | - | 3.10 | 2.91 | - | 0.29 | 0.14 | 6.44 |
| **FLG** | | - | 0.36 | 0.48 | - | 0.09 | 0.05 | 0.98 |
| **FLG-COOH** | - | - | 2.42 | 2.87 | - | 0.20 | 0.12 | 5.61 |
| **rGO** | - | - | 0.73 | 6.88 | 3.72 | - | - | 11.33 |
| **MNPs@GNPs** | 8.45 | 5.03 | 0.42 | 1.26 | - | 0.61 | 0.36 | 16.13 |
| **MNPs@FLG** | 3.59 | 2.14 | - | - | - | 0.65 | 0.087 | 6.47 |
| **MNPs@rGO** | 0.6 | - | - | 0.44 | 0.72 | - | - | 1.76 |

## Section 2 Morphological Analysis

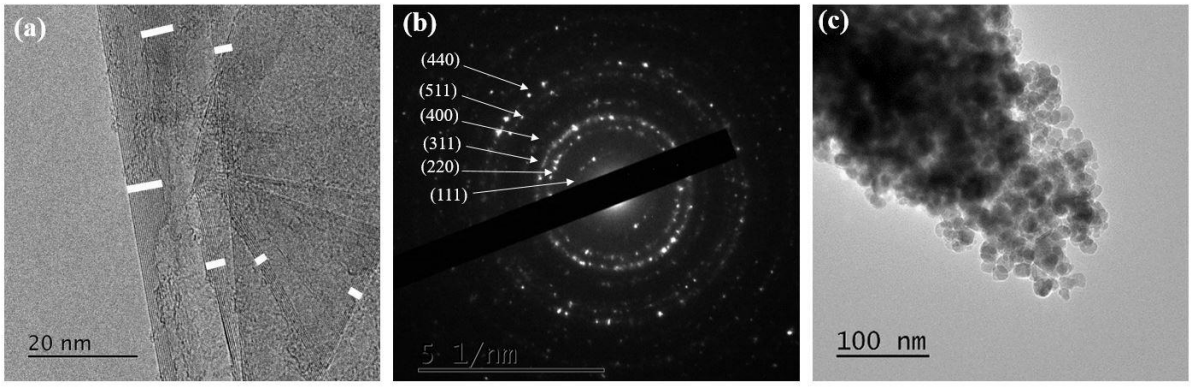


Figure 4.5. A represented example of TEM image of GNPs-COOH (a). Different places were selected and measured the thickness by ImageJ. Electron diffraction pattern of the synthesized magnetite nanoparticles (b), the selected area of the magnetic nanohybrids (c).

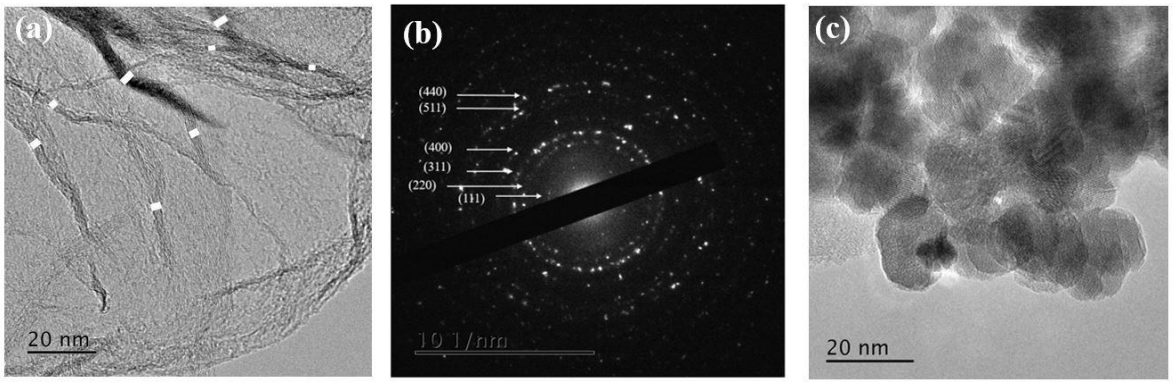


Figure 4.6. A represented example of TEM image of FLG-COOH (a). Different places were selected and measured the thickness by ImageJ. Electron diffraction pattern of the synthesized magnetite nanoparticles (b), the selected area of the magnetic nanohybrids (c).

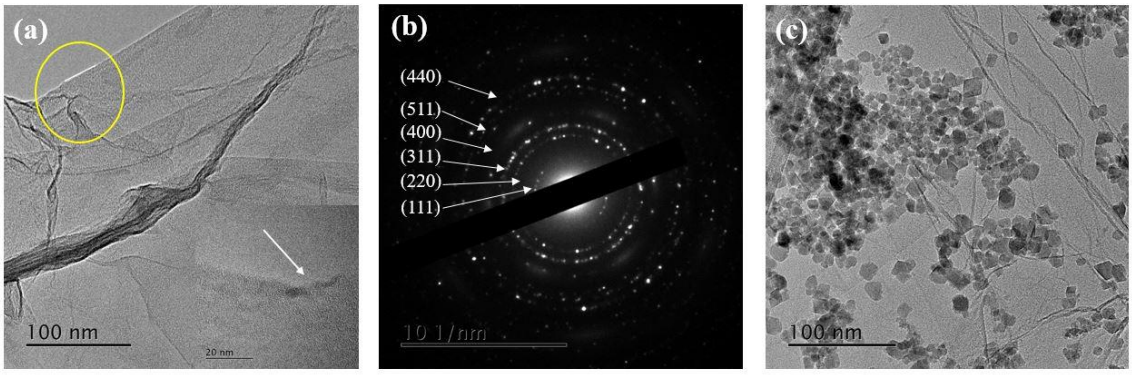


Figure 4.7. A represented example of TEM image of rGO (a). Electron diffraction pattern of the synthesized magnetite nanoparticles (b), the selected area of the magnetic nanohybrids (c). The inset on image (a) show a wavy zone on the rGO surface.

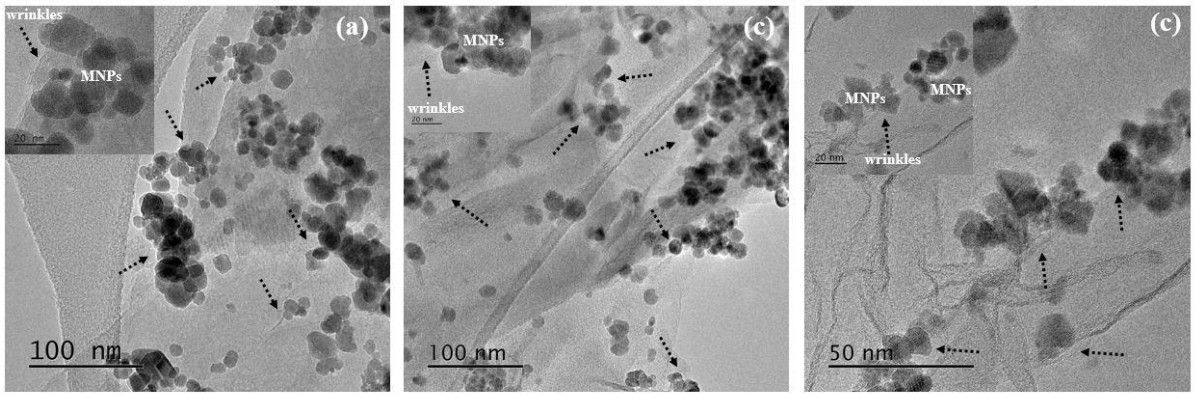


Figure 4.8. TEM images of MNPs attached on GNPs-COOH a), FLG-COOH (b), and rGO (c). The arrows show presence of wrinkles and rough edges on the graphene surface.

# Chapter 5 Appendix

## Section 1 TGA analysis

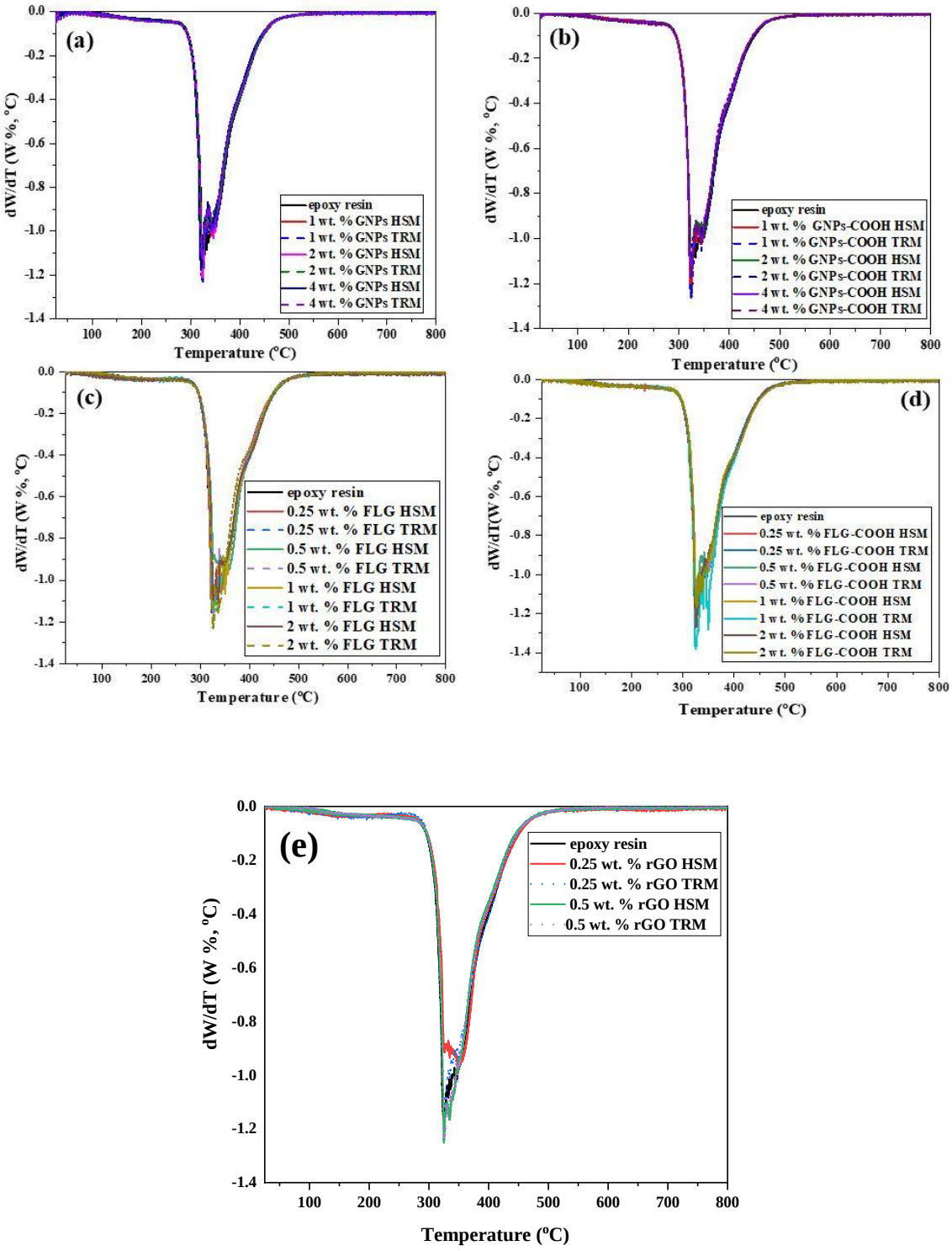


Figure 5.1. Differential Thermogravimetric (DTG) curves of GNPs (a) and GNPs-COOH (b), FLG (c) FLG-COOH (d) and rGO (e)/ epoxy composites mixed by HSM and TRM methods.

## Section 2 Mechanism of reinforcement

Table 1. Storage modulus at 30ºC, the effective modulus ($E_{eff}$) of all the nanocomposites using the rule of mixtures.

| Sample | Storage Modulus 30 ºC (GPa) | $E_{eff}$ (GPa) |
|---|---|---|
| **Epoxy resin** | 1.8±0.07 | - |
| **1 wt. % GNPs HSM** | 1.86±0.11 | 13.8 |
| **1 wt. % GNPs TRM** | 1.9±0.11 | 21.8 |
| **2 wt. % GNPs HSM** | 1.77±0.09 | - |
| **2 wt. % GNPs TRM** | 1.73±0.10 | - |
| **4 wt. % GNPs HSM** | 1.88±0.06 | 5.61 |
| **4 wt. % GNPs TRM** | 1.79±0.12 | 1.32 |
| **1 wt.% GNPs-COOH HSM** | 1.88±0.07 | 18 |
| **1 wt. % GNPs-COOH TRM** | 1.83±0.10 | 7.8 |
| **2 wt. % GNPs-COOH HSM** | 1.5±0.05 | - |
| **2 wt. % GNPs-COOH TRM** | 1.8±0.05 | 1.8 |
| **4 wt.% GNPs-COOH HSM** | 1.7±0.07 | - |
| **4 wt.% GNPs-COOH TRM** | 1.7±0.04 | - |
| **0.25 wt. % FLG HSM** | 1.9±0.11 | 78.76 |
| **0.25 wt. % FLG TRM** | 2±0.09 | 155.69 |
| **0.5 wt. % FLG HSM** | 1.81±0.025 | 5.77 |
| **0.5 wt. % FLG TRM** | 1.8±0.005 | 5.76 |
| **1 wt. % FLG HSM** | 2±0.09 | 41.8 |
| **1 wt. % FLG TRM** | 1.93±0.05 | 27.8 |
| **2 wt. % FLG HSM** | 2.1±0.04 | 31.8 |
| **2 wt. % FLG TRM** | 1.94±0.12 | 15.8 |
| **0.25 wt. % FLG-COOH HSM** | 1.9±0.04 | 78.77 |
| **0.25 wt. % FLG-COOH TRM** | 1.9±0.06 | 78.76 |
| **0.5 wt. % FLG-COOH HSM** | 2.0±0.11 | 78.84 |
| **0.5 wt. % FLG-COOH TRM** | 1.88±0.05 | 32.69 |
| **1 wt. % FLG-COOH HSM** | 1.92±0.05 | 25.8 |
| **1 wt. % FLG-COOH TRM** | 1.94±0.01 | 29.8 |
| **2 wt. % FLG-COOH HSM** | 2.0±0.11 | 21.8 |
| **2 wt. % FLG-COOH TRM** | 2.1±0.12 | 31.8 |
| **0.25 % wt. rGO HSM** | 1.92±0.01 | 94.2 |
| **0.25 % wt. rGO TRM** | 2.04±0.008 | 186.46 |
| **0.5 wt. % rGO HSM** | 2.02±0.04 | 86.54 |
| **0.5 wt. % rGO TRM** | 2.05±0.049 | 98.07 |

*The effective modulus ($E_{eff}$) was calculated for composites that $E_c > E_m$.

# Chapter 6 Appendix

## Section 1 Determination of the minimum magnetic field ($H_{min}$)

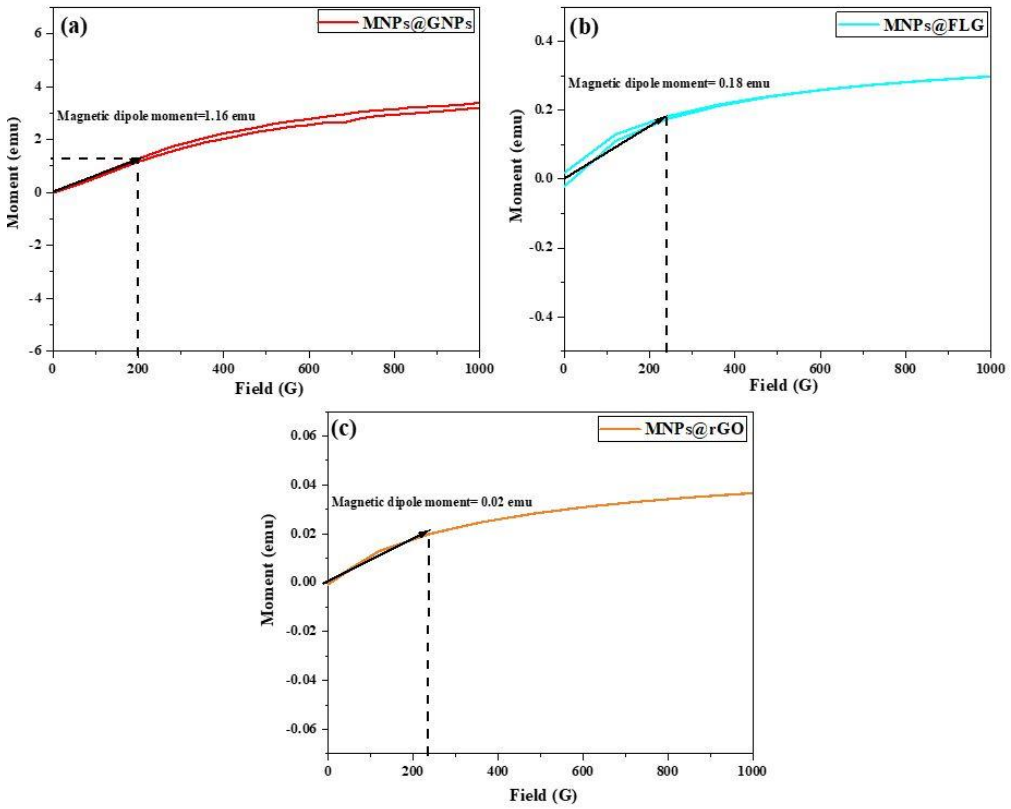


Figure 6.1. VSM plots of MNPs@GNPs (a), MNPs@FLG (b) and MNPs@rGO (c).

## Section 2 Alignment results

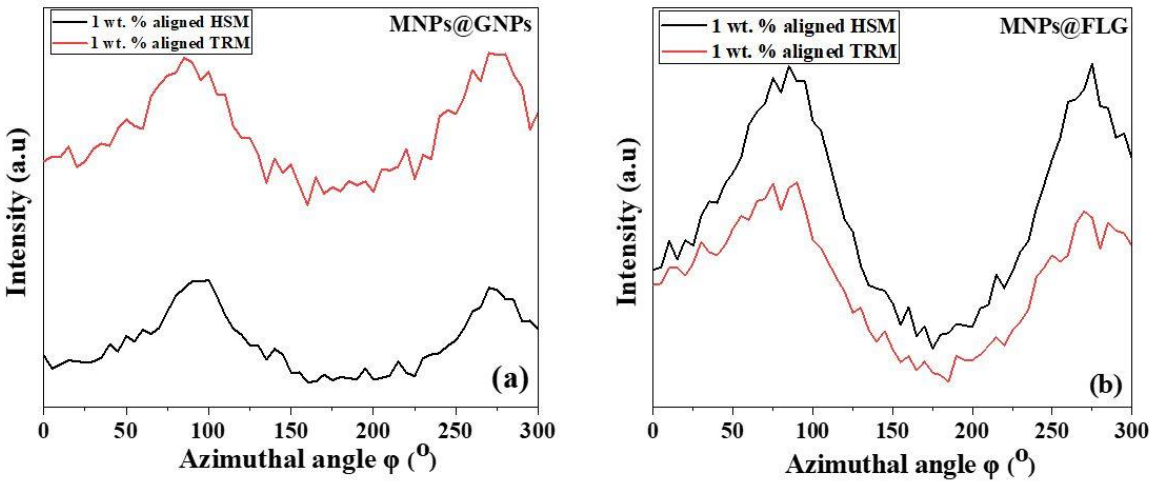


Figure 6.2. Azimuthal angle plots for 2D SAXS images of 1 wt. % aligned MNPs@GNPs/epoxy (a) and MNPs@FLG (b) composites (mixed by HSM and TRM) under the application of 100 mT.

## Section 3 DMA analysis

Table 6.1. Thermomechanical properties of MNPs@GNPs. MNPs@FLG and MNPs@rGO/epoxy composites before and after the alignment. Values of the effective Young's modulus of the MNPs@GNPs, MNPs@FLG and MNPs@rGO reinforcement determined using the measured storage modulus.

| Sample | Storage Modulus 30 ºC (GPa) | $E_{eff}$ (GPa) |
|---|---|---|
| **Epoxy resin** | 1.8±0.07 | - |
| **1 wt. % MNPs@GNPs HSM** | 1.95±0.07 | 95.55 |
| **1 wt. % MNPs@GNPs TRM** | 1.8±0.082 | 1.8 |
| **2 wt. % MNPs@GNPs HSM** | 1.9±0.05 | 33.05 |
| **2 wt. % MNPs@GNPs TRM** | 1.78±0.078 | - |
| **4 wt. % MNPs@GNPs HSM** | 1.9±0.065 | 18.46 |
| **4 wt. % MNPs@GNPs TRM** | 2.01±0.04 | 36.8 |
| **1 wt. % MNPs@GNPs HSM Aligned at 100 mT** | 1.73±0.07 | - |
| **1 wt. % MNPs@GNPs TRM Aligned at 100 mT** | 1.7±0.08 | - |
| **2 wt. % MNPs@GNPs HSM Aligned at 100 mT** | 1.94±0.04 | 45.55 |
| **2 wt. % MNPs@GNPs TRM Aligned at 100 mT** | 1.7±0.05 | - |
| **4 wt. % MNPs@GNPs HSM Aligned at 100 mT** | 1.9±0.02 | 18.46 |
| **4 wt. % MNPs@GNPs TRM Aligned at 100 mT** | 1.9±0.05 | 18.46 |
| **1 wt. % MNPs@GNPs HSM Aligned at 1 mT** | 1.88±0.05 | 51.8 |
| **1 wt. % MNPs@GNPs TRM Aligned at 1mT** | 1.78±0.07 | - |
| **2 wt. % MNPs@GNPs HSM Aligned at 1 mT** | 2.04±0.07 | 76.8 |
| **2 wt. % MNPs@GNPs TRM Aligned at 1 mT** | 1.8±0.08 | 1.8 |
| **4 wt. % MNPs@GNPs HSM Aligned at 1 mT** | 2±0.05 | 35.13 |
| **4 wt. % MNPs@GNPs TRM Aligned at 1 mT** | 1.9±0.07 | 18.46 |
| **0.25 wt. % MNPs@FLG HSM** | 1.65±0.06 | - |
| **0.25 wt. % MNPs@FLG TRM** | 1.77±0.04 | - |
| **0.5 wt. % MNPs@FLG HSM** | 1.9±0.1 | 126.8 |
| **0.5 wt. % MNPs@FLG TRM** | 1.9±0.07 | 126.8 |
| **1 wt. % MNPs@FLG HSM** | 2±0.04 | 126.8 |
| **1 wt. % MNPs@FLG TRM** | 1.87±0.03 | 45.55 |
| **2 wt. % MNPs@FLG HSM** | 1.9±0.097 | 33.05 |
| **2 wt. % MNPs@FLG TRM** | 2.13±0.08 | 104.92 |
| **0.25 wt %. MNPs@FLG HSM Aligned at 1 mT** | 1.77±0.005 | - |
| **0.25 wt. % MNPs@FLG TRM Aligned at 1mT** | 1.96±0.026 | 401.8 |

| | | |
|---|---|---|
| **0.5 wt. % MNPs@FLG HSM Aligned at 1 mT** | 1.71±0.085 | - |
| **0.5 wt. % MNPs@FLG TRM Aligned at 1mT** | 1.7±0.02 | - |
| **1 wt. % MNPs@FLG HSM Aligned at 1 mT** | 1.75±0.075 | - |
| **1 wt.% MNPs@FLG TRM Aligned at 1mT** | 1.95±0.12 | 95.55 |
| **2 wt. % MNPs@FLG HSM Aligned at 1 mT** | 2.05±0.05 | 79.33 |
| **2 wt. % MNPs@FLG TRM Aligned at 1mT** | 2.01 | 67.43 |
| **0.25 wt. % MNPs@rGO HSM** | 2.1±0.075 | 751.8 |
| **0.25 wt. % MNPs@rGO TRM** | 1.9±0.004 | 251.8 |
| **0.5 wt. % MNPs@rGO HSM** | 1.9±0.1 | 126.8 |
| **0.5 wt. % MNPs@rGO TRM** | 1.9 | 126.8 |
| **0.25 wt. % HSM aligned at 7 mT** | 1.88 | 201.8 |
| **0.25 wt. % TRM aligned at 7 mT** | 1.84±0.04 | 101.8 |
| **0.5 wt. % HSM aligned at 7 mT** | 2±0.07 | 251.8 |
| **0.5 wt. % TRM aligned at 7 mT** | 1.9±0.01 | 126.8 |

*The effective modulus ($E_{eff}$) was calculated for composites that $E_c > E_m$.